Modelling and Measurement of the Scatter of Microwaves by Buildings

Ming Sheng Ding

A thesis submitted in partial fulfilment of the requirements of the University of Glamorgan for the degree of Doctor of Philosophy

July 1994

University of Glamorgan

DECLARATION

I declare that this thesis has not been, nor is currently being, submitted for the award of any other degree or similar qualification.

Signed M. S. Ding

Ming Sheng Ding

ACKNOWLEDGEMENTS

I wish to thank my director of studies, Professor Miqdad O. Al-Nuaimi for his guidance and support throughout the research and also to my second supervisor, Dr. Christopher J. Haslett for his help and many useful discussions and suggestions.

I am especially indebted to my colleagues of the radio propagation research group, Mr. Jürgen Richter, Mr. Volker Wille, Dr. Ahkram Hammoudeh and Mr. Richard Stephens, and also Mr. Harmen Sthamer of the software testing group for providing invaluable assistance in measurements. Many thanks go to Chairman of the management committees of the COST projects 210 and 235 Mr. Martin Hall for valuable discussions at meetings and also to Dr. Mireille Levy of the Rutherford Appleton Laboratory (collaboration) for her valuable comments and discussions on theoretical matters.

Special thanks go to the Radiocommunication Agency of DTI for sponsorship of the project and to Mr. Keith Dunk in particular who has worked tirelessly in putting the University of Glamorgan's case for funding.

I would like to thank my mother Kun Fang and my beloved wife Xin Chun for their support, inspiration and understanding.

ABSTRACT

The growing usage and demand for microwave communications has led to the increase in system density, particularly in urban areas, and consequently to the increase in the probability of mutual interference between systems sharing the same frequency band. Satellite and point to point microwave communication systems might have to rely on site shielding to reduce the level of this co-channel interference. In urban areas, there is a great possibility of a building obstructing the interference path, thus providing protection. However, there could be more than one interference path. Scattered interference from other buildings in the vicinity of the site is one which can be found to be almost as harmful as the direct interference.

Although site shielding has long been identified as an interference reduction technique, most studies have been devoted to the protection obtained from the obstruction of interference paths, namely diffraction. There is little information available regarding the effects of building scatter in site shielding. The work reported in this thesis was set to carry out theoretical and experimental investigations and characterisation of building scatter. The studies are aimed at the effects of building scatter on site shielding at microwave frequencies.

Building scatter prediction models are developed based on Fresnel-Kirchhoff diffraction theory and verified against results obtained from measurement campaigns conducted at a frequency of 11.2 GHz using firstly a perfectly conducting reflector and later a number of buildings in urban environments as the scattering obstacles. Scattering prediction models are developed as extending to that originally applicable to the far field for use in the near and very near field regions of the scattering surface. The very near field model is found to be particularly useful in site shielding applications in urban environments. Furthermore, it has been possible to establish the scattering characteristics in terms of angular and distance dependence of the scattering coefficient using the expansions of the Fresnel integral with appropriate approximations. The effects of building features and surface variations, e.g. protruding and recessed features, windows and surface deviations, are analysed and characterised. These effects are particularly significant in the interpretation of measurement results obtained from buildings in typical urban environments.

The thesis provides a prediction procedure which radio system planners and design engineers can use for determining the effects of building scatter on the site shielding factor for specified radio path geometries. The procedure is expected, through UK study group 3, to add considerably to a revised ITU-R (CCIR) procedure and recommendations for building scatter effects in radiowave propagation. The work has also contributed regularly to the technical output of European COST project 235.

LIST OF SYMBOLS AND ABBREVIATIONS

a	building width (m)
a_e	effective width of corner (m)
a_{edge}	width of edge affected area (m)
$\mathbf{A}(r,\theta,\phi)$	amplitude term of electric field intensity (Vm^{-1})
b	building height (m)
BW	beamwidth of scattering patterns (deg)
CCIR	International Radio Consultative Committee
COST	European Collaboration in the Field of Science and Technology
d_p	1/e depth of penetration (m)
$\mathbf{E}$	electrical field intensity (Vm^{-1})
$\mathbf{e}_p$	electric field polarisation factor (dimensionless)
f	frequency (Hz)
$F(\alpha,\beta)$	angular spectrum (dimensionless)
$F(\omega)$, $G(\omega)$	Fresnel integrals
$F(f,\theta,\varepsilon,\mu,\sigma)$	Fresnel reflection coefficient (dimensionless)
g	Rayleigh roughness parameter (dimensionless)
G_s	system gain (dB)
GTD	Geometrical Theory of Diffraction
h	irregularities height of a building surface (m)
$\mathbf{H}$	magnetic field (Am^{-1})
h_{bg}	building ground height above sea level (m)
h_r	receiver height (m)
h_{rg}	receiver ground height above sea level (m)
h_t	transmitter height (m)
h_{tg}	transmitter ground height above sea level (m)
ITU	International Telecommunication Union
$\mathbf{J}$	electric current sheet (Am^{-1})
k	phase constant of free space (rad m^{-1})
L_{fs}	free space loss (dB)
$\mathbf{M}$	magnetic current sheet (Vm^{-1})
MM	Method of Moment
$\mathbf{n}$	normal of surface
P_t	transmitted power (dBm)
P_0	incident interference power (dBm)
P_r	received scattering power (dBm)

r	receiver-building distance (m)
r_a	radius of the first Fresnel zone with respect to azimuth (m)
r_e	radius of the first Fresnel zone with respect to elevation (m)
r_0	transmitter-building distance (m)
R_a	normalised receiver-building distance with respect to azimuth (m)
R_c	radius of a cylinder (m)
R_e	normalised receiver-building distance with respect to elevation (m)
$\mathbf{S}$	scattering coefficient (dB)
$\mathbf{S}_p$	polarisation factor of scattering coefficient (dB)
S_a	azimuth angular dependence of scattering coefficient (dB)
S_{ar}	azimuth distance dependence of scattering coefficient (dB)
S_e	elevation angular dependence of scattering coefficient (dB)
S_{er}	elevation distance dependence of scattering coefficient (dB)
T	ratio of edge effect free area to building width (dimensionless)
$\mathbf{u}_x$, $\mathbf{u}_y$, $\mathbf{u}_z$	unit vectors in rectangular coordinates (dimensionless)
$\mathbf{u}_r$, $\mathbf{u}_\theta$, $\mathbf{u}_\phi$	unit vectors in spherical coordinates (dimensionless)
Z_0	characteristic impedance of free space (Ω)
α_0, β_0, γ_0	incident direction cosines (dimensionless)
α, β, γ	scattering direction cosines (dimensionless)
λ	wavelength (m)
θ	scattering azimuth angle (deg)
θ_c	characteristic angle of corner (deg)
θ_i	incidence angle (deg)
θ_0	incidence azimuth angle (deg)
θ_n	plane azimuth oblique angle (deg)
θ_t	refraction angle (deg)
θ_{trn}	range of azimuth randomly tilted angles (deg)
ϕ	scattering elevation angle (deg)
ϕ_0	incident elevation angle (deg)
μ	permeability (Hm^{-1})
ε	permitivity (Fm^{-1})
σ	conductivity (mho m^{-1})
σ_h	height standard deviation of surface roughness (m)
ρ	reflection coefficient (dimensionless)
Δ	path difference (m)
$\Delta\theta_s$	azimuth specular region (deg)
$\Delta\phi_s$	elevation specular region (deg)
$\Psi(x,y)$	scattering phase term of electric field (dimensionless)

$\Psi_0(x,y)$	incidence phase term of electric field (dimensionless)
ν	propagation constant (dimensionless)
η	refraction index (dimensionless)

TABLE OF CONTENTS

CHAPTER 1 INTRODUCTION

1.1 Introduction

To achieve maximum use of the radio frequency spectrum it is desirable that frequencies are shared between users, such as satellite and terrestrial services. Unless caution is exercised, such sharing can lead to co-channel interference rendering both systems unavailable. Engineers responsible for planning and coordinating radio systems must therefore have access to internationally agreed interference prediction procedures in order to work effectively.

These procedures required for predicting the levels of various interference signals have customarily been published by the International Radio Consultative Committee (CCIR) of the International Telecommunication Union (ITU) in their 4-yearly reports. However, these methods are subject to constant revision in the light of new findings and new demands. In particular, current understanding of the scattering mechanisms giving rise to co-channel interference problems is by no means complete. Moreover, the problems become even more acute as radiocommunication usage intensifies and frequency band sharing increases in urban areas.

In 1984, "European Collaboration in the field of Science and Technology" (COST) established a 6-year project, COST 210 entitled "Influence of the atmosphere on interference between radio communications systems at frequencies above 1 GHz". This is followed in 1991 by COST 235. The primary objective of the projects is to recommend improved procedures for the prediction of statistics of signal levels likely to cause co-channel interference, and for establishing co-ordination distances, so as to minimise the safe distance between radio systems in Europe. The improvements include the reduction in distances between radio systems (and consequent increase in re-use of frequencies in the radio spectrum).

Under the COST projects, the University of Glamorgan, in collaboration with Radiocommunication Agency, the Rutherford Appleton Laboratory and the British Telecom Laboratories has been investigating a potentially very useful interference reduction technique, known as site shielding for reducing the consequences of interference at the receiving terminals of radio systems.

1.2 Site Shielding

Site shielding is an interference reduction technique which utilises obstacles to shield a radio terminal from an interference signal. The shielding may be provided by naturally occurring terrain obstacles, tree banks and man-made obstacles like buildings. The effectiveness of such an interference reduction technique has been the subject of the study by many researchers. The effect of terrain was investigated by Millington [1962], Deygout [1966], Boithias [1973] and King [1966]. Lucia [1972] investigated the possibility of placing an earth station in a pit in order to protect it from terrestrial interference. Additional artificial site shielding measures such as the erection of conducting, solid or small mesh fences was investigated by Scheeren [1988], Lucia [1970] and Gould and Schmitt [1977]. The shielding provided by buildings and trees was investigated by Al-Nuaimi and Haslett [1990] and Al-Nuaimi and Hammoudeh [1993].

Not long ago, the possibility of a building obstructing an interfering path would have been very small. Since that time rapid growth has occurred in both satellite and terrestrial microwave systems to the extent that it is now common for an earth station (particularly mobile and small aperture antennas) to be located in an urban environment with other users of the same frequency band in the vicinity. For example, in a survey carried out by Haslett [1993], it was found that there was only one single parabolic dish antenna on the roof of the Pearl Assurance building in Cardiff in 1986. Presently, there are 23 such antennas on the roof of this building. In such circumstances, site shielding by buildings might prove to be the most effective interference reduction technique for those systems compared to other methods.

In the final report of COST project 210 [1991], the Site Shielding Factor (SSF) is defined as the ratio of the received interference signal power in the absence of the obstacle to that received in the presence of the obstacle. Recent work carried out by Al-Nuaimi and Haslett [1990] to measure the diffraction loss, caused by vertical and horizontal edges of a building in the radio path, showed that a protection level of the order of 35 dB can be obtained when the receiving antenna is placed behind buildings of moderate dimensions. However with trees and other buildings in the vicinity of the site which are commonly found in the urban environment, the protection level is limited to a much lower value by scattering originating from those trees and buildings, particularly the latter. Therefore, the SSF will normally be different from the diffraction loss. Briefly, site shielding is influenced by the following propagation mechanisms [COST 210 (1991)]:

(i) diffraction over and around the building used to shield the receiver;
(ii) scattering from one or more surfaces of other buildings in the vicinity of the site;
(iii) scattering from vegetation (e.g. a group of trees or a single tree) in the vicinity of the site;
(iv) transmission of the signal through buildings.

1.3 Building scatter

Scattering from buildings is an important factor in the context of site shielding since a building can be a significant source of scattering power. The "worst case" is when a building even with moderate dimensions lies in the main beam of a terrestrial station and has an orientation such that specular reflection can take place from one of its sides towards a receiver sharing the frequency band. For the case above, it was found that a scattered signal level could be only 6 dB below that of a direct signal. This happened, for instance, with the building 10 km away from the source and the receiver at 5 km away from the building, for typical system parameters at 10 GHz [COST 210 (1991)]. If this interference arrives at an earth-station which is normally operating with very low wanted signal power a serious interference situation could prevail, even though the site of the earth-station has been shielded by a building from

the direct signal of the terrestrial station.

In these situations as stated in the final report of COST project 210, the effects of scattering from buildings in the vicinity of the radio site will be a limiting factor on the realised values of the site shielding factor.

Buildings have a wide variety of structural details, surface materials, dimensions and locations, all of which determine its scattering characteristics. In general since most buildings consist of, at least partially, a number of flat plane surfaces, building scatter appears to have a strongly directional dependence.

1.4 Building scatter studies and CCIR reports

Building scatter has been studied by a number of researchers for over twenty years. Many experiments of scattered interference from buildings were carried out in urban areas by Bramley and Cherry [1973], Lee [1981], Violette [1983], Noerpel [1986 and 1989] and Ranade [1986 and 1987], etc.. Only recently by Bell Communications Research [Ranade (1987)], a data base of measurements on 2500 buildings has been gathered. These studies provide strong evidence of building scatter interference and its harmful effects in urban areas.

It was Bramley and Cherry [1973] who firstly conducted building scatter study consisting of experimental as well as theoretical investigations. Their experimental work involved measurements, using bistatic radar techniques, of scattered signal levels from tall buildings in urban areas. The geometrical factors determining the level of scattering signal were considered theoretically using a method of physical optics derived from the Helmoltz integral [Baker (1950)], in essence the Huygens-Kirchhoff method [Clemmow (1966), Clarke (1980) and Jull (1981)]. It was shown that the measured results could be reasonably explained using a number of smooth flat elements and corner reflectors which correspond to visible features of the building.

In the late eighties, Noerpel and Ranade [1989] developed a computer aided analysis using the Geometrical Theory of Diffraction (GTD). Their measurements showed that the amount of scattered interference may vary by up to 30 dB depending upon the orientation of buildings, city blocks and streets. Particularly, analysis was conducted for buildings with gross rough features revealing some broadening of the reflected beam. A method was developed to characterise the effect of such building features and the predictions from this method were compared with existing building scattering measurements.

The above two studies, when compared, lead to some similar scattering characteristics of buildings even though the theoretical analyses are different. However, as far as site shielding is concerned, the work of Bramley and Cherry has a more general appeal since it is applicable in the near field range while the work of Noerpel and Ranade is known to be valid only in the far field range which is less relevant when buildings are in the vicinity of a shielded site.

When scatter from large clusters of buildings is being investigated, e.g. city blocks and streets, methods developed for predicting scatter from hillsides are often used. Significant deviations between measured values and estimates from these methods have been shown. Methods were proposed which take into account additional interference caused by scattering from the ground [Giger (1983, 1986a and 1986b)] and [King (1970)]. These models assume scattering to depend on an effective radar cross-section, which is a function of the type of terrain and geometry of the incidence and reflected rays. The implicit distance dependence in such models is that of an isotropic scatterer.

At present in CCIR report 569-4 "The evaluation of propagation factors in interference problems between stations on the surface of the earth at frequency above 0.5 GHz" [1990] planning engineers are directed to CCIR reports 1054 [1990] and 1146 [1990] of terrain scatter [Giger (1983, 1986a and 1986b)] and investigation of building scatter carried out by Bramley and Cherry [1973]. However, since the solutions of building scatter problems are neither complete nor expressed in the form of a general comprehensive prediction procedure,

according to report 569-4, it is necessary to conduct further analytical and experimental investigation to establish a prediction procedure for the evaluation of the scattered signal strength from buildings. This is also identified as one of three main areas of COST 235 which is the investigation of the influence of the radio propagation medium and terrain features on site shielding. Here terrain is also meant to include buildings.

1.5 Objectives of the research

The overall aim of this research project has been to respond to radio system planners and users needs by carrying out experimental and theoretical investigations of building scatter of radiowaves and its effects on site shielding. The main objectives are listed below:

i) To theoretically characterise the behaviour of building scattering and develop a prediction model which can be used as a suitable tool to identify and analyse the building scattering problems arising in site shielding applications;

ii) To experimentally investigate scattering properties of buildings by carrying out measurements of scattered signal levels from various buildings at suitable sites in various measurement configurations;

iii) To develop a prediction procedure based on Objectives 1 and 2 for use by planning and design engineers primarily aimed at installing microwave radio systems in urban areas.

A license was obtained to operate a 10 mW carrier wave transmitter at a frequency of 11.2 GHz needed in experimental measurement campaigns. Measurements obtained would be extremely relevant and useful to radio system designers as this frequency band is heavily used and shared between terrestrial and satellite services yet no interference problem would be posed to existing services as this frequency lies in the guard band between the high and low band allocations of British Telecom's national microwave network.

1.6 Summary of the Thesis

Following this introductory chapter, Chapter 2 reviews the theory used by Bramley and Cherry [1973] and terrain scatter [Giger (1983 and 1986)] recommended as possible solutions for building scatter by the CCIR report. Other theories applied in general to scattering problems are also examined. In particular, discussion is conducted into the Fresnel-Kirchhoff diffraction theory and the ray trace technique of the Geometric Theory of Diffraction (GTD). A decision is made emphasising the need to consider, in site shielding applications, short radio paths whose lengths are comparable to building dimensions. Kirchhoff diffraction theory is introduced using a coordinate system suitable for building scattering problems.

Chapter 3 describes the development of theoretical prediction models in the far, near and very near field models. The very near field prediction model particularly applies to site shielding applications involving a more accurate consideration of ray path lengths from building surfaces. These theoretical prediction models are verified using the measured results of scattering signal levels from a 2.44 m by 2.44 m perfectly conducting reflector erected in an open field.

Chapter 4 contains a theoretical study of the scattering behaviour of building structural and surface features such as protruding and recessed sections, windows and surface deviation roughness. It is noted that the results of this study are not necessarily meant to predict accurately the effects of building features on building scattering, but to identify those features which most significantly affect radiowave propagation and give estimates of their effects on the scattering signal levels.

The validity of any prediction model can only be ascertained by means of experimental verification. A significant part of the work reported in this thesis is the conduction of an experimental campaign which yielded results against which prediction models can be compared using real buildings as scattering obstacles. Chapter 5 describes this experimental

programme and give details of measurements of scatter signal levels from a number of buildings carefully selected in urban areas.

Chapter 6 is devoted to discussion of the measured results and contrast these with predicted results to characterise the scattering behaviour of buildings with regard to azimuth angle variation, distance dependence and polarisation of incident signal. The comparisons which show generally good agreement have led to simpler representation of the scattering patterns in terms of pattern beamwidth, angular and distance dependence in both specular and non specular regions. Consideration of reflection loss coefficients of building surface materials is also given both experimentally and theoretically. In addition building structural features of corners, window contents and surfaces deviation roughness are analysed and discussed in the light of the results obtained.

Chapter 7 utilises the closely related results of the scattering properties of buildings obtained from both experimental and theoretical studies to establish a well structured prediction procedure for building scatter suitable for use in site shielding. The procedure can also be used for building scattering in urban radiowave propagation for well defined path geometries. In the final chapter conclusions of the research project are summarised. One main conclusion is that the proposed prediction procedure represents a significant improvement to the current CCIR procedure on building scatter. The project has also contributed significantly to the measurement data available on building scatter.

CHAPTER 2 THEORETICAL METHODS FOR BUILDING SCATTER

2.1 Introduction

Building scatter as a mechanism of microwave propagation is essentially a process of electromagnetic wave radiation. In theoretically describing such a process, the complexity of the problem when applied to practical buildings becomes clear. Realistically speaking, an exact mathematical solution is virtually impossible and practically unnecessary. All well established theories for radiation problems and applications, in physical optics [Baker (1950), Beckmann (1968) and Fock (1965)] or geometrical optics with asymptotic diffraction theory [Keller (1953) and Kouyoumlian (1975)] are subject to certain simplifying assumptions. In an attempt to approach a mathematical solution of the problem, appropriate assumptions and approximations made are justified. The solution is provided by considering the microwave frequency used and the scattering geometry in the site shielding environment. Fresnel-Kirchhoff diffraction theory is closely examined and its wide application to radiation problems at high microwave frequencies and for large dimension apertures is demonstrated.

2.2 General approach

Electromagnetic wave scatter is the term used to describe the phenomenon by which energy is transported by means of a wave re-radiated from scattering obstacles.

2.2.1 Radiation of reflection and scatter

Building scatter is basically a process of electromagnetic interaction which takes place at the boundary between free space and building surfaces, when an electromagnetic wave in free space is incident on the surfaces. Currents and voltages of varying intensities are induced in the surfaces. The intensities of such distributions are dependent on the electrical properties of

building surface materials such as brick, concrete, window glass and frames, etc. These oscillations set up electric and magnetic fields in the region around the surface which represent both stored and radiated energy. The total field scattered from the surface in a certain direction is the sum of elementary waves scattered in that direction by each elementary scatterer on the surface. As each elementary wave is described not only by its amplitude, but also by its phase, this sum will be a phasor sum. The phases of these elementary scatters are dependent on building surface geometry and materials. Different phases usually result from different ray paths. The directional characteristic of this radiated energy is known as the radiation pattern. This is usually defined as the plot of the electric field intensity at a fixed distance from the surface as a function of angle measured in the particular plane for which the pattern applies.

2.2.2 Possible assumptions about buildings

With respect to the radiation process discussed above, a complete building of a general type is clearly much too complex an object to permit making an exact theoretical prediction of its scattering properties. Indeed, in order to arrive at a solution that lends itself to a characterisation of the general scattering properties of a building surface, not involving too complex mathematical calculations, certain simplifying assumptions have to be made. These are outlined below:

2.2.2.1 Perfect conductivity

The first assumption is that building surfaces are considered to possess perfect conductivity. Although perfect conductivity is never realistic, it would considerably simplify the theoretical analysis. The errors introduced are actually not as serious as they might appear at first sight. Assuming building surfaces to be perfectly conducting amounts to a worst case, as far as interference is concerned, since a perfect conductor has no absorption or transmission losses, resulting in all the incident energy being reflected. The variety of lossy dielectric materials that

make up building surfaces such as bricks, concrete and glass etc. will have complex reflection coefficients, and in general, their magnitudes will be less than 1. Therefore, treating these materials as perfect conductors will not actually affect the relative phase of the reflected signal.

2.2.2.2 Rectangular smooth surfaces

The most modern buildings consist, at least in part, of vertical rectangular flat surfaces of brick, concrete, glass and pebble-dash etc. extending over dimensions much larger than the wavelengths considered. Whether a surface is smooth or rough can be generally decided in comparison with the wavelength according to the Rayleigh criterion of rough surfaces [Kerr (1951)]. This is

$$h \leq \frac{\lambda}{8\cos\theta} \qquad 2.1$$

where h represents the height irregularities of a building surface, λ is the wavelength and θ is the incident angle relative to the normal of the surface. A surface satisfying equation 2.1 can be considered as smooth. Generally speaking, most of building surfaces are smooth at the frequency of interest (11.2 GHz) except those covered with pebble-dash which appears rough with large values of h at small incident angles.

Nevertheless, it is helpful and relevant to consider the basic scattering properties of buildings as those corresponding to rectangular, smooth and perfectly conducting reflectors. After the establishment of a theoretical framework, the realities can be restored by further incorporating the reflection coefficients of building surfaces and in the case of statistical surface roughness, encountered in pebble-dash, introducing the Rayleigh roughness parameter [Beckmann (1967)].

2.3 Theoretical solutions of reflections from a perfectly conducting reflector

The calculating of radiated fields can be based on current distribution on the radiating structure or the principle of Huygens who proposed a geometrical theory of light propagation based on wavelets.

2.3.1 Current distribution radiation

The earliest practical electromagnetic wave radiation was with antennas of wire structures operating at relatively low frequencies. In the case of a dipole antenna, for example, the dimension of the structure is proportional to the wavelength of radiated electromagnetic waves. Calculation of their radiated field is based on the current in the structure. For electrically small surfaces, the principal approach is to use the method of moments (MM) [Newman (1984) and Medgyesi-Mitschang (1985)]. With numerical computation techniques and tools, it is a powerful means to calculate the scattering field of complex structures. In principle the method is exact, but usually the current distribution is not known exactly and approximations have to be made. This approach is computationally intensive. At the frequency 11.2 GHz, the analysis of radiation problems of a perfectly conducting reflector as large as practical buildings, whose dimensions extend over a thousand wavelengths, would be very tedious and inappropriate.

2.3.2 Babinet's principle

Babinet's principle [Booker (1946) and Jordan (1968)] states that the sum of the fields, taken separately, beyond any two complementary absorbing screens will add to produce the field that would exist there without any screen. In electromagnetic wave propagation at radio frequencies, thin perfectly absorbing screens are not available, and one is concerned with perfectly conducting screens. Hence, Babinet's principle relates the diffracted field produced by a conducting plane of arbitrary shape to the diffracted field of an aperture of the same

shape in a conducting screen. The diffracting obstacles are complementary in the sense that, fitted together, they form a plane conducting surface of infinite extent. According to this, the reflected or scattered field produced by a perfectly reflecting plane can be considered as the diffracted field produced by an aperture of the same shape in a conducting screen with its imaginary source located at the virtual image of the actual source reflected in the plane of the screen.

2.3.3 Huygens principle

The explanation of the phenomenon of diffraction really began with Huygens famous construction, now known as Huygens principle which is a cornerstone of classical physics and is often used as the starting point of classical diffraction theory. The principle states that each point on a propagating wave front can be considered as a secondary source radiating a spherical wave. The diffraction of electromagnetic waves can be demonstrated using Huygens principle. This is understandable in view of the simplicity and strength of Huygens original idea. But, the difficulty seems to arise from the fact that whereas spherical waves are a natural physical entity, they are rather clumsy from a mathematical viewpoint.

2.3.4 Diffraction theories using plane waves

A perfectly conducting reflector may be described in two ways when it is illuminated by electromagnetic waves. Firstly, as an area of a surface with a radiating field distribution across it, the field being negligible outside the illuminated area. Calculation of this reradiated field in the forward direction can be derived from the tangential field in the plane of the radiating aperture. The approximations made are that the field outside the aperture is usually assumed negligible and that in the aperture is taken as the incoming wave. The method is essentially that of optics called the Huygens-Kirchhoff method, or simply the Kirchhoff method, and is well established as sufficiently accurate for the fields of apertures large compared to the wavelength [Clemmow (1966), Collin and Zucker (1969) and Rhodes (1974)].

Secondly, considering the diffraction effects of the aperture boundary edges together with the reradiation due to the induced currents at the conducting screen outside the aperture. This method is the so called the Geometric Theory of Diffraction (GTD). It is Keller's [1953] name for an approximate method of solving diffraction problems which combines the principles of geometrical optics with asymptotic diffraction theory. Following Keller, the other main contributions are by [Kouyoumlian (1975), Jones (1979) and James (1976)].

Generally speaking in relation to the above two methods, one is based on aperture field radiation, the other is on aperture edge diffraction. Both apply to large apertures. In other words, the surface outside the area in the first case is absolutely absorbing and in the second is perfectly reflecting. They tend to be complementary in that where one fails the other may succeed. Clearly in practice, none of these two idealised situations is strictly true.

Comparing the two methods, one of the decisive factors would be in the emphasis of their applications. GTD has its discontinuity across geometrical optical boundaries around for which the solutions are essentially obtained from Kirchhoff diffraction theory. For the fields in the lateral and rear directions of apertures, it is convenient to assume diffraction is due to an edge, rather than an aperture, effect. In cases of reflection and scatter [Beckmann (1963)] and [Bramley and Cherry (1973)], Kirchhoff method is found to be usually adequate for field calculations in front of apertures. In practice, it is perfectly sound to consider the aperture illumination only simply due to the fact that fields reradiated from the screen are much weaker than actual background scatter experienced in practical situations. If these fields are ignored, Kirchhoff diffraction theory will be relatively simple to apply. Most importantly, the solution of Kirchhoff-method has an explicit phase expression representing ray path differences from building surfaces which allow diffraction fields to be considered in the near field while the geometric theory of diffraction has to assume the observation point is in the far field range. This has proved to be a key point in the applications of the former to scattering problems in the site shielding environment.

2.4 Coordinates, plane waves and boundary conditions

It is useful to discuss in this section some relevant theoretical considerations to solutions of the scatter problems.

2.4.1 A coordinate system

A coordinate system is shown in figure 2.1. It consists of both rectangular and spherical systems. Noticeably this spherical system is different from the conventional spherical system described in text books. In the latter, the direction u of an elementary plane-wave component is specified in terms of polar angle θ and azimuth angle ϕ of figure 2.2 see for example [Jull (1984)]. The polar angle θ is the angle between the direction of u and the z-axis. The azimuth plane is the x-y plane, and the azimuth angle ϕ is taken as the angle between the directions of the projection of u on to the azimuth plane and the x-axis. The x-z plane is usually considered as the aperture plane. The original direction cosines are

$$\begin{aligned} \alpha &= \sin\theta\cos\phi \\ \beta &= \sin\theta\sin\phi \\ \gamma &= \cos\theta \end{aligned} \qquad 2.2$$

and $\alpha^2+\beta^2+\gamma^2=1$.

It is somewhat inconvenient that these definitions are inconsistent with the conventional concepts of azimuth angle θ and elevation angle ϕ in radio propagation applications. The azimuth angle θ should be the angle between the direction of **u** and the y-z plane. The elevation angle ϕ should be the angle between the direction of **u** and the x-z plane. The x-y plane can be considered as the aperture plane. It can be shown that the direction cosines are

$$\alpha = \sin\theta\cos\phi$$
$$\beta = \sin\theta \qquad 2.3$$
$$\gamma = \cos\theta\cos\phi$$

and confirm that $\alpha^2 + \beta^2 + \gamma^2 = 1$.

The direction **u** of a plane wave propagating in free space can be conveniently specified by the direction cosines (α, β, γ) and the unit vectors ($\mathbf{u}_x$, $\mathbf{u}_y$, $\mathbf{u}_z$), which are the components along the Cartesian axes. Thus

$$\mathbf{u} = \mathbf{u}_x\alpha + \mathbf{u}_y\beta + \mathbf{u}_z\gamma \qquad 2.4$$

The unit vectors of direction **u** in the spherical system are

$$\mathbf{u}_r = \mathbf{u}_x \sin\theta\cos\phi + \mathbf{u}_y \sin\phi + \mathbf{u}_z \cos\theta\cos\phi$$
$$\mathbf{u}_\theta = \mathbf{u}_x \cos\theta - \mathbf{u}_y \sin\theta \qquad 2.5$$
$$\mathbf{u}_\phi = -\mathbf{u}_x \sin\theta\sin\phi + \mathbf{u}_y \cos\phi - \mathbf{u}_z \cos\theta\sin\phi$$

and the converse can be shown if the spherical components are known, i.e.

$$\mathbf{u}_x = \mathbf{u}_r \sin\theta\cos\phi + \mathbf{u}_\theta \cos\theta - \mathbf{u}_\phi \sin\theta\sin\phi$$
$$\mathbf{u}_y = \mathbf{u}_r \sin\phi + \mathbf{u}_\phi \cos\phi \qquad 2.6$$
$$\mathbf{u}_z = \mathbf{u}_r \cos\theta\cos\phi - \mathbf{u}_\theta \sin\theta - \mathbf{u}_\phi \cos\theta\sin\phi$$

2.4.2 The general plane wave solution

A plane wave, which is a simple mathematical entity, can never exist as such in the real physical world. However, the plane wave is an exact solution of Maxwell's fundamental field equations. More importantly, its practical significance has long been known as that naturally

occurring fields can be represented by the superposition of either a discrete set or a continuum of plane waves travelling in different directions. In general such a set of plane waves is known as the angular spectrum.

For a plane wave propagating in the direction **u**, fields behave as $\exp(-jk\xi)$ with ξ measured from the origin of figure 2.3. If its vector electric field is $\mathbf{E}_0$ over the plane containing the origin O, then the vector electric field at point P, whose vector position with respect to the origin O is **r**, will be

$$\mathbf{E}(r) = \mathbf{E}_0 \exp(-jk\mathbf{u}\cdot\mathbf{r}) \qquad 2.7$$

k is the phase constant of free space, $k = 2\pi/\lambda$. The distance between the origin and the plane is $\xi = \mathbf{u}\cdot\mathbf{r}$. Since $\mathbf{r} = \mathbf{u}_x x + \mathbf{u}_y y + \mathbf{u}_z z$, the electric field can be written

$$\mathbf{E}(x,y,z) = \mathbf{E}_0 \exp[-jk(x\alpha + y\beta + z\gamma)] \qquad 2.8$$

The electric field, whatever the polarisation, must be orthogonal to u, which is expressed by

$$\mathbf{u}\cdot\mathbf{E}(r) = (\mathbf{u}_x\alpha + \mathbf{u}_y\beta + \mathbf{u}_z\gamma)\cdot(\mathbf{E}_x + \mathbf{E}_y + \mathbf{E}_z) = 0 \qquad 2.9$$

The vector magnetic field **H**(r) must be orthogonal to both **u** and **E**(r), and its phasor amplitude is related to that of **E**(r) by the characteristic impedance $Z_0 (= 120\pi\Omega)$ of free space, so that

$$\mathbf{H}(r) = \frac{1}{Z_0}\mathbf{u}\times\mathbf{E}(r) = \frac{1}{Z_0}(\mathbf{u}_x\alpha + \mathbf{u}_y\beta + \mathbf{u}_z\gamma)\times(\mathbf{E}_x + \mathbf{E}_y + \mathbf{E}_z) \qquad 2.10$$

The vectors **E**, **H** and **u** form a right-hand set.

2.4.3 Kirchhoff's boundary conditions

When an incident plane wave with fields **E**, **H** arrives at an aperture in a conducting screen (in the $z = 0$ plane conveniently) with a unit normal **n**, electromagnetic wave diffraction takes place through the aperture. The Huygens-Kirchhoff method of calculating the diffraction pattern of an aperture as given, for example, by Silver [1984] requires that both electric and magnetic fields in the aperture plane are specified. The diffracted electric field strength can be obtained by calculating the field of a fictitious magnetic current sheet of density $\mathbf{M} = \mathbf{E} \times \mathbf{n}$ in the aperture with **E** the incident electric field [Clemmow (1966)]. Putting $\mathbf{M} = 0$ in the $z = 0$ plane outside the aperture satisfies the boundary condition on the conductor, but $\mathbf{E} \times \mathbf{n} = 0$ in the aperture is not a correct boundary condition and there is an approximation in assuming that the aperture tangential electric field is its undisturbed value. On the other hand, the diffracted electric field can be obtained when an electric current sheet $\mathbf{J} = \mathbf{n} \times \mathbf{H}$ is assumed in the aperture, with **H** the incident magnetic field [Smith 1987]. This is in accordance with the tangential **H** being undisturbed in the aperture but $\mathbf{n} \times \mathbf{H} = 0$ on the conductor is not a valid boundary condition. But Huygens' principle, which requires that there is no backward radiation of the wave front, is satisfied.

2.5 Plane waves representation of aperture radiation fields

Using plane waves, the principle of linear superposition applies, and superposition of individual plane waves travelling in different directions in free space constitutes an exact field solution.

2.5.1 Plane wave spectrum

The fields radiated from an aperture into the half-space $z \geq 0$ will be described in terms of an angular spectrum of plane waves based on a knowledge of the tangential component of the electric field (which can also be the magnetic field) in the aperture plane. The tangential

component of the electric field of any polarisation in the aperture plane can be resolved into two orthogonal, linearly polarised components, conveniently along the x-axis and y-axis. They are independent from each other, so are their radiated fields into the half-space $z \geq 0$. It is convenient to consider the problem as the superposition of two cases: one dealing with y-component only (with x-component set to zero) and the second dealing with x-component only (with y-component set to zero).

If the tangential electric field in the aperture is wholly y-directed, then the x-component of the electric field is identically zero over the entire aperture plane and hence is zero everywhere in the half-space $z \geq 0$ while the other field components are in general non-zero. An angular spectrum $F_y(\alpha,\beta)$ is defined to be such that the y-component of the electric field of the elemental plane wave travelling in the direction (θ,ϕ) is $F_y(\alpha,\beta)d\alpha d\beta$. Then it follows from equations 2.7 and 2.8 that the elemental contribution to the y-component of the electric field at point P in figure 2.3, distance r from O, is

$$dE_y(x,y,z) = F_y(\alpha,\beta)d\alpha d\beta \exp\left[-jk(x\alpha + y\beta + z\gamma)\right] \qquad 2.11$$

The field equations are linear so each wave may be added and integrating this elemental contribution over all allowable values of α and β yields the y-component of electric field at the point P(x, y, z) as

$$E_y(x,y,z) = \int_{-\infty}^{\infty}\int_{-\infty}^{\infty} F_y(\alpha,\beta)\exp\left[-jk(x\alpha + y\beta + z\gamma)\right]d\alpha d\beta \qquad 2.12$$

2.5.2 Inhomogeneous plane waves

For plane waves radiating into the half-space $z' \geq 0$, the domain of the double integration would be $\alpha^2 + \beta^2 \leq 1$. However to be complete, the integration has to be extended to cover all real values of α and β from $-\infty$ to $+\infty$. If $\alpha^2 + \beta^2 \leq 1$, the third direction cosine γ is real, and

must be chosen to be positive so that the plane waves travel into the half-space $z \geq 0$. The plane waves are of the homogeneous type. The wave travels with characteristic speed $1/\sqrt{\mu_0 \varepsilon_0}$ (permeability μ_0 and permittivity ε_0) in free space, and transfers power into the half-space $z \geq 0$.

But if $\alpha^2 + \beta^2 > 1$, the character of the wave changes because γ is purely imaginary

$$\gamma = \sqrt{1 - \alpha^2 - \beta^2} = \pm j\chi \qquad 2.13$$

Substituting this into the phase term of equation 2.12, and the root $\gamma = -j\chi$ must be chosen in order that the field remains finite as $z \rightarrow +\infty$. This leads to equation 2.14.

$$\exp[-jk(x\alpha + y\beta + z\gamma)] = \exp[-jk(x\alpha + y\beta)]\exp(-k\chi z) \qquad 2.14$$

This is a plane wave of inhomogeneous type. The direction of propagation of the wave is parallel to the aperture plane. The amplitude of the field decreases exponentially in the +z-direction, away from the aperture plane. For this reason they are often called evanescent, or disappearing waves.

A complete representation of the fields in the half-space $z \geq 0$ in terms of the angular spectrum of plane waves $F_y(\alpha,\beta)$ must include spectral components over the entire domain $\alpha^2 + \beta^2$. Transitions in the nature of the field occur at $\alpha^2 + \beta^2 = 1$. The completion has important practical consequences. For immediate purposes the most significant thing about being able to extend α and β over all real values is that this formulation lends itself to being expressed in terms of Fourier transforms. In particular it leads to the fundamental Fourier-transform relationship between the field in the aperture in the $z = 0$ plane and the angular plane-wave spectrum.

2.5.3 Fourier transform of angular spectrum

Consider the y-component of the electric field over the aperture plane $z = 0$, and denote it by the additional suffix 'a' as an aperture field. Thus

$$E_{ay}(x,y) = E_y(x,y,0) \qquad 2.15$$

and for the field of equation 2.12

$$E_{ay}(x,y) = \int_{-\infty}^{\infty}\int_{-\infty}^{\infty} F_y(\alpha,\beta)\exp[-jk(x\alpha+y\beta)]d\alpha d\beta \qquad 2.16$$

which states that the aperture field $E_{ay}(x,y)$ is the Fourier transform of the angular plane-wave spectrum $F_y(\alpha,\beta)$. The inverse formula for Fourier transforms yields the angular spectrum as

$$F_y(\alpha,\beta) = \frac{1}{\lambda^2}\int_{-\infty}^{\infty}\int_{-\infty}^{\infty} E_{ay}(x,y)\exp[jk(x\alpha+y\beta)]dxdy \qquad 2.17$$

This means that if we know the tangential component of the electric field over the aperture plane $z = 0$, we can deduce by means of equation 2.17 the angular spectrum. Using this in equation 2.12 leads to knowledge of the fields everywhere in the region $z \geq 0$. This statement is exact, and applies to all the fields in the half-space $z \geq 0$.

2.5.4 Far field approximation

Field propagating into the half-space $z \geq 0$ can be represented by the single function as in equation 2.12. In principle $E_y(x,y,z)$ is determined everywhere in the half space $z \geq 0$ by the double integral; but in practice the integral can be difficult to evaluate. However, there is one important general result which can be obtained immediately for the field at very large distances from a diffracting aperture of finite size. This result will be obtained by evaluating the integral

by the method of stationary phase [Silver (1949)] and [Born and Wolf (1964)].

First, the direction OP of the field point P(x,y,z) in the half-space $z \geq 0$ is identified by a set of direction cosines (α,β,γ). Substituting for the rectangular coordinates $x = r\alpha$, $y = r\beta$ and $z = r\gamma$, the y-component of the electric field becomes

$$E_y(x,y,z) = \int_{-\infty}^{\infty}\int_{-\infty}^{\infty} F_y(\alpha',\beta')\exp\left[-jkr(\alpha\alpha'+\beta\beta'+\gamma\gamma')\right]d\alpha'\,d\beta' \qquad 2.18$$

The integration variables have been written with primes in order to distinguish them from (α,β,γ). The phase of the integral in equation 2.18 can be written in terms of the angle between the two directions (α,β) and (α',β') as

$$kr(\alpha\alpha'+\beta\beta'+\gamma\gamma') = kr\cos\Phi \qquad 2.19$$

If we suppose that the point P is many wavelengths distant from the point of origin O, that is, $kr>>1$, for most of the domain of $\alpha'^2+\beta'^2$ evanescent waves will not contribute. As $\alpha'^2+\beta'^2$ varies over the range of real values the phase in the exponential term of the integrand in equation 2.19 will rotate rapidly through many multiples of 2π, except when $\cos\Phi$ is stationary. This condition of the phase being stationary clearly occurs when $\Phi = 0$ and $\alpha' = \alpha$, $\beta' = \beta$, $\gamma' = \gamma$, which is when the direction of the elemental plane wave coincides with the direction to the field point.

Now suppose that $F_y(\alpha,\beta)$ is bounded and continuous, which means, for example, that it must not contain any discrete delta-function components. This condition implies that the aperture field can be non-zero only over a finite area of the aperture plane, which is a perfectly acceptable condition in practice. Then as angles θ' and ϕ', and hence α' and β', vary over the integration range, neighbouring values of $F_y(\alpha',\beta')$ can occur which have approximately the same amplitude but appear in the integrand of equation 2.19 with opposite phases, hence

almost cancelling each other. Pairs of values of the integrand tending to cancel one another can be expected to occur throughout the entire range of integration, except in the direction in which the stationary-phase condition is satisfied. The only non-negligible contribution to the integrand of equation 2.18 will therefore come from such a direction and its immediate neighbourhood, and the y-component of the electric field at point P may be written as the approximate equation

$$E_y(x,y,z) \approx CF_y(\alpha,\beta)\exp(-jkr) \qquad 2.20$$

in which C is a constant of proportionality. Equation 2.20 shows that the field as $kr \to \infty$ is approximately proportional to the angular spectrum.

This result can be obtained by using the stationary-phase algorithm (see appendix 1) for the double integral of the form

$$I = \iint_D f(x,y)\exp[jKg(x,y)]dxdy \qquad 2.21$$

which has the asymptotic value as $K \to \infty$ given by

$$I \approx \frac{\pm j2\pi}{K\sqrt{g_{xx}g_{yy} - g_{xy}^2}} f(x_0,y_0)\exp[jKg(x_0,y_0)] \qquad 2.22$$

where the positive sign is taken, unless both $g_{xx} < 0$ and $g_{xx}g_{yy} > g_{xy}^2$.

In order to apply the stationary-phase algorithm to the double integral of equation 2.18, it has to change the integration variables $d\alpha' d\beta'$ to $d\theta' d\phi'$, which can be given by the Jacobi's formula ($J \neq 0$) [Abramowitz 1964] of changing integration variables of double integrals as

$$J=\frac{\partial(u,v)}{\partial(x,y)}=\begin{vmatrix}\frac{\partial u}{\partial x} & \frac{\partial v}{\partial x}\\ \frac{\partial u}{\partial y} & \frac{\partial v}{\partial y}\end{vmatrix}\neq 0 \qquad 2.23$$

this leads to $\iint\limits_{\Omega} f(u,v)dudv=\iint f[u(x,y),v(x,y)]|J|dxdy$.

Using the above transformation equation 2.18 can be rewritten in terms of variables θ' and ϕ' as

$$E_y(x,y,z)=\int_{-\infty}^{\infty}\int_{-\infty}^{\infty}F_y(\sin\theta'\cos\phi',\sin\phi')\cos\theta'\cos^2\phi'\exp[-jkr(\alpha\alpha'+\beta\beta'+\gamma\gamma')]d\theta'\,d\phi' \qquad 2.24$$

Then referring to equation 2.21, we can identify the integration variables x with θ', y with ϕ', K with -kr, g(x,y) with $\alpha\alpha'+\beta\beta'+\gamma\gamma'$, f(x,y) with $\cos\theta'\cos^2\phi' F(\sin\theta'\cos\phi',\sin\phi')$, and the stationary conditions x with $x_0=\theta$, y with $y_0=\phi$. Hence with $g_{xx}=-\cos^2\phi$, $g_{yy}=-1$, $g_{xy}^2=0$ and $g(x_0,y_0)=1$, the y-component of the electric field has the asymptotic value, as kr $\rightarrow\infty$, of

$$E_y(x,y,z)\approx\frac{j\lambda}{r}\cos\theta\cos\phi F_y(\alpha,\beta)\exp(-jkr) \qquad 2.25$$

which is the complete version of equation 2.20.

2.5.5 The complete fields

Since the electric field has zero x-component, by assumption, the z-component of the electric field in the half-space $z\geq 0$ follows from equation 2.9 applied suitably in the ratio of

$$E_x:E_y:E_z=0:1:-\frac{\beta}{\gamma} \qquad 2.26$$

Therefore the complete electric field in the half-space $z \geq 0$ is in terms of the angular spectrum $F_y(\alpha,\beta)$

$$\mathbf{E}(x,y,z) = \left(\mathbf{u}_y - \mathbf{u}_z \frac{\beta}{\gamma}\right) \int_{-\infty}^{\infty} \int_{-\infty}^{\infty} F_y(\alpha,\beta) \exp[-jk(x\alpha + y\beta + z\gamma)] d\alpha d\beta \qquad 2.27$$

which has the asymptotic solution for $kr \rightarrow \infty$

$$\mathbf{E}(x,y,z) \approx (\mathbf{u}_y \gamma - \mathbf{u}_z \beta) \frac{j\lambda}{r} F_y(\alpha,\beta) \exp(-jkr) \qquad 2.28$$

If the tangential electric field in the aperture is wholly x-directed, then the y-component of the electric field is identically zero over the entire aperture plane and hence is zero everywhere in the half-space $z \geq 0$. The x-component of the electric field of a plane wave in the direction (θ, ϕ) can be written in terms of an angular spectrum $F_x(\alpha,\beta)$

$$E_x(x,y,z) = \int_{-\infty}^{\infty} \int_{-\infty}^{\infty} F_x(\alpha,\beta) \exp[-jk(x\alpha + y\beta + z\gamma)] d\alpha d\beta \qquad 2.29$$

The x-component of the electric field over the aperture $E_{ax}(x,y)$ is the double Fourier transform of the angular spectrum $F_x(\alpha,\beta)$ as

$$E_{ax}(x,y) = \int_{-\infty}^{\infty} \int_{-\infty}^{\infty} F_x(\alpha,\beta) \exp[-jk(x\alpha + y\beta)] d\alpha d\beta \qquad 2.30$$

The inverse Fourier transform yields the angular spectrum

$$F_x(\alpha,\beta) = \frac{1}{\lambda^2} \int_{-\infty}^{\infty} \int_{-\infty}^{\infty} E_{ax}(x,y) \exp[jk(x\alpha + y\beta)] dx dy \qquad 2.31$$

The complete electric field in the half-space $z \geq 0$ is then expressed in terms of the angular

spectrum $F_x(\alpha,\beta)$ due to the x-component of the aperture field

$$\mathbf{E}(x,y,z)=\left(\mathbf{u}_x-\mathbf{u}_z\frac{\alpha}{\gamma}\right)\int_{-\infty}^{\infty}\int_{-\infty}^{\infty}F_x(\alpha,\beta)\exp[-jk(x\alpha+y\beta+z\gamma)]d\alpha d\beta \qquad 2.32$$

As $kr\rightarrow\infty$, equation 2.31 has the asymptotic value as

$$\mathbf{E}(x,y,z)\approx(\mathbf{u}_x\gamma-\mathbf{u}_z\alpha)\frac{j\lambda}{r}F_x(\alpha,\beta)\exp(-jkr) \qquad 2.33$$

The electric fields radiated into the half-space $z\geq 0$ due to the tangential component of the electric field of any polarisation, by superposition, can be given by the sum of equations 2.27 and 2.32 as

$$\mathbf{E}(x,y,z)=\int_{-\infty}^{\infty}\int_{-\infty}^{\infty}\left[\left(\mathbf{u}_x-\mathbf{u}_z\frac{\alpha}{\gamma}\right)F_x(\alpha,\beta)+\left(\mathbf{u}_y-\mathbf{u}_z\frac{\beta}{\gamma}\right)F_y(\alpha,\beta)\right] \exp[-jk(x\alpha+y\beta+z\gamma)]d\alpha d\beta \qquad 2.34$$

in terms of the two independent angular spectra $F_x(\alpha,\beta)$ and $F_y(\alpha,\beta)$ which are themselves defined by two orthogonal components of the tangential electric field over the aperture plane.

The electric field in far field obtained by combining equations 2.28 and 2.33 is asymptotically for very large $kr\rightarrow\infty$

$$\mathbf{E}(x,y,z)\approx\frac{j\lambda}{r}\exp(-jkr)\left[(\mathbf{u}_x\gamma-\mathbf{u}_z\alpha)F_x(\alpha,\beta)+(\mathbf{u}_y\gamma-\mathbf{u}_z\beta)F_y(\alpha,\beta)\right] \qquad 2.35$$

Converting equation 2.35 from Cartesian components into spherical-polar components, which are a more natural choice for a spherical wave, yields

$$\mathbf{E}(x,y,z)\approx\frac{j\lambda}{r}\exp(-jkr)\left[\mathbf{u}_\theta\cos\phi F_x(\alpha,\beta)+(\mathbf{u}_\theta\sin\theta\sin\phi+\mathbf{u}_\phi\cos\theta)F_y(\alpha,\beta)\right] \qquad 2.36$$

Alternatively, the above electric field components in the half space $z \geq 0$ can be derived from the magnetic field in the aperture plane. When it is assumed that the magnetic aperture field has an x-component while its y-component is zero, so is the y-component of the magnetic field in the half-space $z \geq 0$. The other four components in the half-space $z \geq 0$ exist ($\mathbf{H}_z$, $\mathbf{E}_x$, $\mathbf{E}_y$, $\mathbf{E}_z$). The angular spectrum is given as

$$F_y(\alpha,\beta) = \frac{Z_0}{\lambda^2} \int_{-\infty}^{\infty} \int_{-\infty}^{\infty} H_{ax}(x,y) \exp[jk(x\alpha + y\beta)] dxdy \qquad 2.37$$

Referring to equation 2.10, this corresponds to that derived from the y-component of the electric aperture field. The electric field components are in the ratio of, compared to the x-component of the magnetic field following equation 2.10 as

$$H_x : E_x : E_y : E_z = 1 : \frac{\alpha\beta}{\gamma} : -\frac{\alpha^2 + \gamma^2}{\gamma} : \beta \qquad 2.38$$

Similarly if the magnetic aperture field is in the y-direction while its x-component is zero, the electric field components are in the ratio of, compared to the y-component of the magnetic aperture field as

$$H_y : E_x : E_y : E_z = 1 : \frac{\beta^2 + \gamma^2}{\gamma} : -\frac{\alpha\beta}{\gamma} : -\alpha \qquad 2.39$$

Due to the tangential component of the magnetic field in the aperture plane, the complete electric field radiating into the half space $z \geq 0$ is thus given as

$$\begin{aligned} \mathbf{E}(x,y,z) = \int_{-\infty}^{\infty} \int_{-\infty}^{\infty} \Bigg[& \left(\mathbf{u}_x \frac{\beta^2 + \gamma^2}{\gamma} - \mathbf{u}_y \frac{\alpha\beta}{\gamma} - \mathbf{u}_z \alpha \right) F_x(\alpha,\beta) \\ & + \left(\mathbf{u}_x \frac{\alpha\beta}{\gamma} - \mathbf{u}_y \frac{\alpha^2 + \gamma^2}{\gamma} - \mathbf{u}_z \beta \right) F_y(\alpha,\beta) \Bigg] \exp[-jk(x\alpha + y\beta + z\gamma)] d\alpha d\beta \end{aligned} \qquad 2.40$$

As kr→∞, equation 2.40 has the asymptotic value as

$$\mathbf{E}(x,y,z) \approx \frac{j\lambda}{r}\exp(-jkr)\cos\theta\cos\phi\left[\left(\mathbf{u}_x\frac{\beta^2+\gamma^2}{\gamma}-\mathbf{u}_y\frac{\alpha\beta}{\gamma}-\mathbf{u}_z\alpha\right)F_x(\alpha,\beta)\right.$$
$$\left.+\left(\mathbf{u}_x\frac{\alpha\beta}{\gamma}-\mathbf{u}_y\frac{\alpha^2+\gamma^2}{\gamma}+\mathbf{u}_z\beta\right)F_y(\alpha,\beta)\right] \qquad 2.41$$

In spherical coordinates, it is given as

$$\mathbf{E}(x,y,z) \approx \frac{j\lambda}{r}\exp(-jkr)\left[\left(\mathbf{u}_\theta\cos\theta-\mathbf{u}_\phi\sin\theta\sin\phi\right)F_x(\alpha,\beta)+\mathbf{u}_\phi\cos\phi F_y(\alpha,\beta)\right] \qquad 2.42$$

Equations 2.36 and 2.42 are essentially identical. The Huygens-Kirchhoff method calculating the radiation pattern of an aperture as given by Silver requires that both electric and magnetic fields in the aperture are specified. This is most commonly adopted by superimposing equations 2.36 and 2.42, giving on average

$$\mathbf{E}(x,y,z) \approx \frac{j\lambda}{2r}\exp(-jkr)\left\{\left[\mathbf{u}_\theta(\cos\theta+\cos\phi)-\mathbf{u}_\phi\sin\theta\sin\phi\right]F_x(\alpha,\beta)\right.$$
$$\left.+\left[\mathbf{u}_\theta\sin\theta\sin\phi+\mathbf{u}_\phi(\cos\theta+\cos\phi)\right]F_y(\alpha,\beta)\right\} \qquad 2.43$$

2.6 Interim conclusion

It is useful and adequate to investigate the basic properties of building scatter by considering the radiated field from a perfectly conducting, flat and smooth plane. This simplified model enables a suitable theoretical framework to be established. The method proposed is aperture analysis based on Kirchhoff diffraction theory. With fields assumed negligible everywhere outside the aperture, the limits of integration are the aperture boundaries. A plane wave spectrum field representation is shown by the Fourier transform relationship to aperture fields. It uses the fact that any field can be represented by a superposition of plane waves with amplitudes which can be calculated from the tangential field in the aperture plane. This method

has the advantage of containing explicitly the radiation ray paths which will be found useful in its future application to the near and very near fields.

It should be noted that currently the radiation field expression is only valid at distances very large compared to the radiating aperture dimensions. The accuracy decreases as the angles of observation move away from the main beam of the radiation pattern.

In the next chapter, experiments on a near-ideal reflector are described and the results are analysed. A theoretical model is developed to consider the highly relevant situation to site shielding applications where distances of the order of aperture dimensions are considered.

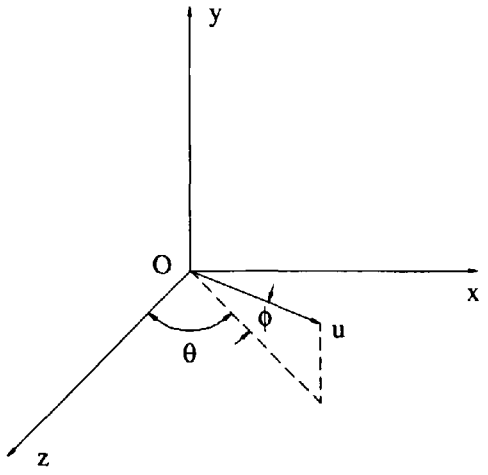

Figure 2.1 The coordinate system.

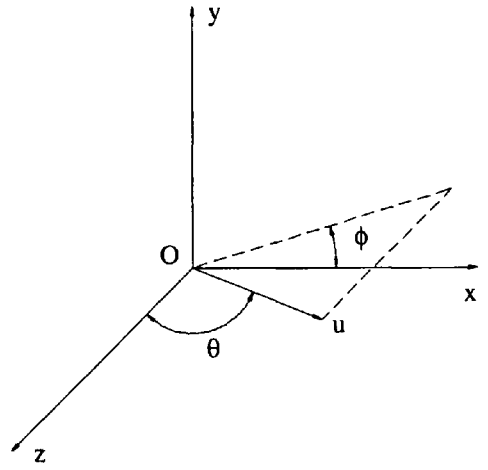

Figure 2.2 An ordinary spherical coordinate system.

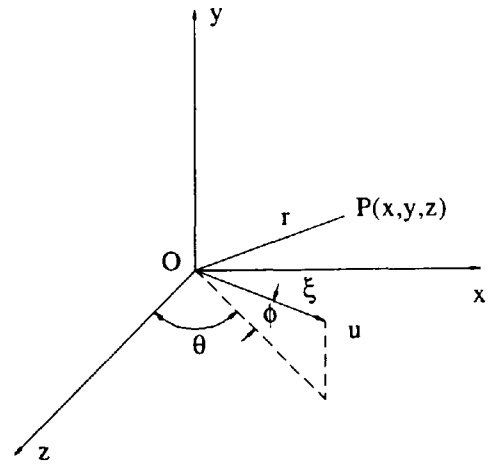

Figure 2.3 Geometry of plane wave propagation in the coordinate system.

CHAPTER 3 DEVELOPMENT OF PREDICTION MODELS

3.1 Introduction

It has become clear throughout the previous chapter, that the Kirchhoff method is going to be used as one of the solutions for building scatter problems. One of the main objectives in this study is to be able to calculate the scattered field strength from buildings. In this chapter, the prediction model in the far field is obtained based on the results of the previous chapter and presented analytically in the form of the angular power spectrum. A preliminary experimental programme using a perfectly conducting reflector is set up to examine the basic scatter properties of a plane surface so that the validity of the theoretical method can be tested. This has led to a further development of the prediction model extending its applicability to the near and very near field regions which have more significance in site shielding applications. The former brings the calculations of scattering field strengths to the well-known Fresnel integral. In the latter case, the approximations inherent in the Fresnel integral render it unsuitable. A very useful field model is described whereby extra terms are considered. A new approximation is introduced which greatly simplifies the numerical calculations and extends the ability to calculate scattering field strengths in closer near field regions, or so-called very near field of the building.

3.2 Theoretical prediction model in the far field

A rectangular building surface a by b is postulated centred in the x-y plane in the coordinate system as shown in figure 3.1. r_0 and r are the transmitter-building and receiver-building distances from the origin O respectively. The azimuth and elevation angles of incidence are θ_0 and ϕ_0 respectively which define the incident direction cosines $(\alpha_0,\beta_0,\gamma_0)$. The azimuth and elevation angles of scattering are θ and ϕ respectively which define the scattering direction cosines (α,β,γ).

3.2.1 Aperture field

Incident waves, namely interference, arriving at a building from wherever the source is, are essentially spherical waves. The aperture field resulting from this illumination consequently has the same form too. However, the most common situations are that interference waves have travelled some considerably long distance before arriving at the building. In this case, even if the incident waves are spherical waves in essence, the spherical radius, which is the distance between the interference source and the building, is much larger than the dimensions of the building, satisfying the Rayleigh far field distance criteria $r \geq 2a^2/\lambda$. Therefore, the part of the wave-front faced by the building can be considered as a plane wave without significant error.

For a perfectly conducting reflector, its aperture field due to plane wave illumination is taken to be the negative of the tangential component of the incoming wave to satisfy the boundary conditions. This tangential component of incident plane waves of any polarisation can be resolved into two orthogonal, linear components with respect to x and y

$$\mathbf{E}_a(x,y) = \mathbf{E}_{ax}(x,y) + \mathbf{E}_{ay}(x,y) \qquad 3.1$$

In fact in the coordinate system of figure 3.1, the x-component and y-component of the aperture field can be conveniently obtained from the two orthogonal components of incident fields which are both in a wave-front plane polarised in azimuth direction $\mathbf{u}_\theta$ and elevation direction $\mathbf{u}_\phi$ of the spherical coordinate respectively. Since the azimuth direction $\mathbf{u}_\theta$ is always parallel to the x-z plane, it is always horizontally polarised. From equation 2.5, it has both x-component and z-component in Cartesian coordinates. The elevation direction $\mathbf{u}_\phi$ has all three components in Cartesian coordinates. The y-component is vertically polarised. When the elevation angle is zero, there is only a y-component. The elevation direction is thus exactly vertical polarisation. These components are unique and complete so that the principle of superposition is satisfied. If assuming that azimuth polarisation and elevation polarisation

components of the incident plane waves have equal amplitude E_0, then the aperture field of equation 3.1 can be given as

$$\mathbf{E}_a(x,y) = -\left[\mathbf{u}_x(\cos\theta_0 - \sin\theta_0 \sin\phi_0) + \mathbf{u}_y \cos\phi_0\right] \\ \text{rect}_a(x)\text{rect}_b(y)E_0 \exp\left[jk(x\alpha_0 + y\beta_0)\right] \qquad 3.2$$

where

$$\text{rect}_a(x) = 1;\ -\frac{a}{2} \le x \le \frac{a}{2} \qquad \text{0 elsewhere} \qquad 3.3$$
$$\text{rect}_b(y) = 1;\ -\frac{b}{2} \le y \le \frac{b}{2}$$

The two orthogonal components of the aperture field are only different in geometrical parameters. Further, so are all the field components based on the Fourier transform of aperture field and angular spectrum. Therefore, identifying any one of them due to one of two orthogonal components of the aperture field would be sufficient. Conveniently, it is assumed to use the aperture field of vertical polarisation.

3.2.2 Analytical solution in the far field

The field solutions obtained in the previous chapter are not yet expressed in their readily usable form since the double integral has not been solved. In terms of the y-component of the electric aperture field given in equation 3.2, the electric field strength of equation 2.43 and $F_y(\alpha,\beta)$ of equation 2.17 in the far field can be written as

$$\mathbf{E}(r,\theta,\phi) = -\left[\mathbf{u}_\theta \sin\theta \sin\phi + \mathbf{u}_\phi(\cos\theta + \cos\phi)\right]\cos\phi_0 \\ \frac{jE_0}{2r\lambda}\exp(-jkr)\int_{-\frac{a}{2}}^{\frac{a}{2}}\int_{-\frac{b}{2}}^{\frac{b}{2}} \exp\left[jk(x\alpha_0 + y\beta_0)\right]\exp\left[jk(x\alpha + y\beta)\right]dxdy \qquad 3.4$$

Since the aperture field is zero outside the surface, the double integral has reduced to the size of the surface. Since its phase term is separable with respect to the integration variables x and y, the double integral is the product of two single integrals.

$$\mathbf{E}(r,\theta,\phi)=\mathbf{e}_p\frac{jE_0}{r\lambda}\exp(-jkr)\int_{-\frac{a}{2}}^{\frac{a}{2}}\exp\left[jkx(\alpha+\alpha_0)\right]dx\int_{-\frac{b}{2}}^{\frac{b}{2}}\exp\left[jky(\beta+\beta_0)\right]dy \qquad 3.5$$

where $\mathbf{e}_p=-\frac{1}{2}\left[\mathbf{u}_\theta\sin\theta\sin\phi+\mathbf{u}_\phi(\cos\theta+\cos\phi)\right]\cos\phi_0$. Using the standard integral

$$\int_{-x_0}^{x_0}\exp(jKx)dx=\frac{2\sin(Kx_0)}{K} \qquad 3.6$$

let $x_0=a/2$ and $K=k(\alpha+\alpha_0)$ with respect to x and x_0=b/2 and $K=k(\beta+\beta_0)$ with respect to y respectively, equation 3.5 becomes

$$\begin{aligned}\mathbf{E}(r,\theta,\phi)&=\mathbf{e}_p\frac{jE_0ab}{r\lambda}\exp(-jkr)\frac{\sin\left[\frac{a\pi}{\lambda}(\alpha+\alpha_0)\right]}{\frac{a\pi}{\lambda}(\alpha+\alpha_0)}\frac{\sin\left[\frac{b\pi}{\lambda}(\beta+\beta_0)\right]}{\frac{b\pi}{\lambda}(\beta+\beta_0)} \qquad 3.7\\ &=\mathbf{e}_p\frac{jE_0ab}{r\lambda}\exp(-jkr)\operatorname{sinc}\left[\frac{a\pi}{\lambda}(\alpha+\alpha_0)\right]\operatorname{sinc}\left[\frac{b\pi}{\lambda}(\beta+\beta_0)\right]\end{aligned}$$

This is the solution of the electric field in the form of sinc functions in the far field.

3.2.3 Power radiation pattern and the scattering coefficient

Complete specification of a field expression includes amplitude and phase. Therefore, in microwave measurements, there are mainly two kinds of measurements. Measurements called scalar are restricted to the amplitudes of waves. Amplitude is usually derived from a power measurement. The method is simple and low cost. The others are called vector measurements which include amplitude and phase of waves. Phase measurements present greater difficulties and consequently are more expensive. Nevertheless, a more important fact from the viewpoint

of radio system planning and interference reduction, scattered signal strengths measured in terms of their relative power are practically sufficient and useful to characterise interference.

The power flow of the scattered waves given by the Poynting vector $\mathbf{S}_r$ is

$$\mathbf{S}_r = \frac{1}{2}\mathbf{E}\times\mathbf{H}^* = \mathbf{u}_r \frac{1}{2Z_0}|\mathbf{E}|^2 \qquad 3.8$$

$\mathbf{H}^*$ is the conjugate of the magnetic field. Replacing the field strength of equation 3.7 leads to a power radiation pattern given by

$$\mathbf{S}_r = \frac{\mathbf{u}_r|\mathbf{e}_p|^2}{2Z_0}\left(\frac{E_0 ab}{r\lambda}\right)^2 \operatorname{sinc}^2\left[\frac{a\pi}{\lambda}(\alpha+\alpha_0)\right]\operatorname{sinc}^2\left[\frac{b\pi}{\lambda}(\beta+\beta_0)\right] \qquad 3.9$$

The power flow of the scattered waves given in equation 3.9 is related to the direct interference signal incident on the front of a building. A more useful quantity is the scattering coefficient which is defined as a ratio of the scattered signal received at some distance away from the building to the direct incident interference signal. The power flow of the direct interference signal is also given by the Poynting vector as

$$S_0 = \frac{E_0^2}{2Z_0} \qquad 3.10$$

The scattering coefficient is then, defined as

$$\mathbf{S} = \frac{\mathbf{S}_r}{S_0} = \mathbf{u}_r|\mathbf{e}_p|^2\left(\frac{ab}{r\lambda}\right)^2 \operatorname{sinc}^2\left[\frac{a\pi}{\lambda}(\alpha+\alpha_0)\right]\operatorname{sinc}^2\left[\frac{b\pi}{\lambda}(\beta+\beta_0)\right] \qquad 3.11$$

From equation 3.11, the scattering coefficient of a reflector can be calculated approximately in the far field. Thus, it is a far field formula, or namely a far field model. The scattering pattern of equation 3.11 consists of two independent patterns with respect to azimuth and elevation

respectively which are a function of building dimensions a and b, incident direction cosines (α_0,β_0) and scattering direction cosines (α,β) but both independent of distance. The amplitude of scattering coefficient has a distance dependence which is inversely proportional to r^2.

The scattering coefficient can be conveniently presented as the logarithmic difference between the power of the scattered signal $\mathbf{P}_r$ and the direct interference signal P_0, it is thus

$$\mathbf{S}(\mathrm{dB}) = \mathbf{P}_r(\mathrm{dB}) - P_0(\mathrm{dB}) \qquad 3.12$$

The direct interference signal power usually can be measured and calculated as the sum of transmitter power P_t, system gain G_s (includes antennas and low noise amplifier gains) and the free space loss L_{fs} as

$$P_0(\mathrm{dBm}) = P_t(\mathrm{dBm}) + G_s(\mathrm{dB}) - L_{fs}(\mathrm{dB}) \qquad 3.13$$

where $L_{fs}(\mathrm{dB}) = 53.43 + 20\log r_0(\mathrm{m})$ at frequency of 11.2 GHz.

3.3 Preliminary experimental programme

In a subject as practical as building scatter, a theoretical prediction model with appropriate assumptions will be useful to radio system planners only if it offers a sensible guide to the physical processes involved and leads to a reasonably accurate quantitative assessment of their effects. The main purpose of this programme is to design suitable experiments to examine the basic scattering properties of a perfectly conducting reflector and the validity of the theoretical prediction model.

3.3.1 Experimental measurements using a basic reflector

Measurements made using a perfectly conducting reflector were designed such that the initial experimental investigation was carried out in a controlled way. This is by no means a substitution of experimental measurements on real buildings but it would help to set up an experimental process which can give validity to the theoretical prediction and observations of the basic scattering properties. This experimental method, using a simplified ideal model to establish a framework, capable of treating real problems is widely used in similar subjects, e.g. [Lee (1981)] and [Violette (1983)].

A perfectly conducting reflector was constructed using a 2.44 m by 2.44 m wooden board covered with aluminium foil. Since the conductivity of aluminium is very large, only wave penetration might be a factor which could affect the reflection. The 1/e depth of penetration d_p can be calculated as [Kraus (1992)]

$$d_p = \frac{1}{\sqrt{f\pi\mu\sigma}} \qquad 3.14$$

For aluminium, conductivity $\sigma=3.5\times10^7$ mho/m and $\mu=1.26\times10^{-6}$ H/m, thus at frequency of 11.2 GHz, the 1/e depth of penetration d_p is less than 1 μm. Therefore, aluminium foil is considered sufficiently thick to ensure that the reflector can be assumed as perfectly reflecting.

Although the size of the reflector was much smaller than those of real buildings, it was very large in terms of the wavelength. It does not substantially differ from real buildings as far as the wavelength implication is concerned. Additionally the relatively small size of the reflector would be advantageous since it requires less experimental space and offers a more controllable path geometry and hence better accuracy.

3.3.2 Experimental arrangement

The basic requirement for such an experiment is to send microwave signals from a source aimed at the reflector situated at a relatively far distance away and to subsequently measure the scattered signals from the reflector at various angles and at some distance away. The source-reflector distance was set to satisfy plane wave incidence, which means that a transmitter should be in the far field of the reflector according to the Rayleigh far field criterion. The measurements at various receiver positions were used to construct scattering patterns with respect to angles and distances. Inevitably, there would always be some unwanted interference signals arriving on spurious paths. These can be ground reflections, diffraction and scattering from obstacles on the transmission path or in the background. To reduce the level of these interference components, an open area was required to make it possible to be away from potential surrounding obstacles, such as buildings, road bridges and trees, etc., particularly on the far side of the reflector.

The sports field of the University of Glamorgan proved to be a suitable place. It is an open field about 400 m long and 250 m wide and covered with grass. One long side of the field is extensively open beyond its boundary. It allows the experimental layout of figure 3.2 to be configured. The reflector was placed in the middle of the one edge of the field which was taken as the reference line of the x-axis in the coordinate system. The centre height of the reflector was 2.64 m above the ground. The transmitter was located 278 m away from the reflector. The source signal level of 10 dBm was sent through a 20 dBi horn antenna vertically polarised towards the reflector with an incident angle of -40 degrees in azimuth. The transmitter antenna was mounted on the top of a mast at the same height of the reflector so that the elevation angle was zero degrees.

Because a scattering pattern is a function involving several parameters, effects involving more than one of these parameters on the pattern should be avoided. Therefore, the experiment should be conducted in a way so that only one parameter is varied while the others are kept

unchanged. The experiment involved moving a receiver horizontally at various azimuth angles but at a fixed distance of 268 m (>100a and about 10,000λ) to the reflector. The receiving 15 dBi horn antenna mounted on the top of a mast was pointed at the centre of the reflector. The height of the mast was often adjusted to maintain an elevation specular direction. In this way a matrix of points was formed at which the measurements of received scattering power were made. With appropriately selected measurement intervals, the matrix would yield the azimuth scattering pattern. Unfortunately, the possible observation of the elevation radiation pattern could not be made because the measuring equipment was ground based. Nevertheless, since the scattering pattern from equation 3.11 has the identical angular dependence with respect to azimuth and elevation respectively, the results obtained in azimuth would have the same significance to the elevation plane.

The measuring equipment will be discussed in details later in section 6.3. Briefly, the system gain in the experiment was 90 dB. The dynamic range was typically 70 dB. For operational reasons, the experiments were carried out in reasonably fine, dry and calm summer days. Possible weather disturbances of rain and wind were thus minimised.

3.4 Discussion of the experiments

Measurements showing azimuth variations of the scattering field from the reflector were carried out. In discussing the measurements, it is useful to refer to the specular condition and background scattering which are relevant.

3.4.1 Specular and non-specular conditions

In describing the experiments, reference will be frequently made to a specular direction and a specular region. By Snell's law, a specular direction in azimuth is the azimuth angle of scattering which equals to the azimuth angle of incidence in amplitude but is opposite in sense relative to the z-axis at the centre point of a building. In fact, such a specular condition is not

only held at the centre point, but also continuously across the building surface as shown in figure 3.3. Speaking in relation to the coordinate system, there is an azimuth region corresponding to the points of the specular condition on the surface. This region is known as the azimuth specular region. The width of the specular region in distance is the product $a\cos\theta_0$. It is a constant and does not change whilst the angle subtended by this region at the centre of the reflector varies with distance. This angle decreases as distance increases, it is given by

$$\Delta\theta_s \approx 2\sin^{-1}\frac{a\cos\theta_0}{2r} \qquad 3.15$$

The azimuth specular region is centred on the azimuth specular direction for reflection at the centre of the board. The rest of the azimuth range which excludes this region is called the azimuth non-specular region. The elevation specular region is similarly defined as

$$\Delta\phi_s \approx 2\sin^{-1}\frac{b\cos\phi_0}{2r} \qquad 3.16$$

It is centred on the elevation specular direction. The rest of the elevation range which excludes the specular region is called the elevation non-specular region.

3.4.2 Incident signal and background scatter

Before the reflector scattering measurements, the incident signal was measured in line-of-sight at the position of the reflector. The height of the receiver was varied from 2 m to 4 m to detect any ground reflection. A constant level of the incident wave of about -7 dBm was obtained which agreed with the calculated incident signal level of -6.7 dBm given by equation 3.13. This result showed that there were no significant disturbances from ground reflections to the incident waves.

The level of background scatter was measured at the receiver positions without the reflector. This was found to be about 30 dB below the level of the incident signal. The background scatter was caused by the existence of trees and other buildings in the far distance behind the reflector. A scattered signal level from the reflector similar to or below this level would be rather difficult to distinguish from the background scatter.

3.4.3 Measurement results

The measurements started at the specular position in both azimuth and elevation specular (azimuth 40 degrees and elevation 0 degrees). Strong scattered signals were observed within a region slightly less than one meter on both sides of the azimuth specular direction. The signal level was about 7 dB below that of the incident signal. While the elevation specular was always maintained, the receiving azimuth angle was changed gradually by moving away from the azimuth specular direction towards either side. Around the azimuth specular region (40± 0.2 degrees), the measurement interval was 1 m which corresponded to an angle 0.15 degrees in azimuth ($\pi r/180°$). At 1 m to each side, the scattering signal levels were as high as that measured in the specular direction. At 2 metres away, there was a slight decrease by about one or two dB. At 3 metre away, a sharp reduction of the scattering signal level of more than 20 dB was experienced on both sides. After about 6 m away from the specular region, the scattered signal level dropped to 30 dB below that of the incident signal. In this transition region between the specular and non specular regions, the scattered signal level dropped by about 25 dB (from 7 dB below incident signal level to more than 30 dB below this level). Moving away further, the scattering signal level remained at this low level. Here, the background scatter appeared to be more influential as expected, well into the non specular region. The measured results are shown as the scattering coefficient (in dB) against azimuth angle in degrees in figure 3.4.

3.4.4 Comparison to predictions

Using the same geometry of that used in the measurements, the scattering coefficient of the reflector is calculated at 268 m, using the far field model of equation 3.11, in the azimuth range at every quarter degree with the elevation specular. This predicted scattering pattern is plotted together with the measured results in figure 3.5 to allow comparison to be made.

The comparison between measured and predicted results shows that the measured and predicted scattering patterns of the reflector generally have a good agreement. Particularly around the specular direction, their strong azimuth angle dependence is seen to be almost identical with regard to the "beamwidth" of the patterns as well as the relative amplitudes.

3.5 Further Experiments

Further experiments were carried out in the near and very near fields of the reflector. Results from these experiments would be more relevant to practical situations arising in site shielding applications and urban radiowave propagation.

3.5.1 Moving into the near field of the reflector

The distance of 268 m is in the far field range of the reflector which is true when the reflector has the dimensions given in section 3.3.2. The size of the reflector is however sufficiently large compared to the wavelength as far as the measured and predicted results are concerned, but rather too small compared to real buildings. In contrast, a building of modest dimensions, say 20 m by 20 m, has a Rayleigh far field distance of nearly 30 km at frequency of 11.2 GHz. In typical urban areas, clearly such a distance is far too large to consider for building scatter by any standard. Particularly in site shielding applications, the most harmful effects of building scatter on the site shielding factor (SSF) come from those buildings near the receiver site which are seen by the receiver rather than those which may be present in the far distance.

Realistically speaking, spaces between buildings in urban areas can range from tens of metres to a few hundred metres at most. Accordingly, the distances concerned might be ten times and even hundred times less than their corresponding far field values. Therefore, knowledge of only the far field behaviour of scatter clearly is insufficient. The scattering behaviour in the near field range of the building is more relevant and appropriate prediction methods applicable to this range for site shielding applications are needed.

To this end, further investigations are carried out into near field range. In the experiment, the measuring receiver was moved closer to the reflector. Similar measurements to those at 268 m were carried out at 26.8 m and 2.68 m from the reflector respectively. These correspond to what may be referred to as near field and very near field distance respectively.

3.5.2 Scatter measurements at 26.8 m

At 26.8 m (>10a and about 1000λ), the measurements were started at azimuth 90 degrees. The measuring receiver was moved horizontally towards the azimuth specular direction of azimuth 40 degrees and further beyond it. The elevation specular condition was always maintained as previously. The measurement intervals were taken at 3 m, 2 m and 1 m. Close to the azimuth specular direction, the interval was reduced to half metre. In the non specular region, the scattering signal levels were relatively low; about 25 to 30 dB below that of the incident signal. As the measuring receiver was moved closer to the specular region, the scattering signal level started to increase. At the boundary of the specular region (40±2 degrees), the scattering signal level rose sharply attaining a value as high as that of the incident wave. Similarly on the other side of the specular direction, the scattering signal level dropped sharply back to the low level again (-25 to -30 dB). The measured results at 26.8 m are plotted in figure 3.6.

Comparing these results to those previously measured at 268 m in figure 3.4, the pattern at 26.8 m shows clearly a wider angular pattern than that at 268 m. The scattering signal levels

are generally higher in both specular and non specular regions compared to their previous counterparts. In relative terms however, namely the difference between the scattering signal levels in the specular region and those values in the non specular region observed at 26.8 m was less than that seen at 268 m. Using the far field prediction model, the scattering coefficient at 26.8 m is calculated in the azimuth range and given in figure 3.7. From comparison between the measured and predicted results, the far field model clearly fails to adequately represents the scattering pattern when the receiver-reflector distance falls considerably below the far field distance.

3.5.3 Scatter measurements at 2.68 m

The measuring receiver was moved even closer to the reflector. The receiver-reflector distance is 2.68 m (>a and about 100λ). This distance represents only 0.6% of the Rayleigh far field distance of the reflector. Scatter measurements were made over the azimuth range −90 to +90 degrees. In the non specular region, the scattering signal levels were constantly low around 25 dB below that of the incident signal. Closer to the specular region (40±20.41 degrees), the scattering signal level started to rise gradually. Into the specular region, the scattering signal level rose to as high as that of the incident signal. At some positions, the measured levels were even about 2 dB higher. Moving out of the specular region to the other side, the signal level dropped again. The measured results are plotted in figure 3.8 to show the scattering pattern obtained at 2.68 m.

Comparing these measured results to the previous two, the scattering pattern appears to be much wider. In the specular region, the consistently high scattering signal levels are spread over a much wider angular range. However, it is not much higher than that value seen at 26.8. In the non specular region, the scattering signal levels are low, but slightly higher than those observed at 26.8 m so that the difference between the scattering signal levels observed in the specular region and those in the non specular region is reduced. At the transition region between the specular and non specular regions, the scattering signal levels do not change as

sharply as is seen in the other two cases. Clearly, it would be pointless to compare the measured results obtained here to predicted results using the far field model of equation 3.11.

3.6 Further development of prediction models

The measured results obtained at the close distances suggest strongly that the far field model is inadequate to represent the scattering patterns in regions which fall well below the far field region. Development and extension of the model are necessary.

3.6.1 Review of the far field model

The scattered electric field expression of equation 3.4 has amplitude and phase terms which may be separated and written as

$$\mathbf{E}(r,\theta,\phi) = \mathbf{A}(r,\theta,\phi)\iint_S \Psi_0(x,y)\Psi(x,y)dxdy \qquad 3.17$$

where $\mathbf{A}(r,\theta,\phi) = \mathbf{e}_p \dfrac{jE_0}{r\lambda}\exp(-jkr)$

$$\Psi_0(x,y) = \exp\left[jk(x\alpha_0 + y\beta_0)\right]$$

$$\Psi(x,y) = \exp\left[jk(x\alpha + y\beta)\right]$$

The phase term $\Psi(x,y)$ is the exponential term $\exp(-jk\Delta)$ involving the path difference Δ between the ray path r from the centre to a field point P(x,y,z) and the ray path r_1 from a point S(x,y) on the reflector surface to the same field point. From the geometry shown in figure 3.9 and using cosine rule, the following relationship between r and r_1 can be deduced:

$$r_1^2 = r^2 + x^2 + y^2 - 2r(x\alpha + y\beta) \qquad 3.18$$

leading to $(r_1 + r)(r_1 - r) = x^2 + y^2 - 2r(x\alpha + y\beta)$.

Let $\Delta = r_1 - r$ be the path difference and assume that $r_1 + r \approx 2r$ is a justifiable approximation, the path difference can be written as

$$\Delta = \frac{x^2}{2r} + \frac{y^2}{2r} - x\alpha - y\beta \qquad 3.19$$

When the receiver-reflector distance r is much longer than the building dimensions a and b, the quadratic terms may have values which are much less than half of the wavelength so that they can be ignored. In principle, the smaller the value of the quadratic term, the less the error involved in ignoring them. According to Rayleigh, the error would become acceptable if each of the quadratic terms $x^2/2r$ and $y^2/2r$ is less than $\lambda/16$. This gives rise to a minimum receiver-reflector distance above which it is justified to ignore the quadratic terms. This minimum distance has its worst case value when x and y are at their maximum i.e. $(x = a/2,\ y = b/2)$ and can be easily derived as

$$r \geq \frac{2a^2}{\lambda} \text{ and } r \geq \frac{2b^2}{\lambda} \qquad 3.20$$

This is identical to the Rayleigh far field criterion referred to in the previous chapter. Discounting the quadratic terms, equation 3.19 becomes

$$\Delta = -x\alpha - y\beta \qquad 3.21$$

This is the phase term in equation 3.4. It is a linear approximation to the path difference. The ray paths from anywhere on the scattering surface to a field point are essentially parallel to each other as shown in figure 3.10. The phase term is independent of the receiver-reflector distance. This determines the scattering characteristics in the far field range. The choice of the far field criterion allowing the quadratic terms to be ignored has a certain arbitrariness allowing some flexibility. For the reflector in the experiment, its Rayleigh far field distance is about 445 m. The receiver-reflector distance of 268 m used is then only 60% of that.

However, the scattering properties of the reflector at 268 m have been shown to display the characteristics of the far field patterns. Clearly, the transitions between distinct regions are not rigidly defined, rather, they occur gradually.

In the near field region of the reflector, the assumption of parallel ray paths no longer stands. The failure of the far field approximation in the near field range has been demonstrated by the measured results carried out at 26.8 m and 2.68 m.

3.6.2 The near field cases

It has been shown that the far field model produces inaccurate predictions when the receiver is moved closer to the reflector. The implementation of a rigorous model is unrealistic as it would be extremely intensive in computational requirements. This section looks at two established near field techniques, namely those of Jull [1981] and Bramley and Cherry [1973]. The approximations made for the purpose of computational simplification are examined and conclusions are drawn regarding the range of validity for each model.

3.6.2.1 Jull's near field assumption

When receiver-reflector distances are not long enough to satisfy the far field criterion, namely that the quadratic terms are not less than $\lambda/16$, they have to be included in the path difference expression as equation 3.19. It should be noted that the assumption of $r_1 + r \approx 2r$ is still made. A near field geometry is shown in figure 3.11.

Replacing the phase term of the double integral of equation 3.17 by the expression obtained in equation 3.19 gives

$$\mathbf{E}(r,\theta,\phi)=\mathbf{e}_p\frac{jE_0}{r\lambda}\exp(-jkr)\int_{-\frac{a}{2}}^{\frac{a}{2}}\int_{-\frac{b}{2}}^{\frac{b}{2}}\exp\left[jk(x\alpha_0+y\beta_0)\right]$$
$$\exp\left[jk\left(-\frac{x^2}{2r}-\frac{y^2}{2r}+x\alpha+y\beta\right)\right]dxdy \qquad 3.22$$

This path difference is the sum of two independent components with respect to x and y as $\Delta \approx \Delta_x + \Delta_y$. Therefore, the double integral is separable into two single integrals with respect to x and y. This gives

$$\mathbf{E}(r,\theta,\phi)=\mathbf{e}_p\frac{jE_0}{r\lambda}\exp(-jkr)\int_{-\frac{a}{2}}^{\frac{a}{2}}\exp\left\{jk\left[-\frac{x^2}{2r}+x(\alpha+\alpha_0)\right]\right\}dx$$
$$\int_{-\frac{b}{2}}^{\frac{b}{2}}\exp\left\{jk\left[-\frac{y^2}{2r}+y(\beta+\beta_0)\right]\right\}dy \qquad 3.23$$

Using the derivation in appendix 2, equation 3.23 can be developed to

$$\mathbf{E}(r,\theta,\phi)=\mathbf{e}_p\frac{jE_0}{2}\exp(-jkr)\exp\left\{j\frac{\pi r}{\lambda}\left[(\alpha+\alpha_0)^2+(\beta+\beta_0)^2\right]\right\}$$
$$\left[F(u_1)+F(u_2)\right]\left[F(v_1)+F(v_2)\right] \qquad 3.24$$

where $F(\omega)=\int_0^{\omega_{2,1}}\exp\left(-j\frac{\pi}{2}\omega^2\right)d\omega$

$$\begin{matrix}u_2\\u_1\end{matrix}=\frac{a}{\sqrt{2r\lambda}}\mp\frac{\sqrt{2r\lambda}}{\lambda}(\alpha+\alpha_0)$$
$$\begin{matrix}v_2\\v_1\end{matrix}=\frac{b}{\sqrt{2r\lambda}}\mp\frac{\sqrt{2r\lambda}}{\lambda}(\beta+\beta_0) \qquad 3.25$$

The integral $F(\omega)$ is the Fresnel integral. From equation 3.24, the scattering coefficient is given by

$$\mathbf{S}=\mathbf{u}_r\frac{|\mathbf{e}_p|^2}{4}\left|F(u_1)+F(u_2)\right|^2\left|F(v_1)+F(v_2)\right|^2 \qquad 3.26$$

3.6.2.2 Bramley and Cherry's near field assumption

The path difference is considered essentially separable with x and y as $\Delta \approx \Delta_x + \Delta_y$. The difference from the Jull's assumption is that the assumption $r_1 + r \approx 2r$ is removed. With respect to x, let $\Delta_x = r_1 - r$ and $r_1 + r = 2r + \Delta_x$, then, equation 3.18 can be written as

$$2r\Delta_x + \Delta_x^2 = x^2 - 2rx\alpha \qquad 3.27$$

Let $\Delta_x \approx \frac{x}{2}\sin\theta$, but only replace it in Δ^2_x so that equation 3.27 becomes

$$2r\Delta_x + x^2\sin^2\theta \approx x^2 - 2rx\alpha \qquad 3.28$$

thus

$$\Delta_x \approx \frac{x^2\cos^2\theta}{2r} - x\alpha \qquad 3.29$$

Similarly with respect to y. The total path difference is thus given by

$$\Delta \approx \Delta_x + \Delta_y \approx \frac{x^2\cos^2\theta}{2r} + \frac{y^2\cos^2\phi}{2r} - x\alpha - y\beta \qquad 3.30$$

It can be seen that equation 3.30 differs from Jull's equation 3.19 by factors $\cos\theta$ and $\cos\phi$ in the quadratic terms. When both azimuth and elevation angles are small, the two near field models are close. As the angles increase, Jull's model becomes less accurate. In general, equation 3.30 should be used. Comparing the terms of equations 3.19 and 3.30, the Rayleigh far field criteria with respect to x and y are changed accordingly from equation 3.30 as

$$r \geq \frac{2(a\cos\theta)^2}{\lambda} \text{ and } r \geq \frac{2(b\cos\phi)^2}{\lambda} \qquad 3.31$$

In the original Bramley and Cherry's model small elevation angles are assumed so that in this case equation 3.30 reduces to

$$\Delta \approx \frac{x^2 \cos^2\theta}{2r} + \frac{y^2}{2r} - x\alpha - y\phi \qquad 3.32$$

Equation 3.32 appears as equation 4 in Bramley and Cherry's paper [1973]. Replacing the path difference of equation 3.30 in the phase term of equation 3.17 and using the derivation of appendix 2 (similarly to that in equation 3.24) gives

$$\mathbf{E}(r,\theta,\phi) = \mathbf{e}_p \frac{jE_0}{2\cos\theta\cos\phi} \exp(-jkr) \exp\left\{ j\frac{\pi r}{\lambda}\left[\left(\frac{\alpha+\alpha_0}{\cos\theta}\right)^2 + \left(\frac{\beta+\beta_0}{\cos\phi}\right)^2\right]\right\} \qquad 3.33$$
$$\left[F(u_1)+F(u_2)\right]\left[F(v_1)+F(v_2)\right]$$

where

$$\begin{aligned} u_2 \\ u_1 \end{aligned} = \frac{a\cos\theta}{\sqrt{2r\lambda}} \mp \frac{\sqrt{2r\lambda}}{\lambda\cos\theta}(\alpha+\alpha_0)$$
$$\begin{aligned} v_2 \\ v_1 \end{aligned} = \frac{b\cos\phi}{\sqrt{2r\lambda}} \mp \frac{\sqrt{2r\lambda}}{\lambda\cos\phi}(\beta+\beta_0) \qquad 3.34$$

The scattering coefficient may be stated as follows

$$\mathbf{S} = \mathbf{u}_r \frac{|\mathbf{e}_p|^2}{4\cos^2\theta\cos^2\phi} \left|F(u_1)+F(u_2)\right|^2 \left|F(v_1)+F(v_2)\right|^2 \qquad 3.35$$

Both equations 3.26 and 3.35 are the near field models. The latter is more suitable for generally oblique incidence. The calculation of the scatter signal levels in the near field, using either of these equations, needs the evaluation of the Fresnel integrals.

3.6.2.3 Evaluation of the Fresnel integral

Various approximate expansions and tables of the Fresnel integral are available, for instance, those prepared by Van Wijingaarden and Scheen [1949] with interval of 0.01 allow linear interpretation achieving modest accuracy. $F(\omega)$ is tabulated as a function of x , where

$$x = \frac{1}{2}\pi\omega^2 \tag{3.36}$$

For small values of ω, the Fresnel integral is conveniently evaluated using

$$F(\omega) = \omega\left(1 + j\frac{x}{3} - \frac{1}{2!}\frac{x^2}{5} - \frac{j}{3!}\frac{x^3}{7} + \frac{1}{4!}\frac{x^4}{9} + \ldots\right) \tag{3.37}$$

The series given above, although absolutely convergent, requires computation to excessive number of significant figures as ω increases. For large values of ω, there is an asymptotic expansion for $G(\omega)$

$$G(\omega) \approx \frac{j}{\pi\omega}\left[1 - \frac{j}{2x} - \frac{3}{(2x)^2} + j\frac{3\cdot 5}{(2x)^3} + \frac{3\cdot 5\cdot 7}{(2x)^4} - \ldots\right]\exp(jx) \tag{3.38}$$

where

$$G(\omega) = \int_{\omega_1}^{\infty} \exp\left(j\frac{\pi}{2}\omega^2\right)d\omega \tag{3.39}$$

Thus

$$F(\omega) = G(0) - G(\omega) \text{ and } G(0) = \frac{1}{2} + \frac{j}{2} \tag{3.40}$$

It should be noted that the series is not absolutely convergent. It falls into the category of what is known as asymptotic series and is suitable for large values of ω. Therefore, this approximation is generally not valid near the specular region including the transition region between the specular and non specular regions. In such cases the full Fresnel integral should be employed.

In figure 3.12, u_2 and u_1 are plotted in the azimuth range based on the experimental arrangement at 26.8 m. It shows that u_2 and u_1 vary over a considerably large range from positive to negative values. For longer distances, the values of the parameters will be even larger. Therefore, the asymptotic expansion $G(\omega)$ will be applicable over most of the azimuth range with the exception of that falling the vicinity of the specular regions. To obtain an accurate estimate of the Fresnel integral in the specular region, the two expansion series should be changed accordingly. This can be inconvenient and somewhat arbitrary.

As an alternative to the series expansions, the full Fresnel integral can be evaluated numerically with a computer aided approach. The approximation to a definite integral is given by Simpson's rule as

$$\int_{x_0}^{x_n} f(x)dx \approx \frac{\Delta x}{3}\left[f(x_0)+4f(x_i)+2f(x_j)+f(x_n)\right] \qquad 3.41$$

where $\Delta x = \frac{x_n - x_0}{n}$, $i = 1,3,5,7,\ldots (i < n)$ and $j = 2,4,6,8,\ldots (j < n)$.

The accuracy of numerical integration largely depends on the sampling method used and computer rounding off errors. To satisfy a minimum accurate representation of an original function, the sampling frequency is required to be no less than twice the maximum frequency of the periodic function. In the Fresnel integral, $\exp(j\pi u^2/2)$ can be regarded as a periodic function which can be written in the form $\exp(j2\pi fu)$, where $f = u/4$. Thus the cross-over frequency increases with u and a minimum sample frequency of u/2 is required.

3.6.2.4 Predicted results using the near field models

The scattering patterns of the reflector are numerically calculated using the methods of Jull and Bramley and Cherry. At 268 m, the predicted results of Jull and Bramley and Cherry are shown in figures 3.13 and 3.14 respectively. Both show a good agreement with the measured results. They are identical to the predicted results given by the far field model. Further on, at 26.8 m, the predicted results of both near field models show good agreement with the measured results as shown in figures 3.15 and 3.16 (for Jull's and Bramley and Cherry's models respectively). In particular, the latter appears to fit the measured results better. The better agreement obtained at 26.8 m clearly is due to the more precise considerations of path differences employed by the two near field models. To appreciate the extent of the improvement, the predictions of figures 3.15 and 3.16 may be compared to the far field prediction made for a similar site geometry and shown in figure 3.7.

3.6.3 The very near field case

As the observation point is moved nearer to the reflector, the approximations made for the path differences by both the near field models outlined above will be seriously tested. This is made clear in an attempt to use the near field models to predict the scattering pattern at 2.68 m. Jull's near field model can be seen to give a rather poor prediction when it is compared to the measured results as shown in figure 3.18. Bramley and Cherry's near field model gives the predicted results shown in figure 3.19. It can be seen that the predicted beamwidth is slightly narrower than that measured. However, the main discrepancy is that the predicted scattering pattern suffers a shift in azimuth relative to the measured results.

As with the far field model, predictions by both near field models are largely influenced by the approximations made in the expressions for the path differences.

The exact expression of the path difference is obtained from equation 3.18, as

$$r_1 = \pm\sqrt{r^2 + x^2 + y^2 - 2r(x\alpha + y\beta)} \qquad 3.42a$$

Using the root with the positive sign gives the exact expression of the path difference

$$\Delta = r_1 - r = -r + \sqrt{r^2 + x^2 + y^2 - 2r(x\alpha + y\beta)} \qquad 3.42b$$

Replacing the path difference into the phase term in the integral of equation 3.17, then the scattering electric field may be expressed as

$$\begin{aligned} \mathbf{E}(r,\theta,\phi) = \mathbf{e}_p \frac{jE_0}{2r\lambda} \exp(-jkr) \int_{-\frac{a}{2}}^{\frac{a}{2}} \int_{-\frac{b}{2}}^{\frac{b}{2}} \exp\left[jk(x\alpha_0 + y\beta_0)\right] \\ \exp\left[jk\left(r - \sqrt{r^2 + x^2 + y^2 - 2r(x\alpha + y\beta)}\right)\right] dxdy \end{aligned} \qquad 3.43$$

However, the phase term of this form is no longer separable with respect to x and y as before so a numerical evaluation operating over a full surface integral has to be employed. This was implemented and the predicted results for the receiver-reflector distances of 268 m, 26.8 m and 2.68 m are shown in figures 3.19, 3.20 and 3.21 respectively. At 268 m and 26.8 m, the predicted results are identical to those of the far and near field models. At 2.68 m, it is seen that the predicted results have been significantly improved using the exact expression of the path difference and compare well with the measured results. Overall, there is good agreement between the measured and predicted results at the three distances corresponding to far, near and very near field regions.

However, it was noted that large computational effort was needed to complete this numerical evaluation. It was observed that execution time as long as two hours was taken to calculate a scattering pattern of the reflector for scattering levels at 360 points at half degree intervals using a 486 DX 33 MHz personal computer. For real buildings whose surface areas are many times larger than that of the reflector, for instance a building 20 m by 20 m is about 67 times

larger, the use of the exact expression will be impractical. The computational constrains would however be relaxed considerably using larger and faster computers.

3.6.4 Approximation in the very near field

The computational requirements can be simplified by keeping the assumption $\Delta \approx \Delta_x + \Delta_y$ as previously in the far and near field ranges while Δ_x and Δ_y are given as the exact expressions of path differences with respect to x and y respectively. The path difference is approximated to be

$$\Delta \approx \Delta_x + \Delta_y \approx -2r + \sqrt{r^2 + x^2 - 2rx\alpha} + \sqrt{r^2 + y^2 - 2ry\beta} \qquad 3.44$$

In this form of the path difference, the double integral would be separable with respect to x and y. Equation 3.43 can be expressed as the product of two single integrals with respect to x and y respectively

$$\mathbf{E}(r,\theta,\phi) = \mathbf{e}_p \frac{jE_0}{r\lambda} \exp(-jkr) \int_{-\frac{a}{2}}^{\frac{a}{2}} \exp\left[jk\left(r - \sqrt{r^2 + x^2 - 2rx\alpha} + x\alpha_0\right)\right] dx \int_{-\frac{b}{2}}^{\frac{b}{2}} \left[jk\left(r - \sqrt{r^2 + y^2 - 2ry\beta} + y\beta_0\right)\right] dy \qquad 3.45$$

Although these two single integrals can only be evaluated numerically, the amount of computation involved (a quarter of a minute) is largely reduced compared to that of a full surface integral. Predicted results were obtained using equation 3.45 for the receiver-reflector distances of 268 m, 26.8 m and 2.68 m and are shown in figures 3.22, 3.23 and 3.24. Comparing these with the predicted results from the exact expression and the measured results at the three distances, it is clear that this simplified very near field model has achieved an agreement with the measured results which is almost as good as that using the exact expression.

3.6.5 Comparisons between path difference approximations

The exact path difference expression in equation 3.42b can be expanded in Binomial series as

$$\Delta = -r + r\left(1 + \frac{1}{2}u - \frac{1}{8}u^2 + \frac{1}{16}u^3 - \ldots\right) \qquad 3.46$$

where $u = \dfrac{x^2 + y^2 - 2r(x\alpha + y\beta)}{r^2}$.

Replacing u into equation 3.46 up to the second order terms of u, it can be rewritten in x and y as

$$\Delta \approx \frac{x^2 + y^2}{2r} - x\alpha - y\beta - \frac{\left(x^2 + y^2\right)^2 - 4r\left(x^2 + y^2\right)(x\alpha + y\beta) + 4r^2(x\alpha + y\beta)^2}{8r^3} \qquad 3.47$$

From equation 3.47, it can be seen that the far field approximation of the path difference of equation 3.21 is obtained by ignoring all the terms above the first order terms in x and y. Jull's near field approximation of equation 3.19 takes only the first order term of u which consists of the first and second order terms in x and y, but not the second order terms of x and y contained in the second order term of u. Bramley and Cherry's near field approximation of equation 3.32 complements Jull's near field approximation by adding the second order term $\dfrac{x^2 \sin^2\theta}{2r}$ of x present in the second order term of u assuming small elevation angles. This largely improves the accuracy of the approximation in the cases of azimuth oblique incidence. But, all the higher order terms above the second order and the products of x and y are neglected.

The very near field approximation of equation 3.44 can not be compared directly to the Binomial series of the exact expression. Nevertheless, it can be represented by the sum of two Binomial series with respect to x and y respectively as

$$\Delta \approx -2r + r\left(1 + \frac{1}{2}u_1 - \frac{1}{8}u_1^2 + \frac{1}{16}u_1^3 - \ldots\right) + r\left(1 + \frac{1}{2}v_1 - \frac{1}{8}v_1^2 + \frac{1}{16}v_1^3 - \ldots\right) \qquad 3.48$$

where $u_1 = \frac{x^2 - 2rx\alpha}{r^2}$ and $v_1 = \frac{y^2 - 2ry\beta}{r^2}$, then $u_1 + v_1 = u$. Replacing u_1 and v_1 by these values in equation 3.48 and considering terms of u_1 and v_1 up to the second order terms, equation 3.48 can be rewritten in x and y as

$$\Delta \approx \frac{x^2 + y^2}{2r} - x\alpha - y\beta - \frac{x^4 + y^4 - 4r(x^2\alpha + y^2\beta) + 4r^2(x^2\alpha^2 + y^2\beta^2)}{8r^3} \qquad 3.49$$

Comparing this to the expansion of the exact expression of equation 3.47, the expansion of the very near field approximation of equation 3.49 can be seen to consist of all the higher order terms of x and y except those containing product terms of x and y. When $u_1 = v_1 = u/2$, the sum of the second order terms of u_1 and v_1 in equation 3.49 is half of the second order term of u in equation 3.47. The sum of the third order terms of u_1 and v_1 are one quarter of the third order term of u. Here, the very near field approximation has its maximum error. When $u_1 \neq v_1$, error will be less than the maximum. When $u_1 = u$ and $v_1 = 0$ or vice versa, the error would be zero, and the very near field approximation thus becomes exact.

Generally speaking, both near and very near field approximations have errors compared to the exact expression. These errors would be small if u is small. u varies from point to point over the reflector surface and is essentially related to the ratio of reflector dimensions to the receiver-reflector distance. This means that the errors would increase as the receiver moves closer to the reflector for a certain receiving angle. The error variations of the near and very near field approximations are shown in figure 3.25 for the reflector in the case of the very near field (2.68 m). The errors are calculated across the width of the reflector from the top, middle and half way between them. The receiving angles are set as azimuth 40 degrees and elevation 0 degrees. It can be seen that the errors at the top of the reflector are larger than those corresponding to the middle and the point midway in between and increase as we move towards either side of the reflector since u increases. Therefore, the errors of both

approximations are largest at the corners of the reflector. Both near and very near field models consist of products of two separated integrals with respect to x and y respectively. The azimuth patterns are determined only by the integral with respect to x. Therefore, it is only those path differences from the middle of the reflector are significant. In the middle of the reflector, the near field approximation has the least errors. Significantly, the very near field approximation has no errors giving rise to an exact pattern. Generally, the errors are positive from the far side of the reflector and negative from the near side. This means that the path differences from the far side are overestimated while those from the near side are underestimated. Assuming these errors to be linear, these errors amount effectively to a change in the position of the reflector. In other words, the reflector appears to be tilted due to the errors. This effectively causes a shift of the scattering pattern from the exact pattern towards azimuth zero degrees. Such error effects have been experienced in obtaining prediction results using the near field model for receiver positions in the very near field. However, these effects are eliminated in predictions given by the very near field model.

By the very near field model, reflectors with the same width have the same azimuth pattern regardless of their heights. The azimuth patterns of two reflectors of width 2.44 m and different heights 0.1 m and 4.88 m are shown in figure 3.26. Their azimuth patterns are identically shaped to that of the 2.44 m by 2.44 m reflector. Therefore, the very near field model is generally exact as far as the shape of scattering patterns are concerned. This is very significant from the interference prediction point of view. The very near field model could only have errors in the relative amplitudes of the patterns. In the far field, the very near field model is sufficiently accurate so that errors are negligible. In the near and very near field, it will be shown in the later sections (sections 3.7.2 and 6.2.3) that scattering coefficients in the specular region would vary rapidly within these regions around incident signal levels (for perfect reflectors) by approximately ±2 dB, essentially displaying no distance dependence. Therefore in the near and very near fields, errors in the relative amplitudes would be restricted to within an approximately similar amount. From interference prediction viewpoint the order of such errors is generally considered to be acceptable. Therefore, the very near field model is more

accurate than the far and near field models and more practically useful than the exact solution due to its simplified computational requirements.

Strictly speaking, none of the solutions is in fact exact, including that using the exact expression of the path difference. The "exact" solution has to consider the double integral of the angular spectrum, where the boundary conditions are not exact. Therefore, the receiver-reflector distance can not be reduced indefinitely without introducing increasingly more errors.

3.7 Angular and distance dependence of scattering coefficient

In the previous sections, the scattering patterns of an idealised reflector are calculated using the far, near and very near field models. Scattering characteristics of the reflector have been demonstrated using calculated patterns together with those measured. However, it has always been desirable and advantageous if the scattering characteristics are not only demonstrated, but also mathematically described in terms of their angular and distance dependence. In the prediction models given by the angular spectra (a double Fourier transform of the aperture field), only the far field model has an analytical solution from which angular and distance dependence in the far field can be readily identified. As a result of having more accurate path expressions, near and very near field models are obtained whose solutions involve complicated integrals which can not be solved analytically.

Bramley and Cherry [1973] approximated the expansion of the Fresnel integral and mathematically represented the angular and distance dependence in the near field. However as far as the angular dependence is concerned, this is basically identical to that obtained from the far field model. Problems still remain in the near and very near fields. A new approximation can be made to the expansion of the Fresnel integral. Importantly, the scattering characteristics of the near and very near fields can be described by new formulas with significant specular behaviour.

3.7.1 Far field regions

The angular and distance dependence of the scattering coefficient in the far field can be identified readily from the far field model (equation 3.11). There are two sinc functions of which one involves β and b which determines the elevation pattern. The other, involving α and a, determines the azimuth pattern. Although the scattering coefficient overall has a distance dependence of $1/r^2$, a distance dependence factor of $1/r$ can be associated with each of azimuth and elevation distance dependence respectively. Therefore, the scattering coefficient in equation 3.11 may be expressed as a product of two separated azimuth and elevation patterns as follows

$$\mathbf{S} = \mathbf{u}_r \left|\mathbf{e}_p\right|^2 S(r,\alpha,a)S(r,\beta,b) \qquad 3.50$$

where

$$S(r,\alpha,a) = \frac{a^2}{r\lambda}\,\mathrm{sinc}^2\left[\frac{a\pi}{\lambda}(\alpha+\alpha_0)\right]$$
$$S(r,\beta,b) = \frac{b^2}{r\lambda}\,\mathrm{sinc}^2\left[\frac{b\pi}{\lambda}(\beta+\beta_0)\right] \qquad 3.51$$

In the specular direction $\theta = -\theta_0$ and $\phi = -\phi_0$, both azimuth and elevation sinc functions equal to one. The scattering coefficient is only distance dependent and has the largest value at a given distance. At the Rayleigh far field distances $r = 2a^2/\lambda$ and $r = 2b^2/\lambda$, assuming $a = b$, the azimuth and elevation dependence each gives a 3 dB loss or a total of 6 dB loss in the scattering coefficient. When the elevation specular condition is maintained, which had been the case in the measurements, and the receiving azimuth angle is changed away from the specular direction, $|\alpha+\alpha_0|$ increases, and the azimuth sinc function in turn reduces. At $|\alpha+\alpha_0| = \lambda/a$, $\mathrm{sin\,c}\left[\frac{a\pi}{\lambda}(\alpha+\alpha_0)\right] = 0$ and the scattering coefficient reaches a null in the scattering pattern. The azimuth range between the two nulls immediately located on either side of the azimuth

specular direction is called the beamwidth of the pattern between the first two nulls. This beamwidth of the azimuth pattern is derived in appendix 3 and is given as

$$BW_a \approx 4\sin^{-1}\frac{\lambda}{2a\cos\theta_0} \approx \frac{2\lambda}{a\cos\theta_0} \quad (\text{since } a >> \lambda) \qquad 3.52$$

The azimuth beamwidth (angular range between the first two nulls) in the far field is dependent only on the surface horizontal dimension. It shows that a wider surface has a narrower azimuth beamwidth which is independent of the receiver-reflector distance. Although this azimuth beamwidth is wider than the beamwidth defined by the 3 dB or 6 dB points, it can be demonstrated to provide a useful characteristic quantifying the azimuth angular dependence.

As the receiver azimuth angle moves further away from the azimuth specular direction, $|\alpha+\alpha_0|$ increases and becomes many times the value of λ/a. Therefore, the value of $\sin\left[\frac{a\pi}{\lambda}(\alpha+\alpha_0)\right]$ oscillates up and down fast throughout the azimuth range. This can be seen in the predicted results given by the far field model in figure 3.5. Because of this fast oscillation, $\sin\left[\frac{a\pi}{\lambda}(\alpha+\alpha_0)\right]$ may be taken to be its root mean square value $\sqrt{2}/2$. The azimuth pattern can be written as

$$S(r,\alpha,a) \approx \frac{\lambda}{2r\pi^2}\frac{1}{(\alpha+\alpha_0)^2} \qquad \text{for } |\alpha+\alpha_0| >> \frac{\lambda}{a} \qquad 3.53$$

Similarly, the elevation beamwidth in the far field is given as

$$BW_e \approx 4\sin^{-1}\frac{\lambda}{2b\cos\phi_0} \approx \frac{2\lambda}{b\cos\phi_0} \qquad 3.54$$

The elevation pattern is given as

$$S(r,\beta,b) \approx \frac{\lambda}{2\pi^2}\frac{1}{(\beta+\beta_0)^2} \qquad \text{for } |\beta+\beta_0| >> \frac{\lambda}{b} \tag{3.55}$$

The azimuth angular dependence of the scattering coefficient is plotted in figure 3.27 using equation 3.50. It shows a good representation of the predicted results by the far field model. Although equation 3.53 is not supposed to be valid close to the specular direction where it gives infinitely large values, the curve of the azimuth angular dependence still remarkably fits the predicted results below the highest value of the scattering coefficient.

3.7.2 Near and very near field regions

The scattering characteristics in the near and very near field have been demonstrated to be significantly different from those in the far field by the measured and predicted results. Since the near and very near field models involve complicated integrals which do not have analytical solutions, the angular and distance dependence of the scattering coefficient in the near and very near fields may not be as straightforward as shown in the far field case.

From equation 3.35, the near field model consists of the Fresnel integrals. The scattering coefficient can be also written as equation 3.50 with separated azimuth and elevation patterns,

$$\mathbf{u} = \mathbf{u}_r \left|\mathbf{e}_p\right|^2 S(r,\alpha,a)S(r,\beta,b) \tag{3.56}$$

where

$$\begin{aligned} S(r,\alpha,a) &= \frac{1}{2\cos^2\theta}\left|F(u_2)+F(u_1)\right|^2 \\ S(r,\beta,b) &= \frac{1}{2\cos^2\phi}\left|F(v_2)+F(v_1)\right|^2 \end{aligned} \tag{3.57}$$

The physical meaning of the scattering coefficient represented by the Fresnel integrals lies in the relationship between the scattering surface area and Fresnel zones. The radii of the first Fresnel zone [Donald (1951)] are given, with respect to azimuth and elevation respectively, by

$$r_a = \sqrt{\frac{2\lambda r_0 r}{r_0 \cos^2\theta + r\cos^2\theta_0}}$$
$$r_e = \sqrt{\frac{2\lambda r_0 r}{r_0 \cos^2\phi + r\cos^2\phi_0}} \qquad 3.58$$

When the transmitter-reflector distance r_0 is sufficiently long (e.g. assumed plane wave incidence) compared to the relatively short receiver-reflector distance r (e.g. in site shielding environments) and elevation angles are relatively small, equation 3.58 reduces to

$$r_a \approx \frac{\sqrt{2r\lambda}}{\cos\theta}$$
$$r_e \approx \frac{\sqrt{2r\lambda}}{\cos\phi} \qquad 3.59$$

Therefore, the Fresnel parameters u and v in equation 3.34 can be written in terms of r_a and r_e as

$$\frac{u_2}{u_1} = \frac{a}{r_a} \mp \frac{r_a}{\lambda}(\alpha + \alpha_0)$$
$$\frac{v_2}{v_1} = \frac{b}{r_b} \mp \frac{r_b}{\lambda}(\beta + \beta_0) \qquad 3.60$$

There are two useful ratios p and q which can be defined from the Fresnel parameters u and v, where

$$p = \frac{\frac{r_a}{\lambda}(\alpha+\alpha_0)}{\frac{a}{r_a}} = \frac{r_a^2}{a\lambda}(\alpha+\alpha_0)$$

$$q = \frac{\frac{r_e}{\lambda}(\beta+\beta_0)}{\frac{b}{r_e}} = \frac{r_e^2}{b\lambda}(\beta+\beta_0) \qquad 3.61$$

Importantly, the Fresnel integral takes some typical forms according to the extreme values of p and q. When p<<1 due to $|\alpha+\alpha_0| << \lambda/a$, this corresponds to the case of azimuth specular. The modulus of the Fresnel integral with respect to azimuth can be given approximately by

$$\left|F(u_2)+F(u_1)\right| \approx 2\left|F\left(\frac{a}{r_a}\right)\right| \qquad 3.62$$

Equation 3.62 has the extreme values of $2a/r_a$ for $a << r_a$ and $\sqrt{2}$ for $a >> r_a$. Similarly when q<<1, the modulus of the Fresnel integral with respect to v has the extreme values of $2b/r_e$ for $b<<r_e$ and $\sqrt{2}$ for $b>>r_e$. For $a<<r_a$ and $b<<r_e$ which means that the scattering surface dimensions are much smaller than the radii of the first Fresnel zone, this corresponds to the case of the far field. Replacing the modulus of the Fresnel integrals with $2a/r_a$ and $2b/r_e$ in equation 3.56, one could obtain identical azimuth and elevation distance dependences each of 1/r similarly to those in equation 3.51 in the specular direction. For $a >> r_a$ and $b>>r_e$, this is the case of the near and very near fields. The modulus of the Fresnel integrals have values $\sqrt{2}$ which means that the scattering coefficient in specular conditions has no distance dependence in the near and very near field. This can been seen from both measured and predicted results in the specular region at 26.8 m and 2.68 m which show that the scattering coefficient does not reduce as the receiver-reflector distance decreases in the near and very near field. Therefore, the scattering coefficient in the specular direction can be given by

$$\mathbf{S}=\begin{cases}\mathbf{u}_r\left|\mathbf{e}_p\right|^2\dfrac{a^2}{r\lambda}\dfrac{b^2}{r\lambda} & \text{for } a<<r_a \text{ and } b<<r_e\\ \mathbf{u}_r\left|\mathbf{e}_p\right|^2\dfrac{1}{\cos^2\theta}\dfrac{1}{\cos^2\phi} & \text{for } a>>r_a \text{ and } b>>r_e\end{cases} \qquad 3.63$$

When p>>1, e.g. $\left|\frac{r_a}{\lambda}(\alpha+\alpha_0)\right|>>\frac{a}{r_a}$, let $p=\frac{u'}{\Delta u}$ so that $u_{2,1}=\Delta u\mp u'$, then the modulus of the Fresnel integral can be given by

$$\begin{aligned}\left|F(u_2)+F(u_1)\right| &= \left|F(\Delta u-u')+F(\Delta u+u')\right|\\ &= \left|F(u'+\Delta u)-F(u'-\Delta u)\right|\end{aligned} \qquad 3.64$$

From equation 3.40,

$$\begin{aligned}\left|F(u'+\Delta u)\right| &= \left|G(0)-G(u'+\Delta u)\right|\\ \left|F(u'-\Delta u)\right| &= \left|G(0)-G(u'-\Delta u)\right|\end{aligned} \qquad 3.65$$

so that

$$\left|F(u'+\Delta u)-F(u'-\Delta u)\right|=\left|G(u'-\Delta u)-G(u'+\Delta u)\right| \qquad 3.66$$

Expanding equation 3.66, using equation 3.38 and taking only the zero order term of the expansion, leads to equation 3.66 becoming

$$\left|G(u'-\Delta u)-G(u'+\Delta u)\right|\approx\left|\frac{j}{\pi(u'-\Delta u)}e^{j\frac{\pi}{2}(u'-\Delta u)^2}-\frac{j}{\pi(u'+\Delta u)}e^{j\frac{\pi}{2}(u'+\Delta u)^2}\right| \qquad 3.67$$

Bramley and Cherry [1973] approximated this equation by neglecting Δu in the amplitude terms and expanding the phase term in equation 3.67. As a result, equation 3.67 becomes

$$\left|G(u'-\Delta u)-G(u'+\Delta u)\right|\approx\left|\frac{j}{\pi u'}\left[e^{j\frac{\pi}{2}(u'^2-2u'\Delta u+\Delta u^2)}-e^{j\frac{\pi}{2}(u'^2+2u'\Delta u+\Delta u^2)}\right]\right| \qquad 3.68$$

Let $A = \frac{\pi}{2}\left(u'^2 + \Delta u^2\right)$ and $B = \pi u' \Delta u$, and using these in equation 3.68 gives

$$\begin{aligned} \left|G(u'-\Delta u) - G(u'+\Delta u)\right| &\approx \left|\frac{j}{\pi u'}\left[e^{j(A-B)} - e^{j(A+B)}\right]\right| \\ &\approx \left|\frac{j}{\pi u'} e^{jA}\left[e^{-jB} - e^{jB}\right]\right| \\ &\approx \left|\frac{2}{\pi u'} e^{jA} \sin B\right| \approx \left|\frac{2}{\pi u'} \sin B\right| \end{aligned} \qquad 3.69$$

Using equation 3.66 and replacing B with $\pi u' \Delta u$ in equation 3.69, the modulus of the Fresnel integral in the azimuth pattern is given by

$$\begin{aligned} \left|F(u_2) + F(u_1)\right| &\approx \left|\frac{2}{\pi \frac{\sqrt{2r\lambda}}{\lambda \cos\theta}(\alpha + \alpha_0)} \sin\left[\frac{\pi a}{\lambda}(\alpha + \alpha_0)\right]\right| \\ &\approx \left|\frac{2a\cos\theta}{\sqrt{2r\lambda}} \operatorname{sinc}\left[\frac{\pi a}{\lambda}(\alpha + \alpha_0)\right]\right| \end{aligned} \qquad 3.70$$

Similarly, the modulus of the Fresnel integral in the elevation pattern is given by

$$\left|F(v_2) + F(v_1)\right| \approx \left|\frac{2b\cos\phi}{\sqrt{2r\lambda}} \operatorname{sin\,c}\left[\frac{\pi b}{\lambda}(\beta + \beta_0)\right]\right| \qquad 3.71$$

Using equations 3.70 and 3.71 in equation 3.56, the scattering coefficient is given by

$$\begin{aligned} \mathbf{S} &= \mathbf{u}_r \left|\mathbf{e}_p\right|^2 S(r, \alpha, a) S(r, \beta, b) \\ &= \mathbf{u}_r \left|\mathbf{e}_p\right|^2 \frac{1}{2\cos^2\theta} \left|F(u_2) + F(u_1)\right|^2 \frac{1}{2\cos^2\phi} \left|F(v_2) + F(v_1)\right|^2 \\ &= \mathbf{u}_r \left|\mathbf{e}_p\right|^2 \frac{a^2}{r\lambda} \operatorname{sinc}^2\left[\frac{a\pi}{\lambda}(\alpha + \alpha_0)\right] \frac{b^2}{r\lambda} \operatorname{sinc}^2\left[\frac{b\pi}{\lambda}(\beta + \beta_0)\right] \end{aligned} \qquad 3.72$$

This is exactly the same as equation 3.50 in the far field. Therefore, the azimuth and elevation angular and distance dependence functions derived from this equation could not possibly be of

much use in the near and very near field regions where it has been demonstrated that scatter characteristics are different from those in the far field. In the near and very near fields where $a >> r_a$, this equation may be arguably used to demonstrate some angular dependence in very limited azimuth ranges where $p >> 1$. Such limited azimuth ranges represent however a very small proportion of the whole azimuth range of interest and this portion decreases dramatically as a/r_a increases.

In a wider azimuth range, Δu has to remain in the amplitude terms in equation 3.67. The denominators in the amplitude terms of equation 3.67 are written as

$$\begin{aligned}\pi(u' \mp \Delta u) &= \pi\left[\frac{\sqrt{2r\lambda}}{\lambda\cos\theta}(\alpha+\alpha_0) \mp \frac{a\cos\theta}{\sqrt{2r\lambda}}\right] \\ &= \frac{\pi\sqrt{2r}}{\sqrt{\lambda}\cos\theta}\left(\sin\theta\cos\phi + \sin\theta_0\cos\phi_0 \mp \cos\theta\frac{a\cos\theta}{2r}\right)\end{aligned} \qquad 3.73$$

As the elevation angle ϕ and $\sin^{-1}\frac{a\cos\theta_0}{2r}$ are generally small, equation 3.73 can be approximated to be

$$\begin{aligned}\pi(u' \mp \Delta u) &\approx \frac{\pi\sqrt{2r}}{\sqrt{\lambda}\cos\theta}\left[\sin\theta\cos\left(\sin^{-1}\frac{a\cos\theta}{2r}\right)\cos\phi + \sin\theta_0\cos\phi_0\right. \\ &\quad \left. \mp \cos\theta\sin\left(\sin^{-1}\frac{a\cos\theta}{2r}\right)\cos\phi\right] \\ &\approx \frac{\pi\sqrt{2r}}{\sqrt{\lambda}\cos\theta}\left[\sin\left(\theta \mp \sin^{-1}\frac{a\cos\theta}{2r}\right)\cos\phi + \sin\theta_0\cos\phi_0\right]\end{aligned} \qquad 3.74$$

Then the modulus of the Fresnel integral can be given by

$$|F(u_2)+F(u_1)| \approx \left| \frac{j\sqrt{\lambda}\cos\theta e^{jA}}{\pi\sqrt{2r}} \left[\frac{e^{-jB}}{\sin\left(\theta - \sin^{-1}\frac{a\cos\theta}{2r}\right)\cos\phi + \sin\theta_0\cos\phi_0} \right.\right.$$

$$\left.\left. \frac{e^{jB}}{\sin\left(\theta + \sin^{-1}\frac{a\cos\theta}{2r}\right)\cos\phi + \sin\theta_0\cos\phi_0} \right] \right| \qquad 3.75$$

When the receiving azimuth angle θ is far away from the specular direction, the amplitudes of the two terms with $\mp\sin^{-1}\frac{a\cos\theta}{2r}$ have little difference so that they can be taken out of the bracket to make $e^{jB} - e^{-jB} = 2j\sin B$. Again as the receiving azimuth angle is well away from the specular region, sinB oscillates fast as the receiving azimuth angle varies so that it can be taken to be its root mean square value. Thus, equation 3.75 can be approximately written as

$$|F(u_2)+F(u_1)| \approx \left| \frac{\sqrt{\lambda}\cos\theta}{\pi\sqrt{r}\left[\sin\left(\theta \mp \sin^{-1}\frac{a\cos\theta}{2r}\right)\cos\phi + \sin\theta_0\cos\phi_0\right]} \right| \qquad 3.76$$

When the receiving azimuth angle $\theta > -\theta_0 + \sin^{-1}\frac{a\cos\theta}{2r}$ and is getting closer to $-\theta_0 + \sin^{-1}\frac{a\cos\theta}{2r}$, the term with the negative sign increases significantly and becomes much larger than one with the positive sign. It dominates the value of equation 3.76 while the term with the positive sign remains small. When the receiving azimuth angle $\theta < -\theta_0 - \sin^{-1}\frac{a\cos\theta}{2r}$ and is getting closer to $-\theta_0 - \sin^{-1}\frac{a\cos\theta}{2r}$, the value of equation 3.76 is dominated by the term with the positive sign while the one with the negative sign is small. Additionally, when the receiving azimuth angle is getting closer to the specular region from either side, $\cos\theta$ in $\sin^{-1}\frac{a\cos\theta}{2r}$ can be considered as approaching the value of $\cos(-\theta_0)$. Therefore, $\sin^{-1}\frac{a\cos\theta}{2r}$ is conveniently approximated to be $\sin^{-1}\frac{a\cos\theta_0}{2r}$ which is the half width of the specular region in equation 3.15. The azimuth pattern in the non specular region can be given approximately by

$$S(r,\alpha,a) \approx \frac{\lambda}{2r\pi^2\left[\sin\left(\theta \mp \sin^{-1}\frac{a\cos\theta_0}{2r}\right)\cos\phi + \sin\theta_0\cos\phi_0\right]^2} \qquad 3.77$$

where

$$\theta > -\theta_0 + \sin^{-1}\frac{a\cos\theta_0}{\lambda} \qquad \text{for the negative sign}$$

$$\theta < -\theta_0 - \sin^{-1}\frac{a\cos\theta_0}{\lambda} \qquad \text{for the positive sign}$$

Similarly, the elevation pattern in the non specular region can be given by

$$S(r,\beta,b) \approx \frac{\lambda}{2r\pi^2\left[\sin\left(\phi \mp \sin^{-1}\frac{b\cos\phi_0}{2r}\right) + \sin\phi_0\right]^2} \qquad 3.78$$

where

$$\phi > -\phi_0 + \sin^{-1}\frac{b\cos\phi_0}{\lambda} \qquad \text{for the negative sign}$$

$$\phi < -\phi_0 - \sin^{-1}\frac{b\cos\phi_0}{\lambda} \qquad \text{for the positive sign}$$

Replacing equations 3.77 and 3.78 into equation 3.56 gives the angular and distance dependence of the scattering coefficient in the non specular region for the near and very near fields. When the receiving angle is very close to the specular regions, the above equations could give infinitely large values to the scattering coefficient. In reality, this would never happen. The maximum scattering coefficients are those in the specular region which are given in equation 3.63.

In figures 3.28 and 3.29, the azimuth angular dependence is plotted for the 2.44 m by 2.44 m reflector at 26.8 m and 2.68 m respectively and also compared to the predicted results using the very near field model. It can be seen that the angular and distance dependence clearly

demonstrate the specular nature in the near and very near field and give a good representation of the predicted results even in the very near field. The introduction of the new approximations significantly overcomes the problems associated with "shifting" previously seen in the scattering patterns given by the Fresnel integrals in the very near field.

3.8 Interim conclusion

In this chapter, prediction models have been developed based on Kirchhoff diffraction theory and measurement results from an experimental programme. The geometrical parameters determining the scattering signal levels have been theoretically and experimentally investigated. It has been shown that in the case of a perfectly conducting reflector the measured scattering levels, and the dependence on azimuth, elevation and distance parameters can be explained reasonably well by geometrical considerations arising in different field regions. In the far field, ray paths are essentially parallel and its prediction model shows a pattern of a sinc function which is independent of range. In the near field region the path geometry changes somewhat. The approximation of parallel ray paths in the far field range no longer stands. The introduction of the quadratic terms results in the occurrence of a form of the Fresnel integral in the near field model which shows clearly distance dependence. When the receiver-building distance becomes even shorter, the ray paths have to be defined more precisely than is done in the above two cases. However, the inseparable double integral of the exact solution of the ray paths requires what may be considered to be an impractical amount of computational effort for numerical evaluations. It has been shown that it is possible to have an approximation involving a product of two separated integrals. Sections 3.6.4 and 3.6.5 demonstrate clearly that this approximation is closer to the exact expression than those used by Jull and Bramley and Cherry.

The behaviour of the scattering coefficients has been examined as functions of the angular and distance parameters using the expansion of the Fresnel integral. This has allowed practical approximations to be produced for different regions of the scattering patterns at different

distances. These approximations require relatively little computational effort to be implemented.

Throughout the development of the prediction models, the aperture analysis technique provides a simple and efficient means for characterising the behaviour of scattering from large dimensioned apertures as far as perfectly conducting reflectors are concerned. This method explicit use of the path difference expression has proved to be informative and advantageous. It has enabled us to give appropriate considerations to the geometrical parameters governing scatter from surfaces in their near and very near field regions.

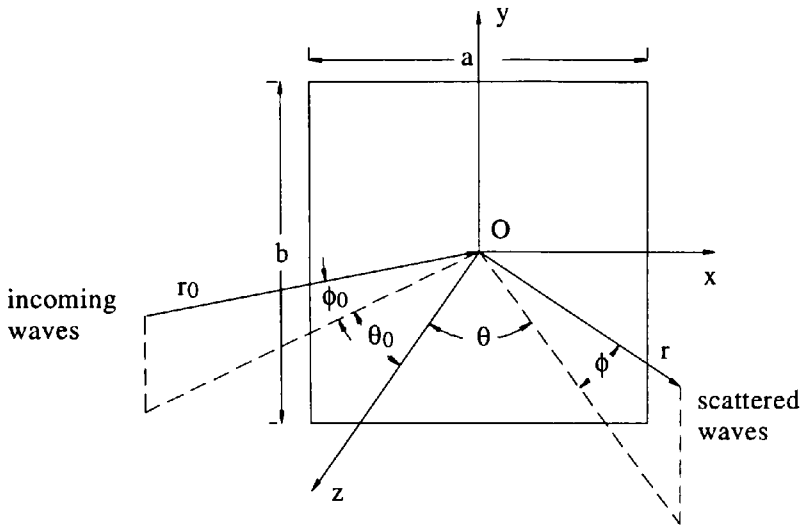

Figure 3.1 Geometry of incidence and scattering relative to a building surface.

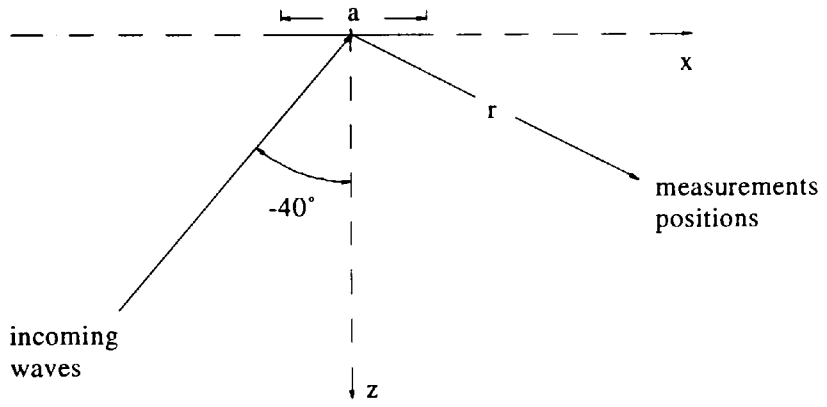

Figure 3.2 Experimental layout.

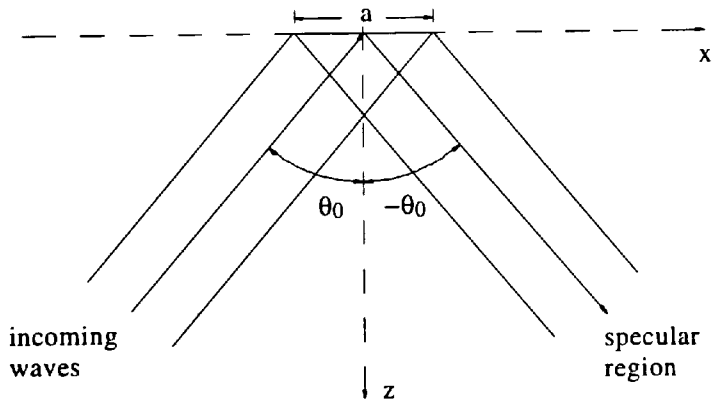

Figure 3.3 Geometry of specular region.

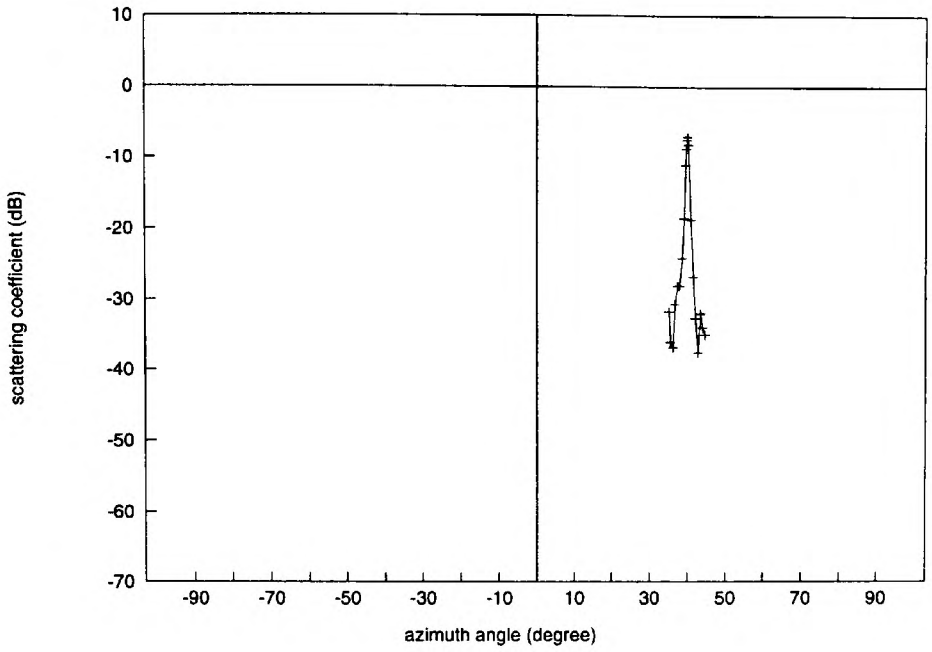

Figure 3.4 The measured results of the scattering coefficient at 268 m.

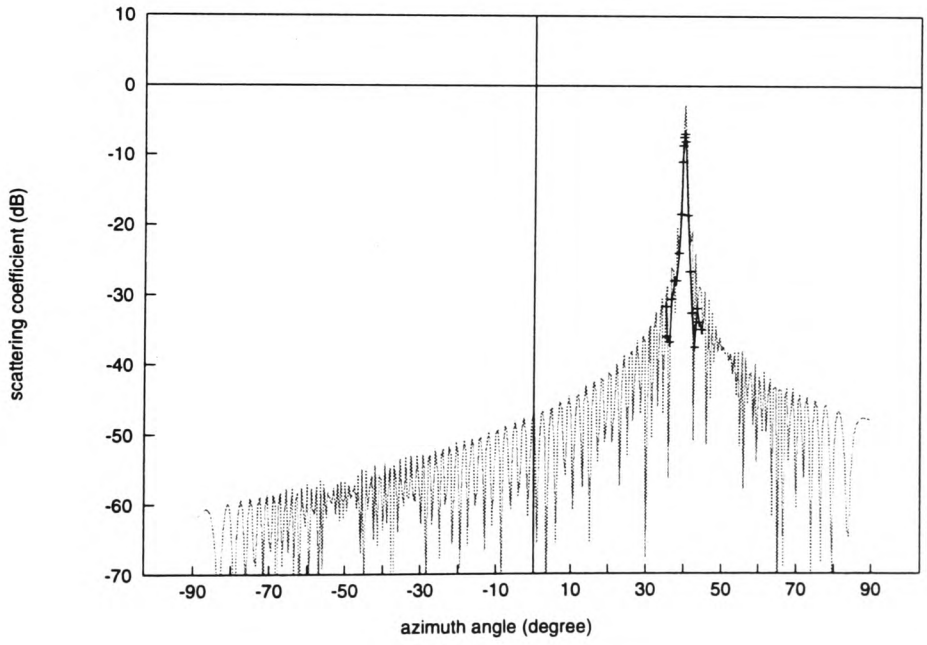

Figure 3.5 The predicted results of the far field model in comparison with the measured results at 268 m.

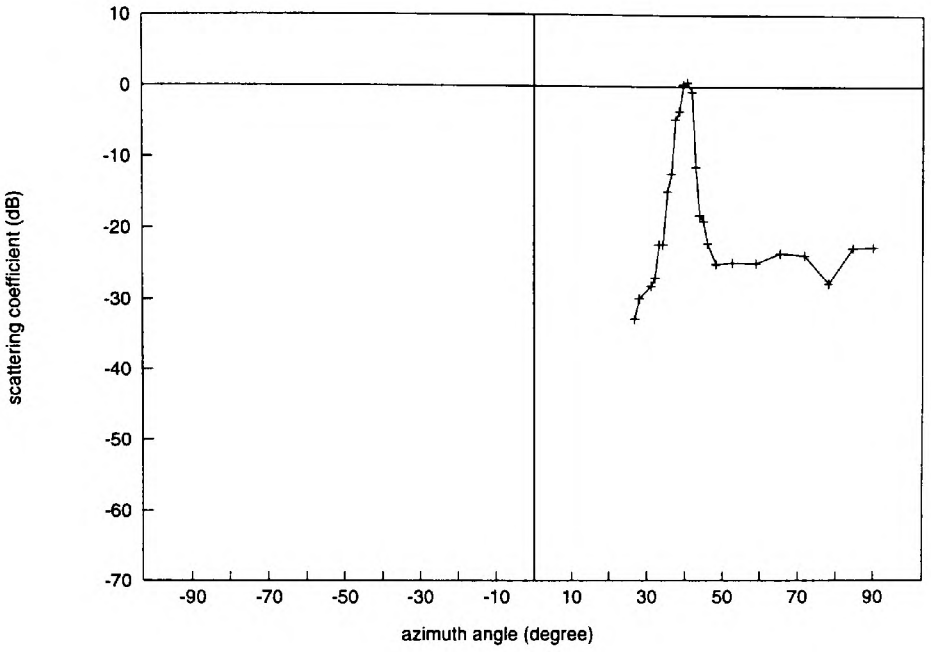

Figure 3.6 The measured results of the scattering coefficient at 26.8 m.

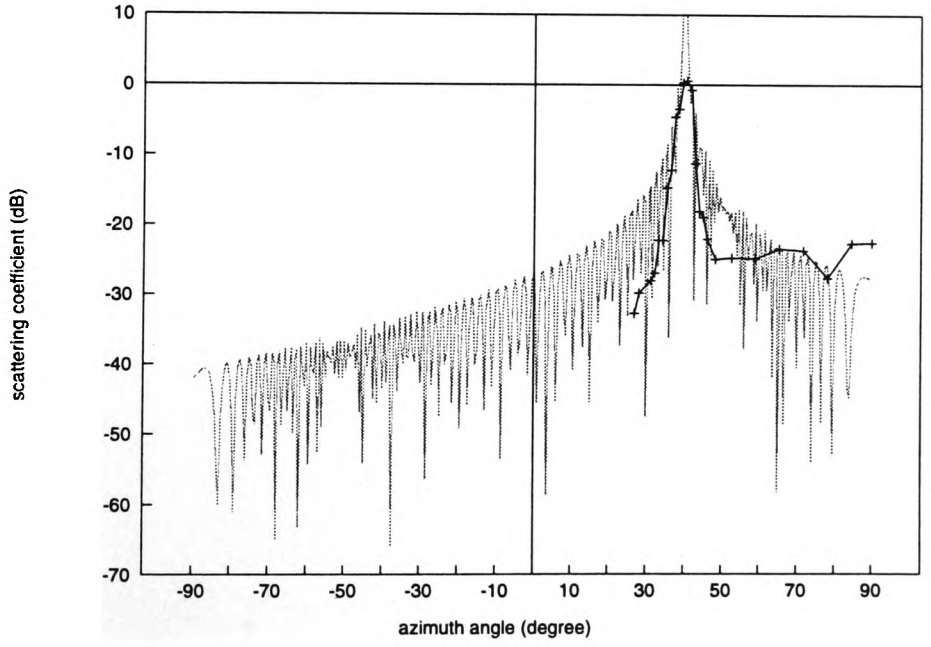

Figure 3.7 The predicted results of the far field mode in comparison with the measured results at 26.8 m.

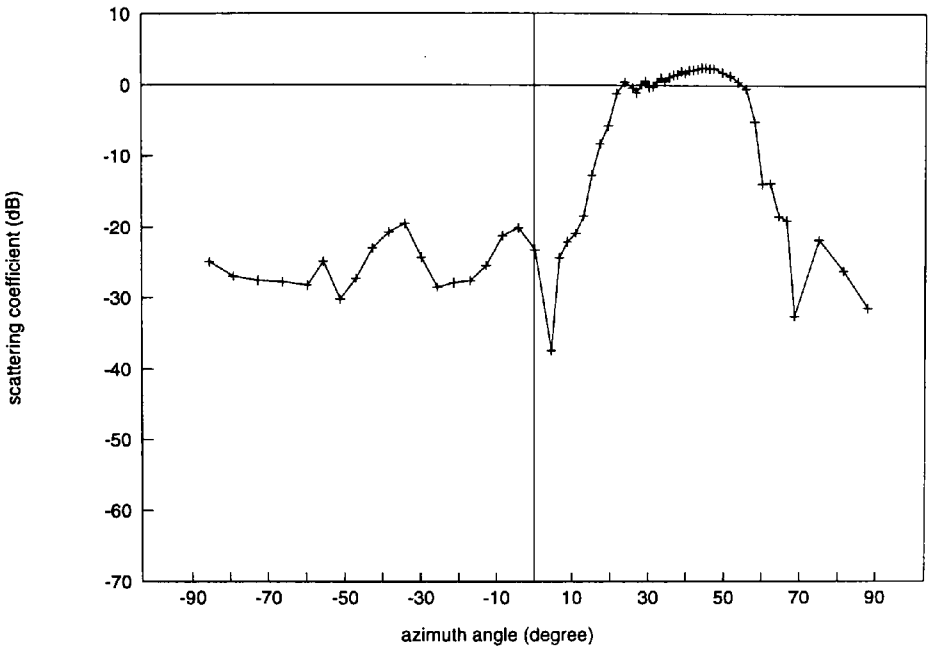

Figure 3.8 The measured results of the scattering coefficient at 2.68 m.

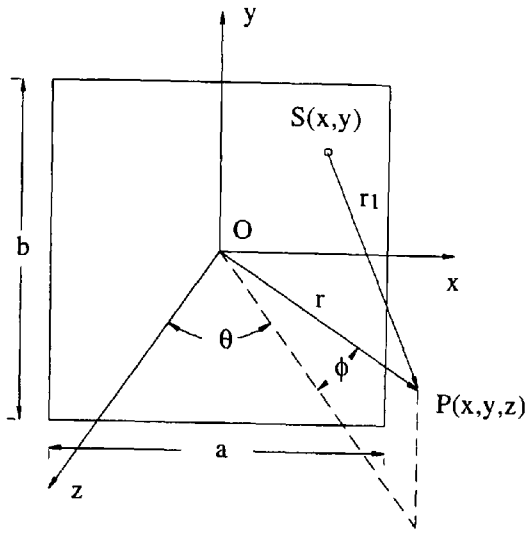

Figure 3.9 Ray path geometry from a plane surface.

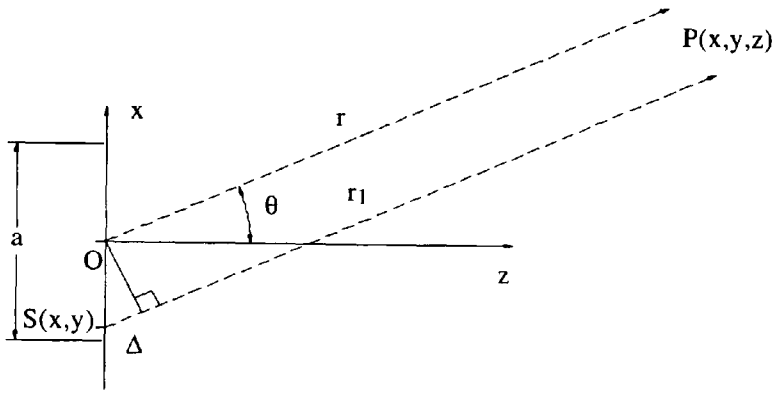

Figure 3.10 Parallel ray path geoemetry in the far field range.

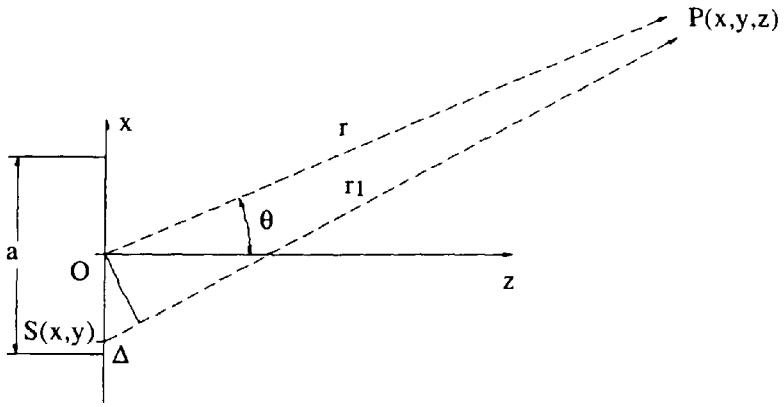

Figure 3.11 Ray path geometry in the near field range.

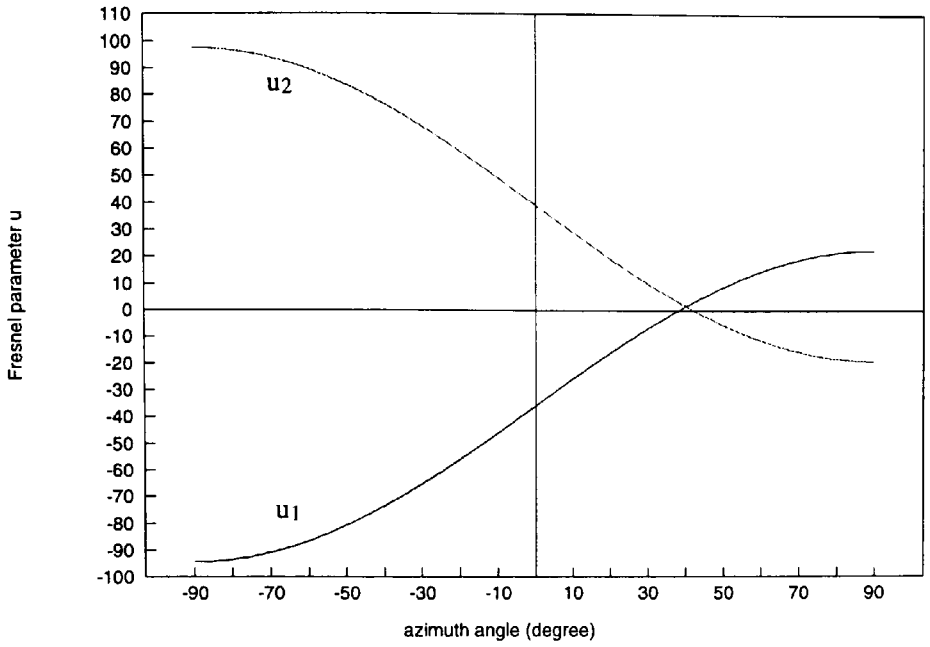

Figure 3.12 Fresnel parameters u_2 and u_1 of the reflector in the azimuth range at 26.8 m.

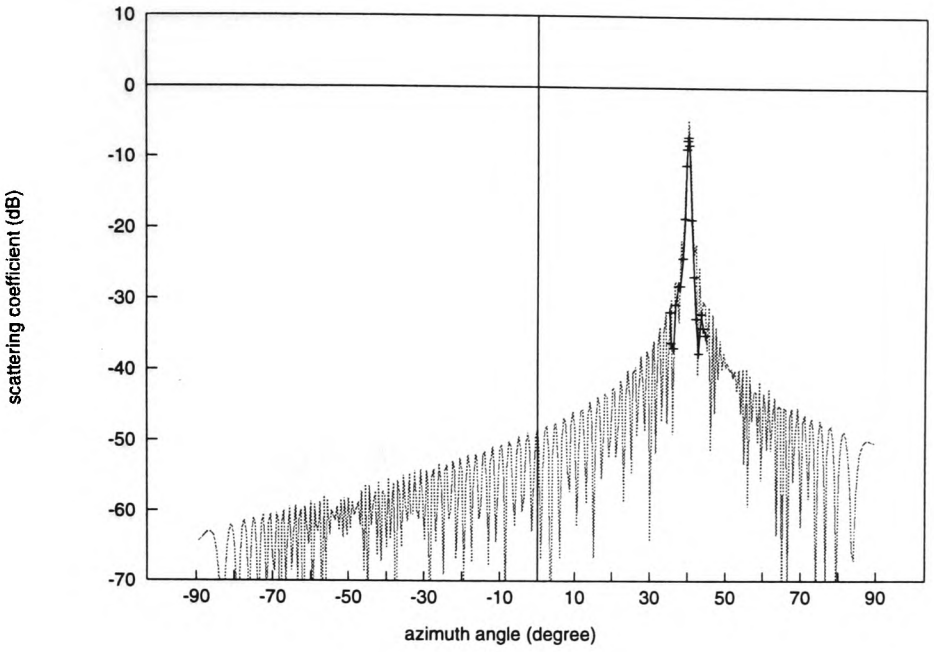

Figure 3.13 The predicted results of Jull's near field model in comparison with the measured results at 268 m.

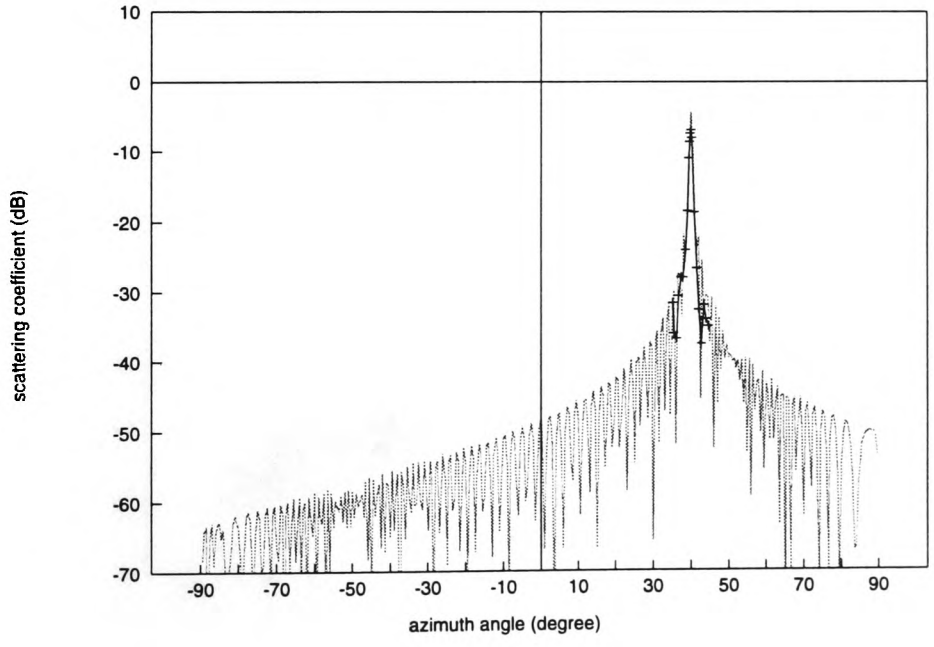

Figure 3.14 The predicted results of Bramley and Cherry's near field model in comparison with the measured results at 268 m.

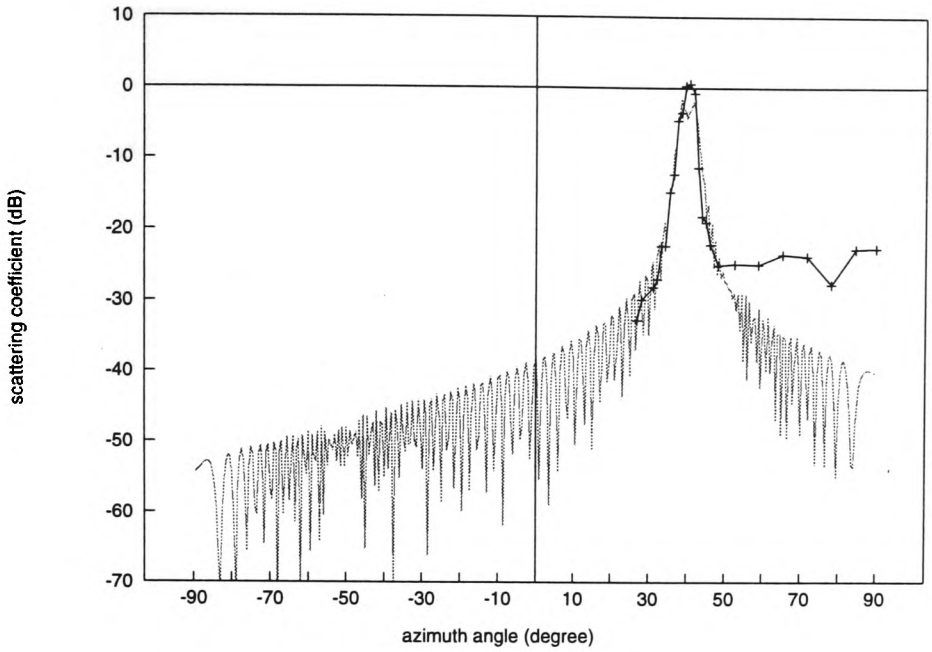

Figure 3.15 The predicted results of Jull's near field model in comparison with the measured results at 26.8 m.

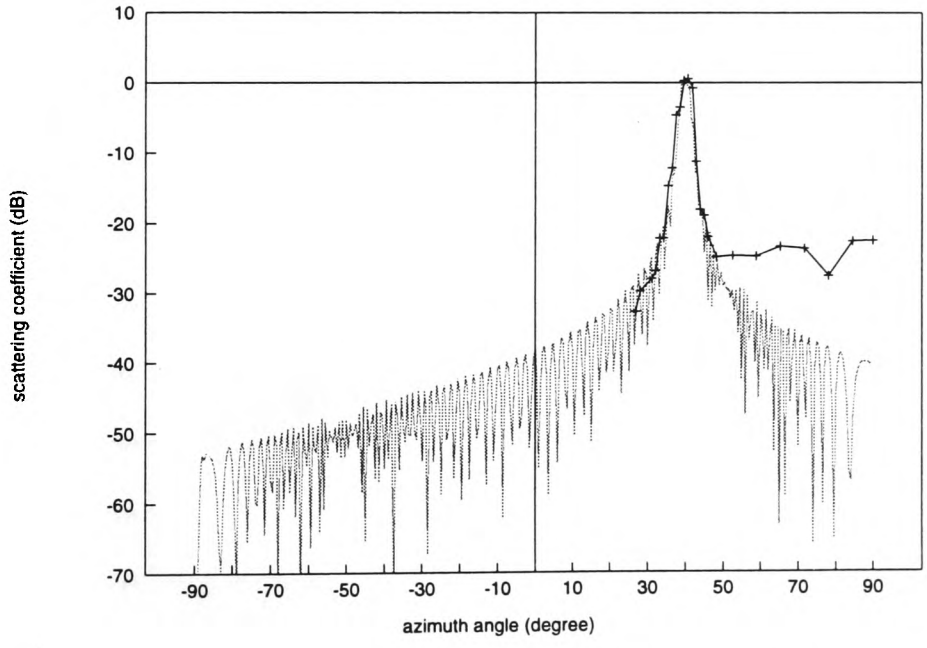

Figure 3.16 The predicted results of Bramley and Cherry's near field model in comparison with the measured results at 26.8 m.

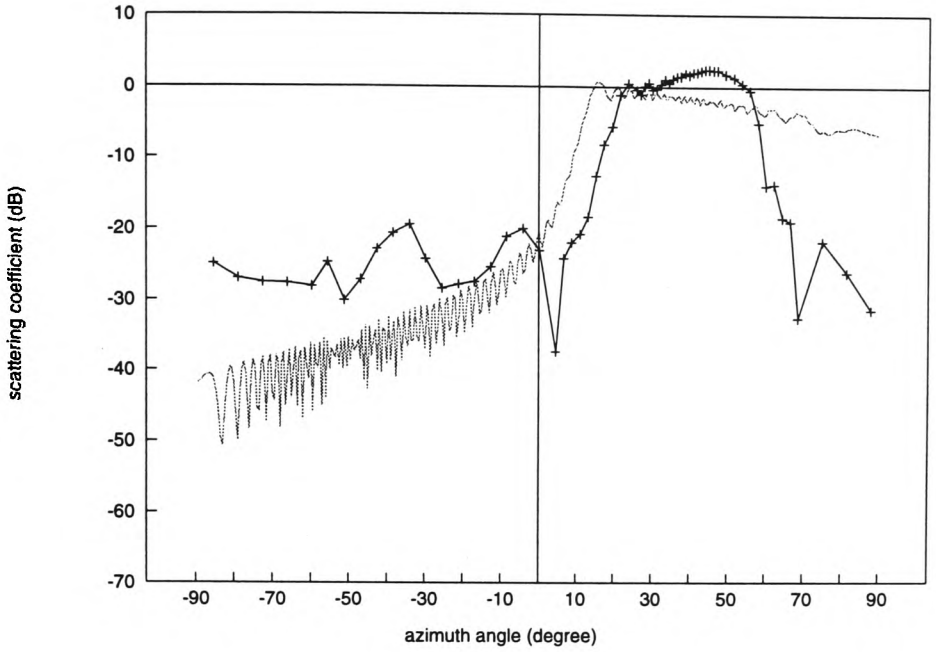

Figure 3.17 The predicted results of Jull's near field model in comparison with the measured results at 2.68 m.

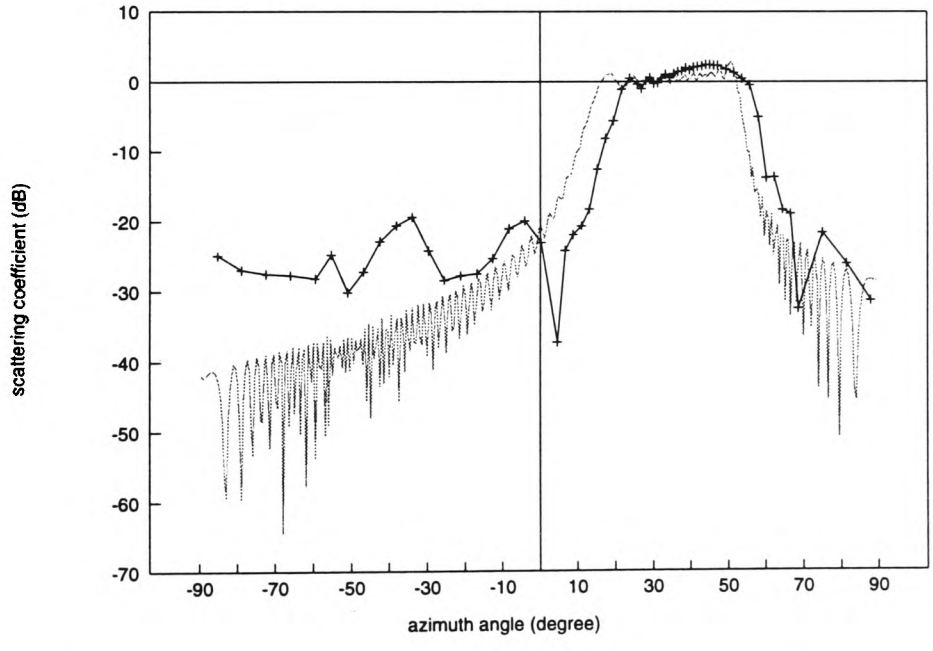

Figure 3.18 The predicted results of Bramley and Cherry's near field model in comparison with the measured results at 2.68 m.

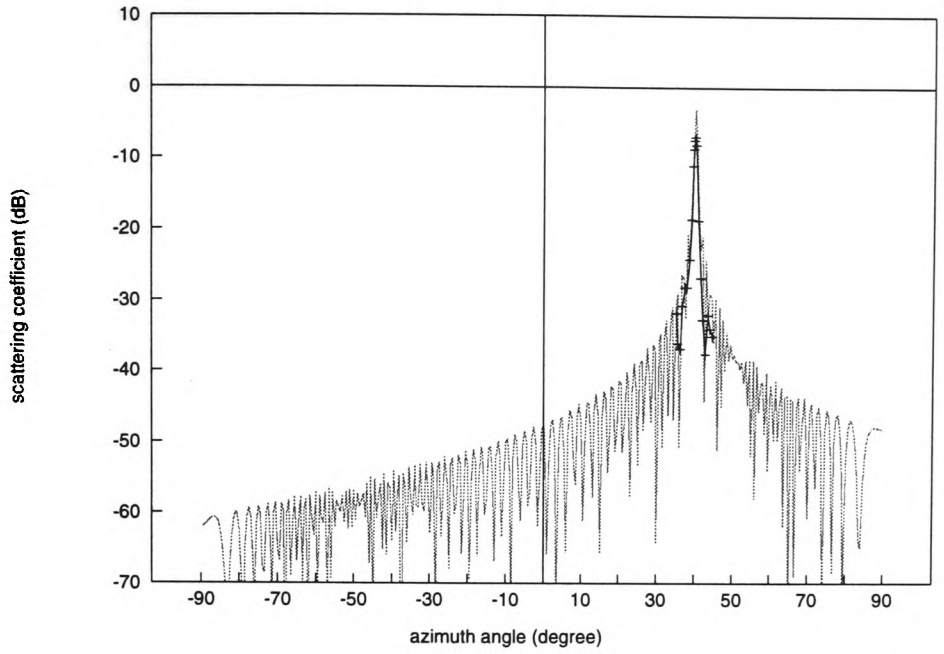

Figure 3.19 The predicted results of the exact path difference in comparison with the measured results at 268 m.

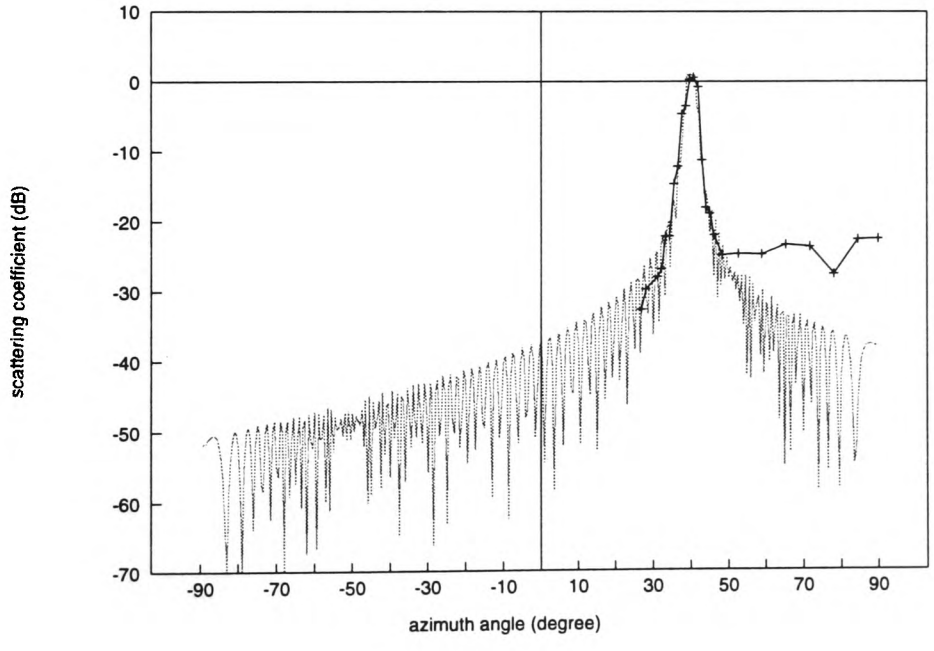

Figure 3.20 The predicted results of the exact path difference in comparison with the measured results at 26.8 m.

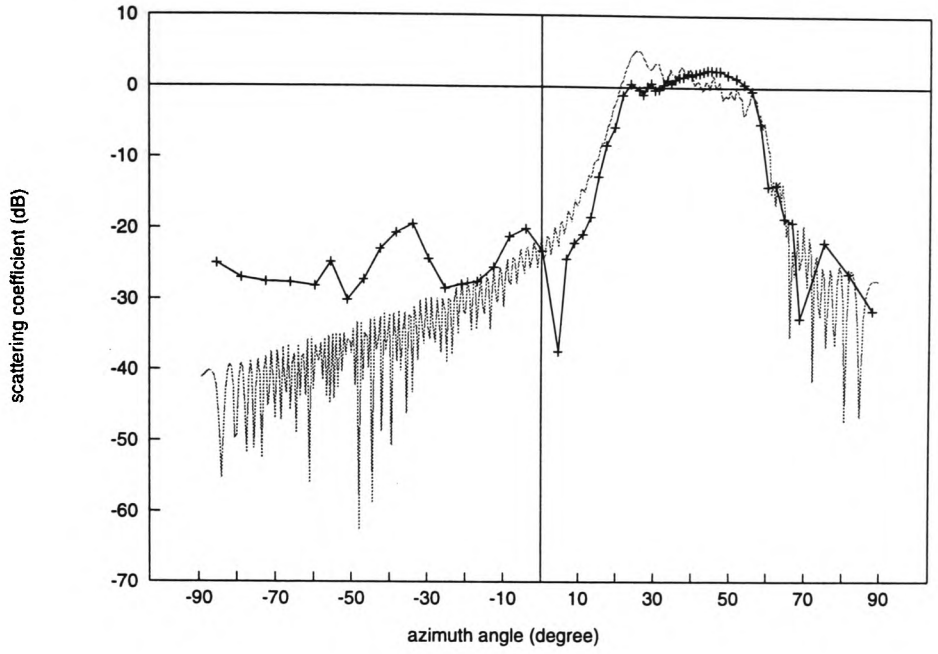

Figure 3.21 The predicted results of the exact path difference in comparison with the measured results at 2.68 m.

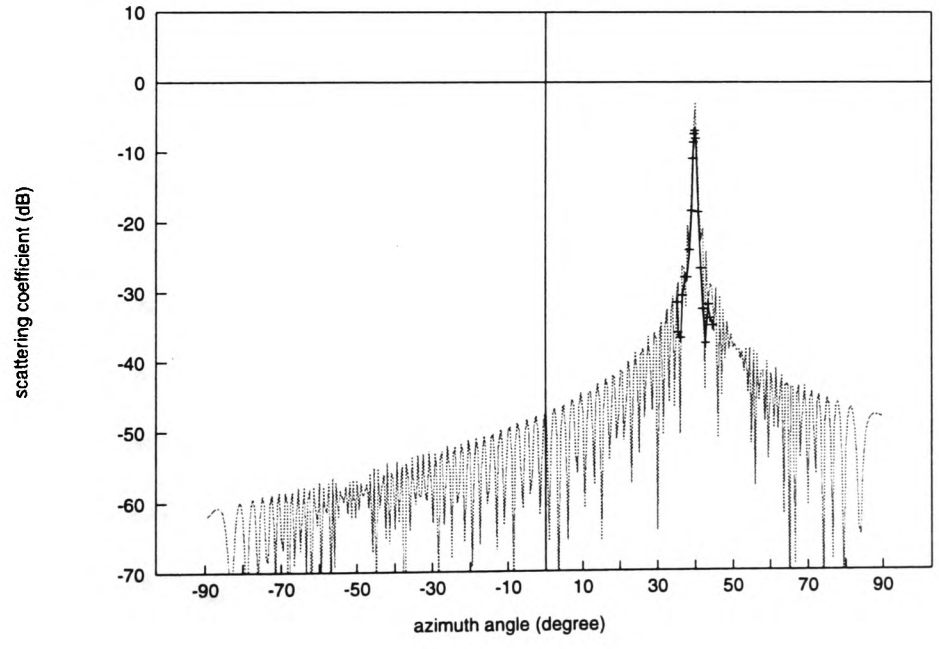

Figure 3.22 The predicted results of the very near field model in comparison with the measured results at 268 m.

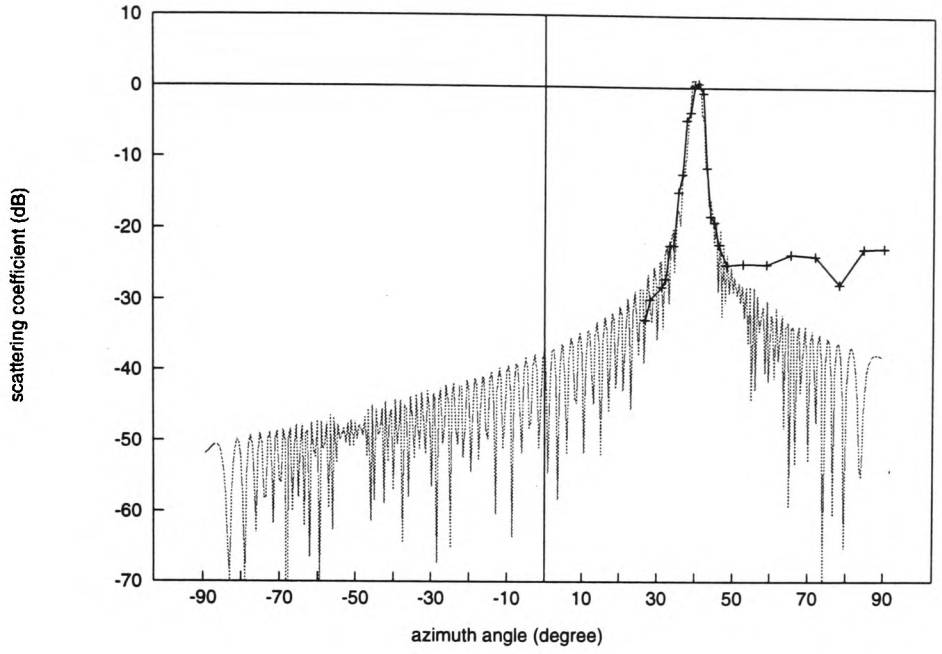

Figure 3.23 The predicted results of the very near field model in comparison with the measured results at 26.8 m.

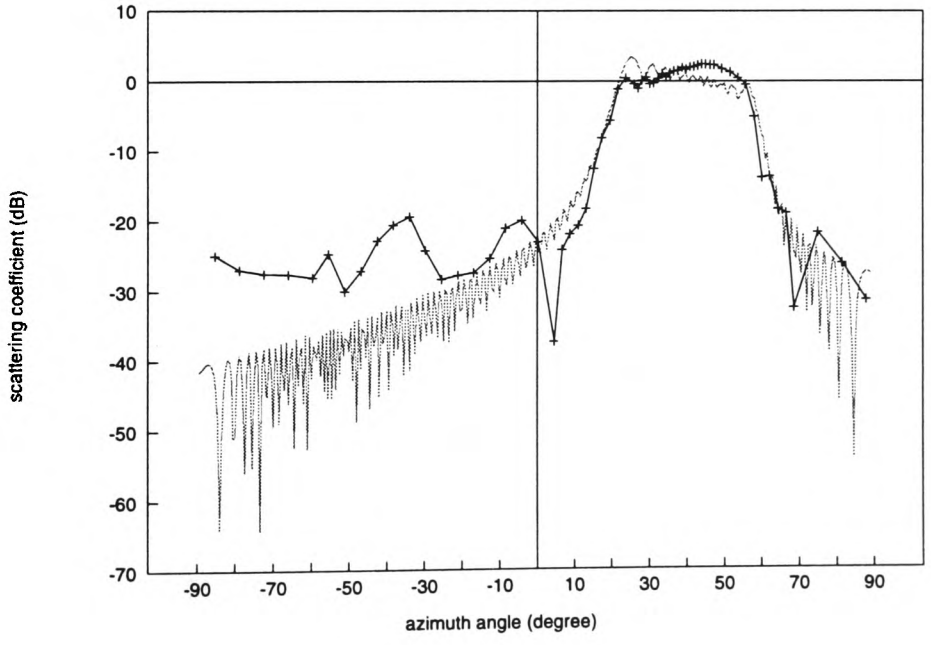

Figure 3.24 The predicted results of the very near field model in comparison with the measured results at 2.68 m.

a. at the top

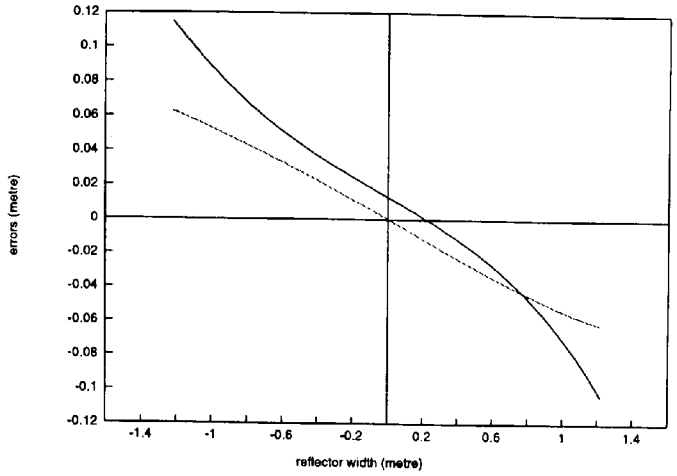

b. between the top and middle

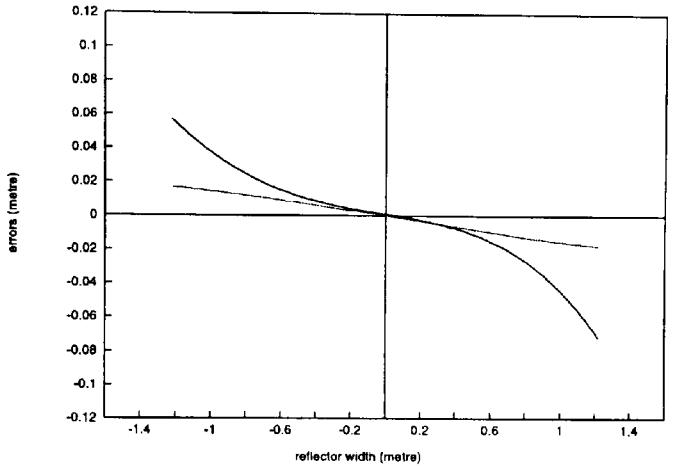

c. in the middle

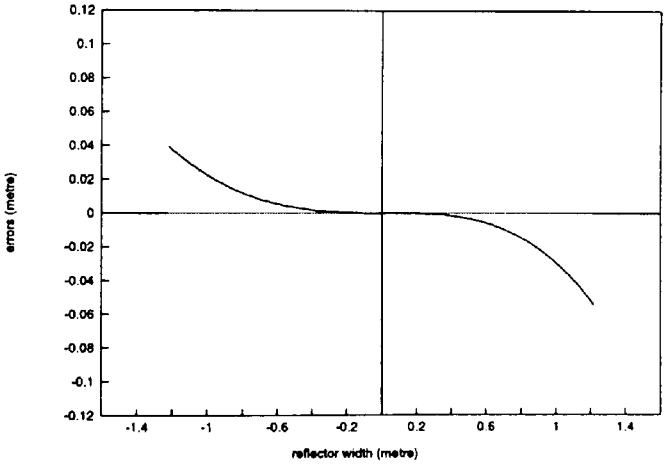

Figure 3.25 Errors of the near (solid curve) and very near field (dotted curve) approximations in the very near field (2.68 m) of the reflector.

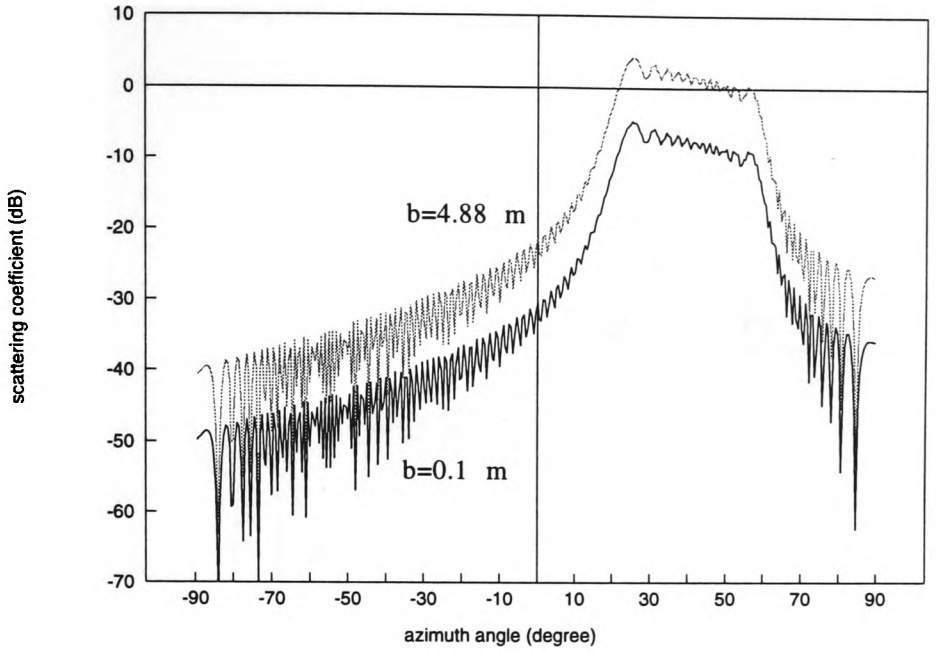

Figure 3.26 The scattering patterns of reflectors 2.44 m by 4.88 m and 2.44 m by 0.1 m at the receiver-reflector distance 2.68 m.

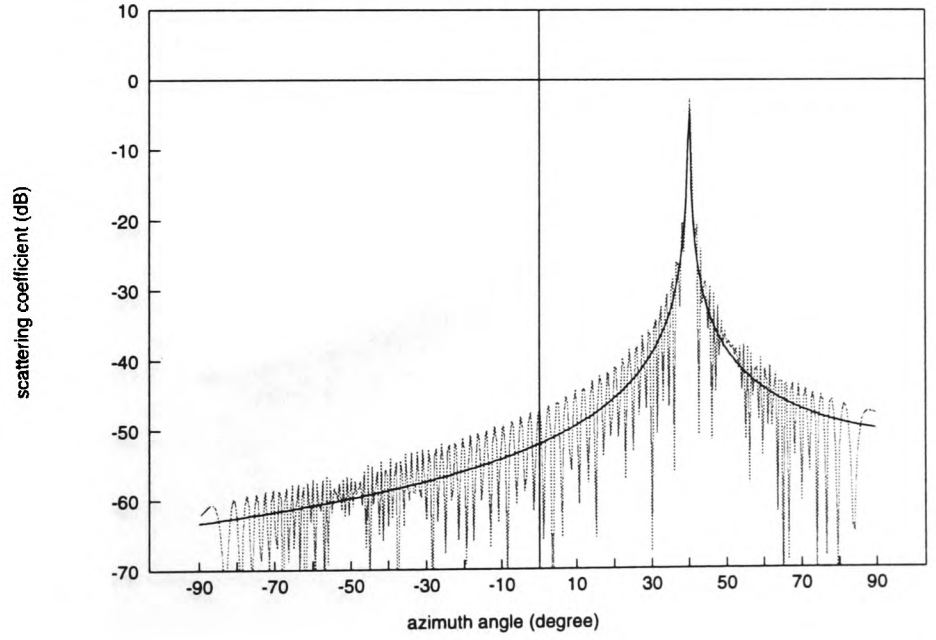

Figure 3.27 Azimuth dependence of the scattering coefficient in the far field (268 m).

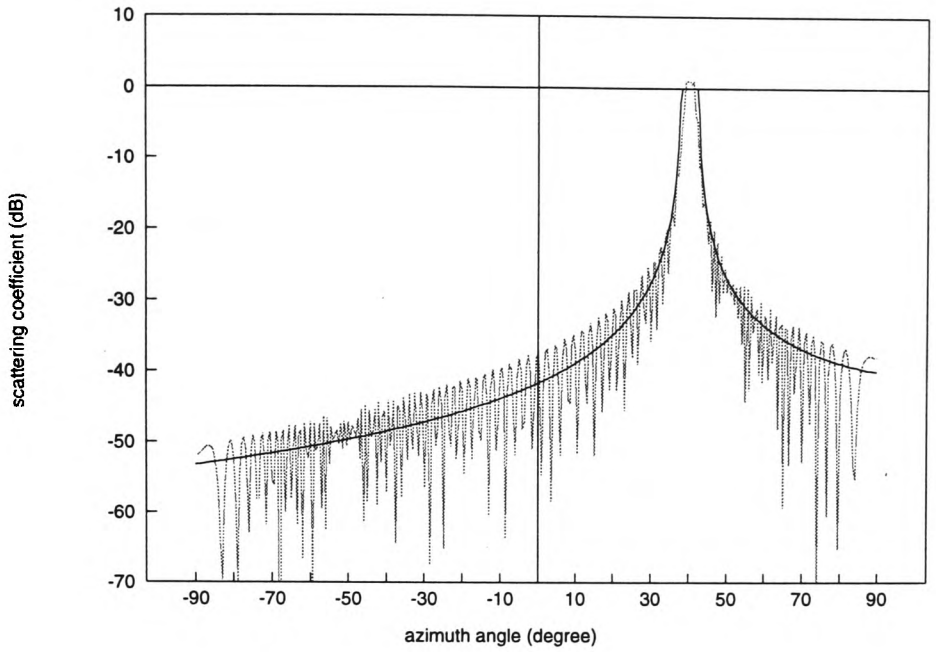

Figure 3.28 Azimuth dependence of the scattering coefficient in the near field (26.8 m).

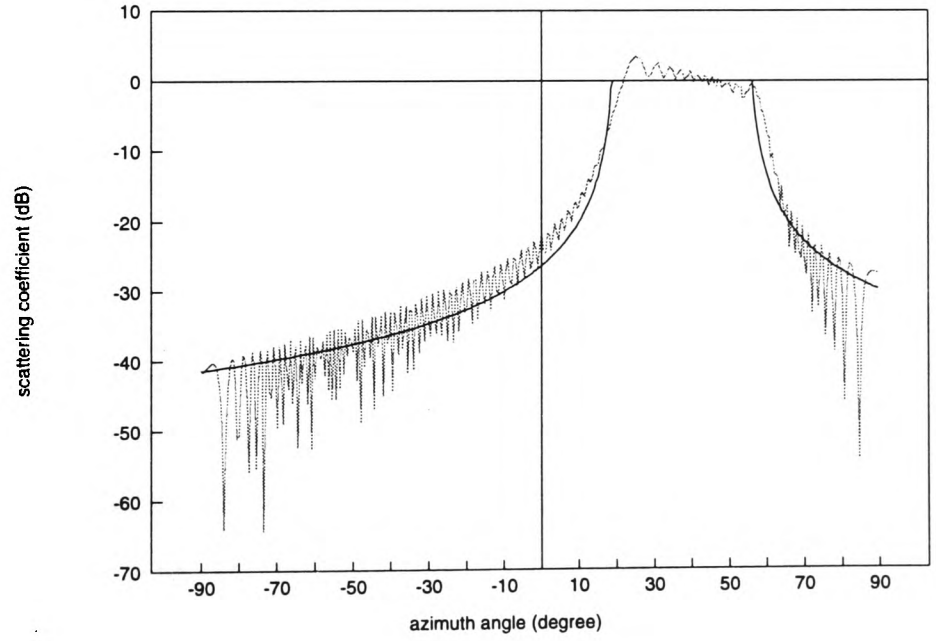

Figure 3.29 Azimuth dependence of the scattering coefficient in the very near field (268 m).

CHAPTER 4 EFFECTS OF BUILDING STRUCTURAL AND SURFACE FEATURES

4.1 Introduction

In the previous chapter, the scattering behaviour of a perfectly conducting reflector was characterised with regard to its dependence on range and angle in various receiver-reflector configurations. The prediction models developed assume that buildings have plane surfaces. However, more complicated scattering situations could be encountered when building surfaces contain typical features in their architecture. There could be similar situations in built-up areas of urban environments where a group of buildings are located close together. Prediction models without appropriate consideration of the scattering behaviour in these situations would be found in practice to be insufficient.

The aim of this chapter is to investigate and characterise the scattering behaviour of building features. In particular those features likely to result in high interference levels are examined closely. Most building features are essentially composed of a number of geometrically ordered planes or curved surfaces. Typical examples of building structural features are protruding or recessed sections and cylindrical features. In the scattering process caused by such features, the individual and relative geometries of the constituent planes become significant. To show the effects of individual plane geometries on scattering, the scatter patterns of offset and oblique plane geometries are examined. As a group of planes, their effects on scattering patterns could arise from shadows and double reflections due to the possible obscuration between planes offset from or perpendicular with respect to each other. In addition, another form of these effects is the diffused interference caused by scatter from a cylindrical feature.

Windows and wall sections of buildings are typical building surface features. Their existence may cause building surfaces to be discontinuous in terms of electrical and geometrical properties. Windows generally consist of glass and frames materially different from those

materials of building wall sections. Defining the electrical characteristics of windows and wall sections using different values of reflection coefficients, a building surface with windows may be represented as one actually consisting of a number of different scattering elements connected together. The total scattered field strength at a point is the phasor sum of the contributions of all the elements. Babinet's principle may be applied to simplify the calculations involved due to the fact that windows and wall sections are geometrically complementary to each other. The possible effects of windows are analysed and illustrated by means of scattering pattern diagrams assuming different values for the reflection coefficients of windows and wall sections and also considering geometrical factors such as window area, number and distributions.

Building surface sections like windows, balconies and wall sections are actually individual planes which are connected together to make the actual building surfaces. In practice, these planes might not sit exactly in the main building surface. This in fact forms a kind of surface deviation roughness due to large scale surface variations since these individual planes are very large compared to the wavelength. Surface deviation roughness of this kind will be shown to cause marked departures from the results predicted theoretically for a smooth surface. The extent of this departure is shown in section 4.8 to be related to the number of panels and the range of random tilt angles.

The analyses and discussion of the effects of building features are carried out in the form of scattering patterns and these are compared with that of 2.44 m by 2.44 m reflector. The predicted results of the very near field model implemented at 26.8 m are used as a reference. The path geometry of incidence, dimensions and receiver positions described in section 3.5.2 is kept unchanged for the analyses throughout this chapter.

4.2 Effects of plane geometry variation

Planes are the most basic elements of building features. In the coordinate system used, a plane reflector entirely situated in the x-y plane represents a simple case. In this section, the effects of other plane geometries on scattering patterns are examined.

4.2.1 Aperture field of arbitrary planes

For an arbitrary plane, its plane geometry is generally given in three dimensions. To define such a plane, it is convenient to use two of three lines which are in the $x = 0$, $y = 0$ and $z = 0$ planes respectively. These line equations are as follows

$$\begin{aligned} x &= k_x y + x_0 \\ y &= k_y z + y_0 \\ z &= k_z x + z_0 \end{aligned} \qquad 4.1$$

where $k_x = \frac{\Delta x}{\Delta y}$, $k_y = \frac{\Delta y}{\Delta z}$ and $k_z = \frac{\Delta z}{\Delta x}$. When plane waves are incident, the aperture field of an arbitrary plane can be generally expressed as

$$\mathbf{E}_{ay}(x,y,z) = -\mathbf{u}_y \cos\phi_0 E_0 \exp\left[jk(x\alpha_0 + y\beta_0 + z\gamma_0)\right] \qquad \text{(unbounded)} \qquad 4.2$$

In practice, the geometries of the majority of planes which form the outline of building structural features are vertical. they do not however lie in the same vertical plane but rather in planes which intersect at various angles. Referring to the geometry of a single plane in the $z = 0$ plane, various horizontal geometries can be said to be relatively offset or oblique to it.

4.2.2 Aperture field of offset planes

An offset plane is defined as being parallel to the $z = 0$ plane, that is it lies in a plane defined by $z = z_0$. The plane geometry of this kind is so called offset relative to the $z = 0$ plane as shown in figure 4.1. The aperture field of offset planes can be expressed as

$$\mathbf{E}_{ay}(x,y,z) = -\mathbf{u}_y \cos\phi_0 E_0 \mathrm{rect}_a(x)\mathrm{rect}_b(y)\exp\left[jk(x\alpha_0 + y\beta_0 + z_0\gamma_0)\right] \qquad 4.3$$

The $kz_0\gamma_0$ term represents the phase difference between an offset plane $z = z_0$ and the $z = 0$ plane. Similarly in the phase term $\Psi(x,y)$ of the scattering field in equation 3.17 there is an additional term representing the offset. The phase term can be given in the form of the very near field model as

$$\exp(-jk\Delta) = \exp\left\{jk\left[2r - \sqrt{r^2 + x^2 + z_0^2 - 2r(x\alpha + z_0\gamma_0)} - \sqrt{r^2 + y^2 - 2ry\beta}\right]\right\} \qquad 4.4$$

4.2.3 Scattering patterns of offset planes

The scatter patterns of offset planes are computed for two offset distances which are -0.61 m and +0.61 m relative to the $z = 0$ plane respectively. The results of the simulations are shown in figure 4.2.

Comparing to the scatter pattern of a single plane in the $z = 0$ plane, the specular region of the $z = z_0$ plane is shifted from the original pattern of the $z = 0$ plane by $\Delta\theta$. When $r >> z_0$, $\Delta\theta$ is approximately given by

$$\Delta\theta \approx 180^\circ \frac{z_0 \sin\theta_0}{\pi r} \qquad 4.5$$

4.2.4 Aperture field of oblique planes

An oblique plane relative to the reference plane is defined as one which has been rotated about a vertical axis passing through the centre of the reflector. Examples of oblique planes are shown in figure 4.3. It is assumed that their oblique angles are $\pm\theta_n$ so that $z = x\tan\theta_n$. The aperture field of oblique planes can be expressed by replacing $z = x\tan\theta_n$ in equation 4.2.

$$\mathbf{E}_{ay}(x,y,z) = -\mathbf{u}_y \cos\phi_0 E_0 \mathrm{rect}_a(x)\mathrm{rect}_b(y)\exp\{jk[x(\alpha_0 + \gamma_0\tan\theta_n) + y\beta_0]\} \qquad 4.6$$

It reduces to a two dimensional aperture field. In the phase term of the scattering field, there is an additional term representing the obliqueness. The phase term becomes

$$\exp(jk\Delta) = \exp\left\{jk\left[2r - \sqrt{r^2 + x^2(1+\tan^2\theta_n) - 2rx(\alpha + \gamma\tan\theta_n)} - \sqrt{r^2 + y^2 - 2ry\beta}\right]\right\} \qquad 4.7$$

4.2.5 Scattering patterns of oblique planes

The scattering patterns of oblique planes are computed for the oblique angle $\theta_n = \pm 10^\circ$. The results of the simulations are shown in figure 4.4.

Comparing to the scatter pattern of the $z = 0$ plane, the specular regions of the oblique planes are shifted away from the original specular direction by $\pm 2\theta_n$. By Snell's law, the angle θ_s' of the specular reflection is equal to the angle θ_0' of incidence in magnitude and opposite relative to the normal of the surface as $\theta_s' = -\theta_0'$. When the surface is oblique with the angle θ_n, Snell's law can be given in the coordinate system as

$$\begin{aligned} \theta_s' &= -\theta_0' \\ \theta_s - \theta_n &= -(\theta_0 - \theta_n) \\ \theta_s &= -\theta_0 + 2\theta_n \end{aligned} \qquad 4.8$$

Thus the specular direction in the coordinate system is shifted away from the original specular direction by an amount twice as much as the oblique angle θ_n. It is also noted that the width of the specular region changes also according to

$$\Delta\theta_s \approx 2\sin^{-1}\left[\frac{a\cos(\theta_0 - \theta_n)}{2r}\right] \qquad 4.9$$

4.2.6 Structural features involving offset and oblique planes

When a group of offset and oblique planes are connected together in a geometrical order, a certain type of building structural feature is formed. The most often seen building structural features are protruding and recessed structures. There could be many other features composed of a variety of possible combinations of offset and oblique planes. It would be tedious and somewhat unnecessary to consider all these combinations. The overall scattering behaviour is essentially dependent on firstly, the scattering behaviour of each individual plane, which has been demonstrated, and secondly, the combined behaviour of these planes. The total scattered field is determined by the phasor sum of the field contributions from each of the planes making up the structural features. Additionally shadows and double reflections would occur due to the possible obscuration of incident and reflected waves between the offset and oblique planes in these features.

4.3 Protruding features analysis

In figure 4.5, a protruding building feature is shown in plan view. This protruding feature is composed of a number of five vertical and flat planes named as AB, BC, CD, DE and EF whose dimensions are all much greater than the wavelength. The planes AB and EF are 0.915 m in width and in the x-y plane. The plane CD is 0.61 m in width and in the $z_0 = +0.61$ m plane. If it was in the $z = 0$ plane, the planes AB, CD and EF would become equivalent to the 2.44 m by 2.44 m plane reflector considered previously. The planes BC and DE with equal

widths are placed orthogonally at each side of the plane CD between the $z = 0$ plane and the CD ($z_0 = +0.61$ m) plane.

As incident waves arrive at such a protruding feature, the incident illumination can be described separately for each plane at their respective positions. There would be five aperture fields defined accordingly.

4.3.1 Aperture fields of the planes

Referring to the geometry in figure 4.5, the planes AB and EF are in the $z = 0$ plane, their aperture fields are respectively given by

$$\begin{aligned} \mathbf{E}_{AB}(x,y) &= -\mathbf{u}_y \cos\phi_0 E_0 \mathrm{rect}_{AB}(x)\mathrm{rect}_b(y)\exp\left[jk(x\alpha_0 + y\beta_0)\right] \\ \mathbf{E}_{EF}(x,y) &= -\mathbf{u}_y \cos\phi_0 E_0 \mathrm{rect}_{EF}(x)\mathrm{rect}_b(y)\exp\left[jk(x\alpha_0 + y\beta_0)\right] \end{aligned} \qquad 4.10$$

The plane CD is defined in the $z_0 = +0.61$ m plane, its aperture field is

$$\mathbf{E}_{CD}(x,y) = -\mathbf{u}_y \cos\phi_0 E_0 \mathrm{rect}_{CD}(x)\mathrm{rect}_b(y)\exp\left[jk(x\alpha_0 + y\beta_0 + z_0\gamma_0)\right] \qquad 4.11$$

The planes BC and DE are in the planes $x_{01} = -0.61$ m and $x_{02} = +0.61$ m respectively, their aperture fields are

$$\begin{aligned} \mathbf{E}_{BC}(y,z) &= -\mathbf{u}_y \cos\phi_0 E_0 \mathrm{rect}_{BC}(z)\mathrm{rect}_b(y)\exp\left[jk(x_{01}\alpha_0 + y\beta_0 + z\gamma_0)\right] \\ \mathbf{E}_{DE}(y,z) &= -\mathbf{u}_y \cos\phi_0 E_0 \mathrm{rect}_{DE}(z)\mathrm{rect}_b(y)\exp\left[jk(x_{02}\alpha_0 + y\beta_0 + z\gamma_0)\right] \end{aligned} \qquad 4.12$$

4.3.2 Obscuration between planes

However, the above aperture fields only stand for individual planes. They do not represent the actual aperture fields of the planes forming the protruding feature. With further consideration

of the incidence and receiver geometries, there are in addition, shadows and double reflections occurring due to the possible obscuration between the planes.

In the process of illumination, whatever the incident direction is, there will always be some planes or a part of a plane, incident rays are incapable of reaching because of geometrical optics limitations. The illumination is determined by both incident geometries and a "characteristic angle" of orthogonally intersecting planes at a corner. The characteristic angles of the corners ABC and DEF can be defined as

$$\theta_{cABC} = \tan^{-1}\frac{AB}{BC}$$
$$\theta_{cDEF} = \tan^{-1}\frac{EF}{DE} \qquad 4.13$$

The fully and partially illuminated planes are classified according to the incident azimuth angles relative to the characteristic angles as shown in table 4.1.

Table 4.1 Fully and partially illuminated planes

incident azimuth angle	fully illuminated planes	partially illuminated planes
$\theta_0 \geq \theta_{cABC}$	CD, EF, DE	
$\theta_{cABC} > \theta_0 > 0$	CD, EF, DE	$AB - BC\tan\lvert\theta_0\rvert$
$\theta_0 = 0$	AB, CD, EF	
$0 > \theta_0 > -\theta_{cDEF}$	AB, BC, CD	$EF - DE\tan\lvert\theta_0\rvert$
$\theta_0 \leq -\theta_{cDEF}$	AB, BC, CD	

Similarly from the receiver point of view, fully and partially illuminated planes might not be visible. Unlike the illumination source, the receiver is in the very near field of the building and hence scattering ray paths will not be parallel. Following this course, visible planes and those partially visible planes are classified by a set of angles as shown in table 4.2.

Table 4.2 Fully and partially visible planes

receiver azimuth angle	fully visible planes	partially visible planes
$\theta \geq \theta'_{cABC}$	CD, EF, DE	
$\theta'_{cABC} > \theta > \theta_{CD}$	CD, EF, DE	$AB - BC\tan\lvert\theta_{cBC}\rvert$
$\theta_{CD} \geq \theta \geq -\theta_{CD}$	CD	$AB - BC\tan\lvert\theta_{sBC}\rvert$, $EF - DE\tan\lvert\theta_{sDE}\rvert$
$-\theta_{CD} > \theta > -\theta'_{cDEF}$	AB, BC, CD	$EF - DE\tan\lvert\theta_{sDE}\rvert$
$\theta \leq -\theta'_{cDEF}$	AB, BC, CD	

The angles in table 4.2 are defined as follows:

$$\theta'_{cABC} = 90° - \left(\theta_{cABC} + \sin^{-1}\frac{a\sin\theta_{cABC}}{2r}\right) \tag{4.14}$$

$$\theta'_{cDEF} = 90° - \left(\theta_{cDEF} + \sin^{-1}\frac{a\sin\theta_{cDEF}}{2r}\right) \tag{4.15}$$

$$\theta_{CD} = \sin^{-1}\left(\frac{CD}{2r}\right) \tag{4.16}$$

$$\theta_{sBC} = \tan^{-1}\left(\frac{r\cos\theta - BC}{r\sin|\theta| + \frac{CD}{2}}\right) \tag{4.17}$$

$$\theta_{sDE} = \tan^{-1}\left(\frac{r\cos\theta - DE}{r\sin|\theta| + \frac{CD}{2}}\right) \tag{4.18}$$

The areas that can be seen from the source are known as the illuminated areas. Those that can be seen from the receiver are known as the visible areas. The illuminated and visible areas are not identical. The contributions to the total scattered field at an observation point must be only from those areas which are jointly illuminated and visible.

4.3.3 Double reflections

Moreover, attention must be also given to what has happened to reflected wave rays from one plane which are blocked by the plane orthogonally adjacent. Generally speaking, reflected waves will be reflected a second time, namely double reflections in corners. Apart from the case of normal incidence, such a situation must take place in one of the two corners ABC and DEF as shown in figure 4.5. From the viewpoint of the planes which block reflected waves rays, reflected waves from the orthogonally adjacent planes can be considered as second incidence onto itself. Therefore in one of the corners, the planes are not only illuminated by the first incident waves, but mutually by their reflected waves as well.

The first and second incident rays are sketched in simple ray paths as shown in figure 4.5. It can be seen that ray paths of the first incidence are coming from one direction while ray paths of their reflections from the two orthogonally adjacent planes as the second incidence go into two different directions respectively. Based on the geometries (θ_0, ϕ_0) of the first incidence, the geometries of the second incidence from the x-y plane to the $x = x_0$ plane are defined as follows

$$\theta_1 = \begin{cases} -180° - \theta_0 & \text{for } \theta_0 < 0 \\ 180° - \theta_0 & \text{for } \theta_0 > 0 \end{cases} \qquad 4.19$$
$$\phi_1 = \phi_0$$

It is the image of the first incidence relative to the $z = 0$ plane. The geometries of the second incidence from a $x = x_0$ plane to the $z = 0$ plane is defined as:

$$\theta_2 = -\theta_0 \qquad 4.20$$
$$\phi_2 = \phi_0$$

It is the image of the first incidence relative to the $x = x_0$ plane.

From the above, two sets of direction cosines can be defined for the second incidence respectively

$$\begin{aligned}\alpha_{01} &= \sin\theta_0 \cos\phi_0 \\ \beta_{01} &= \sin\phi_0 \\ \gamma_{01} &= -\cos\theta_0 \cos\phi_0\end{aligned} \qquad 4.21$$

and

$$\begin{aligned}\alpha_{02} &= -\sin\theta_0 \cos\phi_0 \\ \beta_{02} &= \sin\phi_0 \\ \gamma_{02} &= -\cos\theta_0 \cos\phi_0\end{aligned} \qquad 4.22$$

Then, the aperture fields resulting from the second incidence plane are with respect to the $x = x_0$ plane:

$$\mathbf{E}_{a(x=x_0)}(y,z) = -\mathbf{u}_y \cos\phi_0 E_0 \exp\left[jk(x_0\alpha_{01} + y\beta_{01} + z\gamma_{01})\right] \qquad 4.23$$

and on the $z = 0$ plane:

$$\mathbf{E}_a(x,y) = -\mathbf{u}_y \cos\phi_0 E_0 \exp\left[jk(x\alpha_{02} + y\beta)\right] \qquad 4.24$$

The fully and partially illuminated planes due to the second incidence are defined as shown in table 4.3.

Table 4.3 Second illumination

incident azimuth angle	second illumination on $x = x_0$ plane	second illumination on $z = z_0$ plane
$\theta_0 \geq \theta_{cDEF}$	$\frac{EF}{\tan\lvert\theta_0\rvert}$	EF
$\theta_0 = \theta_{cDEF}$	DE	EF
$\theta_{cDEF} > \theta_0 > 0$	DE	$DE\tan\lvert\theta_0\rvert$
$\theta_0 = 0$	/	/
$0 > \theta_0 > -\theta_{cABC}$	BC	$BC\tan\lvert\theta_0\rvert$
$\theta_0 = -\theta_{cABC}$	BC	AB
$\theta_0 \leq -\theta_{cABC}$	$\frac{AB}{\tan\lvert\theta_0\rvert}$	BC

Considering all the above, the scattered field strength from a protruding feature at one observation point is the phasor sum of the total contributions from those visible and illuminated areas involving the first and second illuminations. A computer programme was developed using the very near field model and was used to calculate the scattering patterns.

4.3.4 Scattering pattern of a protruding feature

The scattering pattern of a building protruding feature in figure 4.5 was computed and is shown in figure 4.6. Comparing it with the scattering pattern of the 2.44 m by 2.44 m plane reflector, significant differences can be seen. In the primary specular region (40±2 degrees), the scattering coefficients are still high relative to values in the non specular region, but about 3 dB lower than that of the plane reflector. The scattering pattern around the specular region has changed. Its top has become narrower while the pattern below -15 dB is widened. There are a number of irregular ridges appearing in and around the specular region. Irregular ridges are also seen in the non specular region and effectively cause the scattering coefficients in the region to rise by about 5 dB. When the observation point moves towards azimuth 0 degree,

the scattering coefficients are generally decreasing. However further into the other half of the azimuth range, the scattering coefficients start to increase again. In the region opposite to the primary specular region relative to azimuth 0 degree, the scattering coefficient values as high as those of the primary specular region can be seen. Relative to the centre of the azimuth pattern, a secondary image of the specular region appears to be created. The pattern of this secondary specular region is a little narrower than that of the primary specular region.

4.3.5 Behaviour of simulation results

The simulation results show the effects of the obscuration of illumination and also reflected waves between the planes comprising the protruding feature. Around the primary specular region, the scattering coefficients are mainly determined by the contributions of plane CD and parts of planes AB and EF which might vary at different azimuth angles. The total effective scattering area is less than that of an equivalent plane reflector and is also discontinuous. The ridges appear as the coherent effects of these discontinuous planes. As a result, the scattering coefficients in the specular region decrease while those in the non specular region increase. The difference in the scattering coefficients between those observed in the specular and non specular regions is reduced. The width of the specular region is somewhat widened.

Most significantly, the simulation results show the effects of double reflections. In the other half of the azimuth range opposite to the primary specular direction, the high scattering coefficients are mainly determined by contributions of the second incident rays on planes AB and BC. From the geometries of the second incidence in equations 4.19 and 4.20, their specular directions are expected to be opposite to the primary specular direction relative to azimuth 0 degree. Although planes AB and BC are discontinuous, all ray paths of double reflections from the two planes are identical in length so that AB and BC form the equivalent of a continuous plane. The scattering pattern can be seen as that of this equivalent plane normal to the first incident direction. In other words, it is effectively the scattering pattern of

an oblique plane $\theta_n = \theta_0$. The effective width a_{eABC} can be defined by the incident azimuth angle relative to the characteristic angle θ_{cABC} and planes AB and BC as

$$\begin{aligned} a_{eABC} &= 2AB\cos\theta_0 \qquad |\theta_0| \geq \theta_{cABC} \\ a_{eABC} &= 2BC\sin|\theta_0| \qquad |\theta_0| \leq \theta_{cABC} \end{aligned} \tag{4.25}$$

Similarly in the corner DEF, an effective width a_{eDEF} can be also defined by the incident angle relative to the characteristic angle θ_{cDEF} and planes DE and EF as

$$\begin{aligned} a_{eDEF} &= 2EF\cos\theta_0 \qquad |\theta_0| \geq \theta_{cDEF} \\ a_{eDEF} &= 2DE\sin|\theta_0| \qquad |\theta_0| \leq \theta_{cDEF} \end{aligned} \tag{4.26}$$

4.4 Recessed features analysis

In figure 4.7, a building recessed feature is shown in its plan view. Basically, a recessed feature behaves in a similar way as a protruding feature does in scattering. Herein lie the same problems of obscuration of illumination and reflected waves between planes which are arranged in a certain geometrical order. The aperture fields, together with visible and illuminated areas involving the first and second illuminations can be determined by referring to section 4.3.

When the incident azimuth angles are in the following range

$$\tan^{-1}\frac{CD}{2DE} > \theta_0 > -\tan^{-1}\frac{CD}{2BC} \tag{4.27}$$

there would be only double reflections. Since the corners BCD and CDE are facing each other, there might be triple reflection or, indeed, higher orders of reflection taking place between planes BC, CD and DE.

In the following range of incident azimuth angles

$$\theta_0 > \tan^{-1}\frac{CD}{DE} \text{ and } \theta_0 < -\tan^{-1}\frac{CD}{BC} \qquad 4.28$$

there would be no double reflections, but triple and even higher order reflections are possible. In practice when reflection loss coefficients of surfaces have to be considered, triple and higher order reflections are considerably weaker than the single and double reflections so that they can be ignored. A computer programme was developed using the very near field model to calculate scattering patterns. In this programme, only the visible areas of the first and second incidence are taken into account.

4.4.1 Scattering pattern of a recessed feature

The scattering pattern of the recessed feature in figure 4.7 is computed and predictions are shown in figure 4.8. Compared to the scattering pattern of the 2.44 m by 2.44 m plane reflector, the scattering pattern has changed significantly. Some of these changes have very similar characteristics to those of the protruding feature. In the primary specular region (40±2 degrees), the scattering coefficients reduce by a few decibels and the width of the region becomes wider. In addition, the specular region is marked by a deep null appearing in the centre. This clearly provides strong evidence of both the non illuminated and invisible areas of plane CD which reduce the scattering contributions from the centre of the total reflector surface. The scattering coefficients in the non specular region are effectively higher due to ridges. It is also seen that in the azimuth range opposite to the primary specular region, there is a secondary specular region with high scattering coefficients caused by double reflections. Different from the protruding feature, the double reflections in one corner can be blocked by another lying opposite. It is seen that the secondary specular region is narrower than that of the protruding feature. The scattering coefficients reduce more sharply as the receiver azimuth angle increases while the visible area of the second incidence decreases. For this reason, double reflections can be completely blocked if the width of the recessed plane decreases and

the recessed depth increases so that $\theta > \tan^{-1}\frac{CD}{DE}$ (or $\theta < \tan^{-1}\frac{CD}{DE}$), there would then be no double reflections and the scattering coefficients in the incident azimuth range would be low.

4.4.2 Discussion and limitations

In the analysis above, shadows and double reflections are highlighted as the major effects of building structural features. The analysis of these effects has been greatly simplified by the use of geometrical optics. Hence, we do not have an exact and complete picture, rather an approximate one. The exact and complete analysis would involve the effects of diffraction wherever shadows or double reflections are concerned. However, it is understood that with the physical size of protrusion (or recesses) and also high frequencies involved, the differences between the results of geometrical optics and diffraction would be very small on this occasion.

In practice, since only small positive elevation angles of incidence would be involved, the areas of shadows and double reflections have been approximated to be rectangular by ignoring some either illuminated or shadowed small areas by the waves arriving over the top of the building.

Since a perfectly conducting plane is assumed, the scattered signal level in the secondary specular is seen to be as high as that in the primary specular. However in practical situations, there would be a second loss for double reflections due to the reflection loss coefficient of the surface. Nevertheless compared to the scattering coefficients in the non specular region of one single plane, the high scattering coefficients of the secondary specular region could potentially present a harmful interference threat as that of the first specular region. From an interference viewpoint, both protruding and recessed features generally display similar scattering behaviours. However the latter feature might cause less problems in certain geometries, e.g. grazing angles and deep recesses. The application of this analysis is not limited only to building structural features. It is also useful in situations where a building and its adjacent neighbours are geometrically erected as perpendicular to each other giving rise to doubly reflected signal paths.

4.5 Cylindrical features analysis

In the preceding sections, building features are considered as consisting of a number of geometrically ordered planes. The building surfaces are discontinuous. However, in some cases, building surfaces are actually continuous while they can not be described by any of the line equations in equation 4.1. A typical example of these is a cylindrical building feature. By investigating such a feature as a basic element, it would generally help to understand the scattering behaviour of other similar features.

4.5.1 Aperture field of a cylindrical feature

A cylindrical building feature of radius R_c is shown in figure 4.9. Let the centre of the cylinder be the origin of the coordinate system. The cylindrical building surface is defined as

$$x^2 + z^2 = R_c^2 \tag{4.29}$$

When the cylindrical building surface is illuminated by incident waves, the aperture field on the surface is given generally in three dimensions as follows:

$$\mathbf{E}_a(x,y) = -\mathbf{u}_y \cos\phi_0 E_0 \text{rect}_b(y) \exp\left[jk(x\alpha_0 + y\beta_0 + z\gamma_0)\right] \tag{4.30}$$

Since $x = R_c \sin\theta'$ and $z = R_c \cos\theta'$ in cylindrical coordinates (r,θ'), replacing x and z in the above equation gives

$$\mathbf{E}_a(x,y) = -\mathbf{u}_y \cos\phi_0 E_0 \text{rect}_b(y) \exp\left\{jk\left[R_c(\alpha_0 \sin\theta' + \gamma_0 \cos\theta') + y\beta_0\right]\right\} \tag{4.31}$$

4.5.2 Obscuration of illumination and visibility

The aperture field of equation 4.31 is not bounded with respect to θ'. In the process of illumination, only part of the cylindrical surface can be illuminated. For plane wave incidence, the maximum illumination covers the half surface of the cylinder ignoring diffraction and creeping waves [Dougherty and Wilkerson (1967 and 1969)]. The illuminated surface is bounded in terms of the incidence angle in the range $\theta_0 \pm 90$ degrees.

At any observation point, only part of the illuminated surface can be seen due to the non parallel ray paths in the near or very near fields of the cylinder. The visible surface is bounded in azimuth angles between $\theta \pm \cos^{-1}\frac{R_c}{r}$.

In this case, only the area which is illuminated and also visible should be taken into account as contributing to the signal at the observation point. Thus, it is the intersection of the visible and illuminated areas which is significant.

In cylindrical coordinates, the phase term of equation 3.17 can be written in the form of the very near field model as

$$\begin{aligned}\exp(-jk\Delta) &= \exp\left\{jk\left[2r-\sqrt{r^2+x^2+z^2-2r(x\alpha+z\gamma)}-\sqrt{r^2+y^2-2ry\beta}\right]\right\} \\ &= \exp\left\{jk\left[2r-\sqrt{r^2+R_c^2-2rR_c(\alpha\sin\theta'+\gamma\cos\theta')}-\sqrt{r^2+y^2-2ry\beta}\right]\right\}\end{aligned} \qquad 4.32$$

A computer programme was developed to calculate the scatter pattern for a cylinder. This is discussed in the next section.

4.5.3 Scatter patterns of a cylindrical feature

The scattering patterns of cylindrical features are computed and shown in figure 4.10. Comparing to the scattering patterns of the 2.44 m by 2.44 m plane reflector and the other building features, the scattering pattern of the cylindrical surface has no significant azimuth variations in the azimuth range. For simulations shown in figure 4.10 the receiver-reflector distance is 26.8 m (from the centre of the cylinder). Simulations are carried out for values of R_c of 0.61 m and 1.22 m. Where $R_c = 1.22$ m, the scattering coefficients are at about -20 dB and virtually independent of azimuth angle. This level is much lower than that observed in the specular region computed for the plane reflector. On the other hand, the scattering coefficient from a cylinder is observed to be much higher than that observed in non specular regions of the plane reflector.

As shown in figure 4.10, when the radius of the cylinder reduces from $R_c = 1.22$ m to $R_c = 0.61$ m, the scattering coefficients reduce slightly by about 3 dB while the shape of the scattering pattern remains virtually unchanged.

4.5.4 Discussion and limitations

The simulated scattering patterns of cylindrical building features, significantly have demonstrated that the scattering behaviour of cylindrical features have isotropic characteristics. As isotropic scatterers, the scattering coefficients from cylindrical features are virtually independent of azimuth. The levels are mainly dependent on the cylinder radius and the receiver-cylinder distance. A larger radius means higher scattering coefficients. Since they are isotropic in azimuth, a longer receiver-cylinder distance results in lower levels in proportion to 1/r. The scattering pattern shape hence does not change in relation to distance. These are the same as the far field characteristics. Generally, it can be said that cylindrical features do not cause interference as harmful as that contributed by specular and double reflections associated with plane surface features.

In practice, obstacles having cylindrical features can be buildings, building sections (tower), chimneys and lamp-posts, etc. Their appearance in the vicinity of a shielding site would generally not constitute a major threat of high scattering interference as harmful as specular reflections from adjacent buildings. In particular, the radius of chimneys and lamp-posts are relatively small compared to the dimensions of buildings so that they are less significant in this respect. Additionally, the receiver-cylinder distance can be very significant in these cases. However, cylindrical features give increased scattering coefficients in non specular regions. Therefore, their effects in these regions should not be totally discounted.

In this study, the analysis has been largely simplified by geometrical optics. In fact, the situation is much more complicated. It is noted that there are some other factors which would influence the scattered patterns of cylindrical obstacles, such as creeping and diffraction waves [Dougherty and Wilkerson (1967 and 1969)]. The creeping waves which are also called as surface waves are involved on both sides of the illuminated area. To some extent, the illuminated area would have fringes extending further into shadow regions due to creeping and diffraction. From the receiver point of view, the scattered waves can also arrive at an observation point by diffraction beyond line-of-sight paths. Nevertheless, compared to the dominant visible illuminated area considered in geometrical optics, these factors are of secondary importance. Discounting these factors is not only mathematically convenient but also practically justified.

4.6 Building surface edge effects

Plane building surfaces are finite so that there are edges around surfaces. In aperture analyses, uniformly distributed aperture fields have been always assumed. In fact, the actual aperture fields can never be exactly uniform since the tangential component of aperture field at edges would not exist according to the boundary condition of the tangential electric field. Therefore, in the area close to building edges, the tangential component of aperture field must decay to zero. As a result, the scatter pattern would be affected to some extent by the existence of

building edges. To evaluate edge effects, this section is devoted to consideration of non uniformly distributed aperture fields over reflector area close to the edges.

4.6.1 Edge-affected regions

The areas on a building surface that are sufficiently close to the edges of the reflector where changes in the current distribution may occur are referred to as edge-affected regions. The distance from this region extending into the surface a_{edge}, is usually a fraction of a wavelength. For the wavelength 0.026 m at the frequency of 11.2 GHz, every building can be regarded as very much larger than one wavelength. If vertical polarisation is assumed and a building surface is rectangular, the possible edge-affected regions are two narrow strips situated at the two vertical sides of the surface. Apart from these regions, the uniform aperture field should remain unaffected. This part of the surface may be referred to as an edge-effect free region (free for short). Let T be the ratio of the width of the "free" region to the total width of the surface. This is given by

$$T = \frac{a - a_{edge}}{a} \tag{4.33}$$

4.6.2 Cosine-law aperture field distribution

If D(x) is the distribution function of the aperture field, the aperture field of any arbitrary distribution can be expressed as

$$\mathbf{E}_a(x,y) = -\mathbf{u}_y \cos\phi_0 E_0 D(x) \mathrm{rect}_b(y) \exp\left[jk(x\alpha_0 + y\beta_0)\right] \tag{4.34}$$

Here, a cosine decay is assumed for the aperture field in edge-affected regions while in the "free" region the distribution is still uniform. The distribution function D(x) is then defined as follows:

$$D(x)=\begin{cases}1 & \frac{Ta}{2}>x>-\frac{Ta}{2} \\ \cos\left[\frac{\pi(2x+Ta)}{2(1-T)a}\right] & -\frac{Ta}{2}\geq x\geq -\frac{a}{2} \\ \cos\left[\frac{\pi(2x-Ta)}{2(1-T)a}\right] & \frac{a}{2}\geq x\geq \frac{Ta}{2}\end{cases} \qquad 4.35$$

Cosine distributions D(x) are shown across the width of the reflector in figure 4.11 for T = 40/50, 45/50, 48/50, 49/50, 49.5/50 and 50/50 which means the widths of the edge-affected region in terms of the wavelength are 9.12λ, 4.56λ, 1.82λ, 0.91λ, 0.46λ and 0λ respectively, assuming the reflector size is 2.44 m by 2.44 m.

4.6.3 Scattering patterns for reflectors including edge effects

The scattering patterns are computed and shown in figure 4.12 for the five values of T shown in figure 4.11. Despite the fact that actual decay distances in practice would be only a fraction of the wavelength, the smaller values of T (where a_{edge} would be a few wavelengths) were used to exaggerate the edge effects for the purpose of the analysis. When compared to the scattering pattern of the aperture field of a uniform distribution (T = 1), the scattering patterns for T < 1 around the specular region are found to have changed insignificantly with respect to the scattering coefficient and the beamwidth of the patterns. Even at T = 40/50 which has an exaggerated edge-affected region width of 9.12λ, the pattern in the specular region is very similar. However in the non specular region, the scattering coefficients for T < 1 are lower than those at T = 1. As the value of T decreases, the scattering coefficient reduces. Meanwhile, as the azimuth angles are moved further away from the specular region, the reduction of the scattering coefficients is more significant. As observed earlier the computed scattering coefficients in the non specular region are considerably lower than those of background scatter encountered in practice.

4.6.4 Discussion and limitations

The cosine distribution is only an assumption which does not necessarily represent the actual way in which aperture fields decay in edge-affected regions. It may be a faster decay like a Gaussian distribution or a slower decay. Nevertheless, the simulation results reveal that edges mainly have their effects on the scattering coefficients in the non specular region while these are much less significant in and around the specular region. As expected, the closer the value of T to one, the less effects the edges would have. The ratio T is an important factor. In the simulation, the width of the reflector is 2.44 m which is less than one hundred wavelengths. In practice, real buildings can be many times larger than the reflector so that the value of T would be very close to one since a_{edge} as a fraction of the wavelength will not change. Therefore at the present frequency band of 11.2 GHz and above, the edge effects would be of very little significance on the scattering patterns of real buildings. At lower frequency bands edge effects would be more prominent.

4.7 Effects of windows

Windows are typical building surface features. Building surfaces with windows are generally considered to be discontinuous due to different construction materials of windows and wall sections.

Windows were firstly considered as effective scattering elements in the study of Bramley and Cherry [1973]. This study stated that the total received scattered power is the sum of the powers contributed by the individual elements of windows and the wall containing them. However, due to the complexity, in general, in expressing the resultant power from a scattering surface, the effects of windows can not be explicitly included in theoretical expressions. Furthermore it has not been possible to systematically analyse and simulate these effects. Thus, they remained largely unknown. This prompted a further investigation aimed at

extending the models to include the effects of windows. This is discussed in the following sections.

4.7.1 Discontinuities in a building surface

Windows consist of glass and frames of wooden, metal and other various synthetic materials. Most building walls are made of stone-like materials such as bricks, concrete and may be covered with pebble-dash, etc. The electrical properties of building window and wall section materials (permittivity, conductivity and permeability) are generally different. As a result, building surfaces with windows are not continuous in terms of electrical properties. In radio propagation, the parameters of electrical properties are included and considered in terms of the reflection loss coefficient which determines the subsequent propagation behaviour of electromagnetic waves incident on the building surface from the air, namely reflection and refraction. Therefore, building windows and wall sections have different reflection coefficients. The reflection coefficients of windows and wall sections will be studied in detail in section 6.3. Here it would be useful to examine an idealised situation in which windows are represented as distinct regions forming a part of a large reflector with variable reflectivities. The effects of these on the scattering patterns are studied.

4.7.2 Modelling the effects of windows

In the theoretical simulation studies, building surfaces with windows are considered as being composed of a number of effective scattering elements, namely windows and wall sections distinguished by their different reflection coefficients. Reflection coefficient is a parameter commonly used to indicate the reflectivity of a material as the ratio of the amplitude of an incidence field to that immediately reflected from the material.

4.7.2.1 Selection of reflection coefficients

To implement the discontinuity of building surfaces, two different reflection coefficients ρ_1 and ρ_2 are assumed for window and wall section materials respectively. The simulations of the effects of windows are conducted into two ways. The first corresponds to the assumption that windows are perfectly reflecting with $\rho_1 = 1$ while the wall section reflection coefficient is changed in steps from perfectly reflecting to non reflecting (i.e. $\rho_2 = 1$, 0.75, 0.5 0.25 and 0). Next the reverse is assumed corresponding to the wall section material being perfectly reflecting while the windows reflection coefficient is changed in steps from perfectly reflecting to non reflecting (i.e. $\rho_2 = 1$, 0.75, 0.5, 0.25 and 0). When $\rho_1 = \rho_2 = 1$, the continuity of the building surface is maintained in terms of electrical properties and this corresponds to one limiting case of the perfectly conducting reflector which has no windows, analysed previously in chapter 3.

Although the above situations represent clearly idealised situations in treating either windows or wall section to be perfectly reflecting, the variability range of the reflection coefficient considered for both windows and wall section materials is reasonably wide to embrace many of the situations arising in practice.

4.7.2.2 Windows geometrical considerations

Window area, number and distribution are important geometrical considerations with respect to their effects on building scattering patterns. Some window models are schematically shown in figure 4.13. A is the area of the whole reflector surface including windows and wall sections which is currently measured to be 2.44 m by 2.44 m. B is the total area of windows. C is the total area of wall section. Since A is the sum of B and C, B and C are thus complementary in relation to A. In figures 4.13a, b and c, there are three cases of one, four and sixteen windows respectively. In the case of one window only, this is assumed to be in the centre of the reflector. For the cases of four and sixteen windows, the simulations assumed geometries in

which the windows are arranged regularly and evenly over the reflector surface as shown in figure 4.13. In the three cases considered, the total area occupied by windows B is kept constant at one quarter of that of the whole reflector A (i.e. B = A/4 in all cases).

4.7.2.3 Discrete aperture fields

For a perfectly conducting surface without windows, its aperture field is uniform and continuous. After the introduction of windows on the wall which have different reflection coefficients, the aperture field of a building surface with windows becomes discontinuous over the surface. There would be a number of discrete aperture fields which have to be separately defined according to the areas of windows and wall sections with different reflection coefficients. Defining an area function C(x,y), the aperture field of the wall section is defined as

$$\mathbf{E}_{aC}(x,y) = -\mathbf{u}_y \cos\phi_0 E_0 C(x,y) \exp\left[jk(x\alpha_0 + y\beta_0)\right] \qquad 4.36$$

Note that C(x,y) is no longer a rectangular area. Similarly defining an area function B(x,y), the aperture field of the windows is defined as

$$\mathbf{E}_{aB}(x,y) = -\mathbf{u}_y \cos\phi_0 E_0 B(x,y) \exp\left[jk(x\alpha_0 + y\beta_0)\right] \qquad 4.37$$

When there is more than one window, B(x,y) is discrete. It consists of a number of window areas $B_1(x,y)$, $B_2(x,y)$, ... and $B_n(x,y)$. Nevertheless, each $B_i(x,y)$ is a rectangular area. The total aperture field $\mathbf{E}_a(x,y)$ is the sum of the aperture fields over windows and wall sections.

4.7.2.4 Simplified calculations by Babinet's principle

By the principle of superposition applied to electric fields, the total scattered field strength from a reflector surface with windows can be expressed as the phasor sum of those of windows and wall sections as follows

$$\mathbf{E}(r,\theta,\phi) = \rho_1 \mathbf{E}_B(r,\theta,\phi) + \rho_2 \mathbf{E}_C(r,\theta,\phi) \qquad 4.38$$

The calculation of scattered field strengths involves the evaluation of a surface integral. Due to the discontinuity, it becomes now a succession of surface integrals separated over areas where the aperture fields of windows and wall sections are defined. The surface integrals over window areas would be conveniently separable with respect to x and y if windows appear to be in regular rows and columns on building surfaces like the cases shown in figure 4.13. However, the evaluation of the surface integral over the wall section area, considering the apertures, is more tedious. Usually, it would have to be divided into small areas over which the surface integral is separable. This is clearly inconvenient, in particular if the number of windows is considerably large. Nevertheless, the evaluation of the surface integral over the wall section area can benefit from the fact that a building surface A(x,y) is the union of window area B(x,y) and wall section area C(x,y) which are geometrically complementary. Hence Babinet's principle can be applied. The scattered field strength from a homogeneous building surface A(x,y) is equal to the phasor sum of those from surface B(x,y) and surface C(x,y). The surface integral over the wall section area is thus equivalent to the difference of the surface integral over whole surface A(x,y) minus that due to window areas B(x,y). Then, equation 4.38 can be rewritten as

$$\begin{aligned}\mathbf{E}(r,\theta,\phi) &= \rho_1 \mathbf{E}_B(r,\theta,\phi) + \rho_2 \left[\mathbf{E}_A(r,\theta,\phi) - \mathbf{E}_B(r,\theta,\phi)\right] \\ &= \mathbf{E}_B(r,\theta,\phi)(\rho_1 - \rho_2) + \rho_2 \mathbf{E}_A(r,\theta,\phi)\end{aligned} \qquad 4.39$$

4.7.3 Simulation results

A computer programme is developed for the window models described in the previous section using the very near field prediction model. The simulation is based on the 2.44 m by 2.44 m reflector at the reflector-building distance 26.8 m and with the azimuth incidence angle of -40 degrees. The simulation results are given for the cases of one, four and sixteen windows in the following sections.

4.7.3.1 A single window case

(i) $\rho_2 = 1$, ρ_1 variable in the range 0 to 1

The graphs on the left hand side of figure 4.14 sequentially show the scattering patterns of the one window case corresponding to the situations where the wall section is perfectly reflecting $\rho_2 = 1$ while the window reflection coefficient is variable i.e. $1 \geq \rho_1 \geq 0$. When $\rho_1 = 0.75$, the scattering coefficient in the specular region reduces by about 3 dB. There is a null appearing in the centre of the specular region. The depth of the null is about 5 dB. The scattering coefficient in the non specular region has also reduced slightly. When $\rho_1 = 0.5$, the scattering coefficient in the specular region reduces further. The null becomes much deeper. The depth of the null is about 18 dB. In the non specular region, there are small ridges appearing which raise the scattering coefficient values in the cases of $\rho_1 = 0.75$ and 0.5 compared with the case $\rho_1 = 1$. When $\rho_1 = 0.25$ and 0, the null gradually disappears. Instead, there is a narrow ridge appearing at the same place. The top part of the specular region is actually seen to have three ridges with two nulls in between. The scattering coefficient in the non specular region continuously rises slightly as ρ_1 reduces.

(ii) $\rho_1 = 1$, ρ_2 variable in the range 0 to 1

The graphs on the right hand side of figure 4.14 sequentially show the scattering patterns of the one window case corresponding to the situations where the wall section reflection coefficient is varied i.e. $1 \geq \rho_2 \geq 0$ while the window is assumed to be perfectly reflecting

$\rho_1 = 1$. When $\rho_2 = 0.75$, the specular region starts becoming narrower. For the following values of $\rho_2 = 0.5$, 0.25 and 0, the pattern of the specular region gradually changes to be further narrower and sharper. The scattering coefficient in the sharpened specular region increases by about 3 dB while that in the non specular region has been decreasing for the values of $\rho_2 = 0.75$ and 0.5 and eventually rises up by about 2 dB higher than the original pattern of $\rho_1 = \rho_2 = 1$. In fact, as ρ_2 approaches to zero, the scattered pattern is that due to one single reflector the size of the window which is a quarter of the original reflector, thus yielding a narrower pattern in the very near field.

4.7.3.2 Four windows case

(i) $\rho_2 = 1$, ρ_1 variable in the range 0 to 1

The graphs on the left hand side of figure 4.15 sequentially show the scattering patterns of the four windows case corresponding to the situations where the wall section is reflecting perfectly $\rho_2 = 1$ while the windows reflection coefficient varies in the range i.e. $1 \geq \rho_1 \geq 0$. When $\rho_1 = 0.75$, there is a null appearing in the specular region. Its depth is much less than those seen in the one window case. The width of the specular region is slightly narrowed while the scattering coefficients rises by about 2 dB. When $\rho_1 = 0.5$, 0.25 and 0, the null only slightly becomes deeper. In the non specular region, wider side lobes are seen and some irregular ridges are appearing as well. The scattering coefficients in the non specular region rise slightly.

(ii) $\rho_1 = 1$, ρ_2 variable in the range 0 to 1

The graphs on the right hand side of Figure 4.15 sequentially show the scattering patterns of four windows corresponding to the cases of the wall section reflection coefficient varying in the range $1 \geq \rho_2 \geq 0$ while the windows are reflecting perfectly i.e. $\rho_1 = 1$. When $\rho_2 = 0.75$, the scattering coefficient in the whole scattering pattern reduces by about 3 dB. There are some irregular ridges appearing in the non specular region. When $\rho_2 = 0.5$, there are two nulls appearing in the specular region. The nulls become deeper when $\rho_2 = 0.25$. The specular

region is split. The scattering coefficient in the specular region reduces continuously while that in the non specular region rises to levels higher than that seen in the original pattern when $\rho_2 = 0$. The width of the specular region becomes slightly narrower.

4.7.3.4 Sixteen windows case

(i) $\rho_2 = 1$, ρ_1 variable in the range 0 to 1

The graph on the left hand side of figure 4.16 sequentially show the scattering patterns of the sixteen windows corresponding to the situations where the wall section is reflecting perfectly $\rho_2 = 1$ while the windows reflection coefficient varies in the range $1 \geq \rho_1 \geq 0$. In the entire range of ρ_1, the scattering coefficients in the scattering patterns only reduce by about 2 dB. Although some side lobes become wider and there are some irregular ridges appearing, the overall scattering pattern does not change significantly.

(ii) $\rho_1 = 1$, ρ_2 variable in the range 0 to 1

The graphs on the right hand side of figure 4.16 sequentially show the scattering patterns of the sixteen windows corresponding to the situations where the wall section reflection coefficient varies in the range $1 \geq \rho_2 \geq 0$ while the windows are perfectly reflecting $\rho_1 = 1$. When $\rho_2 = 0.75$, the scattering coefficients in the whole scattering pattern reduce by about 3 dB. The scattering pattern does not change significantly. When $\rho_2 = 0.5$ and 0.25, the scattering coefficients reduce further. The specular region becomes narrower. Several nulls start appearing in the specular region. In the non specular region, side lobes change gradually their shape to be wider and there are irregular ridges appearing. When $\rho_2 = 0$, the scattering coefficient in the specular region reduces dramatically. The specular region is split by several deep nulls.

4.7.4 Discussion of simulation results

The scattering patterns of a building surface with windows are simulated in a total of twenty four cases which are individually characterised by varying values of reflection coefficients of window and wall section materials and window geometries i.e. number and distribution over the reflector. There are various window effects revealed in these patterns. In the following sections, some major effects on building scattering are discussed with respect to reflection coefficients and window geometrical characteristics.

4.7.4.1 Coherent effects of windows

In the scattering patterns corresponding to various reflection coefficients, there are three extreme cases

(i) $\rho_1 = 1$ and $\rho_2 = 0$ representing the scattering pattern of windows only;
(ii) $\rho_1 = 0$ and $\rho_2 = 1$ representing the scattering pattern of wall sections only;
(iii) $\rho_1 = 1$ and $\rho_2 = 1$ representing the original pattern of the reflector.

Referring to case (iii) (the original pattern), a reduction in reflection coefficient of either windows or wall section materials leading to either case (i) or (ii) essentially means losing scattering energy from the building surface to a certain extent. However, this loss of scattering energy has not been seen in the predicted scattering patterns to lead to an overall reduction of scattering coefficient values in absolute terms. In fact on many occasions, scattering coefficients at some particular points in the scattering patterns are seen to be increased significantly. To compensate for this, deep nulls are observed at other points in the scattering pattern. The appearance of nulls and ridges demonstrates the fact that contributions from all elements on the surface behave as coherent sources.

4.7.4.2 Window geometrical characteristics

Additionally from simulation results of the various cases, window geometrical characteristics can be seen to play a significant role in determining the coherent effects of windows and wall sections. In the one window case, the coherent effects of windows, seen as nulls and ridges or a narrower pattern, are concentrated so their effect looked stronger and much more significant than in the four and sixteen windows cases. In the latter two cases, the number of nulls and ridges is increased and their amplitudes are reduced. Particularly in the sixteen windows case, there are no strong nulls and ridges appearing in the scattering patterns so that the patterns do not change as much as seen in the one window case. It is seen that scattering coefficients reduce. In the extreme case of a very large number of evenly distributed windows, the coherent effects of windows would be widely spread to produce scattering patterns which are equivalent to the pattern of a surface without windows with an equivalent reflection coefficient of effective value lying somewhere between those of the windows and the wall section materials. In this aspect the sixteen windows case is seen as the most typical representation of a practical building. Thus, the difference between scattering patterns of surfaces with and without windows will be seen mostly in terms of the observed scattering coefficient values. In these cases, not only the reflection coefficients of windows and wall sections are important, but also the proportions of the areas occupied by windows and wall sections relative to that of the whole surface.

In the cases considered, the total windows area is one quarter of the total surface area. Particularly in the sixteen windows cases, the overall scattering coefficients in the scattering pattern reduce slightly when the window reflection coefficient ρ_1 is reduced from 1 to 0 but reduce significantly when the wall section reflection coefficient ρ_2 is reduced. This is clearly because of the amount of scattering energy lost when the windows being considered non-reflective form a minor portion of the total area. However the energy reflected from the wall sections represents the majority of the scattered energy. The opposite effect would occur if the

proportions of windows and wall sections are exchanged. It is worth mentioning again that this is only true for a fairly large number of evenly distributed windows.

In practice, buildings usually have a large number of windows and are evenly distributed. The scattering patterns of these buildings are not expected to be changed significantly due to the existence of windows. The scattering coefficients may vary over a range with relatively higher levels where the lager proportion of the surface area has a larger reflection coefficient. For buildings with small number of windows or centrally located windows, the effects of windows can be severe. There may be nulls and ridges appearing in the scattering patterns, particularly in the specular regions. Considering wider applications, the simulation results do not only demonstrate the coherent effects of windows, but also give indications of consequences of discontinuous aperture field on a building surface due to variations other than windows, such as generally non homogeneous building surfaces or perhaps a nonuniform incoming wave. Some similar coherent effects similar to those demonstrated in the prediction of window effects might be expected.

4.7.5 Limitations

Scattered signals occurring due to objects situated behind windows and by window frames have not been taken into account in the simulations. The contribution of scatter from beyond windows is expected to be small. The scattered signals coming in and out through windows would have suffered considerable loss of signal strength and would be difficult to predict in general. Window frames consist of vertical and horizontal strips made of wood, metal and composite materials, etc. The widths of these strips are generally of a comparable order to that of a wavelength for frequencies around 11.2 GHz. This is likely to lead to diffused scatter [Beckmann 1963]. On the other hand, the effective area of window frames are proportionally far less than the other scattering elements considered so far. The scattering signal strength from window frames would decrease more rapidly as receiver-building distance increases than

those of windows and wall sections. Due to these factors window frames appear to play a very limited role in building scatter.

4.8 Surface deviation "roughness"

The specular nature of smooth surface reflections has been demonstrated theoretically and experimentally based on a smooth and perfectly conducting reflector. This reflects specularly and the energy is largely confined to its specular region. However, although practical building surfaces are mostly plane in general, there are windows, balconies, wall facade sections which may give variations or tolerances with respect to perfectly plane reflectors and the specular nature of smooth surface reflections may, as a result, be altered.

In some methods of radio system coordination which attempt to account for interference caused by terrain scattering, terrain geometries are modelled using a number of smooth planes connected at appropriate angles corresponding to the modelled terrain features [Giger (1983, 1986a and 1986b)]. In the models developed by Giger the radiation patterns considered have no distance dependence and may therefore by regarded as far field models. Such model is not directly relevant to this study, possibly due to the different nature of building and terrain scatter.

In contrast, building surface deviation roughness caused by windows, balconies and wall facade sections manifests itself on a much smaller scale than that seen in terrain geometries. However, the major concern with buildings is that these could alter the detailed structure of scattering patterns obtained and may produce some broadening of the reflected beam.

An earlier study was carried out by Noerpel and Ranade [1989]. A method using the geometrical theory of diffraction (GTD) was developed to characterise the effect of buildings with "gross rough" features. These are concerned with so called large scale surface deviations. A theoretical study considering the far field range only indicated that the concerns mentioned

above are justified. In site shielding applications, the same problem has to be investigated in the near and very near fields of buildings and is explored in the next section.

4.8.1 Modelling surface deviation

In the theoretical simulation, building surfaces are considered as being composed of a number of perfectly conducting smooth vertical panels. Each of these panels are given a small random azimuth angle to take into account the possible variations or tolerances. These panels approximate to practical building surfaces with roughness represented by large surface texture variations as shown in figure 4.17 in which the plane surface is replaced by five smaller panels. Figure 4.18 shows a similar approximation involving ten smaller planes. The possible broadening of reflected beam from such a surface will be confined in azimuth planes in a cylindrical region rather than in a spherical region. This would not only simplify the problem, but also satisfy the prediction needs for most practical situations concerning only scattering pattern in azimuth. Scattering patterns from any building with surface deviation roughness may be described in terms of a functionally equivalent surface made up of finite number of smooth panels with small tilts about its normal plane position. Let the surface be made up of N vertical panels and the panels be characterised by a small random azimuth tilt angle θ_t within a maximum range of θ_{tm} about the building nominal surface. The aperture field of such a panel with a tilt angle is given by an oblique plane of equation 4.6. Using the very near field model, the scattering field strength is the phasor sum of the contributions of the N panels.

4.8.2 Simulation results

In the process of the simulation, the range of random azimuth tilt angles is given as $\theta_{tm} = 0$, 0.1, 0.2 and 0.5 degrees. Azimuth tilt angle θ_t is randomly assigned within the range. The random numbers used are from Table F-19. Random Numbers [Korn (1968)]. Two separate simulations were carried out with the number of panels assumed to be $N = 5$ and 10 respectively, so that each panel width is 2.44/N m. The simulation results corresponding to the

various values of the parameters are shown in figure 4.19 and figure 4.20 at the receiver-building distances of 26.8 m and 268 m respectively.

4.8.2.1 Scattering patterns at 26.8 m

In figure 4.19, the graphs on the left-hand side show the scattering patterns at 26.8 m with the number of panels $N = 5$. When the range of random azimuth tilt angles θ_{tm} is equal to zero degrees, the scattering pattern is the same as the smooth plane as if it consists of one plane panel. When $\theta_{tm} = \pm 0.1$ degrees, some changes have already taken place in the scattering pattern. The pattern above -3 dB in the specular region becomes narrower and sharper. In the non-specular region, there are some ridges appearing. As the range of random azimuth tilt angle further increases, the pattern above -3 dB in the specular region becomes even sharper than before. The ridges in the non specular region are raised, in particular those very close to the specular region. It seems that the ridges are the results of the side lobes coherently merging in the non specular region. The number of side lobes is reduced. But they are higher and wider, and the gaps between them are wider too. At $\theta_{tm} = \pm 0.5$ degrees, the scattering pattern changes further. Now, the pattern around the maximum is so narrow that it is only a sharp tip. Due to the ridges, the maximum scattering coefficients in the non specular region are effectively seen to be about 5 dB higher than those predicted from a plane surface. Apart from the sharp tip, the major part of the scattering coefficient in the specular region has reduced to the level of -3 dB which is then seen to merge with the rising ridges beside the specular region. The resultant effects of this is that the beamwidth of the scattering pattern is broadened. The difference between the scattering coefficients in the specular and non specular regions decreases. The scattering pattern becomes less directive.

The graphs on the right-hand side in figure 4.19 show the scattering patterns with the number of panels $N = 10$. Essentially, the changes which have been seen in the scattering patterns with the number of panels $N = 5$ are also seen in these graphs, but on a more noticeable scale. For $\theta_{tm} = \pm 0.5$ degrees, there is again only a sharp tip remaining in the pattern above the level of

-3 dB in the specular region. In the non specular region, the ridges rise higher than the cases of $N = 5$. But, the number of the ridges reduces so that the ridges and the gaps between them are becoming wider. Effectively, the top scattering coefficients in the non specular region are raised by about 10 dB compared with the single panel case. The difference between the scattering coefficients of the specular and non specular regions are further reduced. The beamwidth of the scattering pattern is effectively and noticeably broadened.

4.8.2.2 Scattering Patterns at 268 m

In figure 4.20, the graphs show the scattering patterns at 268 m with the number of panels $N = 5$ on the left-hand side and $N = 10$ on the right-hand side. When the range of random azimuth tilt angles θ_{tm} is zero, the scattering pattern is that of a smooth plane where there are no individual panels. At 268 m, it is in the far field range of the reflector. The scattering pattern should be narrower and there is a larger difference between the scattering coefficients of the specular and non specular regions compared with simulations at 26.8 m if it is a plane surface. As the range of random azimuth tilt θ_{tm} angle increases, the scattering patterns change in a similar way to those shown in figure 4.19. The scattering coefficients in the specular region decrease apart from sharp tips. There are ridges appearing in the non specular region. Effectively, the scattering coefficients in the non specular region increase. Thus, the difference between the scattering coefficients of the specular and non specular regions reduces. The beamwidth of the scattering pattern effectively broadens. Interestingly, comparing the scattering patterns at 26.8 m and 268 m, it is found that the differences between them gradually vanish as the range of random azimuth tilt angles increases. When $\theta_{tm} = \pm 0.5$ degrees, the scattering patterns at 26.8 m and 268 m are very close to each other, apart from amplitude difference of about 10 dB. In these scattering patterns, the same number of ridges are observed. These appear at the same places and are identically shaped in the azimuth range. The difference between the scattering coefficients of the specular and non specular regions are the same for both distances. The beamwidths of the scattering patterns are the same.

4.8.3 Discussion of simulation results

The simulation results suggest that surface deviation roughness can have some significant effects on the scattering pattern of a building surface. These are mainly seen as beamwidth broadening and scattering coefficients increasing in non specular regions. The effects of surface deviation roughness can be modelled in terms of a number of smooth panels and the range of random azimuth tilt angles.

When a surface consists of a number of panels which have a random azimuth tilt angle, the surface no longer has a single specular direction. Instead, there are a number of specular directions determined by individual panels. They are randomly located around the original specular direction within a range twice as big as the range of random azimuth tilt angles. The multiple specular directions result in reflected energy spreading so that the scattering coefficients in the original specular region decrease. This is seen as beamwidth broadening to some extent, restricted to a maximum of about one degree in the cases considered. The scattering signal strength from the rough surface is the phasor sum of those contributions from individual panels. There are also coherent effects between the panels. The side lobes in the non specular region are merging to form some higher and wider ridges which effectively increase the scattering coefficients in this region. Such an increase closer to the original specular region is very significant, responsible for beamwidth broadening and may be used to explain effects observed in practice.

The receiver-building distance of 26.8 m is in the near field range of the reflector surface. If the surface is plane, its scattering pattern would show the same characteristics as those in the near field range described in sections 3.5.3 and 3.6.2. It is shown that the scattering coefficient in the specular region has no distance dependence while the beamwidth of the pattern has. However since panels and random azimuth tilt angles are introduced, the whole surface breaks and individual panels emerge. From the individual narrower panels point of view, 26.8 m is in the far field range as far as the azimuth pattern is concerned. As the number of panels and tilt

angles increases, the characteristics of the radiation patterns can be seen to change from those of a near field model to a far field model. As an example, considering the case where $\theta_{tm} = \pm 0.5$ degrees and $N = 10$ panels, increasing the distance from 26.8 m to 268 m does not significantly change the pattern. This is expected as it is a well known far field characteristic.

4.9 Interim Conclusion

In this chapter, the prediction models developed in chapter 3 are used in the investigation of the scattering behaviour of building features. The investigation into scattering processes of building surfaces with windows and surface deviation roughness provides opportunities to gain knowledge regarding possible scattering behaviour of building surfaces in these circumstances. Scattering by a building surface with these features is a very complicated process. Simplification and idealisation have to be adopted to enable the investigation to be carried out. In general, an arbitrary and complicated feature can be resolved into a number of basic structures discussed. Consequently, the properties of the scattering behaviour of such a feature would exhibit the effects resulting from the superposition of contributions from each of the basic structures involved, mainly offset and oblique planes, planes with different reflection coefficients, orthogonally intersected planes and finally cylindrical surfaces.

Using aperture analysis, the problems encountered become those of defining the aperture fields over these building surfaces. The aperture fields on some features can be defined continuously by either linear or nonlinear surface equations, e.g. oblique planes and curvatures. The others might have to be defined discretely by a group of separate plane structure like windows. In determining the radiation fields due to such aperture fields, exact solutions involving diffraction in both the processes of illumination and scattering would be too complicated. The problems have been studied using geometrical optics. The method is relatively simple, but its implementation can be tedious and complicated so that it is not necessarily suitable for predictions of complex building features. The emphasis has been on identifying those features which most affect the scattering patterns of plane surfaces and

studying their scattering behaviour. The basic pattern of a smooth plane surface is always seen to be highly relevant. With information of surface features available, their effects can be estimated using the methods developed (see section 6.4). In situations where such information is unavailable, the simulation results obtained in this chapter can be used to provide useful estimation which would be helpful to system planners. Using analyses described in this chapter, it is possible to assess the effects of some typical building features commonly found in urban areas.

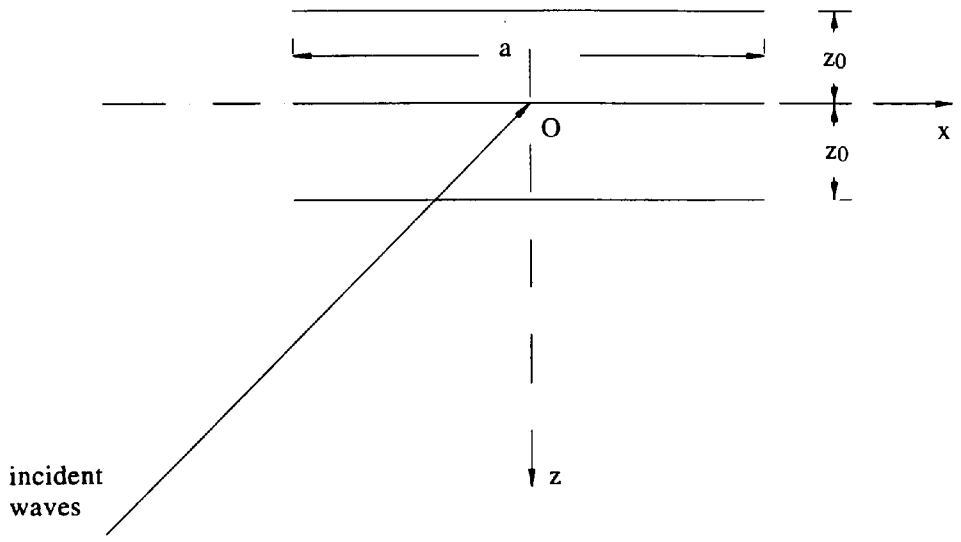

Figure 4.1 Geometry of offset planes.

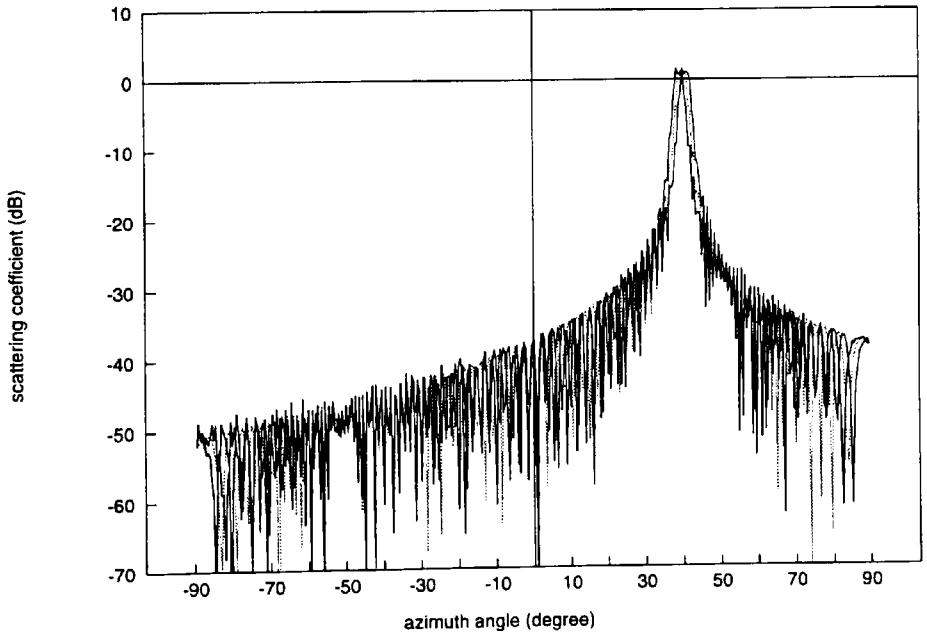

Figure 4.2 The scattering patterns of the offset planes z_0=+0.61 m and z_0=-0.61 m in comparison with that of the reflector in the z=0 plane.

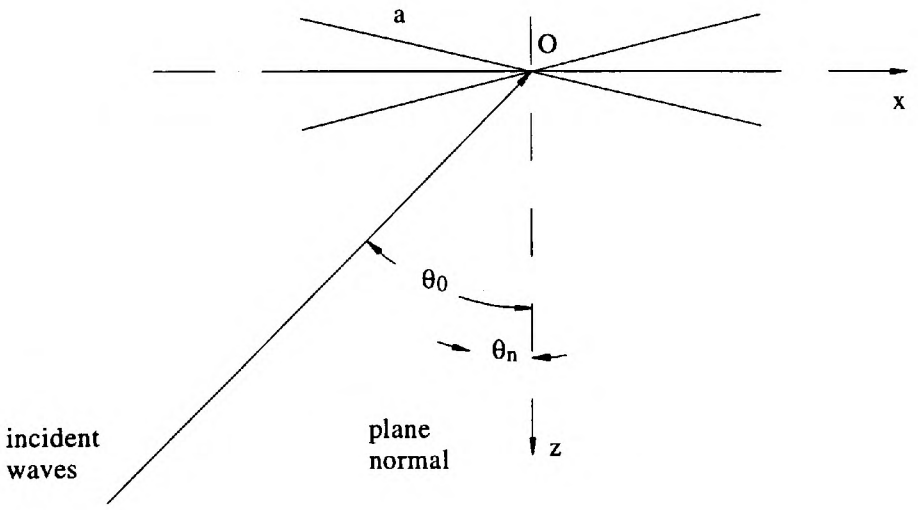

Figure 4.3 Geometry of oblique planes.

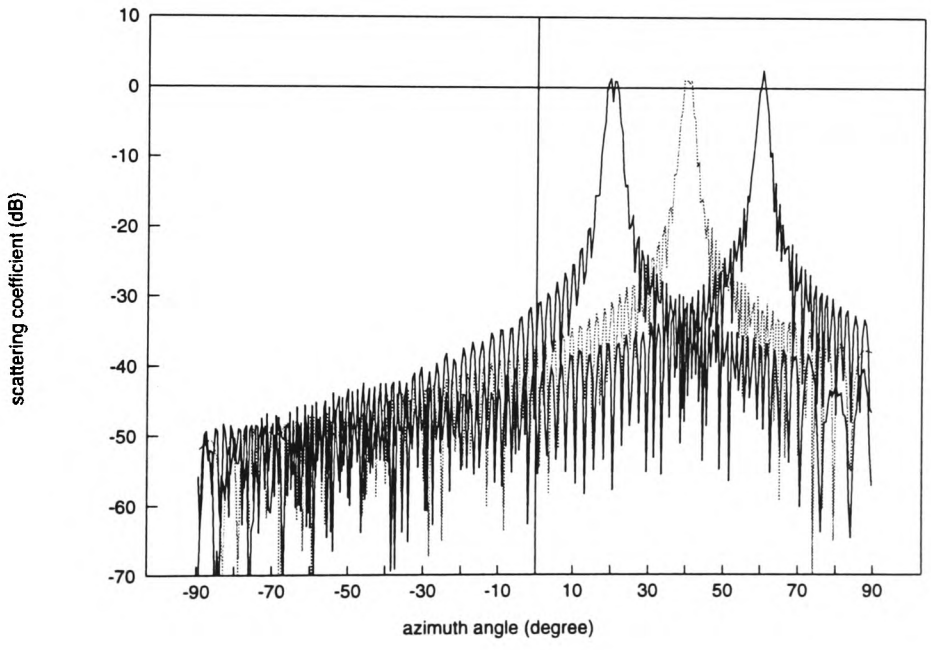

Figure 4.4 The scattering patterns of the oblique planes θ_n=+10° and θ_n=-10° in comparison with that of the reflector in the z=0 (θ_n=0) plane.

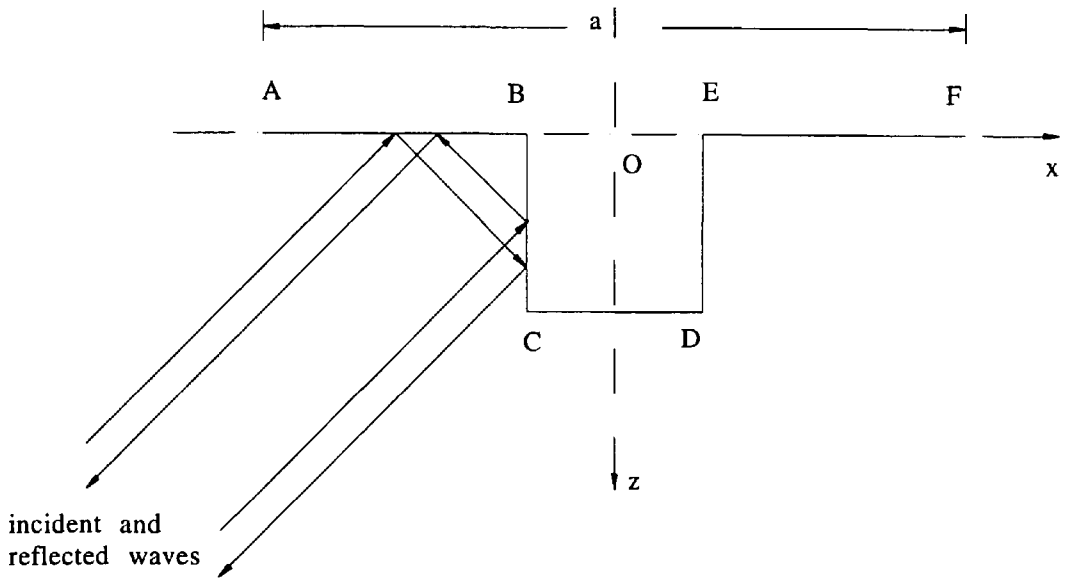

Figure 4.5 Geometry of a building protruding feature.

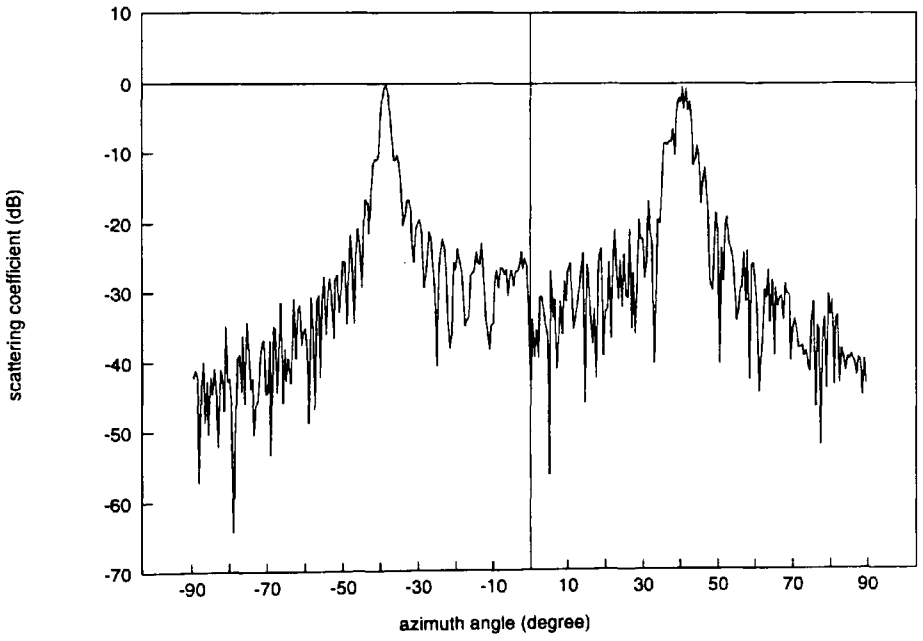

Figure 4.6 The scattering pattern of the protruding feature.

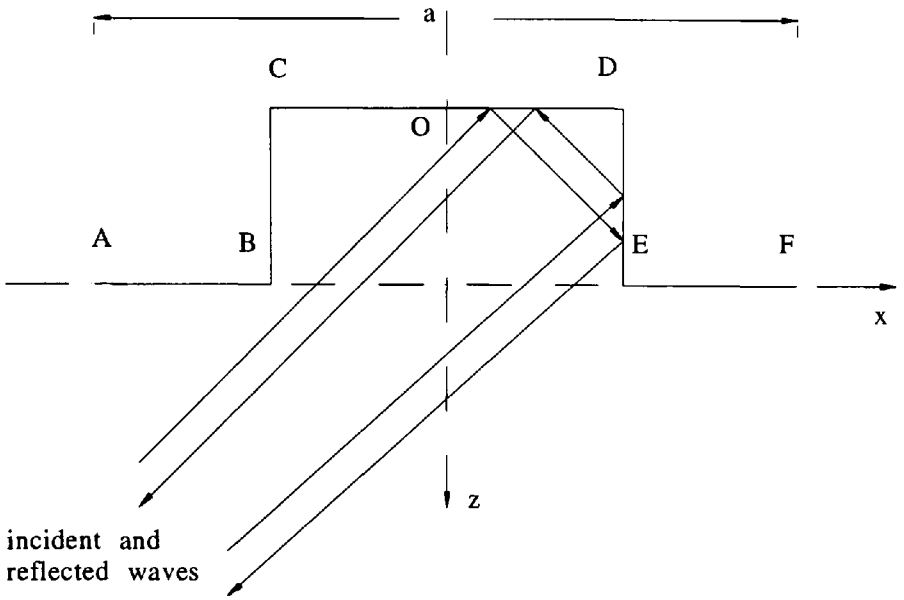

Figure 4.7 Geometry of a recessed building feature.

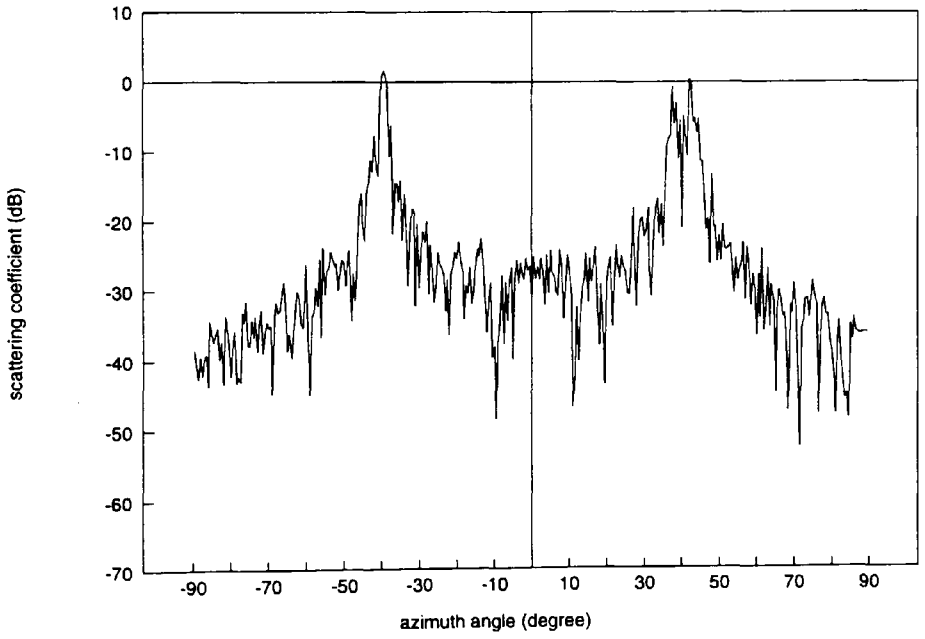

Figure 4.8 The scattering pattern of the recessed feature.

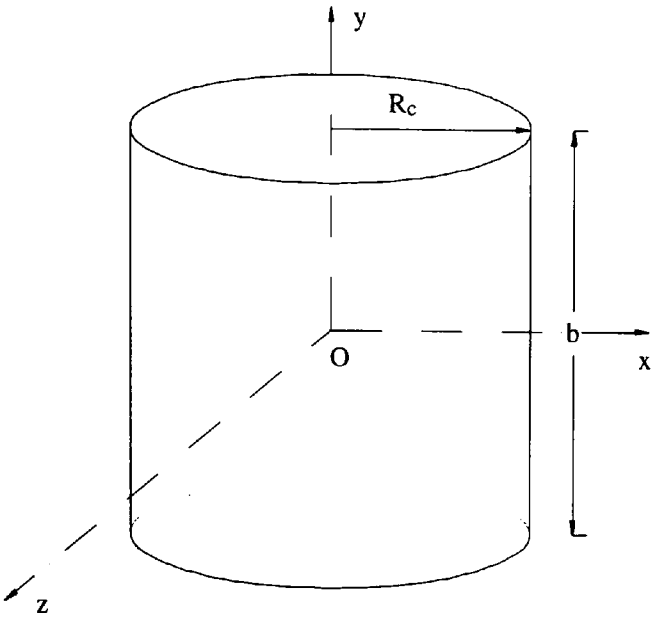

Figure 4.9 Geometry of a cylindrical feature.

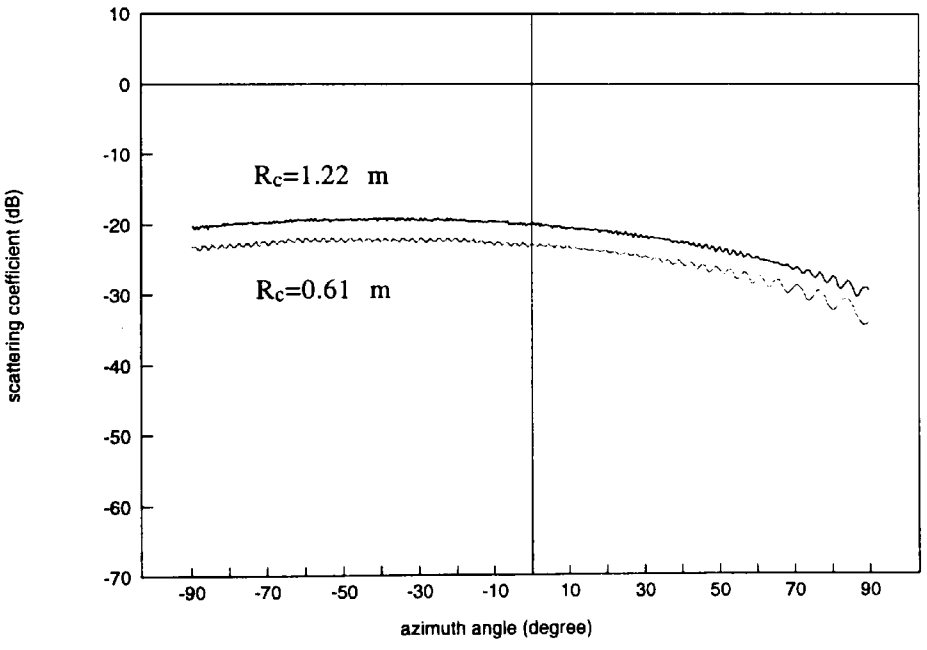

Figure 4.10 The scattering patterns of the cylindrical feature R_c=1.22 m and R_c=0.61 m.

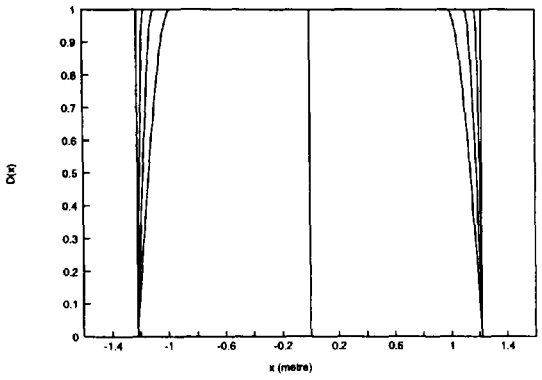

Figure 4.11 (left) Cosine distribution D(x).

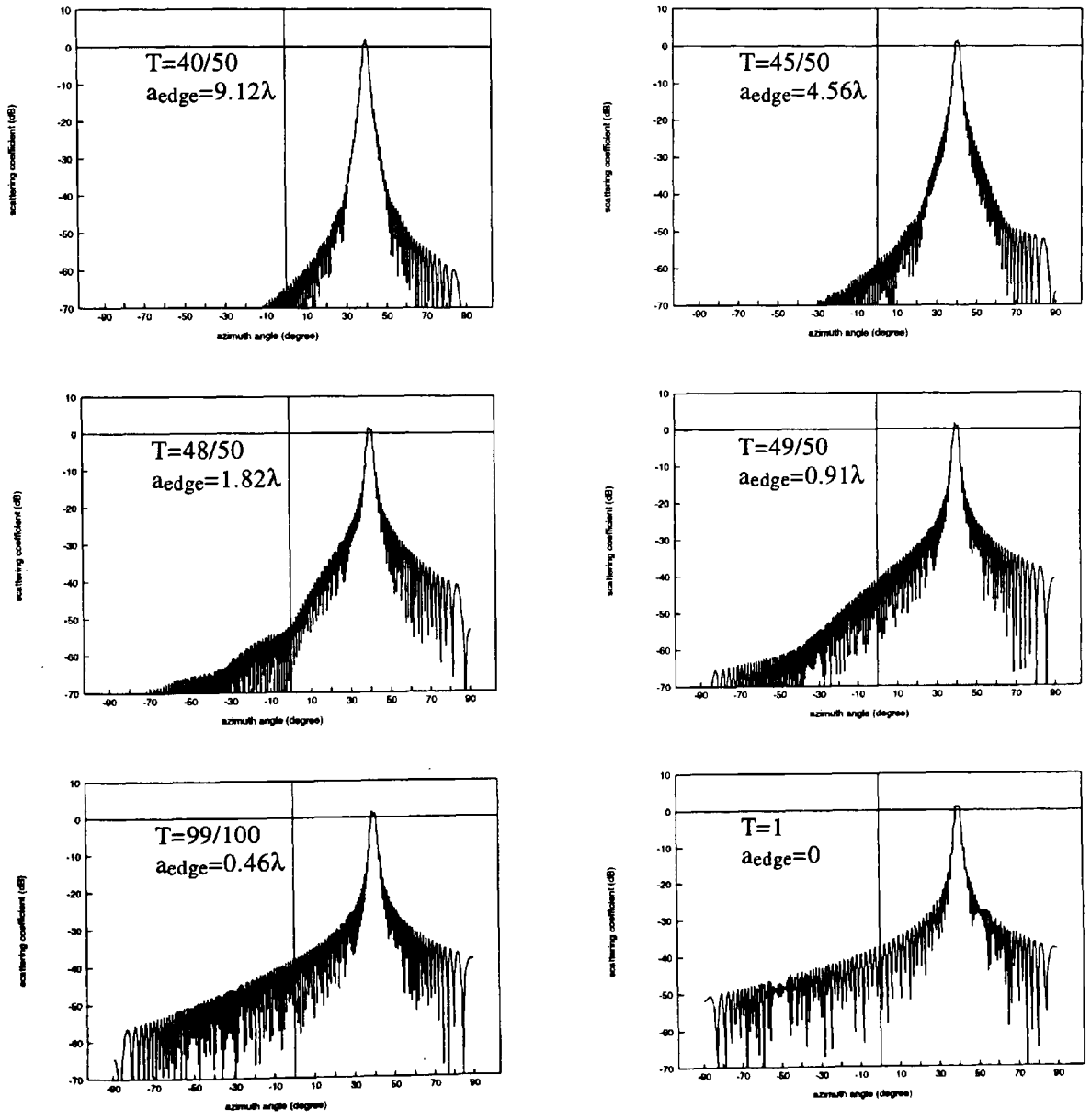

Figure 4.12 The scattering patterns with the edge effects of the aperture field of cosine distribution at the values of T.

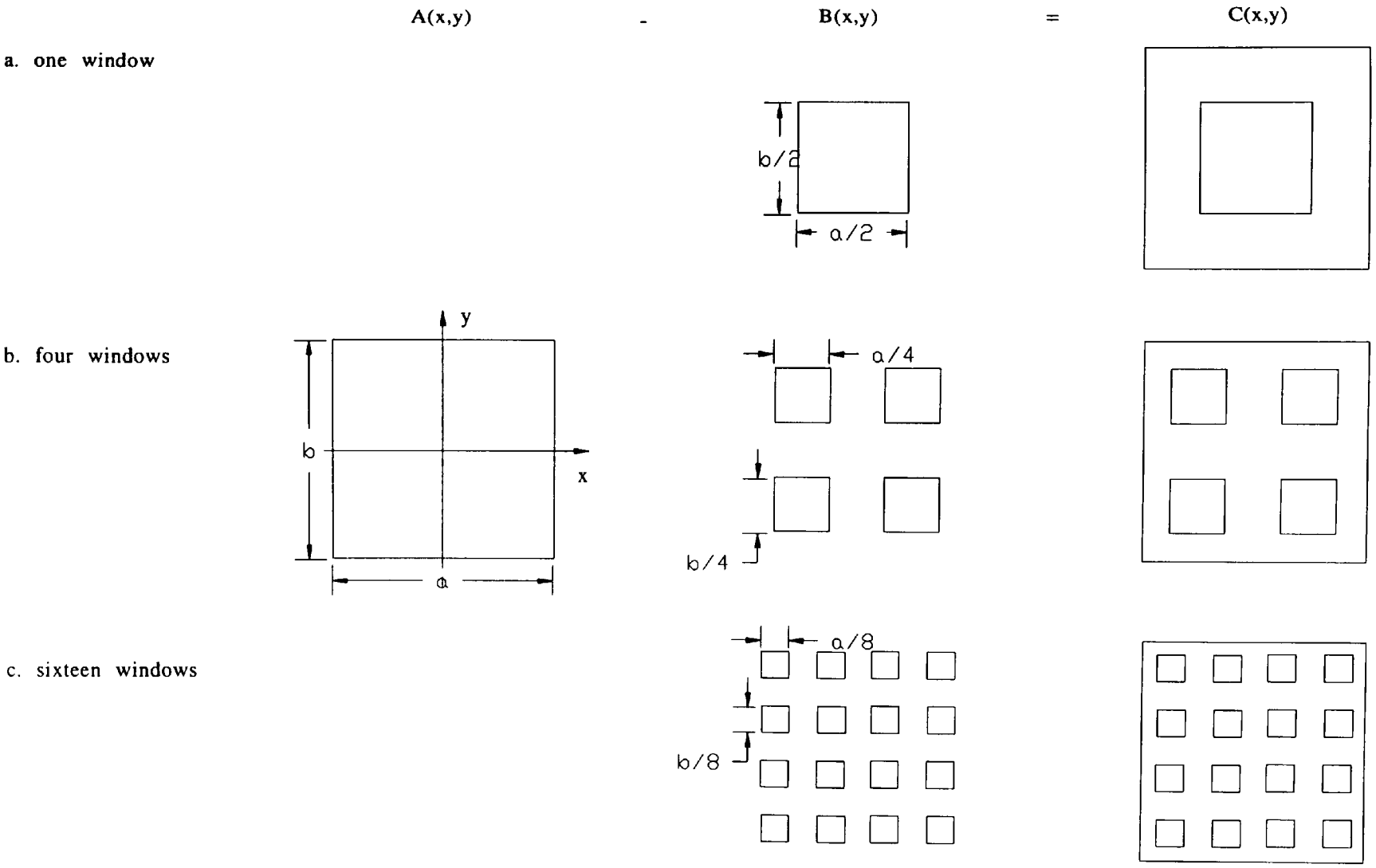

Figure 4.13 Window layout. A(x,y) is surface area. B(x,y) is window area. C(x,y) is wall area.

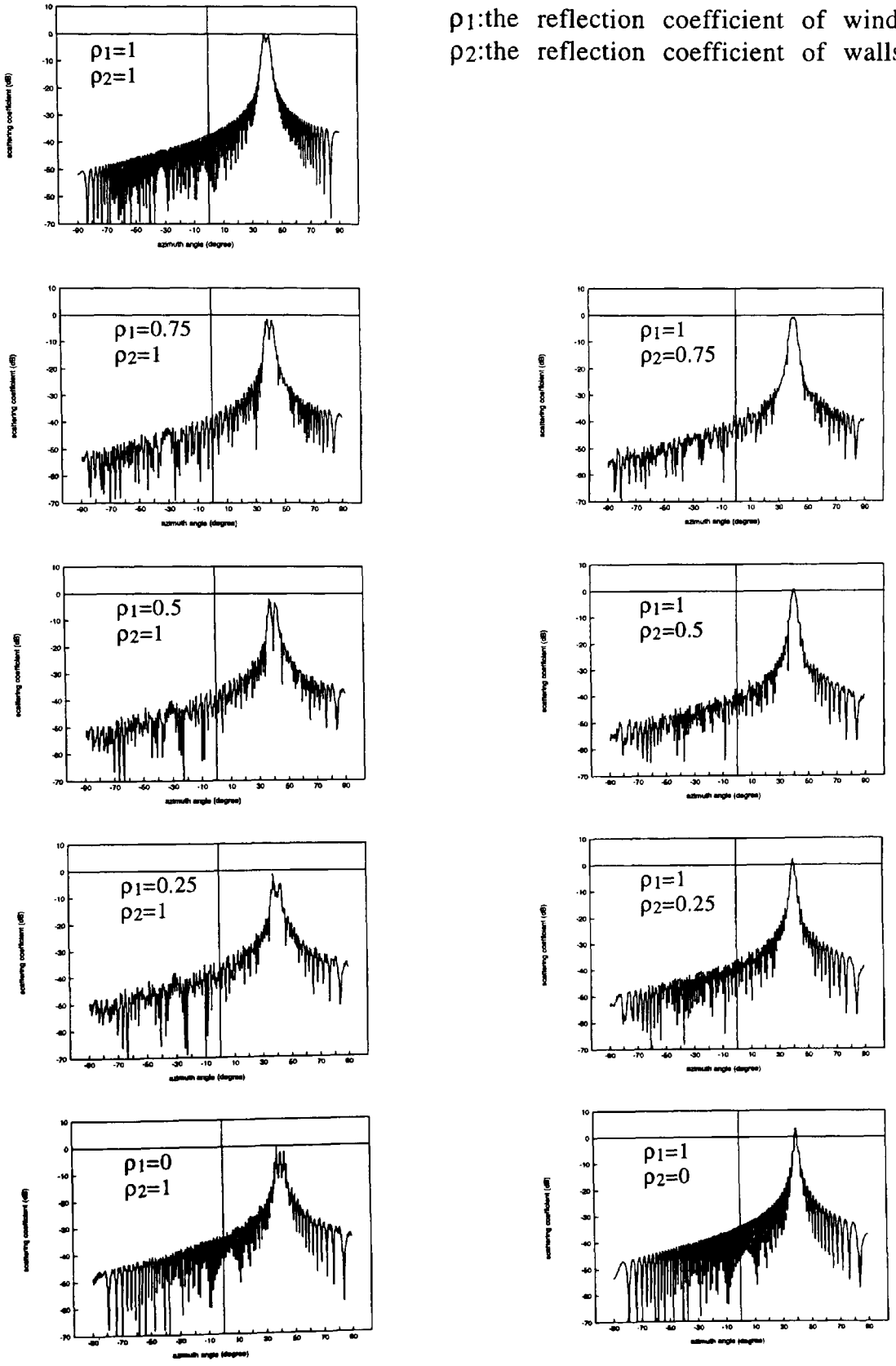

ρ1:the reflection coefficient of windows
ρ2:the reflection coefficient of walls

Figure 4.14 Scattering patterns in one window case.

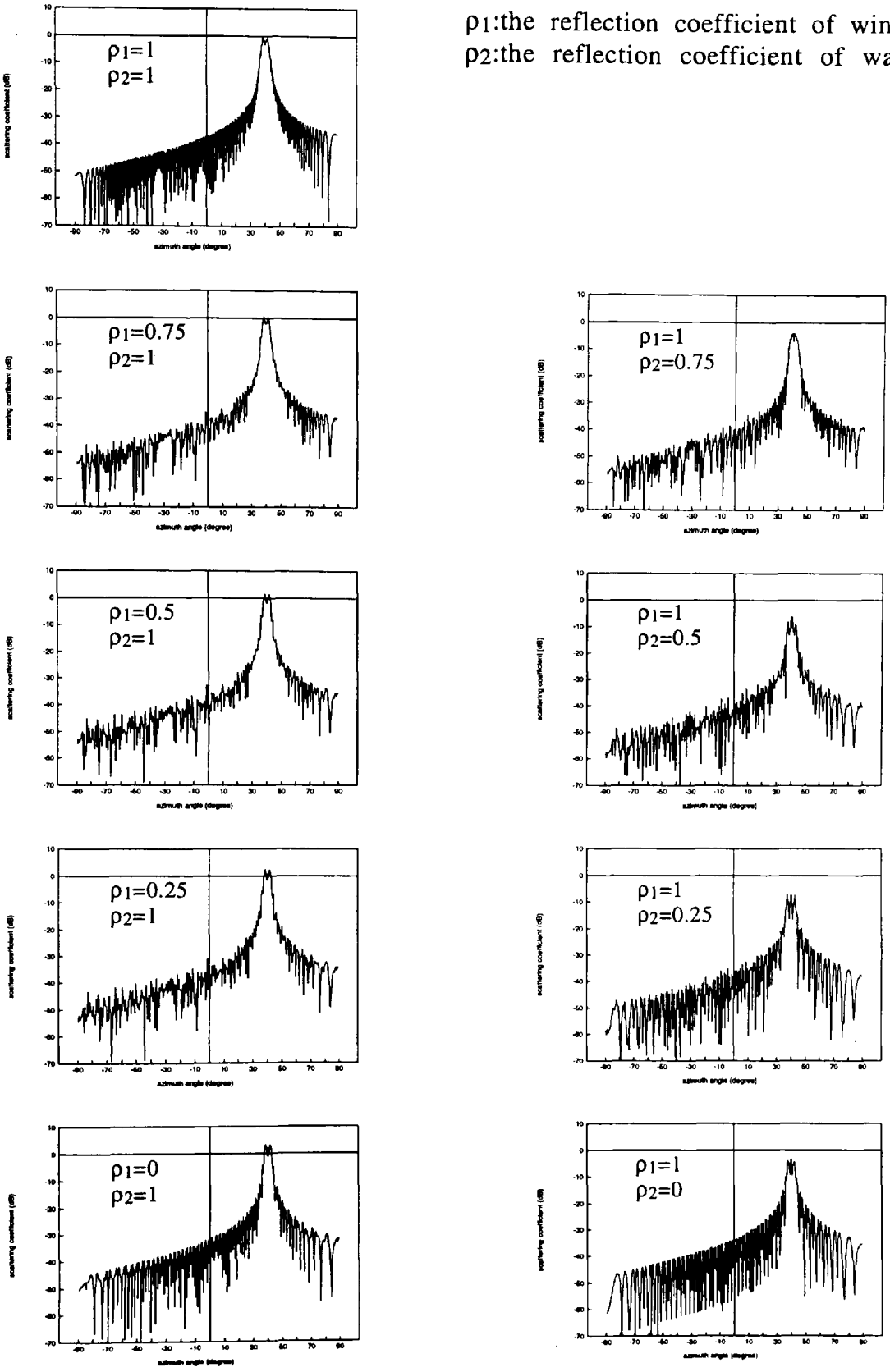

ρ1:the reflection coefficient of windows
ρ2:the reflection coefficient of walls

Figure 4.15 Scattering patterns in four windows case.

ρ1:the reflection coefficient of windows
ρ2:the reflection coefficient of walls

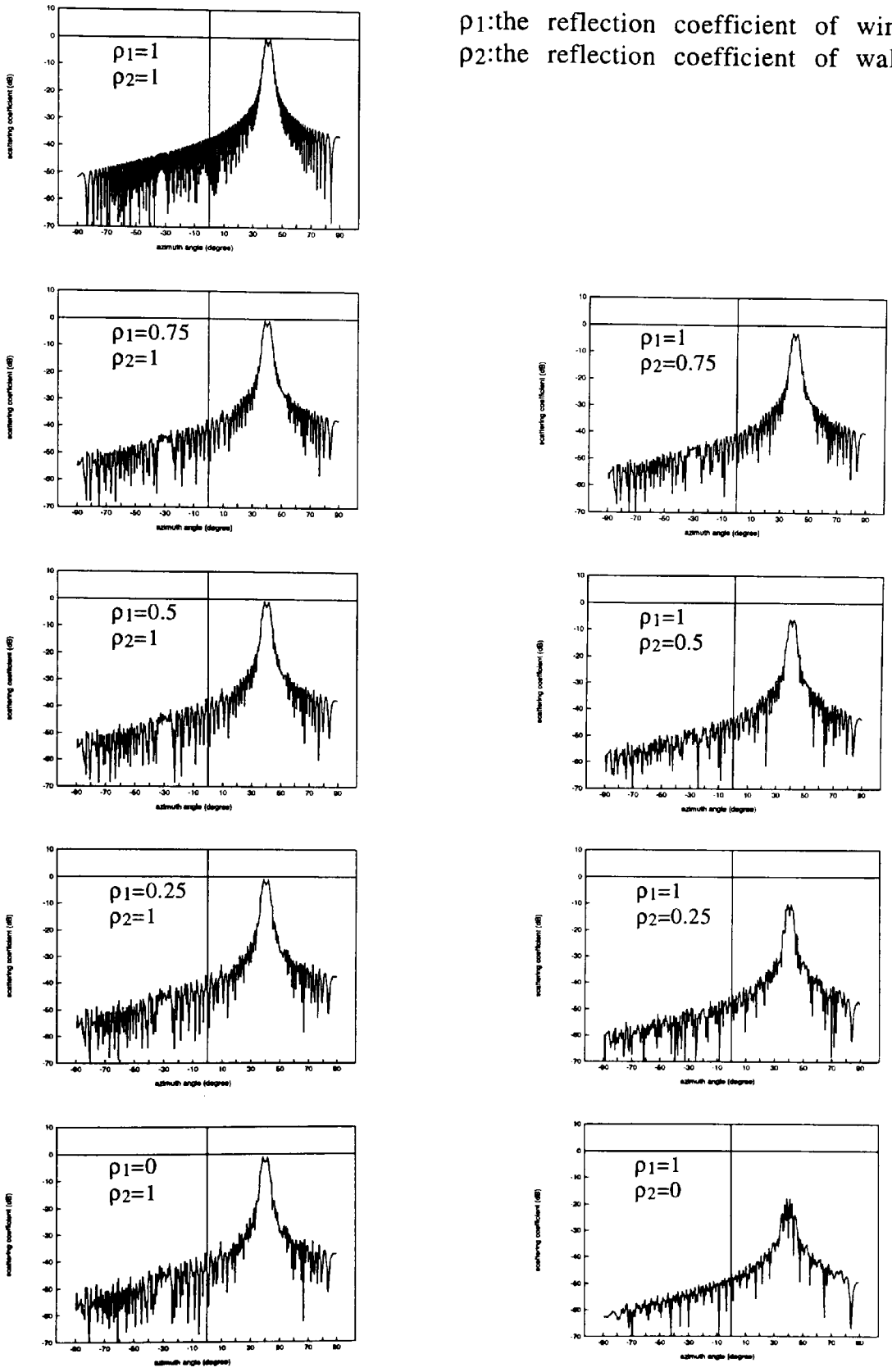

Figure 4.16 Scattering patterns in sixteen windows case.

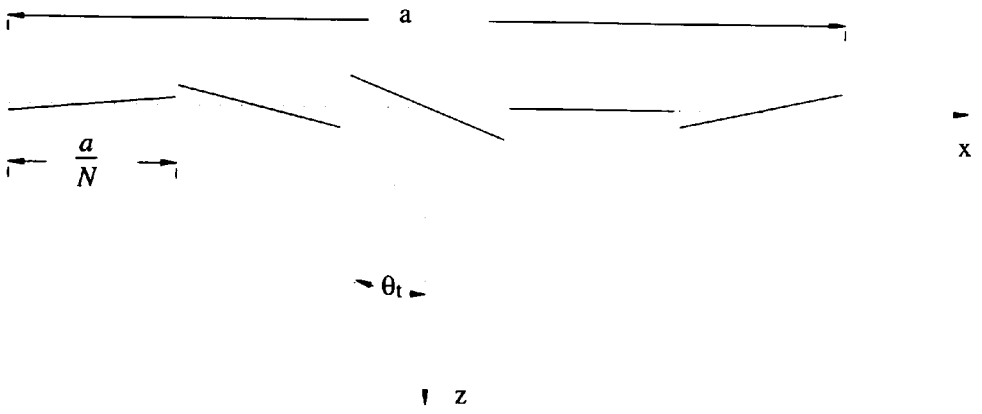

Figure 4.17 The geometry of rough surface (deviation) with N=5.

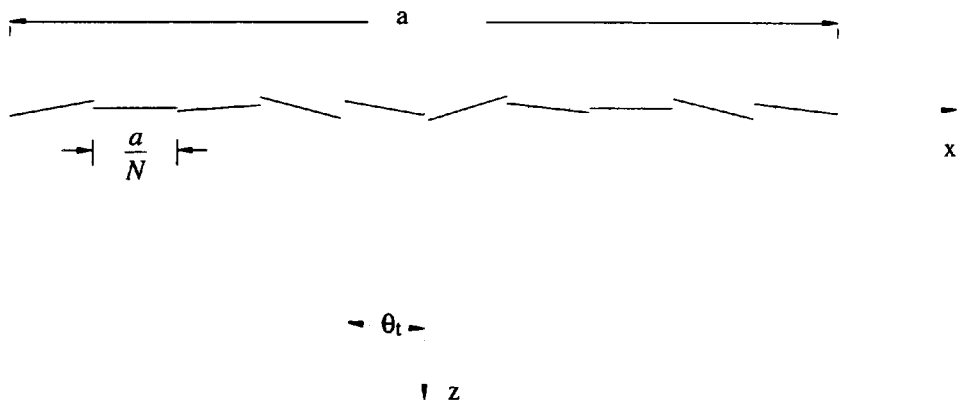

Figure 4.18 The geometry of rough surface (deviation) with N=10.

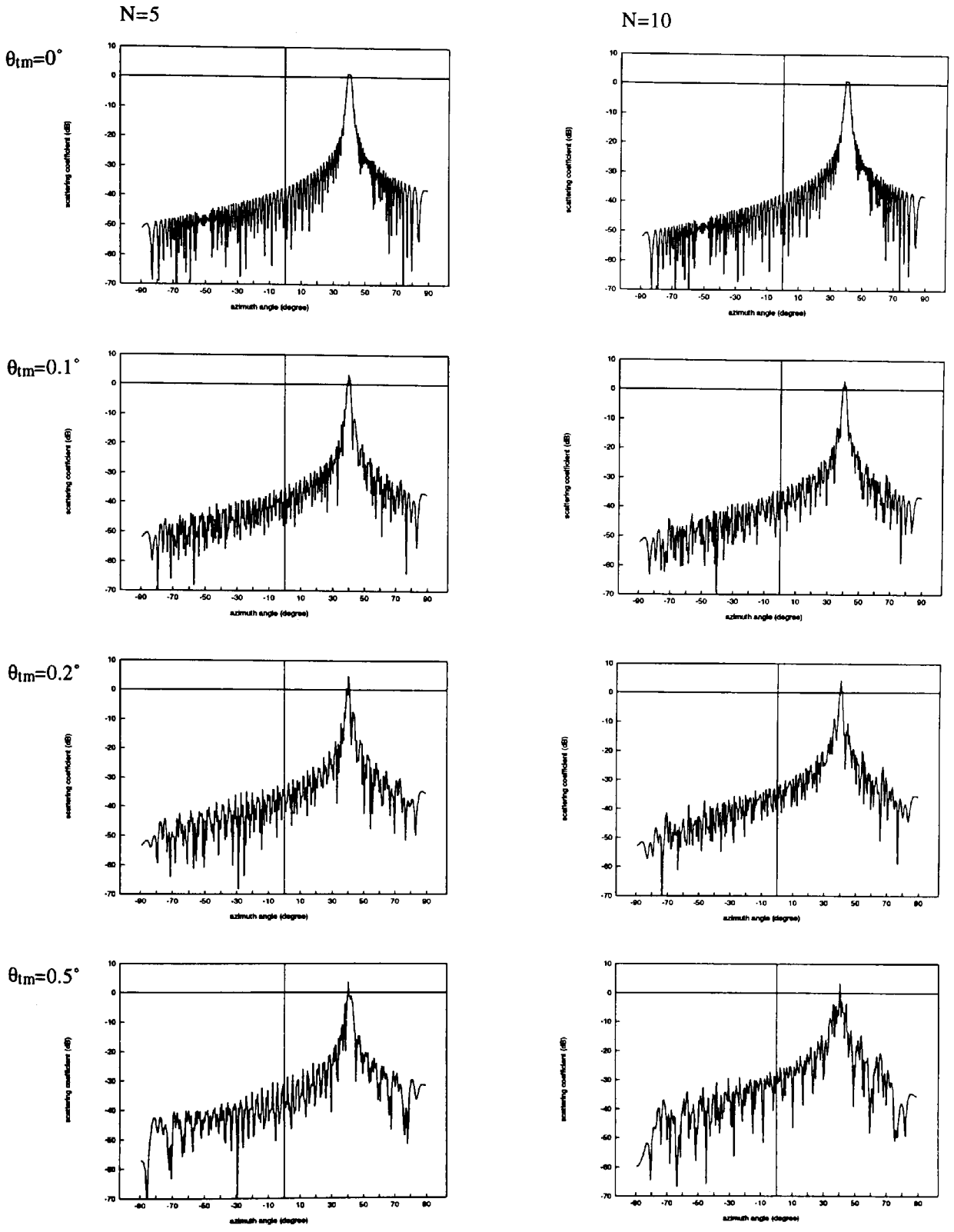

Figure 4.19 Scattering patterns of rough surface (deviation), r=26.8 m.

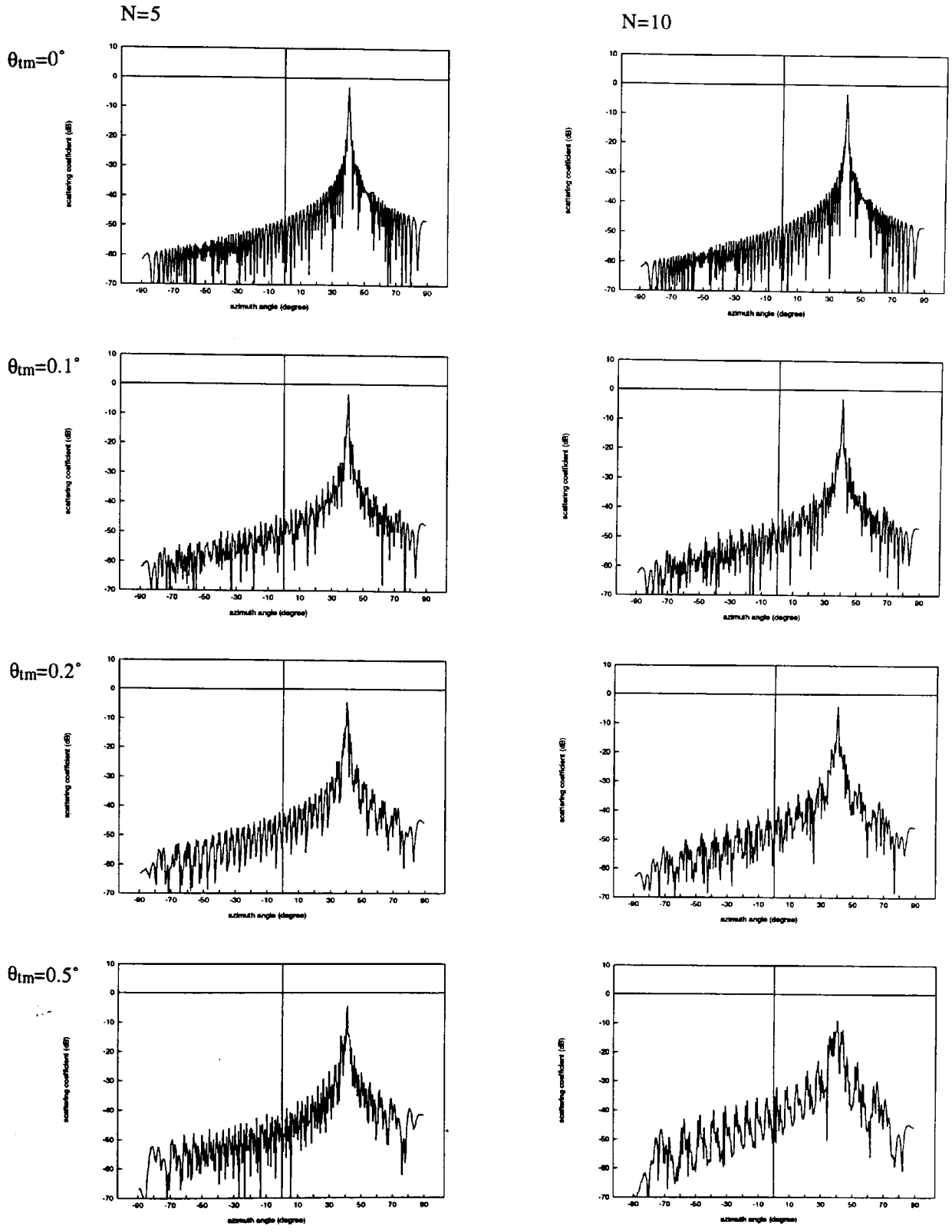

Figure 4.20 Scattering patterns of rough surface (deviation), r=268 m.

CHAPTER 5 EXPERIMENTAL PROGRAMME

5.1 Introduction

This chapter presents an experimental programme carried out to measure scattered signals from buildings. The objective of the programme has been to experimentally characterise the behaviour of building scatter. The principal emphasis is on the evaluation of the effect of building scatter on site shielding as a function of the position of a radio terminal relative to the scattering building.

The programme involved a geometrical survey in which five experimental sites were selected in the South Wales area and another two in Greater Birmingham. At these sites, near plane wave incidence was approximately achieved and buildings were prominently seen from receiver positions. The buildings involved were simple structures each consisting of a single block except in one case where the building consisted of two blocks meeting at right angle. Building surfaces were generally plane constructed in concrete, brick, and in some cases covered with pebble-dash cladding with or without windows.

The carrying out of the programme was essentially based on the work of the theoretical study and the preliminary experimental programme described in chapters 3 and 4. The basic experimental method was to measure the ratio of the amplitude of a signal incident on a building to that scattered to a receiver situated some distance away. Two types of measurement configurations were used, namely azimuth scans and range scans. Data were recorded at points in appropriate intervals. For all cases, scattered signal observations were made using linear vertical polarisation. In addition, horizontal polarisation was also used in three cases. Data was recorded allowing comparisons to be made regarding any polarisation dependence of the scattering mechanism.

A fully mobile measurement system provided a maximum 65 dB dynamic range and a sensitivity of -125 dBm with all three receiving horn antennas used. An initial calibration and gain stability check was performed on an 8 km line-of-sight path with good ground clearance to provide a free space reference for all subsequent measurements.

5.2 Experimental issues

This section covers topics of equipment, measurement system performance, measurement methods and coordinates. These are important issues for experimental work of this kind.

5.2.1 Equipment

The requirement was to radiate a microwave signal from a transmitter, at a known distance towards a target building, and to measure the amplitude of the scattered signals from the building surface at some distance away. These measurements would be compared with the strength of the signal incident on the building. The instrumentation for these measurements was developed from an earlier system used in the investigation of microwave diffraction and scatter by buildings at the University of Glamorgan [1990]. For this experimental programme, a number of improvements were made such as the introduction of a data logging system and an improved receiver terminal portability.

The transmitter was a 10 dBm dielectrically stabilised oscillator operating at the frequency of 11.2 GHz. It was powered by a 15 v DC power supply which consisted of twelve 1.25 V 4 Ah rechargeable nickel-cadmium batteries and coupled directly to the feed of a 20 dBi horn antenna with a beamwidth of 19 degrees. The transmitter terminal was attached to a manual positioner, and mounted on a 9 m variable height mast.

The receiver terminal was totally contained within a van including power sources and storage of hardware and accessories. A receiving horn antenna coupled directly to a low noise down

converter (LNB) was mounted on a remote-controlled positioner on the top of a mast at the side of the van. This positioner permits scans in both azimuth and elevation. The mast was adjustable for heights above ground from 2 m to 9 m. The horn antennas used were 15 dBi, 20 dBi and 25 dBi. Their beamwidths were 35, 19 and 11 degrees respectively. The use of different horns was to enable full visibility of a building surface and possibly to eliminate unwanted signals around buildings by choosing the appropriate beamwidths for a given geometry. The LNB amplified the signal by 50 dB with a noise figure of 1.8 dB and down converted the 11.2 GHz carrier at the input to 1.2 GHz at the output of the LNB. The output of the LNB was connected, via a 10 metre type-N coaxial cable where loss was 2.5 dB and a DC block, to an HP-8059A spectrum analyser which was used to measure the incoming signal. The measured and displayed signal strength was noted and stored by a data-logging system controlled by a portable computer which was programmed to perform data acquisition and storage. A block diagram of the experimental system is shown in figure 5.1.

All the receiving and transmitting antennas were linearly polarised and could be readily changed from vertical to horizontal. During the course of the measurements, only co-polar components were measured.

5.2.2 Link budget and calibration

The LNB used gave a gain of 50 dB. The type-N coaxial cable had a loss of 2.5 dB. The losses of cable couplers were measured to be less than 1 dB. However, the transmit power of the oscillator was actually measured to be 13.5 dBm instead of the nominal value of 10 dBm. The stability of the transmitter with respect to transmitting power and frequency was checked to be stable in the voltage range of 11 v to 17 v. With the receiving antenna feeding directly into the LNB, it was found that a signal level as low as -125 dBm from this antenna could be measured. With the transmitter delivering 13.5 dBm into a 20 dBi horn and a 25 dBi receiving antenna being used, this meant a maximum free space loss plus scatter loss of 180 dB could be accommodated. The free space loss was typically in a range from 115 to 135 dB. Thus the

system dynamic range available for scatter loss was typically from 65 to 45 dB.

The initial instrumentation calibration was performed on a line-of-sight path of 8 km length. The calibration path was chosen to be free of any significant reflecting components from either ground or above ground obstacles so that the received signal amplitude exhibited plane wave characteristics. Its path-profile is shown in figure 5.2. For the relatively short path length used, the effects of the atmosphere at this frequency are negligible. Both receiving and transmitting antennas used were 25 dBi horns giving a combined antenna gain of 50 dB. This gives a total system gain of 100 dB. The free space loss of the path at 11.2 GHz was 131.5 dB. A received signal level of -21.5 dBm was expected according to equation 3.13. The signal level measured at the receiver over this path was actually -22.2 dBm. This was the average value of 50 readings taken using vertical and horizontal polarisation.

5.2.3 Measurement methods and configurations

The basic procedure for these measurements was to measure the ratio of the amplitude of a signal incident on a building to that scattered to a receiver some distance away. The level of the incident signal could be measured or estimated accurately in front of the building when a line-of-sight path between the transmitter and the building was maintained. For scattering measurements, these involved two types of measurement configurations used to optimise each of the several propagation factors investigated.

In the configuration of azimuth scans shown in figure 5.3, the receiver distance was set at a fixed distance to the building. The measurements involved moving the receiver horizontally around a circular portion of radius equal to the distance chosen to the building, and keeping the receiving antenna pointing at the centre of the building. Fixed receiver-building distances in the tests are essential to ensure that angular dependence of building scatter alone can be investigated. In this way, a matrix of points was formed at which the measurement of received power was made. The measurements represented the variation of scattered signals as a

function of azimuth angles.

In the configuration of range scans also shown in figure 5.3, the receiver was moved along the receiver-building distance radial at a chosen azimuth angle from the building. The recorded signals represented the variation of scattered signal amplitude as a function of receiver-building distance at a fixed azimuth angle.

5.2.4 Measurement coordinate system

In the discussion of the measurement configurations used in the models previously developed, the reflector surface concerned was conveniently taken as a reference plane and centred at the origin of the spherical coordinates. To establish the coordinates on measurement sites, Ordnance Survey maps and on-site surveys were employed.

The positions of the building and the transmitter were determined and located on a 1:25000 Ordnance Survey map. The maps gave the ground heights above sea level at the transmitter h_{tg} and building h_{bg} and distance r_0 between them. The incident elevation angle is thus given by

$$\phi_0 = \tan^{-1}\left[\frac{\left(h_{tg}+h_t\right)-\left(h_{bg}+\frac{b}{2}\right)}{r_0}\right] \qquad 5.1$$

where h_t is the height of the transmitter mast and b is the height of the building. Replacing h_{tg} and h_t with the ground height of the receiver h_{rg} and the height of the receiver mast h_r respectively, equation 5.1 was also used to obtain the receiver elevation angle ϕ.

The orientation of the building surface was difficult to determine with sufficient accuracy from the maps. An on-site survey was needed to determine the orientation of the building surface so that the measurement coordinates could be located accurately. The on-site procedure is

illustrated with a plan view in figures 5.4a and 5.4b. In figure 5.4a a theodolite placed at location P_t was aligned with the building surface. An angle θ_t was measured relative to the transmitter-theodolite line-of-sight. The theodolite-building distance was measured as d. The azimuth incident angle is equal to

$$\theta_0 = \cos^{-1}\frac{d\sin\theta_t}{r_0} - \theta_t \qquad 5.2$$

At the receiver site, it was necessary that the mobile receiver would have sufficient freedom of movement so that the scattered signals might be measured at many different points. These receiver positions were usually close to the building concerned and separated by several metres or even less. 1:25000 Ordnance Survey maps appeared to be of little use in this situation. Therefore, the receiver positions in the coordinates could be determined only by on-site surveys.

In the azimuth scan configuration shown in figure 5.4b, a theodolite was initially located at P_{t1} aligned with a side surface of the building at a proposed receiver-building distance r. A point (P_{t2}) on the normal of the building surface (azimuth zero degrees) at the receiver-building distance r could be defined at 90 degrees and half the building width to the side from the theodolite (P_{t1}). Then, the theodolite was moved to the point (P_{t2}) and aligned its zero degrees with the normal to the surface by measuring the angles $\pm\tan^{-1}(a/2r)$ at two side edges of the building surface. For a receiver position at azimuth angle θ and the receiver-building distance r, it was measured from the theodolite (P_{t2}) at an angle $\theta_t = 90 - \theta/2$ and a distance $2r\sin(\theta/2)$.

5.3 Experimental site survey

An experimental site basically involves a building, transmitter and receiver ray paths linked by the building. However in urban environments, there is always a risk that measurements could

be influenced by other unwanted signals, such as background scatter. This situation should be considered and its effects minimised as far as possible in the selection of experimental sites.

5.3.1 Measurements dynamic range

Although the measurement system provided a large dynamic range, the actual measurement dynamic range was constrained by interference, namely from background scatter. In the preliminary experimental programme, scattered signal levels 40 dB below the maximum level were strongly suspected to be due to background scatter, observed to be well above the system noise floor level. Therefore, getting the background scatter level down was a key issue in order to have an effective measurement dynamic range. This relied largely on finding suitable experimental sites with carefully chosen path geometries.

5.3.2 Measurements site selection

A suitable receiver site should have a building situated in a relatively open field. It requires, particularly from the viewpoint of the receiver, that the building under investigation is prominent and away from other artificial constructions and natural obstacles such as other buildings, walls, hills and large trees, etc. These would have to be at relatively long distances from, and off the main-beam of the receiving antenna which would lead to a reduction in the background scatter level. Open space is needed in front of the building so that the receiver can be positioned accurately and to allow sufficient measurement points to cover a suitable range of measurement configurations. In practice, depending on the size of buildings, this could mean several tens of meters to around several hundred metres in both azimuth and radial directions. Meanwhile, the receiver should have a clear view of the building so that scattered signals from the building can arrive at the receiver without being seriously disturbed by other mechanisms such as diffraction, absorption and scattering from intervening structures. Similar precautions are also needed with respect to the transmitter position.

In order to obtain a near plane wave incidence at a building, the transmitter should be set in the far field of the building. However, this could be an unrealistically long distance, at 11.2 GHz, to be satisfied when a good transmitter-building line-of-sight path is also desirable. For near plane wave incidence, the transmitter-building distance might be generally acceptable even if it is only half (e.g. $r \geq (a\cos\theta_0)^2/\lambda$) or even a quarter (e.g. $r \geq (a\cos\theta_0)^2/2\lambda$) of the far field distance.

5.3.3 Experimental sites and buildings

The first part of a geometrical survey was carried out in the South Wales area. From the coast line of South Wales moving 10 to 20 km inland, it is a hilly landscape with large urban areas including the city of Cardiff and towns Newport and Merthyr Tydfil. There are many commercial, industrial and residential areas involving various buildings. However, most buildings in the city centre were not considered suitable for experiments as it was found to be difficult to access them due to limited space and heavy traffic. The emphasis was given to areas on the outskirts of cities where it was relatively easier to access. Five experimental sites were chosen. The second part of the survey was carried out in the outskirts of Birmingham. Here another two experimental sites were chosen. Each of the sites chosen had only one major building targeted. The buildings involved were generally constructed of plane surfaces in concrete aggregate, brick, and pebble-dash cladding. The surfaces contained features such as windows and balconies. In all cases except Merthyr Tydfil, the buildings had one single plane surface which could be viewed by both transmitter and receiver. At Merthyr Tydfil, the building had a structure of two rectangular blocks meeting at right angle and forming a corner reflector. The details of the buildings, site environments and path geometries are described in the next section where a complete file including measurement data obtained from each experimental site are given.

5.4 Building scatter measurements and results

Measurements of scattered signal levels were made using the experimental sites in the measurement configurations involving both azimuth and range scans. In all, fourteen experiments involving variations in azimuth were conducted, eleven using vertical polarisation and three using horizontal polarisation. These included experiments made using two buildings where both polarisations were used. There were no measurements made on cross-polar components of either polarisation. In certain cases two azimuth scans were conducted at different receiver building distances using the same building as the scattering obstacle. In other cases similar azimuth scans were made with the receiver for a variety of angles of incidence achieved by moving the transmitter between scans. Where possible, the receiver was also moved along a radial line from the centre of the building to investigate the distance dependence of the scattering coefficient in both the specular and non specular directions.

The measurement intervals of azimuth scans were determined by the angular sensitivity of the scattered signals, typically these were as small as a quarter of a degree in and around the specular regions while one or two degrees intervals in non specular regions proved sufficient. The measurement intervals of range scans were constant at 5 m. At each measurement point, five readings were made in order to give an average value to increase the stability and reliability of the measurement. The height of the receiver was often adjusted to maintain the condition that the reflection was specular in elevation. The measurement results are presented as scattering coefficients in dB relative to the incident signals at the receiving coordinates in the azimuth range -90 to +90 degrees. Curves superimposed on the measurement points shown in figures are the predicted scattering patterns obtained from the very near field model. This will be discussed in chapter 6.

For operational reasons, all of the experiments were carried out during summer periods of 1991, 1992 and 1993 with reasonably fine and dry weather. In all cases, the buildings could be regarded as being substantially dry at the time of the measurements.

5.4.1 Building 1: a porter's house at the university sports field

This was the same site as was used for the preliminary experimental programme. The building sits at one end of the sports field. It presents one rectangular surface with dimensions a = 7.15 m and b = 5.2 m of brick construction containing no windows. The transmitter-building distance r_0 was set at 385 m. The incident waves were of azimuth angle 31.5 degrees and 0 degrees in elevation. There were only a few small bushes and a lamp post around the building. The main sports building was located about 40 m from the building under consideration. The receiver-building distance r was 15 m so that the main sports building was behind the receiving positions. The geometry of the site is shown in figure 5.6.

The incident signal level for vertical polarisation was measured at -8.3 dBm. Fifty measurement positions were taken in azimuth scan from azimuth 45 to -55 degrees. The measured results of scattering coefficients are shown in figure 5.7. Over the azimuth range 50 to -10 degrees, the scattering coefficients were more or less constant at about -25 to -30 dB. As the receiver positions were moved towards the specular region (-31.5±11.72 degrees), the scattering coefficient rose steadily by about 15 dB to about -10 dB at azimuth -20 degrees. The transition region was less than 10 degrees. The majority of the scattering coefficient measurements made in the specular region were high. However, at some receiver positions in the specular region the scattering coefficients were relatively low. Once the specular region had been passed, the scattering coefficient dropped sharply back to low levels of about -30 dB.

When the receiver positions were in the azimuth specular region, the scattered signal levels were also measured at several different elevation angles by varying the height of the receiving antenna. However, owing to the limited height variation, it was not possible to make measurements over a relatively complete range of elevation angles. Nevertheless, a sharp reduction of scattering coefficient was observed as soon as the specular condition in elevation was lost. The size of this reduction was typically more than 10 dB.

5.4.2 Building 2: a building in Butetown, Cardiff

This site was in Cardiff Dock area. The building presents one rectangular block of dimensions a = 57 m and b = 38 m to the transmitter and receiver. The building is an apartment block of concrete construction and contained a large number of metal-framed windows. The transmitter was set in a residential area at Rumney to the east of Cardiff. It had a clear view of the building. The transmitter-building distance r_0 was 4500 m. The incident wave was 34 degrees in azimuth and 0 degrees in elevation. There were some two-storey houses and trees around the building. However, most of them could not be illuminated by the direct incoming waves since they were shielded by some warehouses and factory buildings of about the same height behind the receiver. The receiver-building distance r was 382 m. The geometry of the experimental site is depicted in figure 5.9.

The vertically polarised incident signal was measured as -20.8 dBm in front of the building. Forty six measurement positions were taken in the azimuth scan from azimuth angles -22 to -46 degrees. The measured results are shown in figure 5.10. Over the azimuth range -22 to -27 degrees, the scattering coefficients were consistently low at about -35 dB. As the azimuth was reduced to less than azimuth -27 degrees, the scattering coefficient started to rise sharply by about 20 dB to -13 dB at azimuth -30 degrees. The high scattering coefficient values above -15 dB were maintained in the specular region (-34±3.55 degrees). At one point, this reached as high as -12 dB. In the specular region, there were some receiver positions at which relatively lower scattering coefficients were also observed. As the azimuth angle was reduced further to less than -38 degrees, the scattering coefficient dropped sharply back to -35 dB.

5.4.3 Building 3: a building in Merthyr Tydfil

The site was in the south of Merthyr Tydfil. The building had two rectangular blocks of flats meeting orthogonally with intersecting surfaces forming a vertical corner with pebble-dash cladding surface containing metal-framed windows. The transmitter was located at the foot of

Aberdare mountain. The transmitter-building distance r_0 was 875 m. The incident wave had an azimuth angle of -55 degrees and 3.5 degrees in elevation. Most of the building could be seen from both transmitter and receiver except the first two storeys which were blocked by trees about 6 m or 7 m high in the foreground of the building. The receiver site was shielded from the transmitter by an old coal mining waste tip. The receiver-building distance r was 100 m. The experimental site geometry is depicted in figure 5.12.

The vertically polarised incident wave was measured at about -12 dBm in front of the building. Sixty five measurement positions were taken in the azimuth scan from azimuth angles -40 to -70 degrees. The measured results are shown in figure 5.13. At azimuth -40 degrees, the scattering coefficients were below -25 dB. Towards azimuth -52 degrees, the scattering coefficient rose gradually up to -12 dB. In the range of about 3 degrees on either side of azimuth -55 degrees, which was the incident direction (and opposite to the original specular direction), the scattering coefficients were mostly high. After that, the scattering coefficients dropped gradually back to below -25 dB towards azimuth -70 degrees. Over the measurement range, the scattering coefficient varied up and down in large amplitudes even in the region around azimuth -55 degrees.

6.4.4 Building 4: a building in the Ringland district of Newport

The site is in a residential area in the east of Newport. The building presents one rectangular block of dimensions $a = 14$ m and $b = 30$ m. Again it was an apartment block where construction consists of a smooth concrete surface containing one column of metal-framed windows. The transmitter was located at Lawrence Hill Newport. The transmitter-building distance r_0 was 1450 m. The incident wave had an azimuth angle of -35 degrees and 1 degree in elevation. There were some two story houses around the building. The receiver positions were shielded from the transmitter by the hilly landscape behind it. There is a playing field in front the building. The existence of a relatively open space allowed measurements to be made in the azimuth scan at two different receiver-building distances $r = 125$ m and 215 m. These

are subsequently referred to as Ringland 1 and Ringland 2 respectively. The experimental site geometry is depicted in figure 5.15.

The incident wave was measured in front of the building at -16 dBm and was initially vertically polarised. At Ringland 1, measurements were taken at 78 positions in the azimuth scan from azimuth 10 to 60 degrees. The measured results are shown in figure 5.16. Over the azimuth range 10 to 25 degrees, the scattering coefficients were about -30 dB. Between 25 and 30 degrees, the scattering coefficient rose slowly by about 9 dB. After this, there was a sharp increase by about 15 dB. In the specular region (35±2.63 degrees), the scattering coefficients were high. Some of them were as high as -6 dB. There were some relatively lower signal levels also experienced in this region. For azimuth angles larger than 38 degrees, the scattering coefficient dropped gradually down to below -20 dB at 66 degrees, but not as sharply as on the other side of the specular region.

At Ringland 2, sixty measurement positions were taken in the azimuth scan in the range from 10 degrees to 55 degrees. The measured results are shown in figure 5.17. At azimuth 10 degrees, the scattering coefficient was about -30 dB. Over the azimuth range 10 to 30 degrees, the scattering coefficient went up slightly by a few decibels. Then, the scattering coefficient rose sharply by about 20 dB. In the specular region (35±1.53 degrees), the scattering coefficients were mostly high. At some of the measurement positions, values were as high as -6 dB. After the specular region, the scattering coefficient dropped sharply by 10 dB. Over azimuth range 40 to 55 degrees, the scattering coefficient steadily went down, but not as sharply as at points closer to the specular region. At azimuth 55 degrees, it was close to -30 dB.

After the above two tests, the polarisation of the incident wave was changed to horizontal. The incident wave was observed to be unchanged in front of the building. The measurements of scattering coefficient were conducted in exactly the same configurations as their vertical counterparts. On Ringland 1, 60 measurement positions were taken in the azimuth scan from

azimuth 15 to 64 degrees. The measured results are shown in figure 5.18. At Ringland 2, 76 measurement positions were taken in the azimuth scan from 10 to 60 degrees. The measured results are shown in figure 5.19. In both horizontal polarisation tests on Ringland 1 and Ringland 2, the measured results of the scattering coefficients appear to be largely similar to those of their respective vertical polarisation counterparts.

In addition at Ringland, two tests were conducted in the range scan using vertical polarisation. One was in the specular direction of azimuth 35 degrees. The measurements of scattering coefficient were taken along the direction in the range of 90 to 230 m. There were 29 measurement positions at 5 m intervals. The measured results are shown in figure 5.20. The scattering coefficients were observed to be consistently high in the range -4 to -8 dB over the 140 m range. The other was in the direction of azimuth 53 degrees. The measurements were taken along the direction in the range of 105 to 230 m. There were 26 measurement positions at 5 metre intervals. The measured results are also shown in figure 5.20. The scattering signal levels were observed at about -21 dB at the nearest distance. In the same direction of azimuth 53 degrees, the scattering coefficient was seen to decrease gradually as the receiver-building distance increased. Ignoring some isolated low values, the scattering coefficient was about -24 dB at the farthest point.

5.4.5 Building 5: a building in the St Julians district of Newport

The site was in a residential area in the north of Newport. The building is a simple rectangular block presenting a surface of dimensions $a = 32$ m and $b = 34$ m to transmitter and receiver. The building is an apartment block with pebble-dashed clad surfaces containing many balconies and windows with metal frames. Two path geometries were used. In St Julians 1, the transmitter was set at a recreational garden. The transmitter-building distance r_0 was 4000 m. The incident wave was, in azimuth, -27 degrees and 0.65 degrees in elevation. The receiver-building distance r was 350 m. In St Julians 2, the transmitter was located at Lower Wenallt near Risca. The transmitter-building distance r_0 was 7250 m. The incident angle was -

55 degrees in azimuth and 0.5 degrees in elevation. The receiver-building distance r was 375 m. The majority of the building could be seen from the transmitter and receiver positions except the first two floors above the ground which were blocked by some two-storey houses around the building. The experimental site geometry is depicted in figure 5.22.

In St Julians 1 path geometry, the incident wave (vertical polarisation) was measured in front of the building to be about -25 dBm. Thirty seven measurement positions were taken in the azimuth scan in the azimuth range from -3 degrees to 40 degrees. The measured results are shown in figure 5.23. Over the azimuth range from -3 degrees to 20 degrees, the scattering coefficients were about -33 dB. As the azimuth angle increased, the scattering coefficient rose sharply by about 25 dB. In the specular region (27±2.33 degrees), a scattering coefficient as high as -7 dB was observed. For azimuth angles greater than 30 degrees, the scattering coefficient dropped sharply by about 25 dB. The scattering coefficient was about -30 dB at azimuth 40 degrees.

In St Julians 2 path geometry, the incident wave was measured in front of building to be -25 dBm, vertically polarised initially. Thirty measurement positions were taken in the azimuth scan from azimuth 10 degrees to 82 degrees. The measured results are shown in figure 5.24. At azimuth 10 degrees, the scattering coefficient was below -30 dB. There was a slow increase by a few decibels as the azimuth approached 40 degrees. Then, the scattering coefficient rose sharply by 20 dB. In the specular region (-55±1.4 degrees), scattering coefficients as high as -7 dB were observed. There was a sharp reduction of the scattering coefficient as the receiver moved into the non specular region. The scattering coefficient was around -30 dB in the azimuth range from 65 degrees to 82 degrees.

Following the measurements using vertical polarisation in St Julians 2, the polarisation of the incident wave was changed to horizontal. The incident wave measured was unchanged in strength in front of the building. In the same measurement configuration as its vertical counterpart, the measurements were repeated in the azimuth scan at the same measurement

positions as previously. The measured results are shown in figure 5.25. At azimuth 10 degrees, the scattering coefficient was below -30 dB. It rose steadily by 10 dB between azimuth angles of 30 and 50 degrees. Further into the specular region, there was no sharp increase of scattering coefficient which only rose slightly by a few decibels. No scattering coefficient value above -16 dB was observed. Into the non specular region again, the scattering coefficient gradually dropped back to around -30 dB from azimuth 65 to 82 degrees.

5.4.6 Building 6: a building in Dudley Greater Birmingham

The measurement site was chosen in a residential area to west of Birmingham. The building presented a rectangular block of dimensions $a = 28.8$ m and $b = 55$ m to transmitter and receiver. The building is an apartment block consisting of a smooth concrete surface containing many metal-framed windows and balconies. The transmitter was situated at Barr Beacon. The transmitter-building distance r_0 was set at 12000 m. The incident wave had an azimuth angle of 42 degrees and 1 degree in elevation. There were some two-storey houses on a sloping hill behind the building. There was a playing field in front the building. Relatively open space was presented and this allowed measurements to be made in the azimuth scan at two different receiver-building distances $r = 375$ m and 675 m. These are referred to as Dudley 1 and Dudley 2 respectively. The experimental site geometry is shown in figure 5.27.

The incident wave (vertical polarisation) was measured in front of the building at -27 dBm. At Dudley 1, eighty measurement positions ware taken from azimuth -28 degrees to -60 degrees. The measured results are shown in figure 5.28. Over the azimuth range -28 to 38 degrees, the scattering coefficients were about -25 to -30 dB. Moving into the specular region (42±1.64 degrees), the scattering coefficient rose sharply by about 20 dB and stayed high mostly about -7 dB in the region. There were some relatively lower signal levels which were also experienced in this region. As the receiver moved into the non specular region, the scattering coefficient dropped sharply back to -30 dB at azimuth 55 degrees. Over the rest of the

measurement positions, scattering coefficient varied around -30 dB by a few decibels.

At Dudley 2, fifty five measurement positions were taken in the azimuth scan from azimuth -34 to -45 degrees. The measured results are shown in figure 5.29. Over the azimuth range from -34 to -40 degrees, the scattering coefficients were around -30 dB varying by a few decibels. Moving into the specular region (-42±0.91 degrees), the scattering coefficient rose sharply by more than 20 dB. The scattering coefficient stayed high and at some positions was as high as -6 dB in the specular region. There was a sharp reduction by more than 20 dB in the scattering coefficient immediately after the specular region was passed.

In addition, at the Dudley site, two tests were conducted in the range scan using vertical polarisation. One was in the specular direction of azimuth -42 degrees. The measurements of scattered signal levels were taken along the direction in the range of 325 to 690 m. There were 74 measurement positions at 5 m intervals. The measured results are shown in figure 5.30. Scattering coefficients were observed to be consistently high around -10 dB over the 365 m range. The other test was in the azimuth direction -36 degrees in the non specular region where measurements were taken along this direction in the range of 375 m to 675 m. There were 61 measurement positions at 5 metre intervals. The measured results are also shown in figure 5.30. The scattering coefficients were generally below -20 dB and decreased as the receiver-building distance increased. Over the distance range, the scattering coefficient dropped by a few decibels.

5.4.7 Building 7: a building in Walsall Greater Birmingham

The site was again in a residential area to north of Birmingham. The building presented one rectangular block of dimensions $a = 25.8$ m and $b = 53.5$ m to transmitter and receiver. The building had a smooth concrete surface containing many metal-framed windows. The transmitter was also situated at Barr Beacon. The transmitter-building distance r_0 was 3500 m. The incident wave had an azimuth angle of 43 degrees and 1.1 degrees in elevation. There

were some two-storey houses and trees around the building. Measurements were made in the azimuth scan at two different receiver-building distances r = 75 m and 375 m referred to as Walsall 1 and Walsall 2 respectively. The experimental site geometry is shown in figure 5.32.

The incident wave (vertical polarisation) was measured in front of the building to be -16 dBm. In Walsall 1, ninety seven measurement positions were taken from azimuth -80 to 60 degrees. The measured results are shown in figure 5.33. Over the azimuth range from 60 to -25 degrees, the scattering coefficients were around -30 dB. The scattering coefficient then rose continuously by about 20 dB over the azimuth range from -25 to -35 degrees. In the specular region (-43±7.23 degrees), the scattering coefficient stayed high mostly at -5 dB. There were again some relatively lower scattering coefficients observed in this region. For azimuth angles less than -50 degrees, the scattering coefficient dropped steadily to -30 dB at azimuth -60 degrees. Over the azimuth range -60 to -80 degrees, scattering coefficients were low around -30 dB varying by a few decibels.

In Walsall 2, fifty five measurement positions were taken in the azimuth scan from azimuth -28 to -65 degrees. The measured results are shown in figure 5.34. In the azimuth range of a few degrees around -30 degrees, the scattering coefficients were low around -40 dB varying by a few decibels. As the receiver was moved towards the specular region, the scattering coefficient rose sharply by about 25 dB. In the specular region (-43±1.44 degrees), the scattering coefficients were relatively high at -12 dB. There was a sharp reduction by about 25 dB of the scattering coefficient immediately after the specular region. The scattering coefficients were low at around -40 dB over the azimuth range -55 to -65 degrees.

5.5 Interim Conclusion

The scattering signals from seven different buildings were studied with respect to their dependence on scattering angle, distance and polarisation. During the course of the measurements, difficulties were experienced in accurately measuring the relatively low level

scattering signals observed in non-specular regions due to either space limitations of the measurement site or because of background scattering. None of the tests performed allowed measurements to cover a complete azimuth scan range. Nevertheless, the azimuth ranges which were covered by the measurements in all the tests consisted of both specular regions and non specular regions. The scattering coefficients measured in non specular regions were typically 20 to 30 dB lower than those in specular regions. Therefore, it is argued that the measurement ranges were sufficient in addressing all situations of potentially high interference represented by contributions from specular regions. They also covered regions of transitions between specular and non specular regions. The measurement values of the scattering signals at most measurement positions were reasonably stable and thus reliable. Fluctuations within a few decibels were generally observed. These were largely accounted for by taking the average value of five readings sampled at each of the measurement positions. The reliability of the measured results has benefited from the careful considerations and precaution made in the selection of measurement sites and also in ensuring accurate path geometry parameter measurements.

In this chapter the experimental programme is considered in terms of the scattering signal levels and patterns associated with real buildings. In chapter 6 the measured results will be discussed in the light of those yielded from current prediction models and further theoretical considerations. The experimental programme described is put forward as a vital contribution to validate the theoretical models developed and to highlight the need for further modification and refinement.

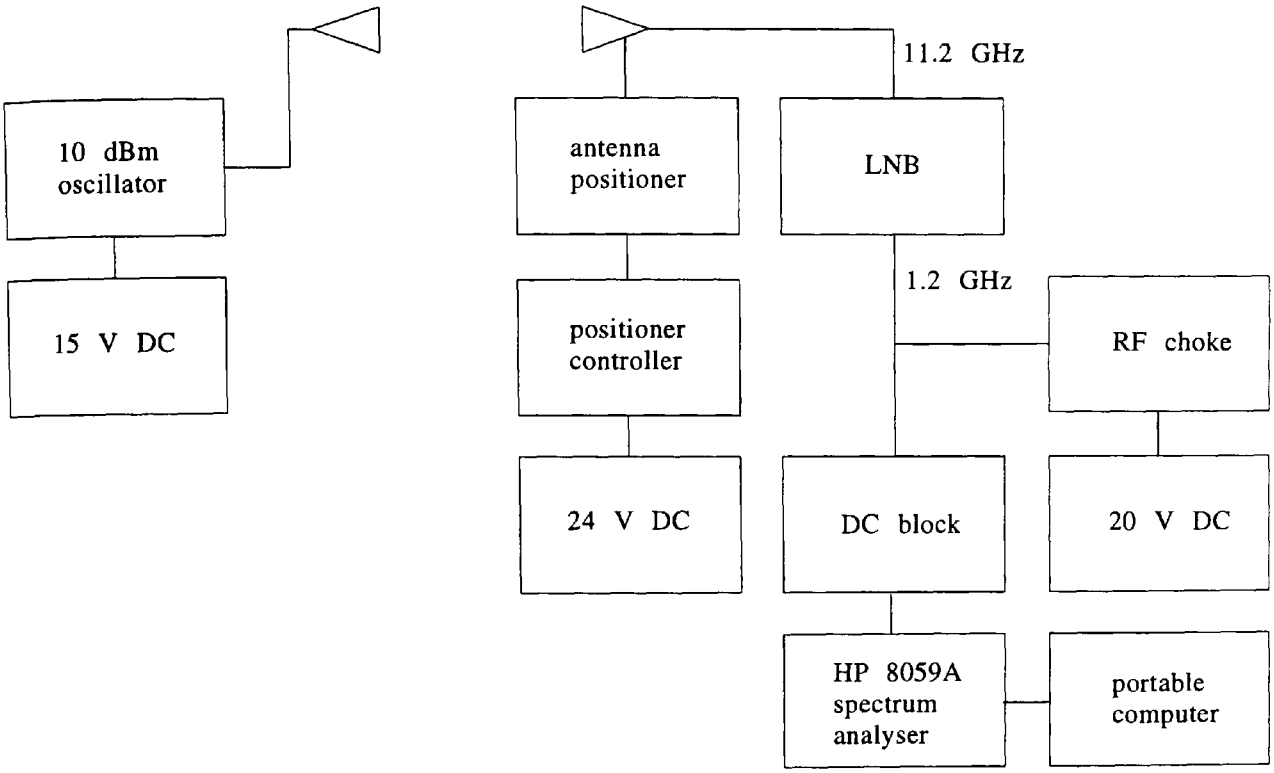

Figure 5.1 The block diagram of the measurement system.

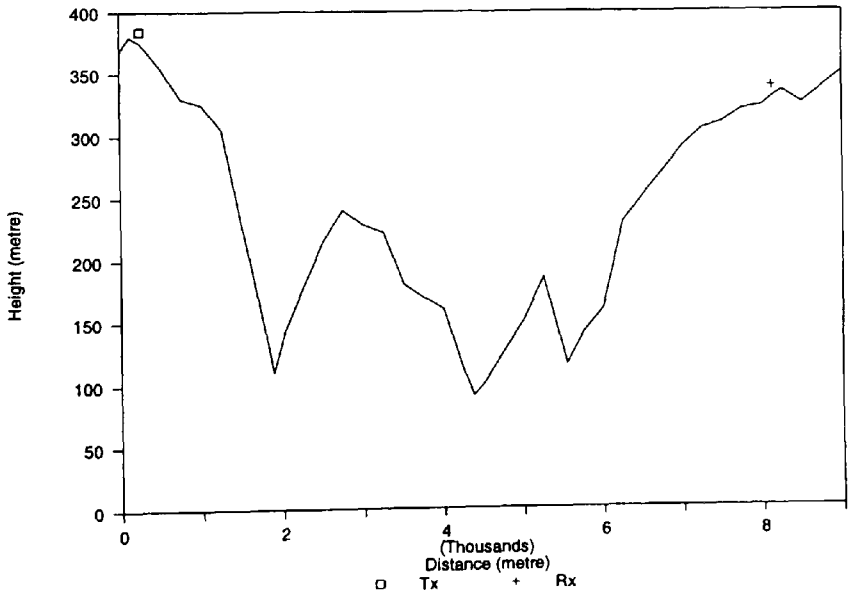

Figure 5.2 The path-profile of 8 km test path.

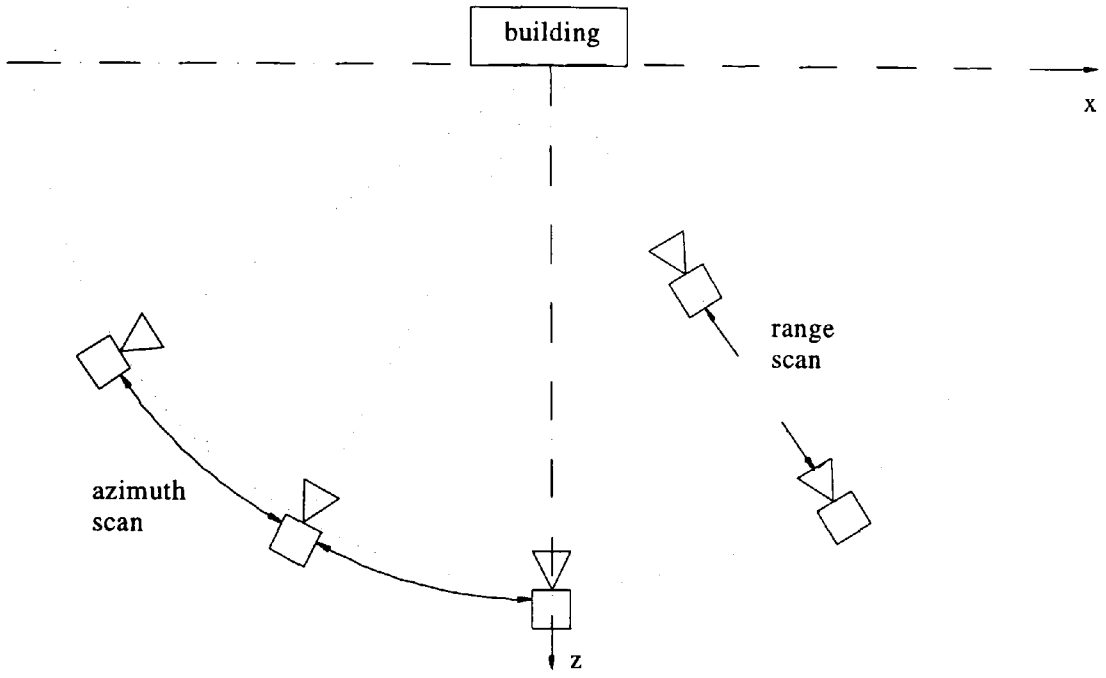

Figure 5.3 Measurement configurations of azimuth and range scans.

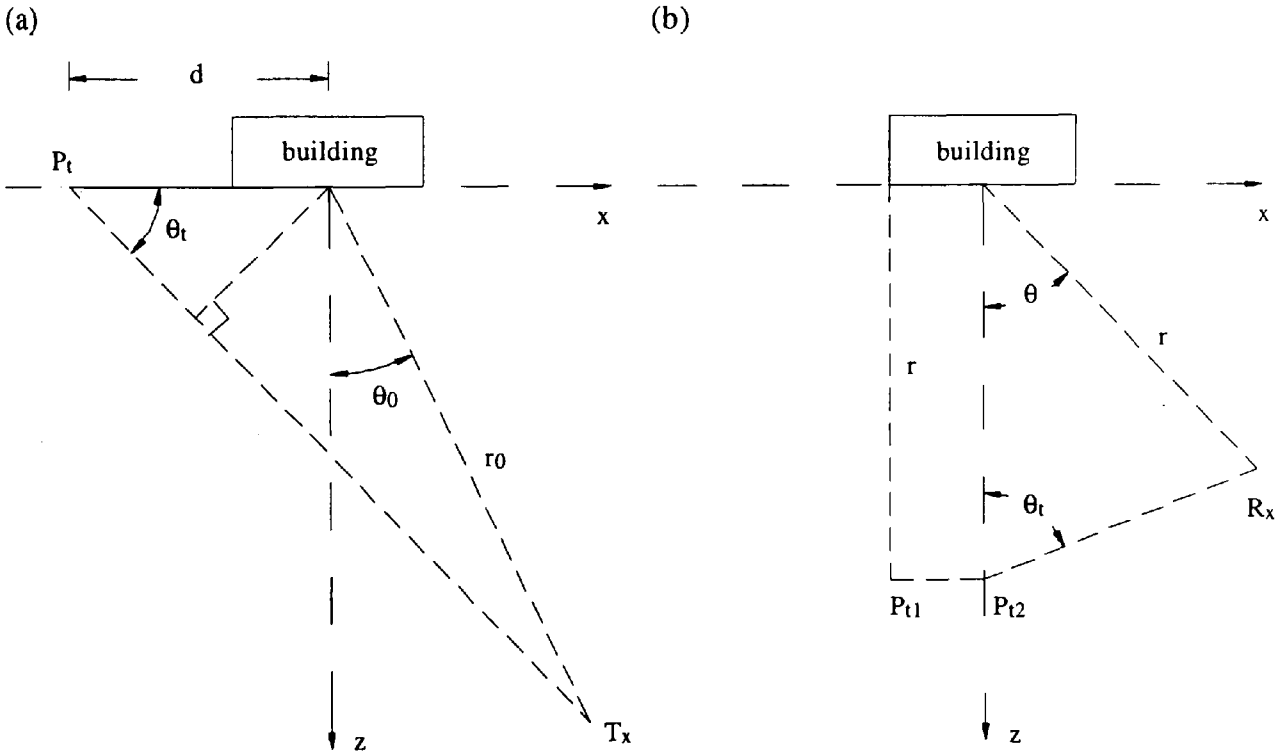

Figure 5.4 On-site survey geometries.

Figure 5.5 The porter's house building at the University playing field.

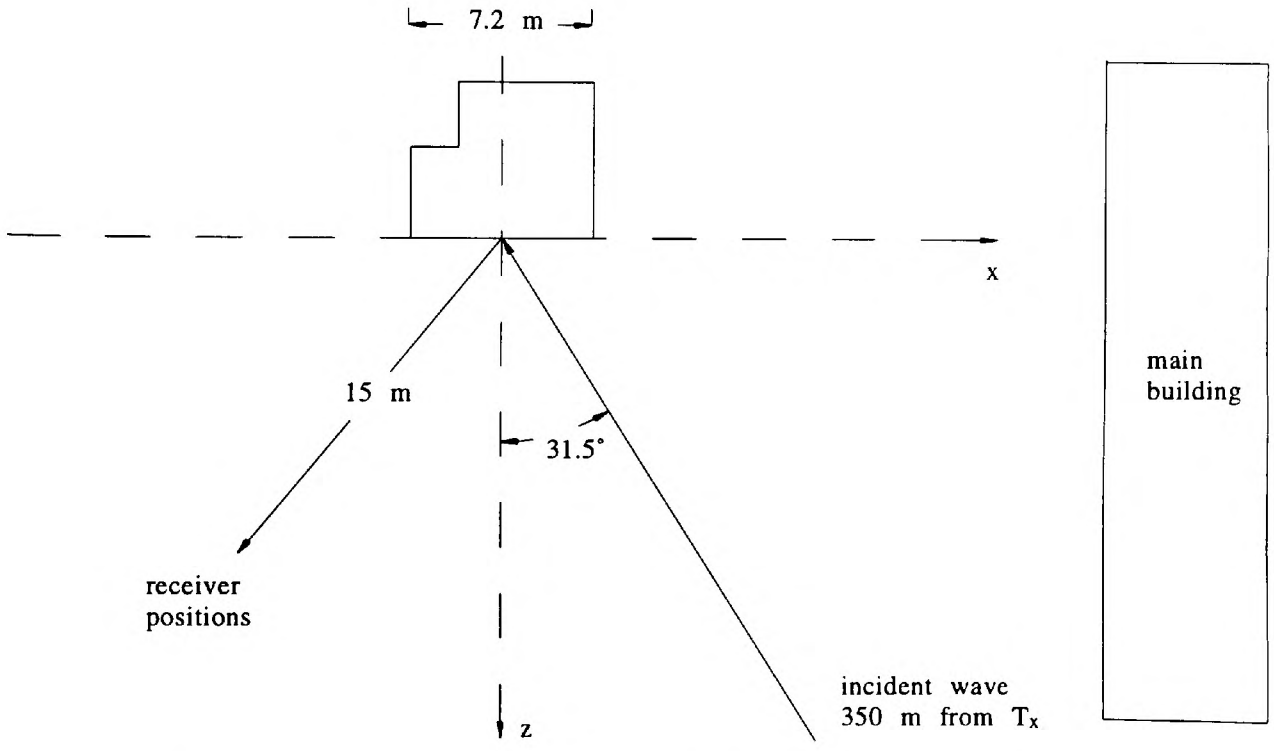

Figure 5.6 The experimental site geometry of the porter's house building.

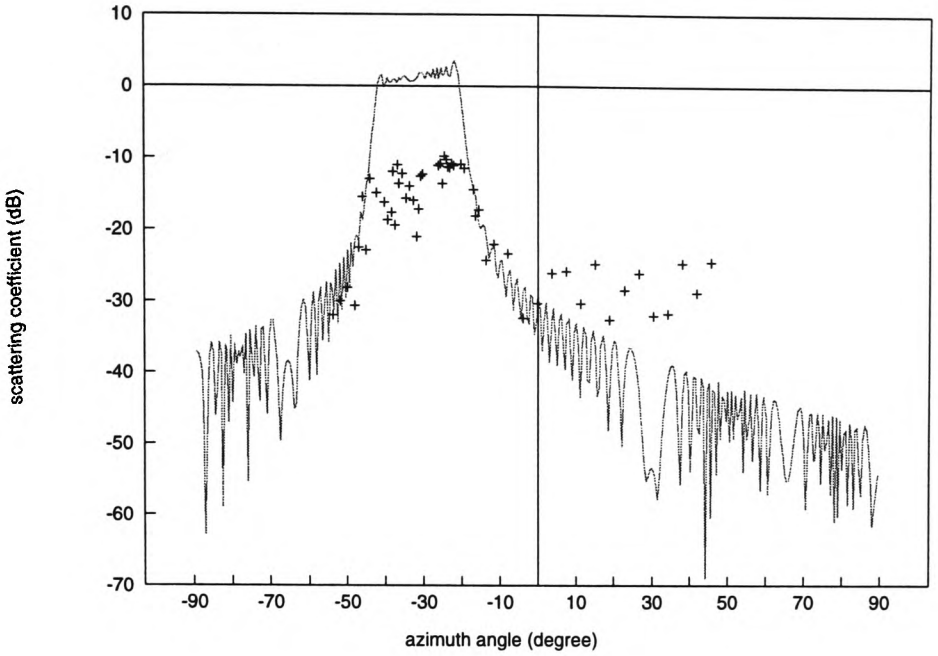

Figure 5.7 The measured and predicted results of the porter's house building.

Figure 5.8 The Butetown building in Cardiff.

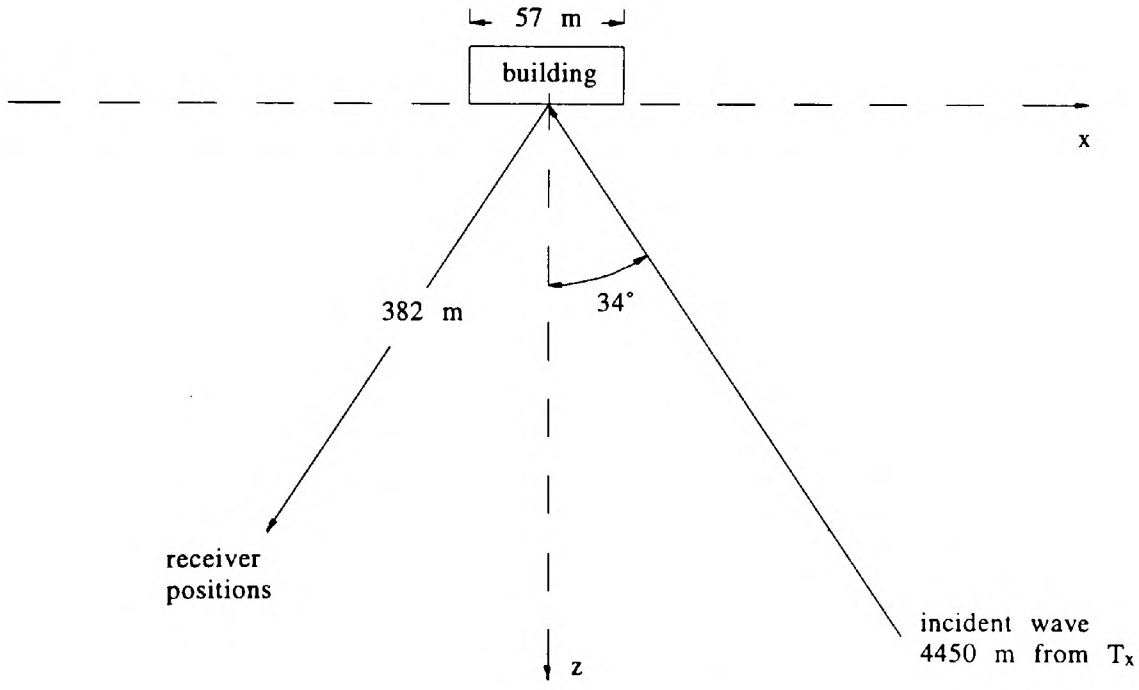

Figure 5.9 The experimental site geometry of the Butetown building.

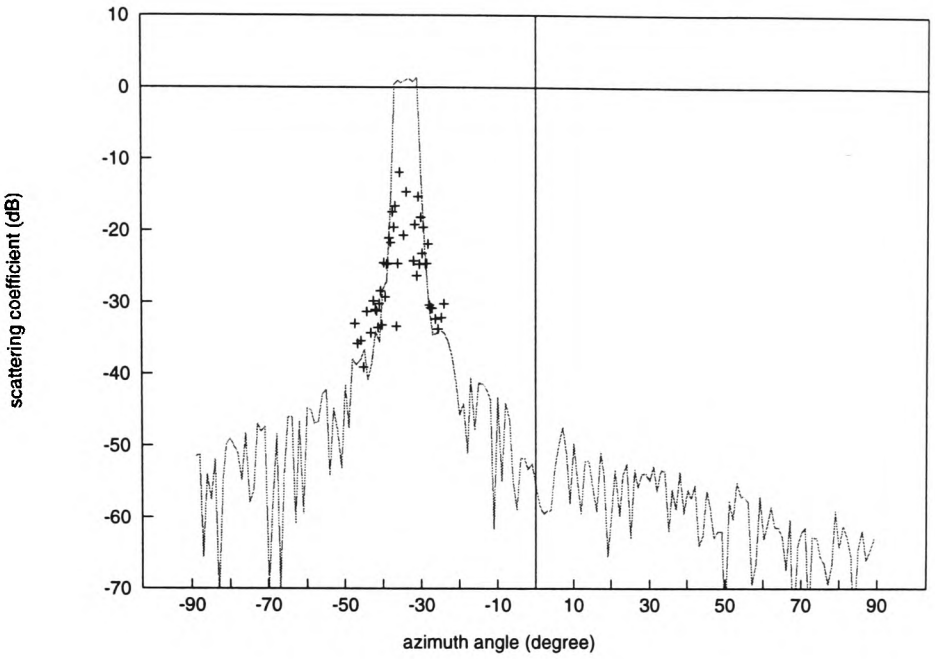

Figure 5.10 The measured and predicted results of the Butetown building.

Figure 5.11 The Merthyr Tydfil building.

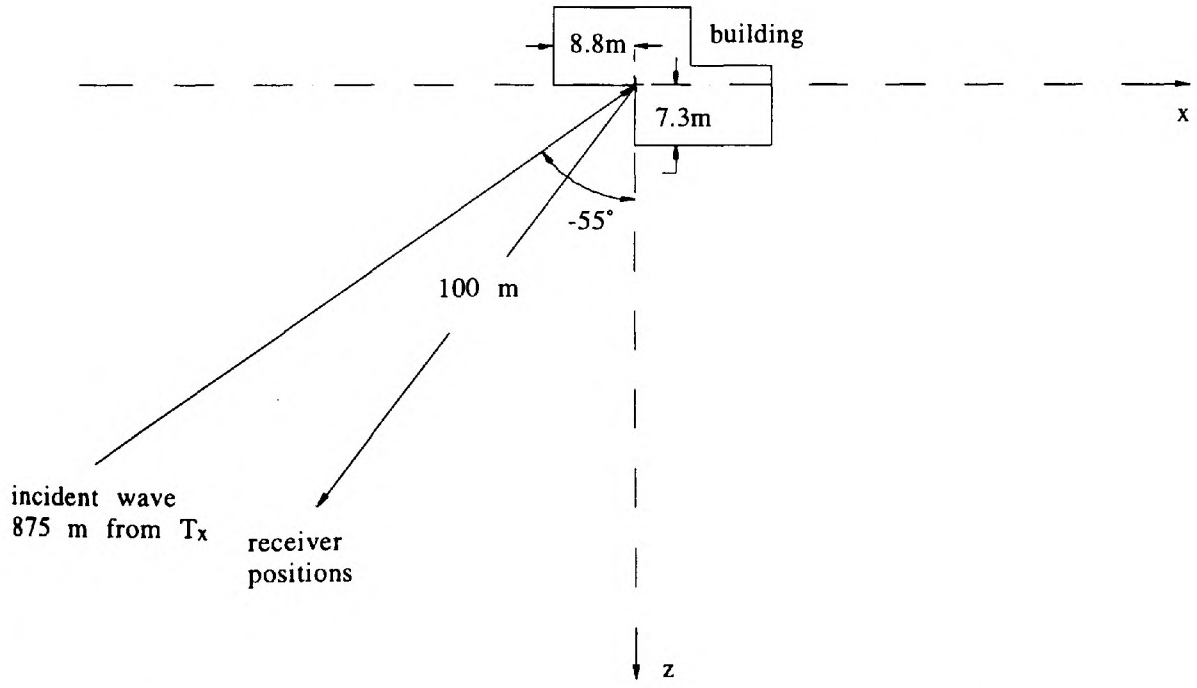

Figure 5.12 The experimental site geometry of the Merthyr Tydfil building.

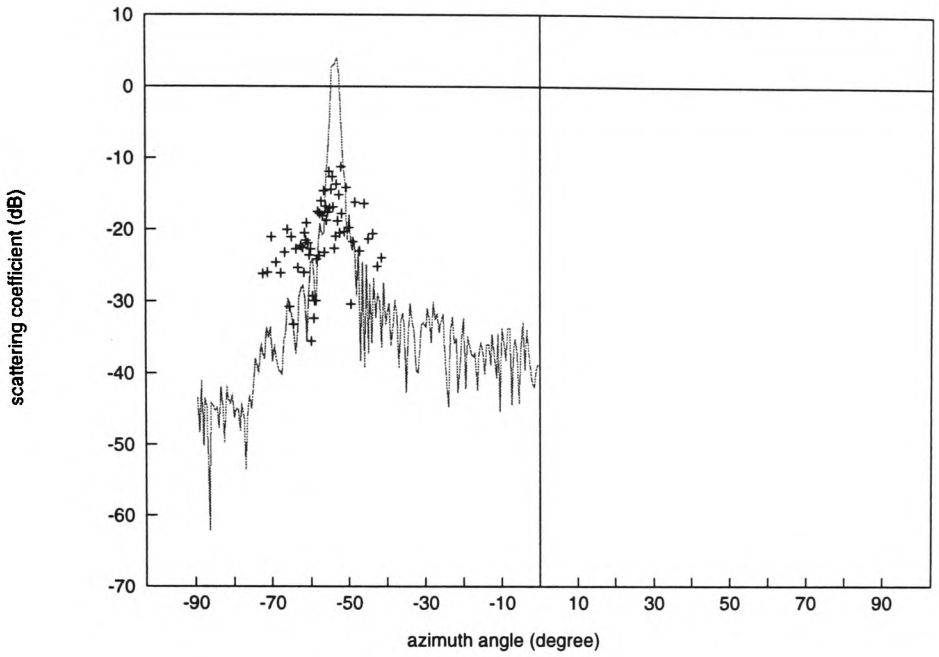

Figure 5.13 The measured and predicted results of the Merthyr Tydfil building.

Figure 5.14 The Ringland building in Newport.

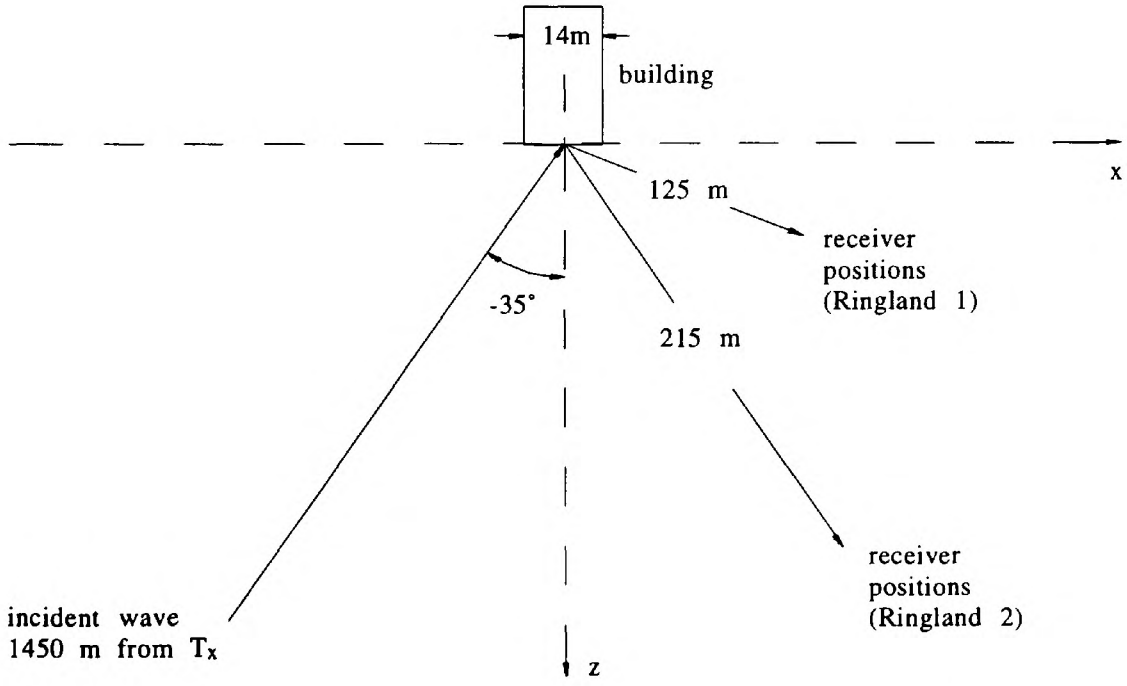

Figure 5.15 The experimental site geometry of the Ringland building.

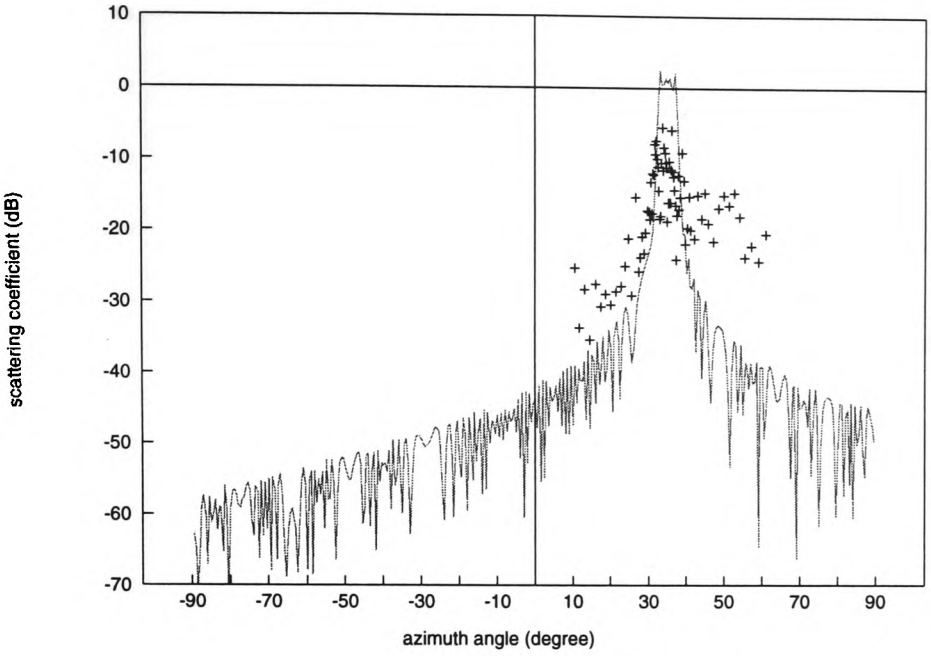

Figure 5.16 The measured and predicted results of the Ringland building, r=125 m (Ringland 1), vertical polarisation.

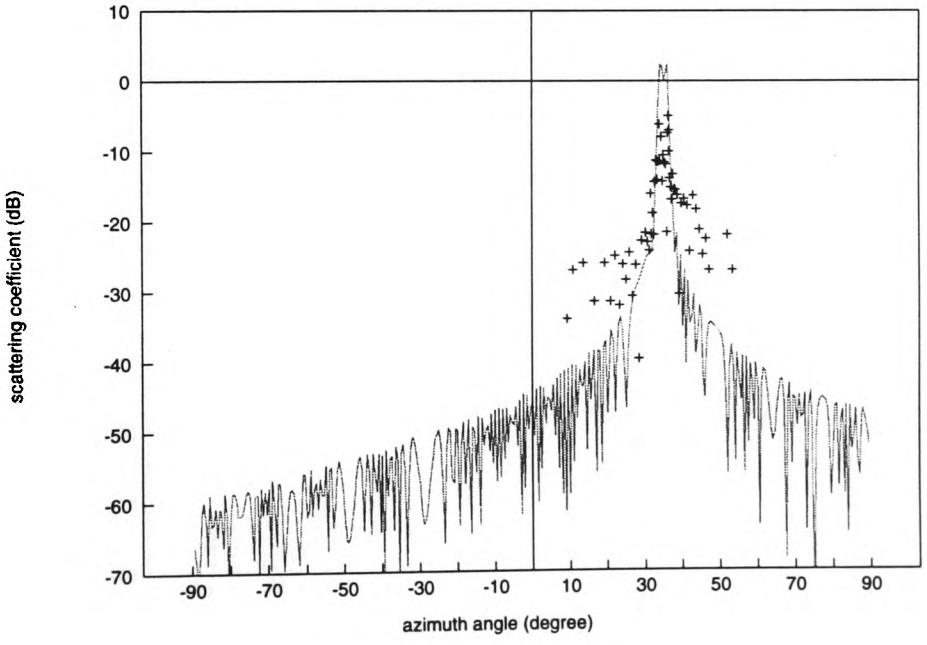

Figure 5.17 The measured and predicted results of the Ringland building, r=215 m (Ringland 2), vertical polarisation.

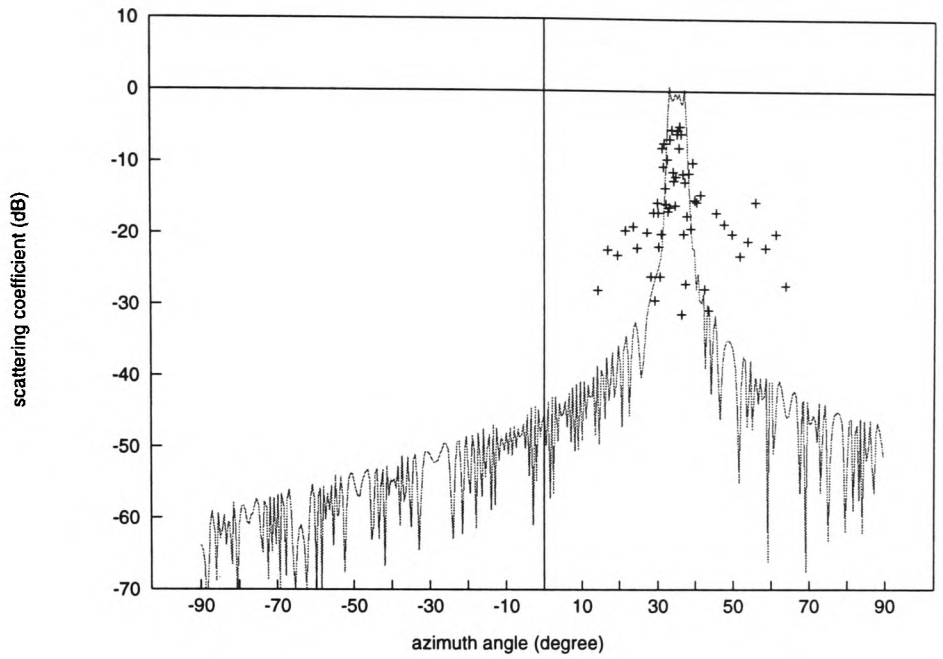

Figure 5.18 The measured and rpedicted results of the Ringland building, r=125 m (Ringland 1), horizontal polarisation.

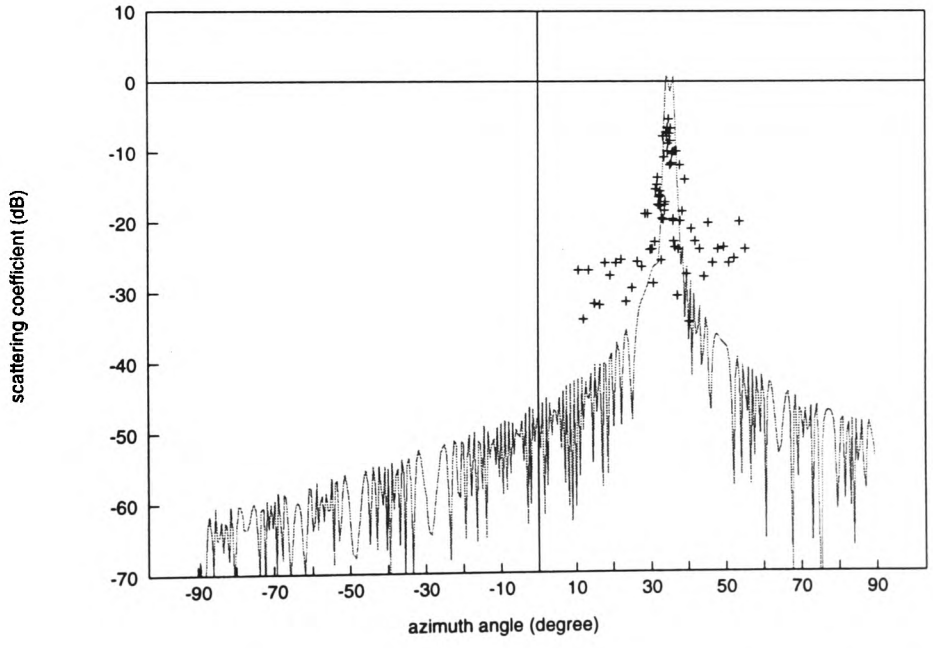

Figure 5.19 The measured and predicted results of the Ringland building, r=215 m (Ringland 2), horizontal polarisation.

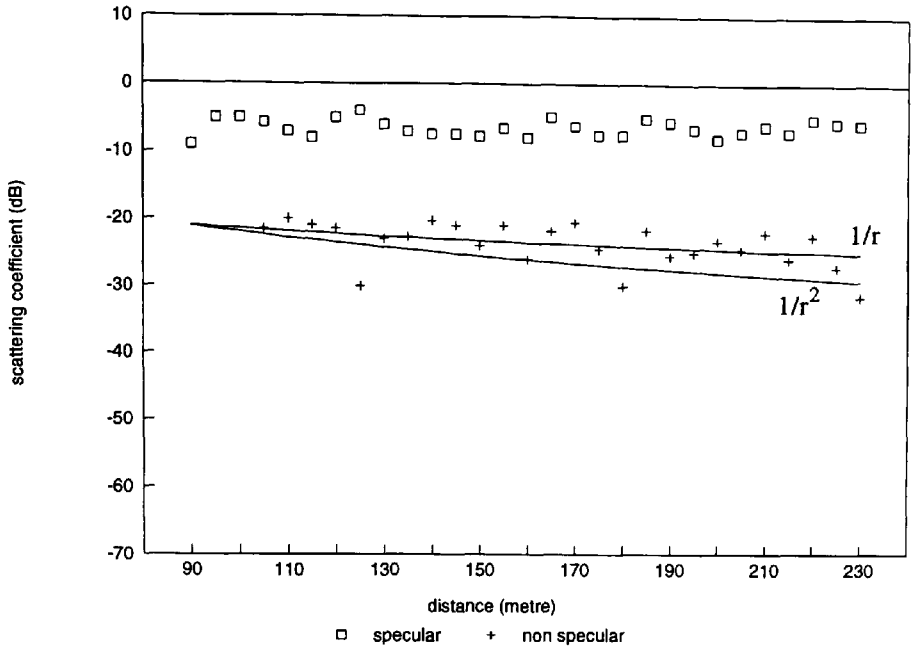

Figure 5.20 Scattering coefficient measured as a function of the receiver-building distance from 90 to 230 m in the specular direction of azimuth 35 degrees and a non-specular direction of azimuth 53 degrees at the Ringland building.

Figure 5.21 The St Julians building in Newport.

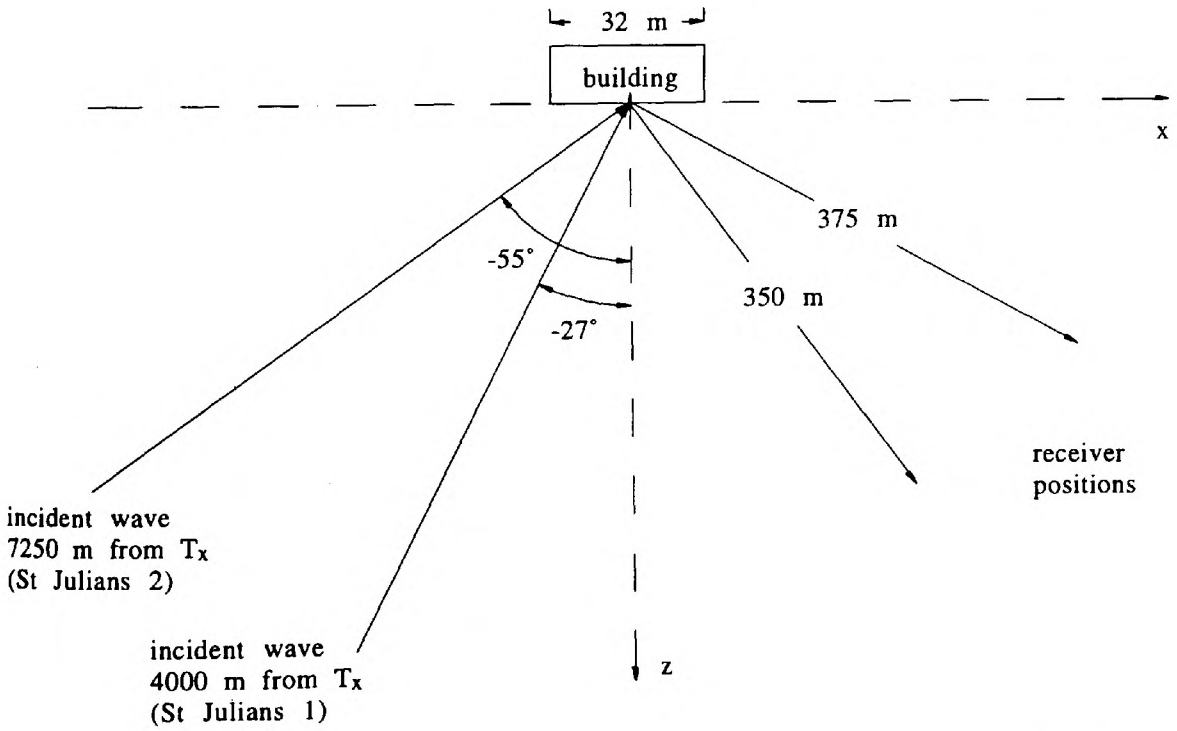

Figure 5.22 The experimental site geometry of the St Julians building.

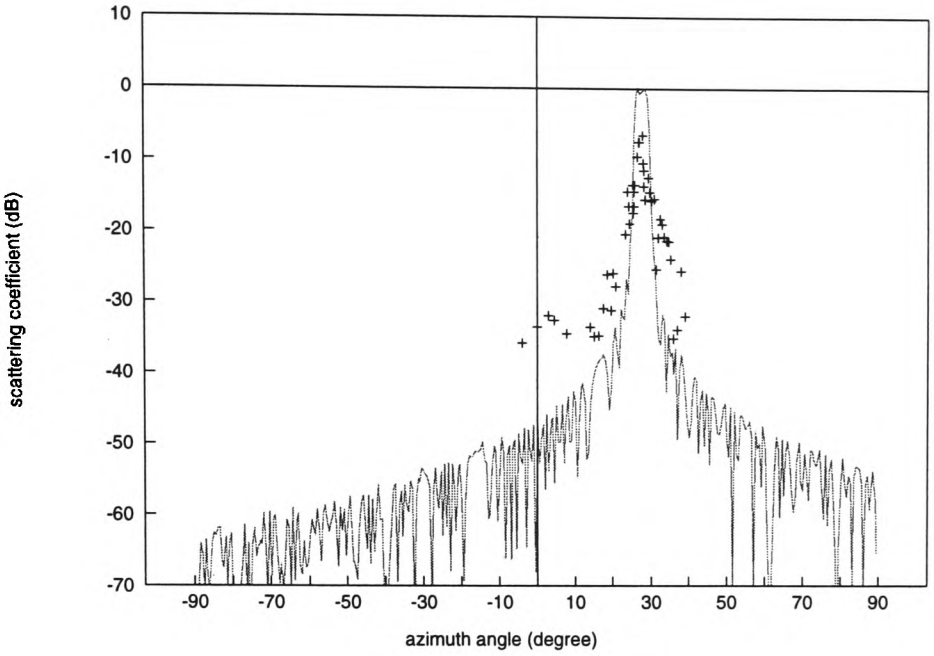

Figure 5.23 The measured and predicted results of the St Julians building, θ_0=-27 degrees (St Julians 1), r=350 m, vertical polarisation.

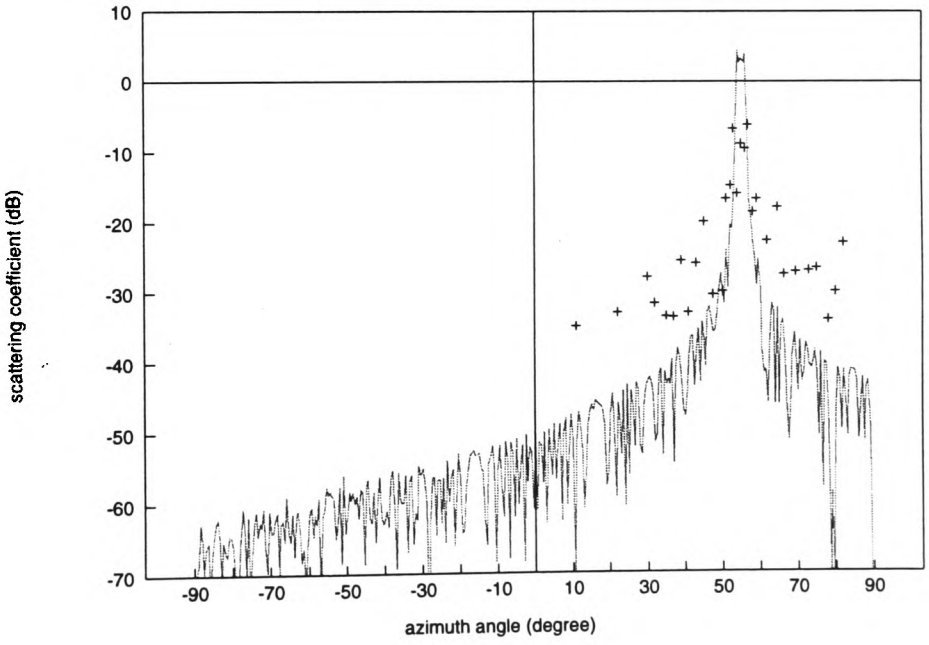

Figure 5.24 The measured and predicted results of the St Julians building, θ_0=-55 degrees (St Julians 2), r=375 m, vertical polarisation.

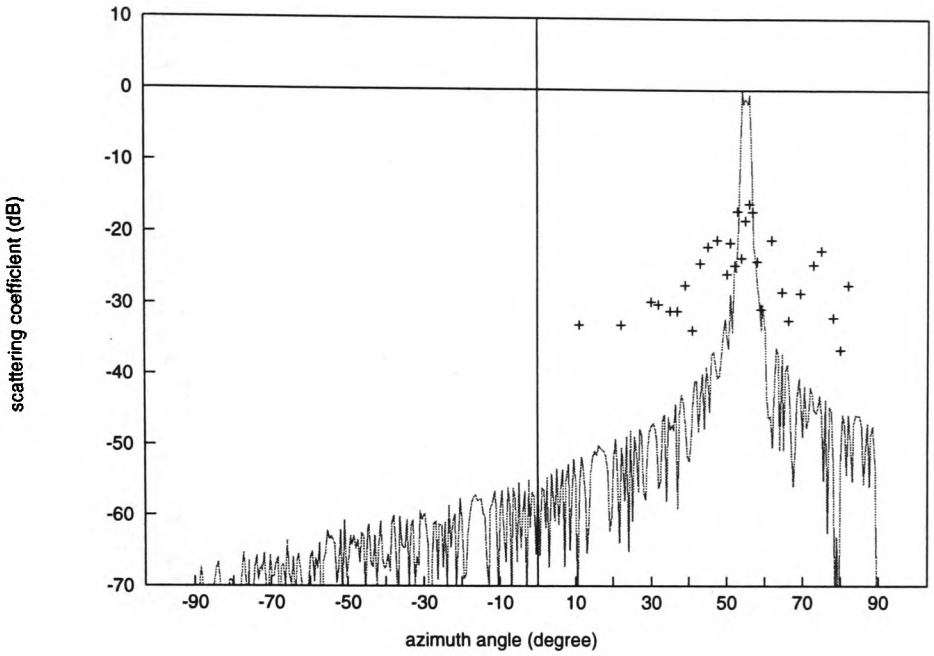

Figure 5.25 The measured and predicted results of the St Julians building, θ_0=-55 degrees (St Julian 2), r=375 m, horizontal polarisation.

Figure 5.26 The Dudley building in Greater Birmingham.

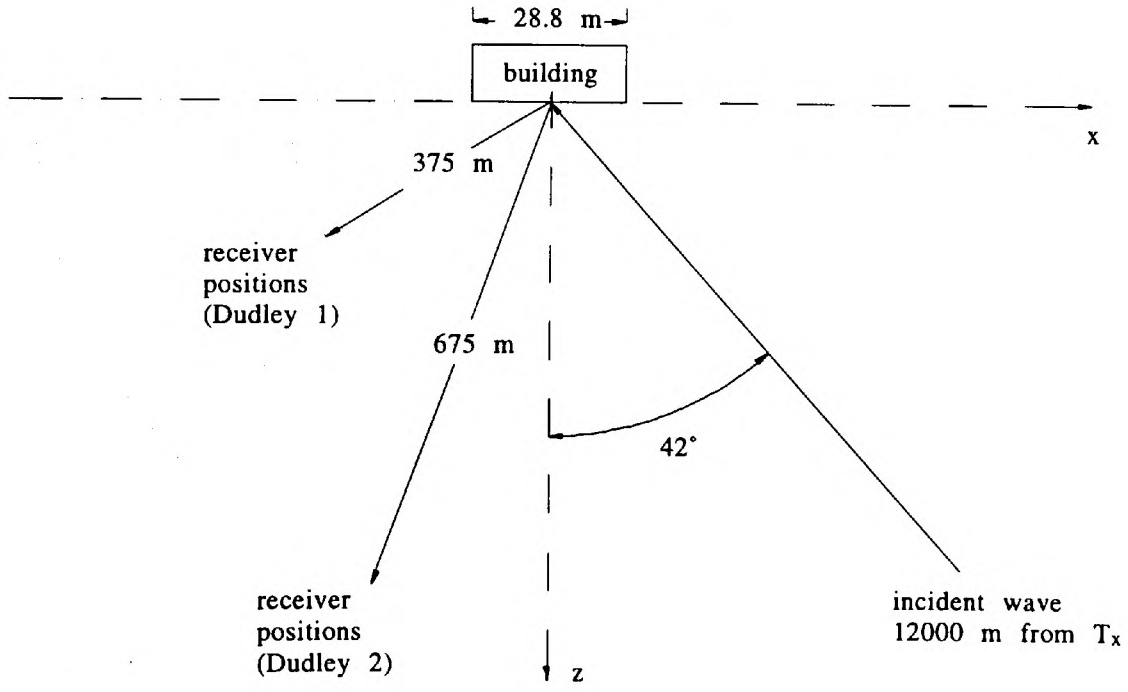

Figure 5.27 The experimental site geometry of the Dudley building.

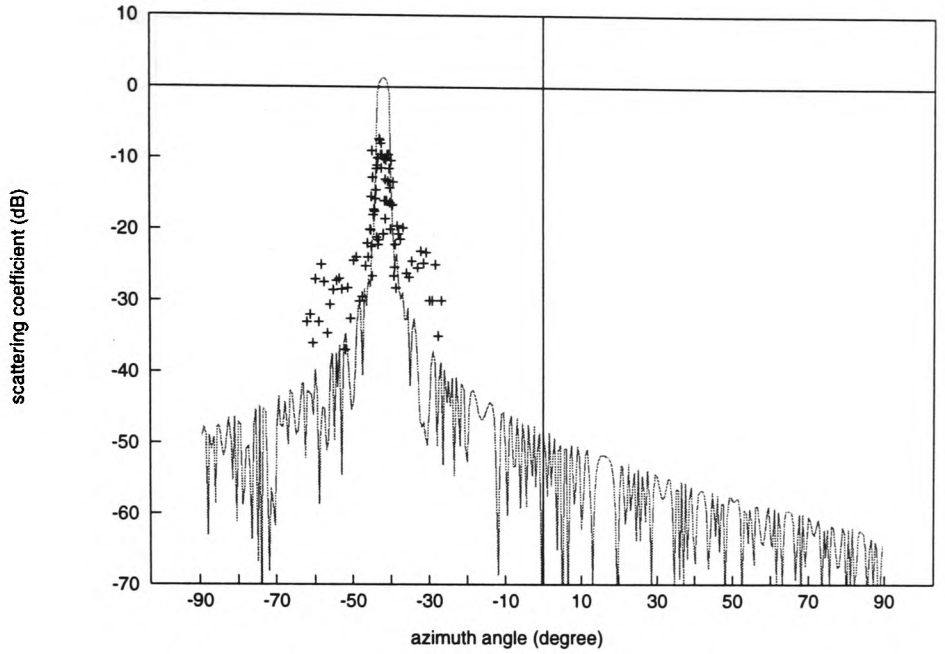

Figure 5.28 The measured and predicted results of the Dudley building, r=375 m (Dudley 1).

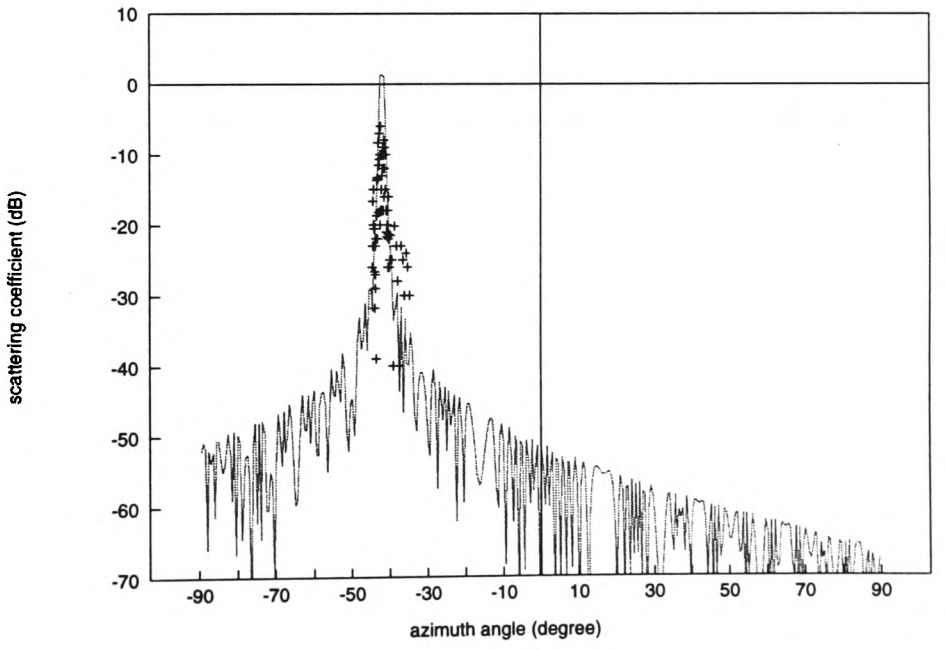

Figure 5.29 The measured and predicted results of the Dudley building, r=675 m (Dudley 2).

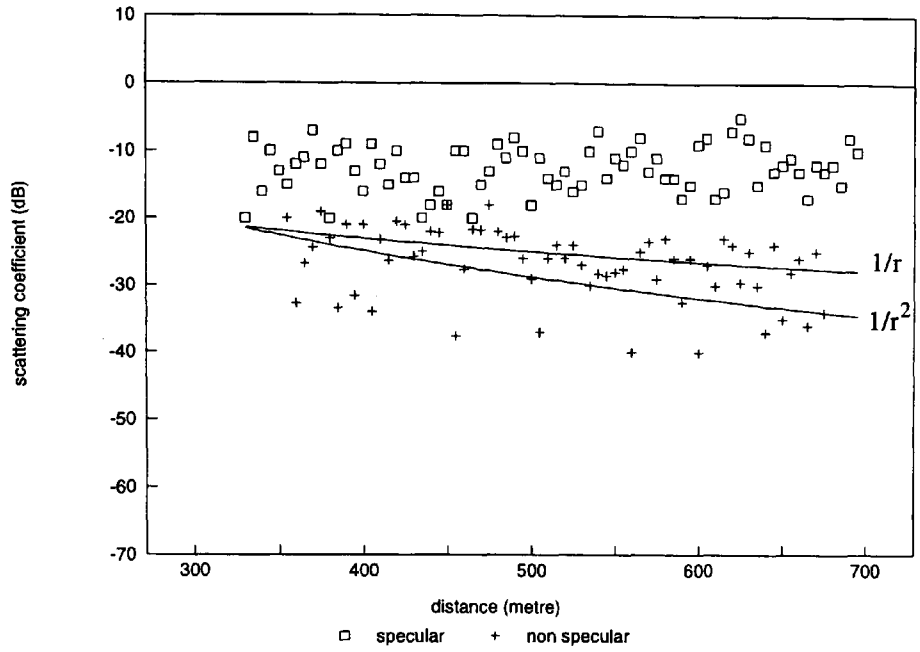

Figure 5.30 Scattering coefficient measured as a function of the receiver-building distance from 325 to 690 m in the specular direction of azimuth -42 degrees and one of the non specular direction of azimuth -37 degrees at Dudley building.

Figure 5.31 The Walsall building in Greater Birmingham.

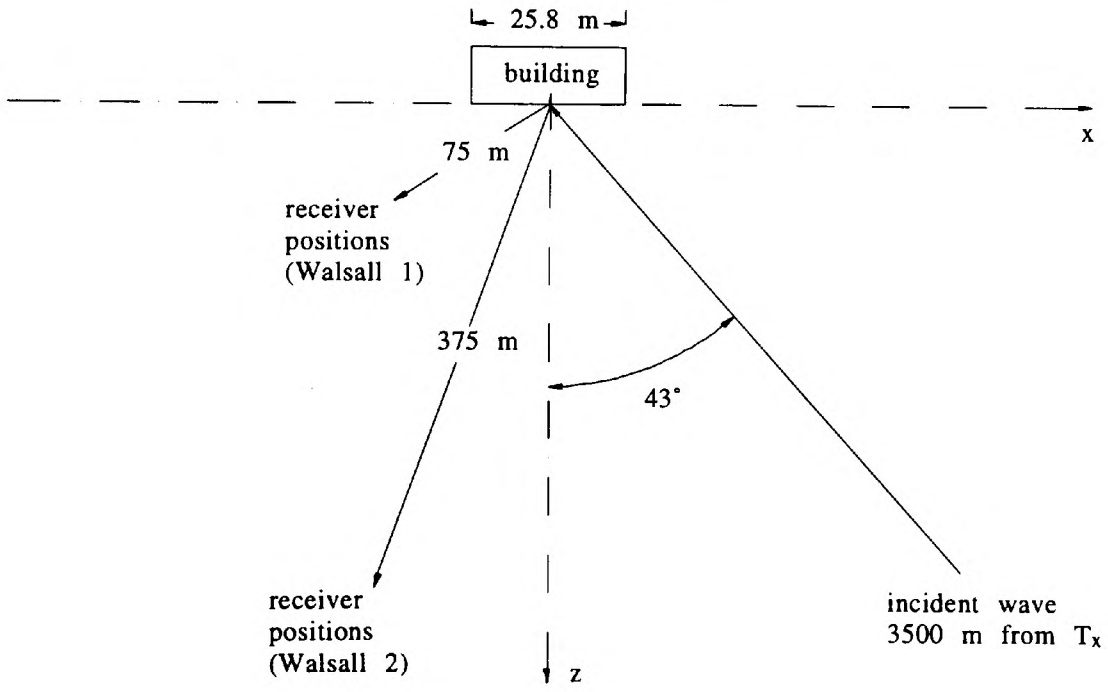

Figure 5.32 The experimental site geometry of the Walsall building.

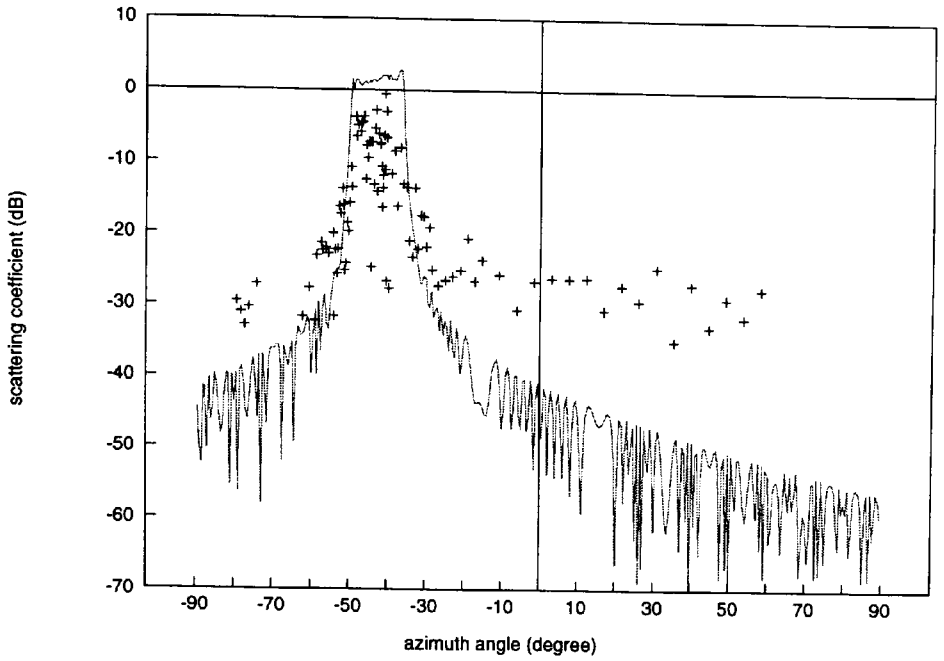

Figure 5.33 The measured and predicted results of the Walsall building, r=75 m (Walsall 1).

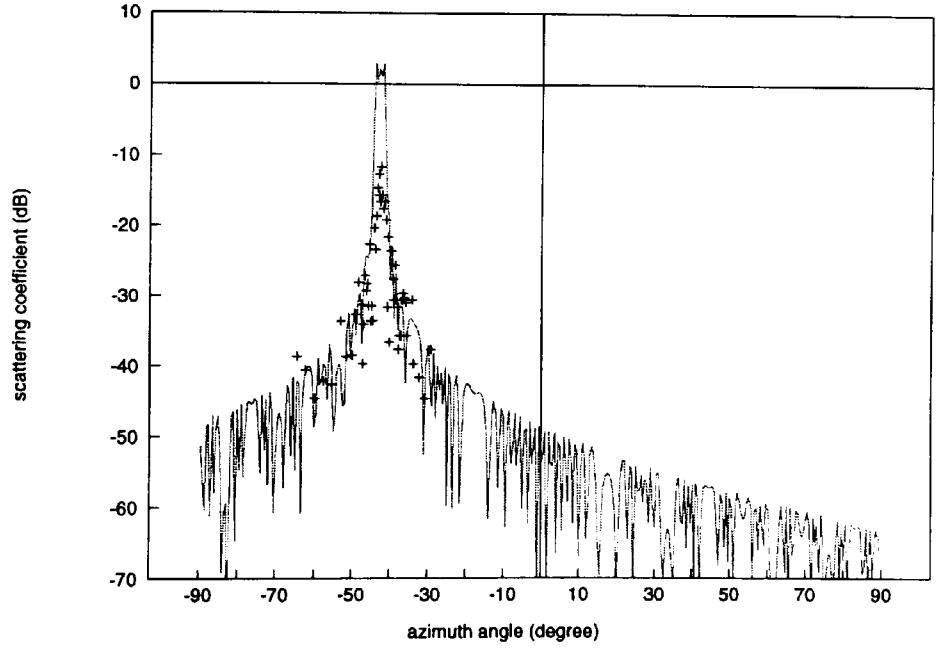

Figure 5.34 The measured and predicted results of the Walsall building, ϕ=-4.2 degrees, r=375 m (Walsall 2).

CHAPTER 6 DISCUSSION OF MEASURED RESULTS

6.1 Introduction

In this chapter, the implication of the measured results is discussed in relation to theory with respect to the characterisation of building scattering and the verification of the prediction models. Theoretical predications are given for each test performed using the prediction models developed in the idealised situation of perfectly conducting smooth plane surfaces. Comparisons made between the measured and predicted results are intended to illustrate the basic scattering properties of these buildings with regard to azimuth variation and distance dependence of their scattering patterns. The geometrical factors which are critical in determining scattering patterns, especially building dimensions and receiver-building distances, are analysed for the purposes of practical prediction procedures. Meanwhile, practical considerations of building surfaces, including both physical and geometrical factors, are investigated. To assist in interpreting the measured results, a number of measurements of reflection loss coefficients of building surfaces were made. The effects of surface conditions of moisture content, material thickness and small roughness on the reflection loss coefficients are assessed theoretically with reference to the Fresnel reflection coefficient. Theoretical effects of windows and large scale surface deviation roughness as discussed in chapter 4 are considered to account for the measured results observed in some tests. The dependence of scattering signal levels on polarisation is discussed in relation to Fresnel reflection coefficients and incident geometries.

6.2 Dependence of scattering coefficient on radio terminal position

As stated in chapter 3, angle and distance dependence of scattering coefficients and beamwidth of scattering patterns are three important aspects in characterising scattering behaviour of idealised surfaces. Measurement data collected from real buildings can be used to

discuss how well they compare with the predicted results using the prediction models developed and to further discuss their implications on a procedure for building scatter.

6.2.1 Predicted results

In the process of discussion, the measured results of all tests in azimuth scan are compared to the theoretically predicted results. In the prediction the buildings are simply modelled as having a perfectly conducting smooth plane surface. The azimuth variations of scattering coefficients are calculated in the azimuth range of -90 to +90 degrees using the very near field prediction model described in section 3.6.4. The geometrical factors involved in the calculations are building surface dimensions, incident and receiving path geometries, which are listed in table 6.1. As mentioned previously, the predicted results are plotted in solid curves and shown alongside the measured results for all buildings described in chapter 5.

Table 6.1 Radio path geometries

building	a (m)	b (m)	r_0 (m)	ϕ_0 (deg)	θ_0 (deg)	r (m)	ϕ (deg)	polarisation
porter's house	5.2	7.15	350	0	31.5	15	0	V
Butetown	38	57	4450	0	34	382	-1	V
Merthyr Tydfil	35	8.8/7.3	875	3.5	-55	100	0	V
Ringland 1	30	14	1450	1	-35	125	0	V,H
Ringland 2	30	14	1450	1	-35	215	0	V,H
St Julians 1	34	32	4000	0.65	-27	350	0	V
St Julians 2	34	32	7500	0.5	-55	375	0	V,H
Dudley 1	55	28.8	12000	1	42	375	0	V
Dudley 2	55	28.8	12000	1	42	675	0	V
Walsall 1	53.5	25.8	3500	1.5	43	75	0	V
Walsall 2	53.5	25.8	3500	1.5	43	375	-4.2	V

6.2.2 Azimuth angular dependence of the scattering coefficient

In all the tests of azimuth scan, measured results show strong azimuth angular dependence of the scattering coefficient. The scattering coefficient in non specular regions is observed typically at about -25 to -35 dB. There are sharp increases in scattering coefficients when receiver positions move into specular regions. The scattering coefficients in specular regions are mostly high typically at about -5 to -15 dB. In comparison with predicted results in the figures, azimuth variations of the measured results are generally in good agreement with those of the predicted results with respect to the azimuth regions corresponding to relatively high and low values of the scattering coefficient. This agreement suggests that the main scattering contribution in the azimuth range is mainly caused by plane surfaces.

The fact that the scattering coefficients in specular regions are high suggests that building scatter is essentially specular in nature and is not significantly affected by surface roughness. This specular nature means that the scattering behaviour of individual buildings may be largely determined by consideration of geometrical factors such as building dimensions, receiver-building distance and incident path geometries. This may be observed by examining the results of the measurement programme.

With the largest horizontal dimension, the Butetown building shows a wider azimuth region of high scattering coefficients than that of the St Julians building which has an almost identical receiver-building distance. St Julians 2 with a larger azimuth incident angle shows a narrower azimuth region of high scattering coefficients than that of St Julians 1 which relates to the same building. These results show that the azimuth region with high scattering coefficients is proportional to building width a or effective width $a\cos\theta_0$. However, with the smallest building width, the porter's house building shows the widest azimuth region of high scattering coefficients. This must be because of the relatively short receiver-building distance. This distance factor on azimuth variations is clearly demonstrated in comparisons between the measured results of Ringland 1 and 2, between those of Dudley 1 and 2 and between the

measured results of Walsall 1 and 2. For a given building, a wider azimuth region of high scattering coefficients is associated with a shorter distance. These observations agree with the derived formula described by equation 3.15 which identifies the width of a specular region as $2\sin^{-1}\left(\frac{a\cos\theta_0}{2r}\right)$.

At the boundary between specular and non specular regions, measured results show that the scattering coefficient drops significantly as soon as the azimuth specular condition is lost. The predicted results generally show a reasonably good representation of the measured results in the transition region. In section 3.7.2, the azimuth variation of the very near field prediction model outside the specular region can be approximately given by equation 3.77. This shows that the azimuth variation of the scattering coefficient in these regions is proportional to $\frac{1}{\alpha'+\alpha}$, where $\alpha' = \sin\left(\theta \mp \sin^{-1}\frac{a\cos\theta_0}{2r}\right)\cos\phi$ in the azimuth range (non specular regions) specified as $-\theta_0 - \sin^{-1}\frac{a\cos\theta_0}{2r} > \theta > -\theta_0 + \sin^{-1}\frac{a\cos\theta_0}{2r}$. The inverse function of $\alpha'+\alpha$ by its nature means that at small values of $\alpha'+\alpha$, i.e. $\theta \to -\theta_0 - \sin^{-1}\frac{a\cos\theta_0}{2r}$ or $\theta \to -\theta_0 + \sin^{-1}\frac{a\cos\theta_0}{2r}$, a significant increase in the scattering coefficient would occur. This behaviour appears to reasonably well represent that of the scattering coefficient in the transition regions which has been observed in predicted and measured results.

There are differences between measured and predicted results in amplitude. In specular regions, the main reason for the measured amplitudes being smaller than those predicted is because none of the building surfaces is perfectly conducting. In non specular regions, the measured results being higher than those predicted is largely due to the effects of building features and background scatter. Some of the differences will be discussed in later sections of this chapter with attention being paid to the effects of building surface conditions.

6.2.3 Distance dependence of the scattering coefficient

In the comparison between the measured results of Ringland 1 and 2 and Dudley 1 and 2, it is

seen that the scattering coefficients in the specular regions were maintained at the same level even though the receiver-building distances were almost doubled from Ringland 1 to Ringland 2 and from Dudley 1 to Dudley 2. In the non specular regions however, the scattering coefficients at shorter distances are clearly higher than those at longer distances. These facts are highlighted by measured results carried out in the range scan tests, one in specular regions and another in non specular regions at the two experimental sites. In figure 5.20 of the Ringland building, the scattering coefficients in the specular direction of azimuth 35 degrees are about -6 dB with small variations of 2 dB observed consistently throughout the receiver-building distance range 90 to 230 m. In figure 5.30 of the Dudley building, there is also an insignificant distance dependence of the scattering coefficients in the specular direction of azimuth -42 degrees over the receiver-building distance range 325 to 685 m though the variations are somewhat larger.

In a theoretical exercise, the scattering coefficient in the specular direction (at normal incidence) is calculated as a function of the receiver-building distance for two different size reflectors of 2.44 m by 2.44 m and 20 m by 20 m. The calculation results are shown in figures 6.1 and 6.2 respectively. On the horizontal axes in the figures, the receiver-building distance is normalised with respect to the Rayleigh far field distances of the two reflectors respectively, as shown:

$$R_a = \frac{r}{\frac{2(a\cos\theta_0)^2}{\lambda}} \quad \text{with respect to building width}$$

$$R_b = \frac{r}{\frac{2(b\cos\phi_0)^2}{\lambda}} \quad \text{with respect to building height} \qquad 6.1$$

The two distance dependence curves for the two different size reflectors show an identical behaviour over their normalised distances. However, the value in real terms representing a "normalised distance" of unity varies dramatically between the two reflectors. For the 2.44 m by 2.44 m screen it would represent 400 m whereas it is 32 km for the 20 m by 20 m screen.

When the value of the normalised distance R_a is small, the curve of the distance dependence oscillates fast. The amplitude of oscillations increases as the normalised distance increases, but the pace of the oscillation slows down gradually. In section 3.7.2, the equations used in determining the scattering coefficient at a receiver position has been classified in near and far field ranges according to the ratio of building dimensions to the radius of the first Fresnel zone, i.e. a/r_a (or similarly b/r_e with respect to building height). When $a/r_a >> 1$, in the near or very near field regions, the building surface intersects a large number of Fresnel zones. As the receiver-building distance increases, i.e. r_a increases, the intersection loses higher order zones. Losing an even order zone enhances the scattering coefficient whereas losing an odd order zone weakens the scattering coefficient. Since higher order zones make a smaller contribution to the resultant, the amplitude of oscillation is small. But it increases steadily as a/r_a approaches a value approximately 1.2 (it would be equal to one in a normal incidence if the surface is circular). When the building surface intersects only the first Fresnel zone approximately, i.e. $a/r_a \approx 1.2$, the scattering coefficient is at its highest. Afterwards, the intersection is only one part of the first Fresnel zone so that the scattering coefficient declines steadily. In equation 3.52, the distance dependence of the scattering coefficient is determined as $2a/r_a$. After the receiver-building distance normalisation, $2a/r_a$ can be written as

$$2\frac{a}{r_a} = \frac{2a\cos\theta}{\sqrt{2r\lambda}} \qquad 6.2a$$

In the specular region, $\theta \approx -\theta_0$, thus

$$2\frac{a}{r_a} \approx \frac{2a\cos\theta_0}{\sqrt{2r\lambda}} \approx \frac{1}{\sqrt{\frac{r\lambda}{2(a\cos\theta_0)^2}}} \approx \frac{1}{\sqrt{R_a}} \qquad 6.2b$$

The relationship between building dimensions and receiver-building distances is included in the normalised distance as a single variable in the equation. Therefore, the distance dependence curve in figures 6.1 and 6.2 is generally valid for buildings of arbitrary dimensions over their

normalised distances.

In Table 6.2, the normalised receiver-building distances in all the tests are listed together with their far-field distances at which the normalised distance is equal to one.

Table 6.2 The normalised receiver-building distances

building	$\frac{2(a\cos\theta_0)}{\lambda}$ (m)	R_a	$\frac{2(b\cos\phi_0)}{\lambda}$ (m)	R_b
porter's house	2775	0.0054	2019	0.0074
Butetown	166735	0.0023	107822	0.0035
Merthyr Tydfil	7617	0.013	91469	0.0011
Ringland 1	9820	0.013	67202	0.0019
Ringland 2	9820	0.022	67202	0.0032
St Julians 1	60702	0.0058	86317	0.0041
St Julians 2	25155	0.015	86317	0.0042
Dudley 1	34203	0.011	225872	0.0016
Dudley 2	34203	0.02	225872	0.003
Walsall 1	26585	0.0028	213720	0.00035
Walsall 2	26585	0.014	213720	0.0018

It is seen that in all the sites the normalised receiver-building distances used in the measurements are very small in proportion to their far field distances. In this normalised distance range, the scattering coefficients in the specular regions do not reduce as the receiver-building distance increases but maybe expected to exhibit variations (oscillations) of a few decibels. This has been demonstrated in the measured results of the tests of range scan and between the tests of azimuth scan. In practice for typical buildings, this means that the scattering coefficients in the specular regions would be equally high over a range of distance stretching many kilometres away from the building.

In contrast in figure 5.20 relating to the Ringland building, the scattering coefficient in the non specular direction of azimuth 53 degree appears to decrease as the receiver-building distance increases from 90 to 230 m. Similarly in figure 5.30 (the Dudley building), there is also a clear declining trend of the scattering coefficient in the non specular direction of azimuth -37 degrees over the receiver-building distance 375 to 675 m. In section 3.7.2, the distance dependence of the scattering coefficient in the azimuth non specular and elevation specular conditions is generally described as 1/r. This distance dependence is plotted in the above figures as solid curves and superimposed on the measurement points. In comparison with the measured results, the declining trend of the distance dependence of the scattering coefficient in the azimuth non specular region is clearly indicated.

Generally speaking in site shielding application involving small values of the normalised distance, the difference between the scattering coefficients in the specular and non specular regions would increase as the receiver-building distance increases. It should be noted that background scatter has its strongest influence in non specular regions because of the weak scattering signal levels from the building. Nevertheless, background scatter mostly results from other surrounding buildings, vegetation and terrain. Apart from specular reflections of plane surfaces in close range, background scatter is expected to be distance dependent of either 1/r or $1/r^2$. This is the main reason why, in the geometrical site survey, the chosen building had to be distinct and were separated from other obstacles in order to keep the background scatter low.

6.2.4 Distance dependence of the scattering pattern beamwidth

The azimuth regions of high scattering coefficients are the most significant part of scattering patterns and conventionally these are measured in terms of the beamwidth of scattering patterns. Identifying and characterising these regions is an important process in the prediction of building scatter as far as interference reduction is concerned. In general, the beamwidth of a plane surface is inversely proportional to the surface dimensions and is independent of

distance.

However, measured and predicted results clearly demonstrate that building scattering is essentially specular in nature and it is seen that the region of high scattering coefficients is closely related to the specular region of a building. The width of the specular region is given in section 3.4.1 as $2\sin^{-1}\frac{a\cos\theta_0}{2r}$. This shows that the width of this region will be inversely proportional to r and directly proportional to the effective building width $a\cos\theta_0$. The beamwidths yielded by the measured and predicted results, are consistent with this relation, but inconsistent with the previously stated general statement. There is an important issue which could resolve the problem of the two opposing beamwidth statements. They address different field regions of a building surface. The first statement refers to the far field of the surface while the second refers to the very near field region within which the reported measurements were carried out.

In order to illustrate the different sides of the argument, the beamwidths of two 2.44 m by 2.44 m and 20 m by 20 m perfectly conducting reflectors were studied as a function of receiver-building distance. The 6 dB beamwidths for the two cases in an azimuth -40 degree incidence are calculated using the very near field prediction model and shown as curve a in figures 6.3 and 6.4 respectively. The receiver-building distance is normalised with respect to the Rayleigh far field distances of the two reflectors.

In figure 6.3 when the normalised distance $R_a < 0.1$, the beamwidth decreases as the receiver-building distance increases. Approaching $R_a = 0.1$, the rate of decrease slows down. When $R_a > 0.1$, the beamwidth becomes virtually constant throughout the remaining range. In figure 6.4, there is an identical tendency of the range dependence of the beamwidth against the normalised distance although the beamwidth is actually much narrower than that in figure 6.3. Curve a shows two distinctive distance dependence regions of the beamwidth.

In the figures, there is a second curve, i.e. curve b. Curve b is the width of specular regions

given by equation 3.15 as $2\sin^{-1}\frac{a\cos\theta_0}{2r}$. Using the normalised distance, equation 3.15 can be expressed as

$$\Delta\theta_s = 2\sin^{-1}\frac{a\cos\theta_0}{2r} = 2\sin^{-1}\frac{\lambda}{4aR_a\cos\theta_0} \qquad 6.3$$

Curve b shows the inverse-law dependence on distance (specular region) throughout the normalised distance range. Importantly when $R_a < 0.1$, curve b has a very good agreement with curve a in both figures. This agreement confirms the specular nature of building scatter observed in the experimental programme. When $R_a > 0.1$, curve b has a different range dependence from curve a. However in the both figures, curve a and curve b intersect at $R_a = 0.24$. Therefore due to this intersection, the constant beamwidth value of curve a for $R_a > 0.1$ can be assigned the value indicated by curve b at $R_a = 0.24$ in a much simplified form as

$$BW_a = \sin^{-1}\frac{\lambda}{4\times 0.24a\cos\theta_0} = \sin^{-1}\frac{\lambda}{0.96a\cos\theta_0} \qquad (R_a > 0.1) \qquad 6.4$$

From the above discussion, it can be said that the two apparently contradictory statements regarding the beamwidth of the scattering patterns are in fact both valid, but in different field regions. Equations 6.3 and 6.4 show that the beamwidth is inversely proportional to the receiver-building distance in the very near field region whereas it is constant in the far field. It is worth emphasising that, referring to the Rayleigh far field distances of the buildings used in measurements as shown in table 6.2, the very near field region $R_a < 0.1$ is the relevant region in site shielding and urban radio propagation.

6.3 Reflection loss coefficient

In comparing measured and predicted results, it is seen that the measured scattering coefficients in the specular regions have always been lower than the predicted results by

amounts varying from 4 to 15 dB. The differences between the measured and predicted results in specular regions can be accounted for by what referred to as the reflection loss coefficients. These differences vary from surface to surface clearly due to different building materials being used. Generally speaking, pebble-dash cladding surfaces give relatively large values of reflection loss coefficients, with brick surfaces giving somewhat smaller values while relatively small reflection loss coefficients would be observed from smooth concrete surfaces.

With practical building surfaces on the one hand and idealised perfectly conducting surfaces on the other, the differences between the measured and predicted results in the specular regions are mainly attributable to the reflection loss coefficients of building surface materials. However, considering the differences as solely due to the reflection loss coefficients of the building surfaces would not be satisfactory. This is because building surfaces used in the experimental programme were not just of a single plane made from one material but rather consisted of a number of different planes involving windows, balconies and pebble-dash strips between concrete walls. Thus, it is of concern that there would be effects due to windows and surface roughness. To evaluate the reflection loss coefficients of practical building surfaces properly, further study was undertaken.

This section gives details of a supplementary experimental and theoretical investigation which looked at the scattering properties of various building materials.

6.3.1 Fresnel reflection coefficient

In theory, reflection loss coefficients of surfaces can be determined by the Fresnel reflection coefficient which is a function of the parameters of incident angles θ, permittivity ε, permeability μ, conductivity σ and frequency f. This is defined by

$$S_\rho = 10\log|\rho|^2 = 10\log\left|F(\theta_0, f, \varepsilon, \mu, \sigma)\right|^2 \qquad 6.5$$

where

$$F_V(\theta_0, f, \varepsilon, \mu, \sigma) = \frac{Z_1 \cos\theta_0 - Z_0 \cos\theta_t}{Z_1 \cos\theta_0 + Z_0 \cos\theta_t} \quad \text{for vertical polarisation} \quad 6.6$$

$$F_H(\theta_0, f, \varepsilon, \mu, \sigma) = \frac{Z_1 \cos\theta_t - Z_0 \cos\theta_0}{Z_1 \cos\theta_t + Z_0 \cos\theta_0} \quad \text{for horizontal polarisation} \quad 6.7$$

and

Z_1 intrinsic impedance of medium $Z_1 = \frac{j\omega\mu_1}{\nu}$ and $\omega = 2\pi f$;

ν propagation constant $\nu^2 = \omega^2\mu_1\varepsilon_1\left(j\frac{\sigma_1}{\omega\varepsilon_1} - 1\right)$;

θ_t refraction angle $\cos\theta_t = \sqrt{1 - \left(\frac{\eta_0}{\eta_1}\right)^2 \sin^2\theta_0}$;

η_0, η_1 refraction indices of free space and medium respectively $\left(\frac{\eta_0}{\eta_1}\right)^2 = \left(\frac{j\omega\sqrt{\mu_0\varepsilon_0}}{\nu}\right)^2$.

For most non-ferrous materials, their relative permeability can be considered to be unity. This is taken as the case for most building surfaces. It is known that reflection loss coefficients can have strong frequency dependence which implies that the relative permittivity is complex. Since only a single frequency is used in the measurements, and for reasons of simplicity, the values of relative permittivity are assumed to be real and referred to as those of urban ground ($\varepsilon_r = 3$). Therefore, the Fresnel reflection coefficient with real permittivity is given as

$$F_V(\theta_0, f, \varepsilon, \sigma) \approx \frac{\cos\theta_0 - \sqrt{\left(\frac{Z_0}{Z_1}\right)^2 - \sin^2\theta_0}}{\cos\theta_0 + \sqrt{\left(\frac{Z_0}{Z_1}\right)^2 - \sin^2\theta_0}} \quad 6.8$$

$$F_H(\theta_0, f, \varepsilon, \sigma) \approx \frac{\sqrt{\left(\frac{Z_0}{Z_1}\right)^2 - \sin^2\theta_0} - \left(\frac{Z_0}{Z_1}\right)^2 \cos\theta_0}{\sqrt{\left(\frac{Z_0}{Z_1}\right)^2 - \sin^2\theta_0} + \left(\frac{Z_0}{Z_1}\right)^2 \cos\theta_0} \quad 6.9$$

For materials of building surfaces used, their conductivities can be very low. For instance in the case of dry, rocky or sandy soil, the conductivity may vary from roughly 10^{-5} to 10^{-2} mhos/m. If the actual conductivity of building surfaces were confined in this range, there would be very little impact on reflection loss coefficients. The reflection loss coefficients with relative permittivity $\varepsilon_r = 3$ and conductivity of 10^{-5} and 10^{-2} mhos/m respectively have a difference less than 1 dB. However, the moisture content of building surfaces might dramatically change the conductivity of building surfaces. Therefore, conductivity is used as a parameter to reflect various conditions of moisture content of building surfaces. Higher conductivity will indicate higher moisture content on building surfaces. The value $\sigma = 4$ for sea water is used to indicate the highest content which a surface can possibly have. The Fresnel reflection coefficients are plotted as the solid curves in figures 6.5 to 6.11 with relative permittivity and conductivity as given in the figures where they are compared to the measured results of reflection loss coefficients of building surfaces.

6.3.2 Reflection loss coefficient measurement

Defining building surfaces in terms of their electrical properties is a complicated problem. The values of the relevant parameters are not specifically defined and can vary considerably according to actual surface conditions. To clarify the effects of the relevant parameters in determining reflection loss coefficients, it was considered necessary to carry out measurements of reflection loss coefficients of common building surfaces in typical practical conditions.

A number of measurements of reflection loss coefficients were made on three types of building surface involving brick, glass and pebble-dash materials. Both vertical and horizontal polarisations were used. The basic experimental method was to measure the ratio of incident waves on a building surface at an angle chosen to be in the specular region. In the measurements, two 15 dBi horn antennas with 35 degrees beamwidth were used at the transmitter and the receiver. The transmitter was located at a distance of fifty metres away from the surface. The receiver was set at a distance of 0.25 m from the surfaces which was in

the far field of the horn antenna. The receiver was so close to the building surface that, from the receiver point of view, the surface of the material was practically equivalent to an infinitely large plane. Therefore, there was no significant contribution from parts of the building surface with different materials. To show the angular dependence of the reflection loss coefficients of building surfaces, measurements were taken at different incident angles of 25, 47 and 60.5 degrees relative to the normal of the building surface respectively. It was not possible to choose very large or very small angles of incidence due to practical difficulties. At very small incident angles, the receiver would block a part of the incident wave while, at very large angles, the incident wave would be directly picked up by the receiving antenna.

6.3.3 Measured results using vertical polarisation

Measurements of reflection loss coefficients using vertical polarisation were carried out on brick, pebble-dash and glass surfaces. These are discussed below.

6.3.3.1 Brick surface

In figure 6.5, the measured results of reflection loss coefficients of two brick surfaces referred to as brick 1 and brick 2 are shown together with the predicted results. At the incidence angle 25 degrees, brick 1 and brick 2 give the reflection loss coefficients of 9 and 6 dB respectively. These coefficients were measured as 5.5 and 4.5 dB respectively at the incidence angle 60.5 degrees. The reflection loss coefficients of both brick 1 and brick 2 decrease as the incident angle increases. Brick 2 shows relatively less reflection loss than brick 1. In the course of the measurements, it was recorded that brick 1 was in a relatively dry condition compared with brick 2 which was in a wet condition a few hours after rain. Accordingly, the moisture content conditions of the two surfaces was noticeably responsible for the difference between the reflection loss coefficients measured in the two cases. Compared to predicted results, measured results are seen to fit closely the theoretical curves of conductivities $\sigma = 1$ and $\sigma = 3$. Brick 1 corresponds to the lower conductivity value and brick 2 corresponds to the

higher one.

The angular dependence of the reflection loss coefficients is seen to be that reflection loss coefficients reduce as the incident angle increases. The variation with incident angle is more noticeable with materials of lower conductivity. The difference between brick 1 and brick 2 thus reduces as the incident angle increases. The measured angular dependence of the reflection loss coefficients are seen to be in good agreement with predicted results. The value of relative permittivity $\varepsilon_r = 3$ seems to be appropriate in this case.

6.3.3.2 Pebble-dash surface

Measurements of the reflection loss coefficient of two pebble-dash surfaces, referred to as pebble-dash 1 and pebble-dash 2 were conducted in a similar dry weather conditions. The measured results are shown in figure 6.6 together with predicted results of the same values of the incidence angle parameter used as in the brick surface cases. At the small incident angle 25 degreès, the reflection loss coefficients of pebble-dash 1 and pebble-dash 2 are 9.5 and 13.5 dB respectively. Pebble-dash 2 has less reflection loss coefficient than pebble-dash 1. At the incident angle 60.5 degrees, the reflection loss coefficients reduce to 5.5 and 7.5 dB respectively. The difference between pebble-dash 1 and pebble-dash 2 thus reduces to 2 dB.

In general, the two pebble-dash surfaces, in particular pebble-dash 1, have larger reflection loss coefficients than the brick surfaces. Noticeably, pebble-dash surfaces were less smooth than brick surfaces due to the pebble-cladding on the surfaces. Pebbles were generally a few to ten millimetres in size. The gaps between pebbles were slightly less than the size of pebbles. Pebbles and gaps formed an undulating profile with the amplitude of a few millimetres. The surface roughness of small scale textures, so called because roughness is less than the wavelength, can be statistically defined by the Rayleigh roughness parameter which is expressed as

$$g = \frac{4\pi\sigma_h \cos\theta_0}{\lambda} \qquad 6.10$$

where σ_h is the height standard deviation of the surface roughness. In general, there are three cases classified according to the value of the Rayleigh roughness parameter

(i) g<<1 is the case of a slightly rough surface

(ii) g=1 is the case of a moderately rough surface

(iii) g>>1 is the case of very rough surface.

For pebble-dash 1 and pebble-dash 2, the height standard deviations were estimated, based on the twenty measured roughness heights of each surface, to be about 1.5 mm and 3 mm respectively. Their Rayleigh roughness parameters are calculated at the three incident angles and listed in table 6.3. The parameter of pebble-dash 1 is less than 1. That of pebble-dash 2 is around 1 so that pebble-dash 2 has a larger value of the parameter than pebble-dash 1. This correctly confirmed that pebble-dash 2 has larger pebbles than pebble-dash 1 so that pebble-dash 2 is rougher. The parameter is seen to have an angular dependence, reducing as the incident angle increases.

Table 6.3 Rayleigh roughness parameters of two pebble-dash surfaces

	σ_h	25.5°	47°	60.5°
Pebble-dash 1	1.5 mm	0.635	0.48	0.35
Pebble-dash 2	3 mm	1.27	0.96	0.7

As a result, an effective reflection loss coefficient of a surface with roughness can be defined as the product of the Fresnel reflection coefficient of a plane surface and the exponential of the Rayleigh roughness parameter [Beckman (1968)] as

$$\rho_r = \exp\left(-\frac{1}{2}g^2\right)F(\theta_0, f, \varepsilon, \sigma) \qquad 6.11$$

The effective reflection loss coefficients of pebble-dash 1 and pebble-dash 2 are calculated at conductivity $\sigma = 2$ and shown in figure 6.7 in comparison with the measured results. There is a better agreement between the measured and predicted results than that displayed in figure 6.6.

6.3.3.3 Glass surface

In the case of glass, the measurements were performed on two different window glass types referred to as glass 1 and glass 2. Glass 1 and glass 2 were of different thickness (about 6 and 4 mm respectively). The measured results are shown in figure 6.8. The reflection loss coefficients of both glass 1 and glass 2 are relatively large at about 12 and 14 dB respectively at the smaller incident angle of 25 degrees. The reflection loss coefficient of the thicker glass 1 is 3 dB less than that of glass 2. Their reflection loss coefficients reduce dramatically as the incident angle increases.

This angular dependence is unexpected according to the predicted results given in figure 6.8 with relative permittivity $\varepsilon_r = 10$ and the same values of conductivities as the other two surfaces. The predicted results assume that the thickness of glass is infinite while in windows it is finite and, in fact, very thin. Generally speaking, small thickness glass will allow more wave energy to penetrate through, in particular at small incident angles. As the incident angle increases, the thickness of the window glass effectively increases. As a result, the penetration of wave energy reduces. Comparing these results to those of the other two cases of brick and pebble-dash surfaces, it can be seen that glass is even more strongly angular dependent. The predicted results are clearly not adequate in representing reflection loss coefficients from window glass.

It is seen from the predicted results that the value of conductivity is no longer significant for cases involving large values of relative permittivity. On the other hand, glass is not a moisture absorbing material when compared with brick and pebble-dash surfaces. Thus, moisture content is unlikely to affect the reflection loss coefficient of glass. The difference between glass 1 and glass 2 shows the effect of glass thickness on reflection loss coefficients. Thicker glass has a smaller reflection loss coefficient than that of thinner glass.

6.3.4 Measurements made using horizontal polarisation

The measurements of reflection loss coefficient using horizontal polarisation were made for all surface materials used except brick 1. The measured results are shown in figures 6.9, 6.10 and 6.11 for brick, pebble-dash and glass surfaces respectively. The predicted results are given using equation 6.6 of the Fresnel reflection coefficient for horizontal polarisation and shown together with the measured results in the figures. The parameters of relative permittivity and conductivity are kept the same as those used for vertical polarisation. It can be seen that, particularly where the conductivity is low, very high values of reflection loss coefficient are predicted around the Brewster angle.

At the small incident angle of 25 degrees, brick 2, pebble-dash 1 and 2 and glass 2 using horizontal polarisation are more or less the same as those for vertical polarisation. Glass 1 is 6 dB less than that of vertical polarisation. However at large incident angles particularly 60.5 degrees, the reflection loss coefficients using horizontal polarisation are much larger than their vertical counterparts. The measured results show an angular dependence of reflection loss coefficients increasing as the incident angle increases. Although pebble-dash 2 and glass 2 do not show this angular dependence clearly, they are consistently at high levels of about 13 and 15 dB respectively throughout the range of incident angles. There was no values of very low reflection loss coefficient observed in any of the cases. The predicted results show the angular dependence of the reflection loss coefficient which increases as the incident angle increases. Indeed it might be expected that larger reflection loss coefficients would be observed for

incident angles around the Brewster angle.

During the course of the measurements of horizontal polarisation, ground reflections were frequently experienced as interference contributions to the measurements. Consequently, some measured results could be affected to some extent particularly for large reflection loss coefficient values. The problems seem to be of less significance in the cases of vertical polarisation. In fact, ground reflection reacting to the two linear polarisations illustrate that reflection loss coefficients are polarisation dependent since a parallel polarisation with respect to the building surface is a perpendicular polarisation with respect to the ground and vice versa.

As far as the conductivity and surface roughness are concerned, measured effects that were explained in detail for the cases of vertical polarisation are in principle valid also for horizontal polarisation. Reflection loss coefficients of more conductive and smoother surfaces should have lower values.

6.4 Effects of building features

In this section implications of building structural features and surface deviation roughness are discussed for measurements of some tests.

6.4.1 A corner structure

The Merthyr Tydfil building consists of two surfaces meeting each other at a right angle. This is a case of a corner structure. The predicted results are given using the protruding feature model developed in section 4.3. and shown together with the measured results in figure 5.13.

It is known that there would be double reflections taking place in the corner if the corner is seen from the transmitter. It is expected that the scattering coefficient would be high around

the incident azimuth direction. This is shown by both measured and predicted results though the measured results were relatively low.

The scattering pattern of such a corner structure can be equivalent to that of a plane surface which is normal to the incident azimuth direction. In the very near field range, the width of the scattering pattern is determined as in the other cases by the width of an equivalent plane defined by equation 4.25. There is a good agreement on the azimuth variations of the scattering coefficient between the measured and predicted results. Similarly to the results obtained for the other buildings, the scattering coefficient is relatively high and stays high in the specular region of the equivalent plane. Comparing these with the measured results of the other tests, the scattering coefficient in the specular region is low due to the double reflections from pebble-dash surfaces. A reduction of the scattering coefficient can also be seen as soon as the specular condition is lost. However, the difference between the scattering coefficients in the specular and non specular regions is the lowest.

6.4.2 Effects of windows

For all the buildings used in the experimental programme except the porter's house, there were a number of windows present on the building surfaces. These windows are very large compared to the wavelength and are arranged regularly in horizontal rows and vertical columns on the surfaces. From section 4.7, it is suggested that windows are effective scattering elements which are characterised by their reflection coefficients, total area and distribution on a building surface.

Considering the effects of windows in the measured results, the results from two tests are examined. The Butetown building has more than one hundred windows and the Ringland building has one column of eleven windows. The reflection loss coefficients of window and wall materials can be referred to section 6.3 based on the types of surfaces and their incidence angles. In both cases, concrete walls have lower reflection loss coefficients than windows. For

reason of simplicity, only the difference between reflection loss coefficients of windows and wall are considered with a higher value being equal to unity. For the Butetown building, the total window area is estimated to be one quarter of the building surface area. The number of more than one hundred windows is replaced by sixteen windows evenly distributed over the surfaces for the purpose of computational analysis. The predicted results are given in figure 6.12 using the window prediction model in section 4.7. Comparing to the predicted results of a plane surface in figure 5.10, there is no significant change apart from some small nulls and ridges. In fact, the effects of windows have been exaggerated. The actual effects should be even less if the predicted results were based on the actual number and size of the windows.

For the Ringland building, the one column of eleven windows is placed in the centre of the building surface and evenly distributed vertically. The windows are 2 m in width and 1.5 m in height. The predicted results are shown in figure 6.13. Comparing these with the predicted results of the plane surface without windows in figure 5.17, there is again no significant change except for some small ridges appearing in the predicted pattern.

At present in the above two cases, the reflection loss coefficients of windows are taken to be greater than those of the walls. The differences between the reflection loss coefficients of windows and wall are small. Furthermore for the Butetown building, a larger number of windows with a quarter of the total surface area are evenly distributed on the building surface. For the Ringland building, the total area of windows is only a very small fraction of the total area of the building surface. According to section 4.7, the effects of windows are limited by these conditions. The effects of windows could be expected to be more significant if the total window area increases or alternatively the reflection loss coefficient of windows becomes significantly larger than that of the walls.

6.4.3 Effects of surface deviation roughness

From the measured results of some tests of the azimuth scan, i.e. Ringland, St Julians, Dudley

and Walsall, the scattering patterns are broadened in comparison with predicted results. This is seen in the transitions of the scattering coefficients at the boundaries between the specular and non specular regions. The scattering coefficients of the measured and predicted results drop correspondingly at the beginning of the transition, then the measured results gradually depart from the predicted results showing a slower reduction of the scattering coefficient than predicted. The measured scattering coefficients are considerably higher than the predicted results in the transition regions from the specular regions and further into the non specular regions. The relatively high scattering coefficients in these transition regions have the effects of broadening the scattering patterns. These effects are also seen from the comparison between the measured and predicted results of the Merthyr Tydfil building.

From section 4.8, it is shown theoretically that surface deviations can cause specular spreading which would result in scattering pattern broadening and a rise in the scattering coefficients in non specular regions. With this in mind, the measured results of Ringland and St Julians are further examined with particular consideration of the effects of surface deviations. According to section 4.8, building surfaces are modelled as consisting of a number of vertically rectangular plane panels. These panels are randomly tilted within a range of azimuth angles while their vertical axes are still situated in the same plane. Since building surfaces as whole are still seen to be plane, the range of randomly tilted angles must be chosen to be small, at a fraction of a degree.

For the Ringland building, it is assumed that there are ten panels $N = 10$, the range of randomly tilted angles is 0.5 degrees. A scattering pattern computed with surface deviations characterised is given in figure 6.14 for Ringland 2. Compared to the prediction results of a plane surface in figure 5.19, the scattering coefficients in the specular region are not significantly changed although there are some null and ridges appearing. These nulls and ridges can be also seen in the measured results. However in the non specular regions, particularly in the vicinity of the specular region, there are some high ridges causing the scattering coefficients to rise by 10 dB higher than previously. As well as seen in the measured

results, the width of the scattering pattern has effectively broadened accompanied by a rise in the scattering coefficients in the non specular regions. In particular, the scattering coefficients can be seen to rise significantly just outside the specular region. The difference between the scattering coefficients in the specular and non specular regions is reduced considerably. Comparing this with measured results of Ringland 2, predictions based on this model appear to offer a better representation of the actual azimuth variations of the scattering coefficients over the azimuth range.

For the St Julians building, a scattering pattern is also computed and shown in figure 6.15 with surface deviations characterised in terms of the parameters of the number of panels $N = 20$ and the range of randomly tilted angles $\theta_{tm} = 0.5$ degrees. Compared to the predicted results of a plane surface in figure 5.23, similar effects due to surface deviations to those seen in the previous case emerge in figure 6.15, i.e. scattering pattern broadening due to the rise of scattering coefficients in the transition region. These effects were observed in the measured results of St Julians 1 shown in figure 5.23.

From the above, measured results of Ringland 2 and St Julians 1 are discussed with consideration of surface deviation roughness. Surface deviation roughness is seen to cause the effects of pattern broadening and a rise in the scattering coefficient in the non specular regions. The two parameters of the number of panels and the range of randomly tilted angles are important parameters quantifying the extent of the effects of surface deviations. A very small range of randomly tilted angles could have a considerable impact on scattering patterns. In practice, windows, balconies and surface sections are all possible elements of such randomly tilted panels. The effects are enhanced by the increasing number of panels. These effects of surface deviations are seen as the major reason for the difference between the measured results for Ringland, St Julians, Merthyr Tydfil, Dudley and Walsall buildings and those predicted and based on plane reflectors.

6.5 Polarisation dependence of scattering coefficient

The measured results discussed so far have used vertical polarisation. In the cases of Ringland 1, Ringland 2 and St Julians 2, horizontal polarisation was also used. These measurements with horizontal polarisation were conducted exactly in the same measurement configuration as their vertical polarisation counterparts.

In figures 5.16 and 5.18 of Ringland 1 and figures 5.17 and 5.19 of Ringland 2, the comparisons between the measured results of the two polarisations show little difference. However in figures 5.24 and 5.25 of St Julians 2, the measured results of the two polarisations have significant differences. Particularly in the specular regions, the scattering coefficient for horizontal polarisation is about 10 dB lower than those from vertical polarisation. In the non specular regions, the scattering coefficients of the two polarisations are broadly at the same levels which decline gradually as the receiver moves further away from the specular region. There is thus no dramatic azimuth variation of the scattering coefficients at the boundaries between the specular and non specular regions. The difference between the scattering coefficients in the specular and non specular regions is small. Therefore, measured results for Ringland 1, Ringland 2 and St Julians 2 tests are clearly showing different polarisation dependence.

The predicted results are given using the very near field prediction model of equation 2.43 applicable to horizontal polarisation and shown together in the figures of the measured results. In equation 2.43 of the scattering coefficients of vertical and horizontal polarisations, their polarisation factors are generally different. In the measurement configuration used, both incident and scattering elevation angles are small. Thus, the polarisation factors are approximately reduced to

$$u_V = u_\phi(\cos\theta+\cos\phi)\cos\phi_0 \qquad \text{for small elevation angles} \qquad 6.10$$
$$u_H = u_\theta(\cos\theta+\cos\phi)\cos\theta_0$$

The vertical and horizontal polarisation factors differ by a factor of $\cos\theta_0$. It is known that reflection loss coefficients are also polarisation dependent. The differences between the scattering coefficients of the two polarisations are jointly determined by polarisation factors and reflection loss coefficients which both are incident angle dependent. In the cases of Ringland 1 and Ringland 2, the incident azimuth angle is -35 degrees. The scattering coefficient for horizontal polarisation is estimated to be less than that corresponding to vertical polarisation by about 1.7 dB due to the polarisation factor and about 2 dB due to the reflection loss coefficient respectively. The difference between the two polarisations is therefore relatively small. In the case of St Julians 2, the incident azimuth angle is -55 degree. The difference between the two polarisations consists of 4.8 and 6 dB due to the same two factors respectively. It is therefore more significantly demonstrated in the comparison between the measured results of the two polarisations.

The effects of polarisation on scattering coefficients in specular regions are clearly azimuth angle dependent. There is little difference when the incidence azimuth angles are small. As incidence azimuth angles increase, the difference becomes significant. On the other hand, the effects of polarisation do not appear to be perceptible in non specular regions.

6.6 Interim conclusion

Comparison of measured and predicted results has generally shown a good agreement. This indicates that the main contribution to building scatter is made by plane surfaces. In the very near field regions of buildings, the strong azimuth dependence of building scatter is essentially specular in nature. In specular regions, scattering coefficients are relatively high and have no angle and distance dependences. In non specular regions, scattering coefficients are low and have a distance dependence of 1/r. Numerical computations using the very near field prediction model yield results which show a reasonably good representation of the azimuth variations of the measured scattering coefficient, particularly in the transition regions between the specular and non specular regions.

The very near field prediction model is also used to numerically demonstrate the distance dependence in the specular region and the beamwidth of the scattering patterns. These characteristics of building scatter are uniformly displayed and classified in terms of the normalised distance for arbitrarily sized buildings. Two characteristic values of the normalised distance are identified. The beamwidth is distance dependent where $R_a < 0.1$ and assumes a constant value over the range $R_a > 0.1$. The scattering coefficient in the specular region has no significant distance dependence where $R_a < 0.4$ while there will be a distance dependence of 1/r when $R_a > 0.4$. For typical size buildings, both of these values of R_a amount to relatively large distances of several and tens of kilometres.

The surface conditions of moisture content, small surface roughness and thickness play significant roles in determining the reflection loss coefficients of building surfaces. The first two cases can be evaluated by the relevant values of conductivity and the Rayleigh roughness parameter. The polarisation dependence of scattering coefficients consists of reflection loss coefficients and polarisation factors which are both incidence angle dependent. Scattering pattern broadening and the rise of the scattering coefficients in non specular regions are identified as the major effects of surface deviation roughness. This surface feature is modelled using a number of randomly tilted planes arranged according to random tilted angles. The effects of windows in the measured results are limited by practical factors relating to their small proportional areas, regular distribution and lower reflection coefficients relative to those of materials used to construct the walls.

Throughout the discussion, measured results are analysed in order to extract information useful for characterising the scattering properties of practical buildings and proceeding to the formulation of prediction procedures in terms of the specified geometries. The results and conclusions would provide a more practical and useful solution for building scatter of radiowaves for use in site shielding applications and radio system planning.

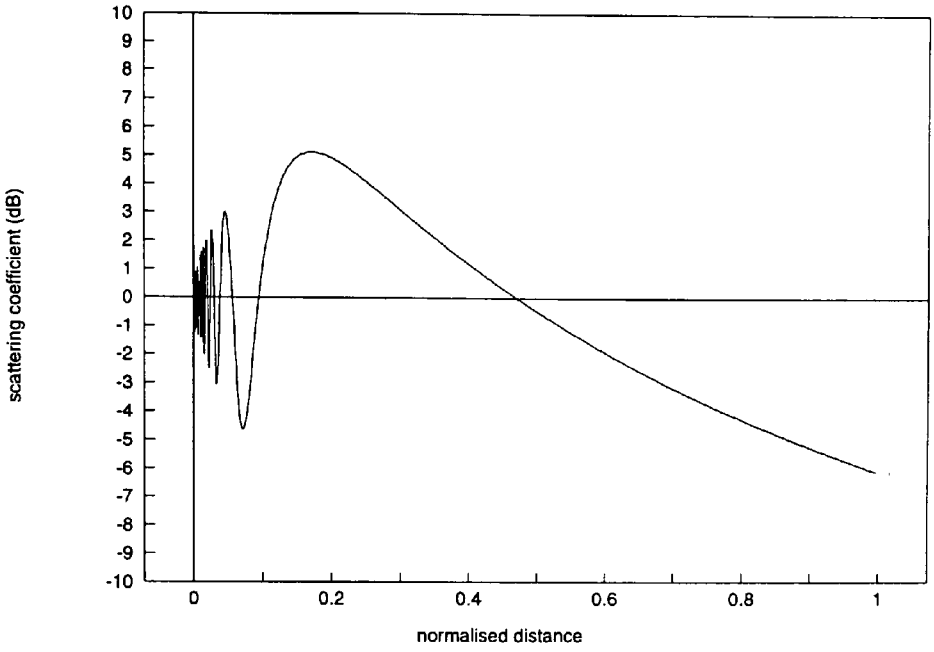

Figure 6.1 Distance dependence of the scattering coefficient in the specular direction (normal incidence) of a 2.44 m by 2.44 m reflector.

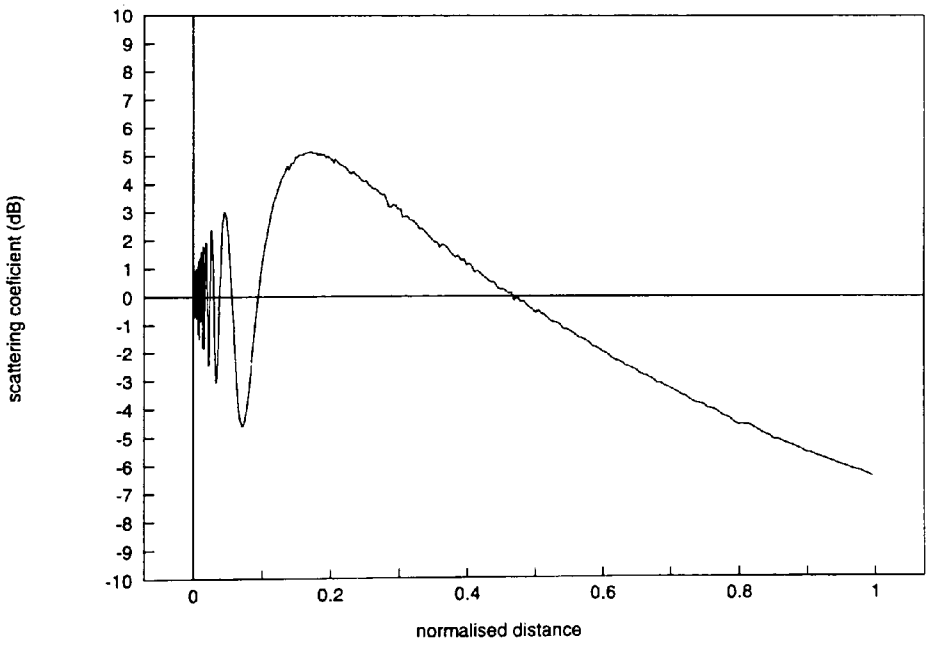

Figure 6.2 Distance dependence of the scattering coefficient in the specular direction (normal incidence) of a 20 m by 20 m reflector.

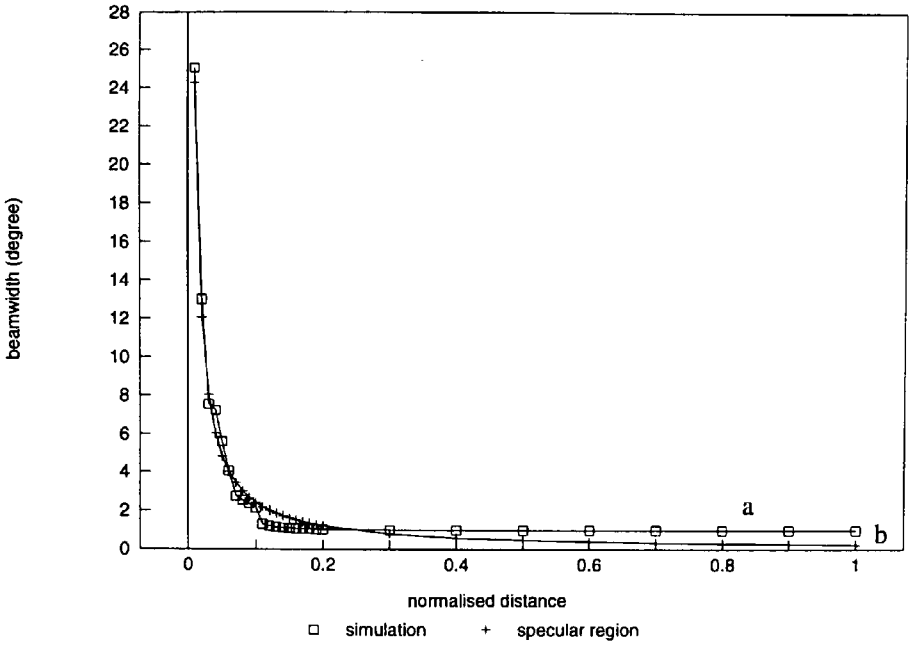

Figure 6.3 Distance dependence of beamwidth (θ_0=40 degrees) of a 2.44 m by 2.44 m reflector.

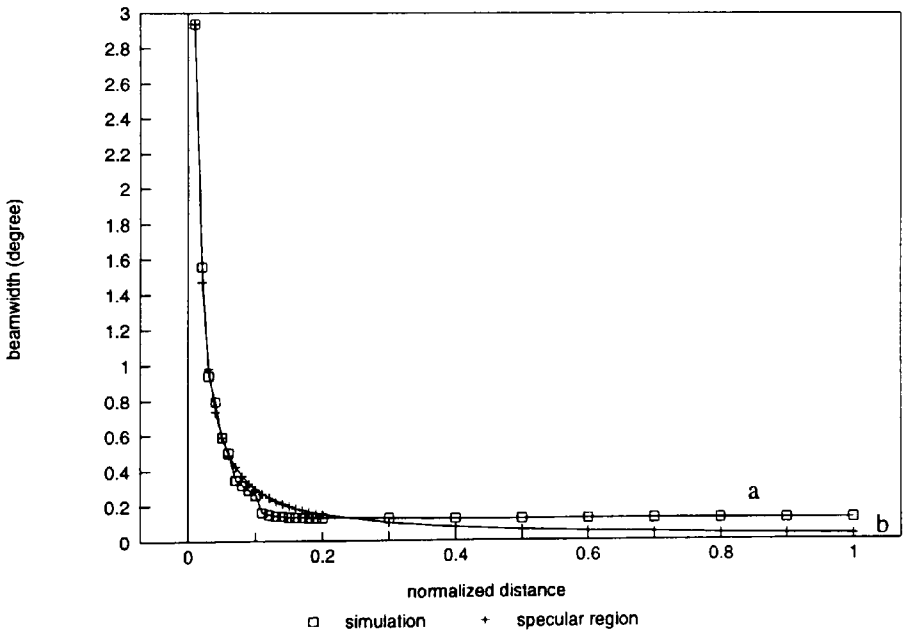

Figure 6.4 Distance dependence of beamwidth (θ_0=40 degrees) of a 20 m by 20 m reflector.

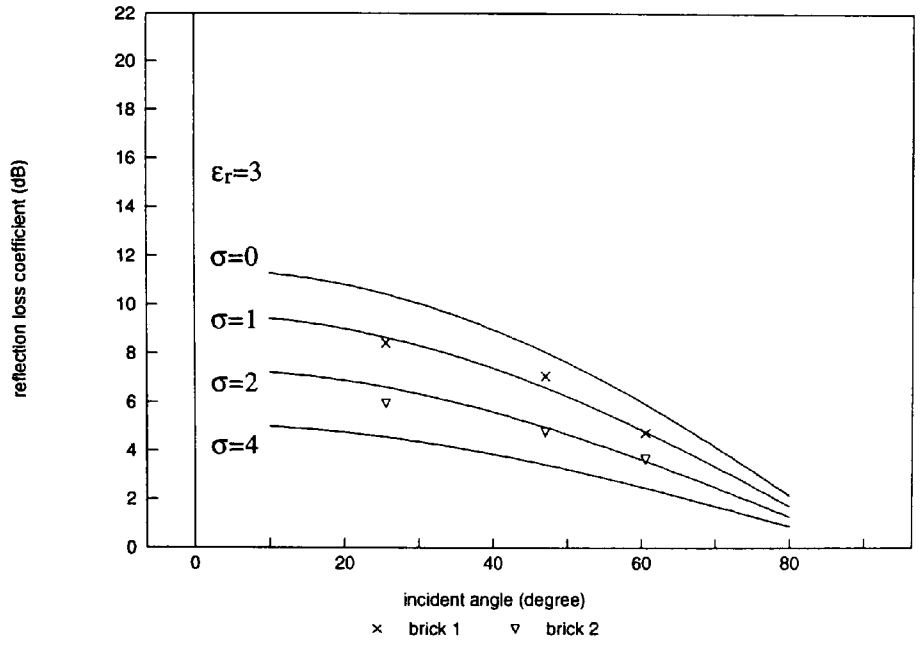

Figure 6.5 The measured and predicted results of reflection loss coefficients of brick surfaces on vertical polarisation.

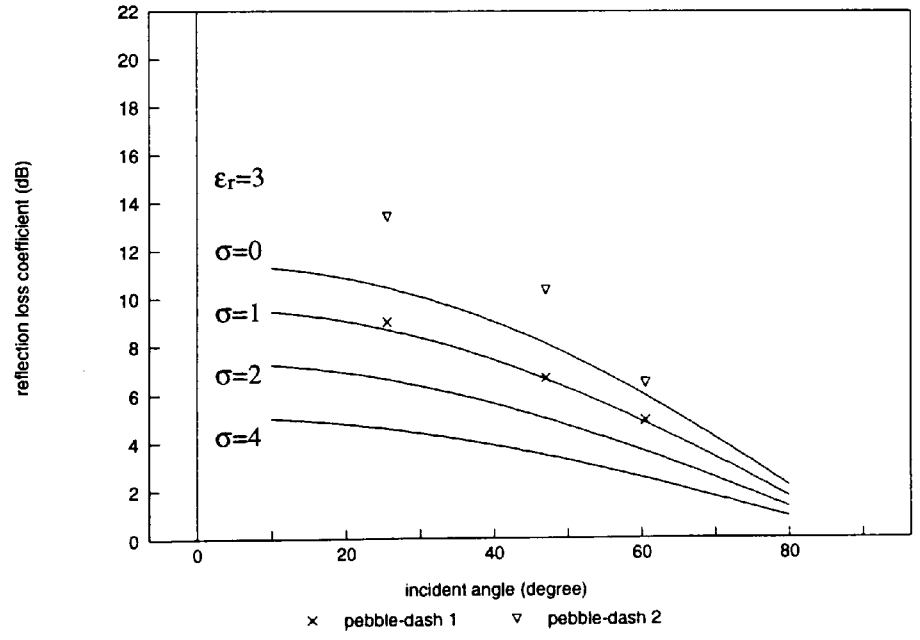

Figure 6.6 The measured and predicted results of reflection loss coefficients of pebble-dash surfaces on vertical polarisation.

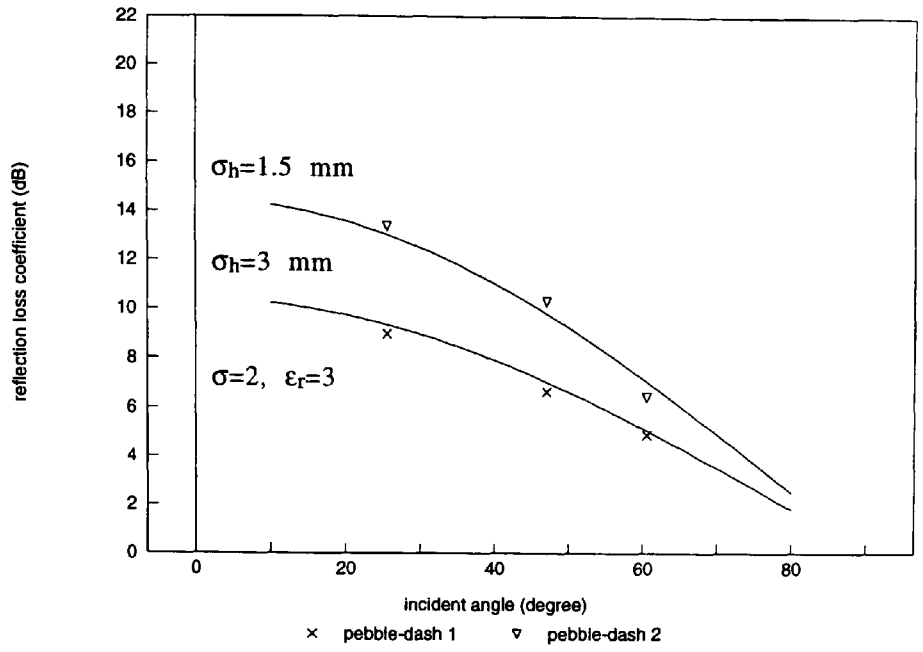

Figure 6.7 The measured and predicted (with surface roughness) results of effective reflection loss coefficients of pebble-dash surfaces.

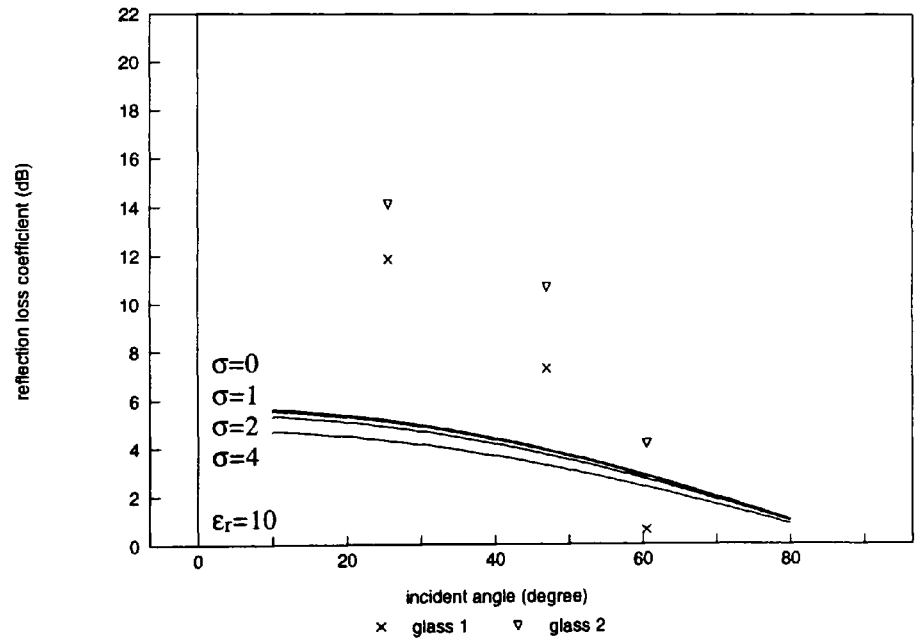

Figure 6.8 The measured and predicted results of reflection loss coefficients of glass surfaces on vertical polarisation.

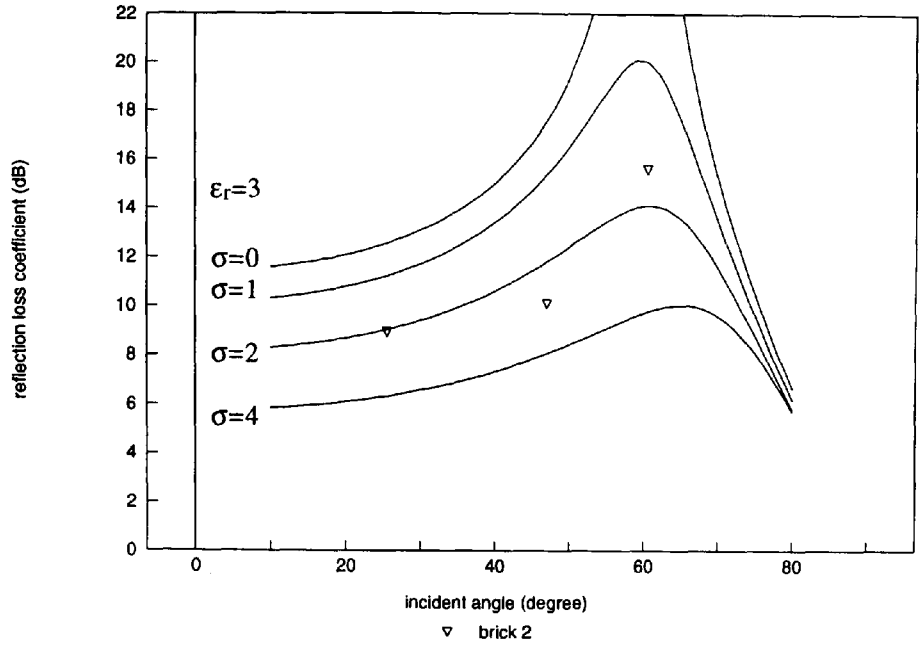

Figure 6.9 The measured and predicted results of reflection loss coefficients of brick surface on horizontal polarisation.

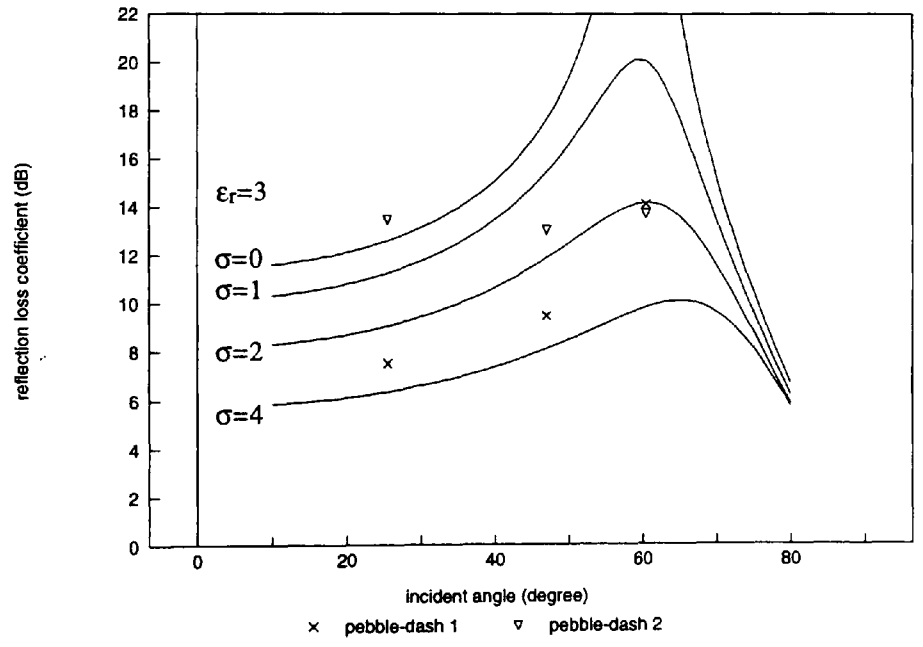

Figure 6.10 The measured and predicted results of reflection loss coefficients of pebble-dash surfaces on horizontal polarisation.

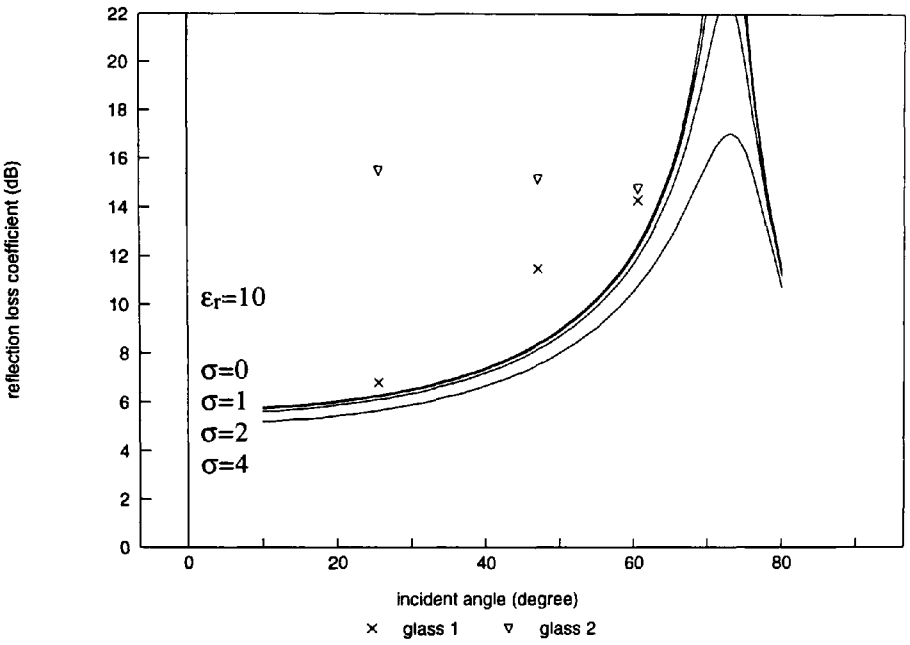

Figure 6.11 The measured and predicted results of reflection loss coefficients of glass surfaces on horizontal polarisation.

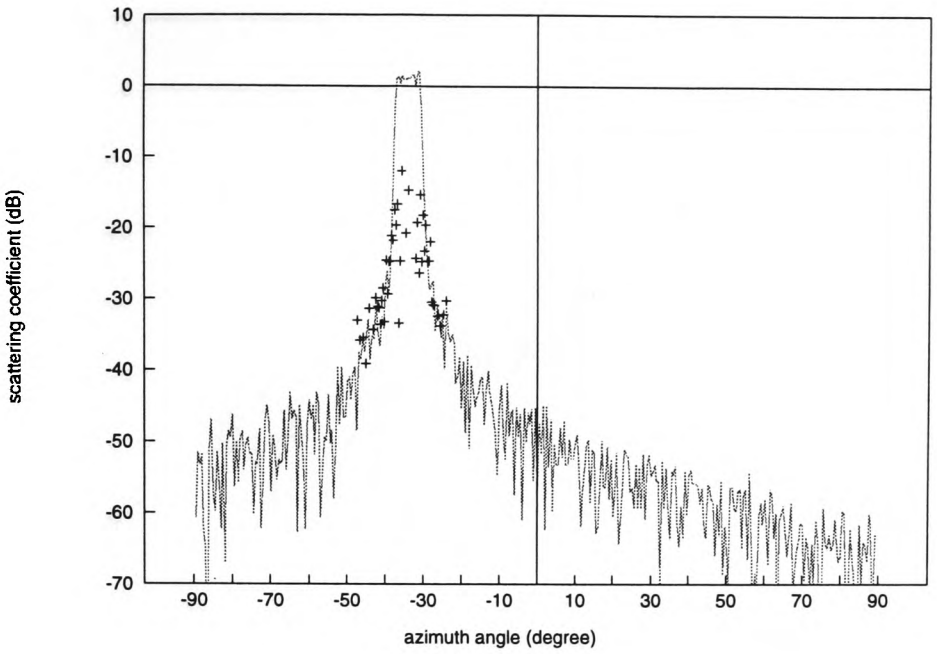

Figure 6.12 The effects of windows at the Butetown building.

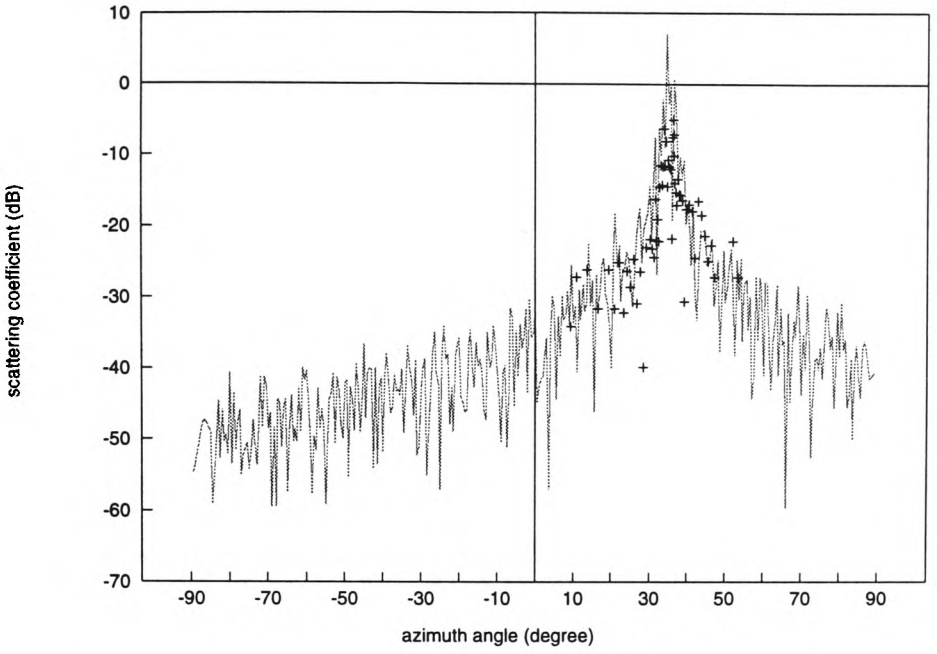

Figure 6.13 The effects of windows at Ringland 2.

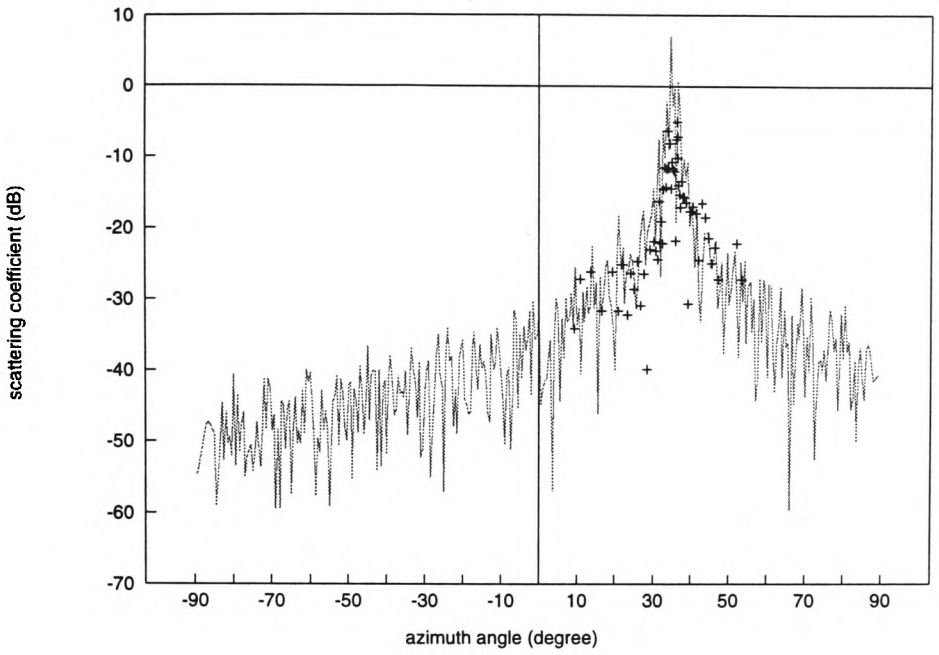

Figure 6.14 The effects of surface deviation roughness of Ringland 2 (N=10, θ_{tm}=0.5 degrees).

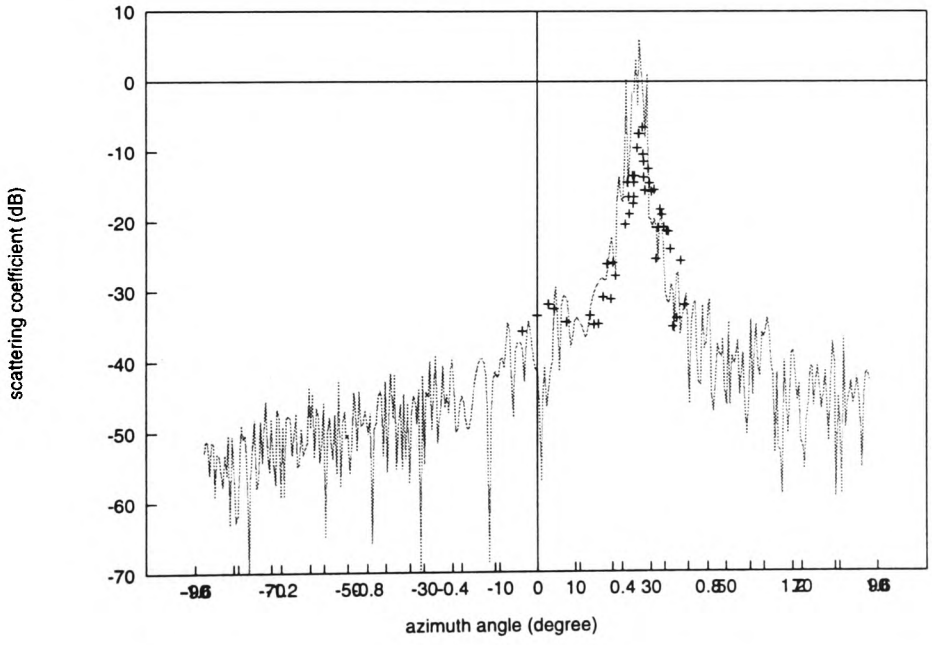

Figure 6.15 The effects of surface deviation roughness on St Julians 2 (N=20, θ_{tm}=0.5 degrees).

CHAPTER 7 BUILDING SCATTER PREDICTION PROCEDURES

7.1 Introduction

One of the main objectives of the project reported in this thesis has been the need to provide radio system planners with useful guidelines and procedures to deal with the presence of building scatter in site shielding situations.

In predicting the effects of building scatter on site shielding due to a specified interference, theoretical prediction models and a simplified engineering model can be used by considering building scattering surfaces each as an idealised single plane surface. The procedures based on these models, of which details are given in this chapter, require that only data obtainable from Ordnance Survey maps (e.g. scale 1:25000) and simple on-site surveys (to work out the dimensions of building scattering surfaces and the proposed position of radio terminals to implement site shielding relative to these surfaces) is specified. Additionally, an engineering model is suggested as a "portable" version of the theoretical prediction models. However, recommendations must be based on appropriate theoretical and engineering prediction models applicable to different situations. For instance in the specular region, the reflection loss coefficients of building scattering surfaces have to be taken into account while in non specular regions, the effect of background scattering is influential. The interference level in the latter case can be estimated according to empirical values of background scatter levels observed in the course of obtaining the measured results.

Extensions to prediction models of plane surfaces are represented by the additional considerations of windows, structural features and surface deviations. It is acknowledged that obtaining this information would be too onerous a task compared to what may be regarded as readily available from site geometry details used for plane surfaces. Alternatively, some typical

characteristics of these building features have been outlined as additional recommendations to the procedures for plane surfaces.

Predictions using these procedures are compared to measurements obtained in the experimental programme and also to the measurements and predictions recommended by CCIR report 569-4 [1990]. The comparisons demonstrate some significant improvement in predictions based on the procedures reported in this chapter.

7.2 Prediction models and their applications in field regions

The analytical work utilised Fresnel-Kirchhoff diffraction theory, in essence aperture analysis, as a basis for developing prediction models. The basic far field prediction model has proved to be a sufficiently accurate and effective analytical solution of building scatter in its Rayleigh far field region. This model is inevitably constrained by the fact that scattered microwave signals by buildings towards radio terminals in site shielding situations are most likely to be in the near and very near field regions of the scattering surfaces of these buildings, which are also very large apertures. More precise ray paths have to be defined to account for scattering contributions from building surfaces in the near and very near fields. Prediction models used in these cases are called appropriately the near field and very near field models.

A preliminary experimental programme has shown that predictions made using these models are in good agreement with measurements made on a perfectly conducting reflector corresponding to its far, near and very near field regions. Even though practical buildings used in the experimental programme have, on the whole, less idealised scattering surfaces than plane surfaces, the predictions of the very near field model generally agree with the measurement results in terms of their dependence of the scattering coefficient on angular and distance positions.

Conventionally, the far field prediction model can be used when the Rayleigh far field criterion ($r \geq 2(a\cos\theta_0)^2/\lambda$ and $r \geq 2(b\cos\phi_0)^2/\lambda$) is satisfied. In fact, the scattering behaviour in far field regions does not change in terms of the angular and distance dependence of the scattering coefficients even if the receiver-building distance is as short as half that given by the Rayleigh far field criterion. Therefore, the far field prediction model can be used at receiver-building distances corresponding to $R_a > 0.5$ and $R_e > 0.5$, where R_a and R_e are the normalised receiver-building distances defined in section 6.2.3 (R_a is the receiver-building distances expressed in units of $2(a\cos\theta_0)^2/\lambda$ where θ_0 is the incident azimuth angle and a is the building width. Similarly R_e is the distance expressed as in units of $2(b\cos\phi_0)^2/\lambda$ where ϕ_0 is the incident elevation angle and b is the building height).

When the receiver-building distance is less than half of the far field distance of a building, the near and very near field prediction models have to be used. In the comparisons of the two prediction models in sections 3.6.5 and 3.6.6, it is shown that the near field model starts to show significant errors of shifted patterns when the ratio of surface dimensions to the receiver-building distance increases to be larger than 0.1. The very near field prediction model is seen to be accurate for receiver-building distances larger than the ratio of 0.1. Since the very near field model is exact as far as the scattering patterns are concerned, it should be generally used. However, none of these two models should be regarded as suitable for use infinitely close to building surfaces. This however amounts to a somewhat trivial problem since, if the receiver-building distance is so small as to make approximations of the very near field model invalid then it is almost certain that scattering levels close to that resulting from a specular reflection will be encountered.

Generally speaking, the very near field prediction model is also valid in the far and near field regions and the near field model is also valid in the far field region. However, the far field prediction model is given explicitly as an analytical expression rather than in a form suitable for numerical computations so that it is definitely a quicker and simpler solution than the other two. The near field prediction model has the form of the Fresnel integrals which can be

expanded to give the angular and distance dependence functions of the scattering coefficient. The results of the derivations obtained can be used to form the salient parts of an engineering prediction model which has been demonstrated to be valid not only in the near field region but in the very near field region as well.

Using the prediction models to calculate the scattering coefficient necessitates computer programming, particularly for integrating numerically the field equations of the near and very near field models. The programmes of the prediction models are suitable and useful for calculating the scattering coefficient whilst varying by increment either the azimuth angle or distance to enable scattering pattern plots for buildings to be obtained. A calculation at a single point which may be located in a null, particularly in non-specular regions, can be meaningless in practice and should be avoided.

7.3 A simplified engineering model

In predicting the scattering coefficients of buildings, the prediction models, particularly for the near and very near field models, can be used in their fully developed forms programmed for numerical integration. However, it is possible that these prediction models may be too time consuming to implement where rapid approximate estimations of the interference caused by a particular building are required.

In chapter 3, the angular and distance dependence functions of the scattering coefficient predicted using the prediction models have been approximately formulated from the expansions of the Fresnel integrals. There are good agreements between the prediction models and these simple angle and distance dependences equations. Later on in the experimental programme, the angular and distance dependences shown by the predictions are confirmed by the measurements. Based on these analyses, it is useful to summarise these equations to form the basis for a simplified engineering model.

From equation 3.56, the scattering coefficient given by separated azimuth and elevation patterns can be presented logarithmically as consisting of five separable factors, independent of each other as follows

$$S(dB) = S_p + S_a + S_{ar} + S_e + S_{er} \qquad 7.1$$

where

S_p: polarisation factor (dB)

S_a: azimuth angular dependence factor (dB)

S_{ar}: azimuth range dependence factor (dB)

S_e: elevation angular dependence factor (dB)

S_{er}: elevation range dependence factor (dB)

The polarisation factor is determined by scattering and incident angles and has been given for vertical and horizontal polarisations by equations 2.43 and 3.2 respectively. The azimuth angular and range dependence determine an azimuth scattering pattern with respect to receiver-building distance, azimuth angle and building width. The elevation angular and range dependence determine an elevation scattering pattern with respect to receiver-building distance, elevation angle and building height. Otherwise, the characteristics of both azimuth and elevation scattering patterns are principally identical.

The angular and distance dependence factors have different characteristics in different angular regions and different ranges. These characteristics of scattering coefficients are classified by the beamwidth of a scattering pattern and the normalised receiver-building distance of a building surface.

The 6 dB beamwidth point is an important parameter which can be used to illustrate the two distinct characteristics of the angular dependence of the scattering coefficient. The scattering coefficient in a region lying within the beamwidth is not significantly angular dependent so that

$$S_a = 0 \qquad -\theta_0 + \frac{BW_a}{2} \geq \theta \geq -\theta_0 - \frac{BW_a}{2} \tag{7.2}$$

$$S_e = 0 \qquad -\phi_0 + \frac{BW_e}{2} \geq \phi \geq -\phi_0 - \frac{BW_e}{2} \tag{7.3}$$

where BW_a and BW_b are the 6 dB azimuth and elevation beamwidths. The scattering coefficient in regions outside the beamwidth are angular dependent as shown

$$S_a = 10\log\left\{\frac{1}{\left[\sin\left(\theta \mp \frac{BW_a}{2}\right)\cos\phi + \sin\theta_0\cos\phi_0\right]^2}\right\} \tag{7.4}$$

where the negative and positive signs in the denominator apply to the following conditions respectively

$\theta > -\theta_0 + \frac{BW_a}{2}$ for the negative sign

$\theta < -\theta_0 - \frac{BW_a}{2}$ for the positive sign

and

$$S_e = 10\log\left\{\frac{1}{\left[\sin\left(\phi \mp \frac{BW_e}{2}\right) + \sin\phi_0\right]^2}\right\} \tag{7.5}$$

where similarly

$\phi > -\phi_0 + \frac{BW_e}{2}$ for the negative sign

$\phi < -\phi_0 - \frac{BW_e}{2}$ for the positive sign

The characteristics of the beamwidth are determined by the normalised receiver-building distance. The critical value of the normalised distance when considering beamwidth is 0.1. When the normalised receiver-building distance is less than 0.1, the scattering coefficient is strongly specular in nature. The beamwidth of the scattering pattern is determined by the specular region as

$$BW_a = 2\sin^{-1}\frac{a\cos\theta_0}{2r} \qquad \text{in azimuth} \qquad 7.6$$

$$BW_e = 2\sin^{-1}\frac{b\cos\phi_0}{2r} \qquad \text{in elevation} \qquad 7.7$$

When the normalised distance is greater than 0.1, the beamwidth becomes constant for a building surface and independent from the receiver-building distance. It is given by

$$BW_a \approx 2\sin^{-1}\frac{\lambda}{0.96a\cos\theta_0} \qquad \text{in azimuth} \qquad 7.8$$

$$BW_e \approx 2\sin^{-1}\frac{\lambda}{0.96b\cos\phi_0} \qquad \text{in elevation} \qquad 7.9$$

The characteristic value of the normalised distance for the distance dependence factor of the scattering coefficient is 0.4. When the value is less than 0.4, there are two kinds of distance dependence in an angular range. In the specular region, the scattering coefficient is not significantly distance dependent so that

$$S_{ar} = 10\log\left(\frac{1}{\cos^2\theta}\right) \qquad 7.10$$

$$S_{er} = 10\log\left(\frac{1}{\cos^2\phi}\right) \qquad 7.11$$

In the non specular region, the scattering coefficient is always distance dependent. The distance dependence function is given by

$$S_{ar} = 10\log\left(\frac{\lambda}{2r\pi^2}\right) \qquad 7.12$$

$$S_{er} = 10\log\left(\frac{\lambda}{2r\pi^2}\right) \qquad 7.13$$

When the value is greater than 0.4, the distance dependence factors are coincident everywhere in an angular range and identically given in equation 7.12 and equation 7.13 with respect to azimuth and elevation respectively.

Clearly from the above, the scattering coefficient presented in terms of its angular and distance dependence functions is much simpler than the forms of the theoretical prediction models. Each of the simple equations can be evaluated using, for instance, a pocket calculator. Another advantage over the theoretical prediction models is that the model can be used for the calculation of scattering coefficient at specified receiver positions which in non specular regions yields results represented by the average values of the scattering coefficient graphs. This is particularly useful since this eliminates the rapid variations seen in those graphs and gives average values which are more useful in radio planning.

However in using these equations, there is complexity and this lies in appropriately classifying the scattering field regions in terms of the normalised receiver-building distance and beamwidth. For further clarification and to simplify application for the user, this engineering model is presented in the form of a flow chart for the evaluation of S_a, S_{ar}, S_e and S_{er} factors as seen in figures 7.1 to 7.4 respectively.

7.4 Procedure using the prediction models

When potentially harmful building scatter is causing concern in site shielding or more general situations of radio communications, the prediction procedure for evaluating interference to a radio system can be proposed for use by system planners and engineers, provided that:

(a) A scattering building surface concerned may be defined justifiably and geometrically in terms of a plane surface with specified dimensions. Where it is possible and necessary, the building surface should also be specified in terms of content of windows, surface features and deviations and surface roughness.

(b) The direction of the incident signal (interference) and the paths along which the signal could arrive at the radio terminal may be determined using ray tracing. Paths may have also to be considered where the signal could suffer double reflections, e.g. because of the existence of corner structures or two adjacent buildings.

According to the above, a set of primary data should be defined in a coordinate system (see section 2.4.1) which is conveniently placed so that the main building surface lies in the x-y plane and the centre of the building surface is at the origin.

7.4.1 Primary data

a: building width

b: building height

θ_0: incident azimuth angle

ϕ_0: incident elevation angle

r_0: transmitter-building distance

θ: scattering azimuth angle

ϕ: scattering elevation angle

r: receiver-building distance

These geometrical parameters can be derived from Ordnance Survey maps and on-site surveys. The prediction models described require only this primary data plus, of course, the frequency of the radiowaves. The scattering coefficient at the radio terminal can be confidently estimated using either the very near field model or the engineering model. If the receiver-

building distance r is greater than $(a\cos\theta_0)^2/\lambda$ and $(b\cos\phi_0)^2/\lambda$ then the far field model may be used with confidence. If r does not meet the above requirement, but is greater than the larger of the dimensions 10a or 10b, then the near field model is more appropriate. For smaller values of r, the very near field model should be used.

It is possible to use the engineering model without the programme. This requires a secondary data list to be generated in addition to the primary data. This is given in the following section.

7.4.2 Secondary data

R_a: normalised receiver-building distance with regard to building width

R_e: normalised receiver-building distance with regard to building height

BW_a: beamwidth with regard to building width

BW_e: beamwidth with regard to building width

7.4.3 Practical refinements of the prediction models

The prediction models detailed in chapters 3 and 4 are based on idealised perfect reflectors. The models are valuable in deriving the scattering patterns as functions of radio path geometries and building dimensions. For more appropriate and accurate predictions, further refinements to these models should be made based on practical considerations.

7.4.3.1 Reflection loss coefficients

In the specular region of a scattering building, the receiving radio terminal will be subject to significantly high interference as indicated by the prediction models. Concerning practical buildings, the reflection loss coefficients of scattering surfaces should be considered to make more accurate estimations of the scattering coefficients in the specular regions.

Reflection loss coefficient is defined according to building surface conditions and is affected by material, moisture content, incident angles and polarisations. The formulations are given in equations 6.8 and 6.9 for both vertical and horizontal polarisations respectively. There are also reflection loss coefficient measurements of several typical building surface materials available in figures 6.5 to 6.11. These are typically in the range of 5 to 15 dB.

There is an extra term added onto the Fresnel reflection coefficient (see equation 6.11) which is used to determine the reflection loss coefficients of surfaces with surface roughness, such as pebble-dash cladding surfaces. A Rayleigh parameter given in equation 6.10 is defined by the standard deviation of irregular heights of the surface concerned. This has to be estimated by a significant number of detailed measurements on the building surface.

7.4.3.2 Background scatter

In the non specular region of scattering buildings, the receiving radio terminal is relatively safer from interference as small scattering coefficient values are given by the prediction models. However in reality, the scattering signal levels would be much higher than the predictions due to other scattering objects near the scattering building concerned. The scattering coefficients in these regions are mainly dominated by background scatter. Generally speaking in urban environments, the scattering coefficient from illuminated regions would be about 25 to 35 dB lower than values arising in specular regions. The level of background scatter may be considerably higher in situations where a rectangular street layout is oriented such that many background buildings form a new specular geometry.

7.4.3.3 Building structural features

Extensions to prediction models of plane surfaces enable the effects of windows, surface roughness and structural features to be considered in the prediction procedure. Modification

to account for building features of windows, surface deviations and structural features can be implemented using the analysis in chapter 4.

Some major effects of building features can be qualitatively estimated based on the predictions of plane surfaces. In involving building features, the potential procedure users may have to anticipate the following effects on the scattering patterns of plane surfaces

i) scattering signal levels, direction and width of the specular regions will be changed when offset or oblique planes are involved;

ii) secondary specular regions manifesting themselves as strong backscatter might appear when protruding, recessed and corner features are involved;

iii) deep nulls and sharp ridges might be seen in the specular region due to windows, rough surfaces and features mentioned in (ii);

iv) the beamwidths of scattering patterns can be widened if a large number of planes such as windows, balconies and wall sections are involved;

v) the scattering signal levels just outside the predicted specular regions can be raised by the presence of building features, but most significantly by surface deviations.

7.5 Improvement to building scatter predictions of the CCIR reports

From the viewpoint of interference predictions, the requirements to prediction procedures are that system planners and engineers can follow certain instructions and implement steps which can lead them to a reasonably accurate assessment of interference problems, caused by building scatter in planning and designing their radio systems. It is essential that predictions given by any prediction procedure are accurate with regard to regions where relatively high interference is most likely to occur enabling planners to devise suitable solutions. When the radio terminals have to be in such regions under certain circumstances, prediction procedures should provide the necessary tools in planning the links. From the predicted and measured results reported in earlier chapters, the behaviour of building scatter has been demonstrated as a function of angular and distance position of the receiver relative to the scattering building

surface. The significance of distance dependence is not only with respect to the amplitudes of scattering coefficient but in determining the scattering patterns as well. In urban environments where the scattering problems of the near and very near fields of buildings are mostly encountered, the scattering pattern beamwidths of buildings are strongly distance dependent. This pinpoints the difficulties of the preliminary recommendations (building scatter predictions) of CCIR reports in which the distance dependence of scatter patterns was not considered. There is clearly a need to improve building scatter predictions.

The prediction procedures described in this chapter are the final outcome of building scatter studies carried out in the project. This responded to CCIR (ITU-R) requirements. Building scatter predictions given in chapter 6 are the results, validated experimentally, of computations and simulations using the very near field models. There are good agreements of scattering characteristics between the predicted and measured results obtained from practical buildings in typical urban environments. To further demonstrate the value and usefulness of the procedures, building scatter predictions obtained using the engineering model are shown in figures 7.5 to 7.18 against building scatter measurements described in chapter 5. It can be seen from comparisons between the predictions and measurements that there are close agreements in the scattering characteristics. Advantageously, the engineering model is also relatively simple and is capable of predicting explicitly the angular and distance dependence of the scattering coefficient.

However, the prediction curves only show the scattering patterns of perfectly conducting reflectors. For more accurate predictions, important amendments have to be considered. In the specular regions, the estimations of the scattering coefficient must take into account the reflection loss coefficients of building surface materials. In the non specular regions, the levels of background scatter would come into force. In urban environments, background scatter would be typically in the range of -25 to -40 dB relative to the incident signal level. It is difficult in practice to judge whether building surfaces, nominally assumed to be plane, have surface deviations which have been modelled as narrower panels arranged randomly (see

section 4.8). The effects of this, which are seen as beamwidth broadening and scattering coefficients attaining high values in non specular regions should not be underestimated. Therefore, users of the building scatter prediction procedures are strongly recommended to account for this particularly in regions just outside the specular region where higher interference levels may be experienced.

In comparison with building scatter measurements and predictions recommended in CCIR reports, building scatter predictions were also produced using the prediction procedure based on the engineering model for buildings used by Bramley and Cherry [1973].

These well known measurements and predictions of the scattering coefficient have been shown in their original forms in figure 7.19 to 7.21 for the buildings Dagenham, Bracknell and Norwich. Measurements of the scattering coefficients were made for each of these buildings in the azimuth range using various values of receiver-building distances (in a range between 250 m to 1000 m) and plotted in one figure to present the scattering pattern of azimuth variations at 1000 m. It should be pointed out here that in constructing these measurement azimuth dependence curves by the authors, range normalisation with respect to the receiver-building distance of 1000 m, was assumed. The paper stated that this normalisation was conducted on the basis of distance dependence of $S \propto 1/r^2$ for Dagenham and Norwich and $S \propto 1/r$ for Bracknell. In carrying out the normalisation, the fact that the beamwidth is strongly distance dependent in the very near fields of the buildings (in these cases the normalised receiver-building distances is well within $R_a < 0.1$) was not considered. Some measurement points can actually change status from one of being inside a relatively wider beamwidth of the scattering pattern observed at a shorter distance (e.g. 300 m) to one outside a relative narrower beamwidth of the pattern observed at 1000 m though their azimuth angles are unchanged. As a result, the measurement azimuth dependence curves have effects of yielding patterns at 1000 m which are significantly wider than they actually are. The predicted azimuth variation curves (curve b in the figures) only show scattering characteristics of the far field, typically with constant beamwidths of the scattering patterns.

For each one of three buildings the prediction of the scattering pattern (at the shortest receiver-building distance) is given based on the geometry of the radio path using the prediction procedure described in this chapter (the engineering model). Figure 7.19 to 7.21 display predicted results superimposed on the Bramley and Cherry's results. Reflection loss coefficient is not considered due to lack of this information.

It is instructive to make the following observations:

(i) Predictions based on the engineering model procedure clearly show better agreement with the measurements in all the cases than those given by the CCIR procedure. It can be seen that these predictions are more adequate and useful corresponding to the scattering characteristics of the scattering patterns in the very near fields of these buildings.

(ii) The modification by raising the prediction curves, say by 10 dB, to consider the effects of surface deviation roughness discussed in section 4.8 could result in an even better agreement with measurements This suggests that a strong practical evidence exists for taking into account the effects of surface deviations.

The prediction procedure outlined in the flow chart shown in figure 7.1 to 7.4 has been shown to give more accurate predictions of building scatter than those of current CCIR procedures. Particularly, this is the case in near and very near field regions which are highly relevant in urban radiowave propagation.

7.6 Interim conclusion

The work presented in this chapter shows how prediction procedures may be used in estimating the interference of building scatter in urban environments. Prediction procedures are formulated, with well established approximations, from the Fresnel-Kirchhoff method. The prediction procedures require only the easily obtainable data relating to simple radio path

geometries and scattering surface properties. This allows the scattered fields to be rapidly predicted thus rendering the method suitable for use in radio system planning. From the cases of predictions and measurements reported in the project and CCIR reports, it is demonstrated that much needed improvement in building scatter predictions has been achieved, with a reasonable confidence, using the prediction procedures together with the practical refinements outlined in this chapter. Although it is primarily targeted at site shielding applications, the prediction procedures should also be useful in estimating building scatter signal strengths for other applications likely to arise in urban radiowave propagation.

In chapter 8, with the main objectives achieved, building scatter studies carried out and reported in this thesis are concluded.

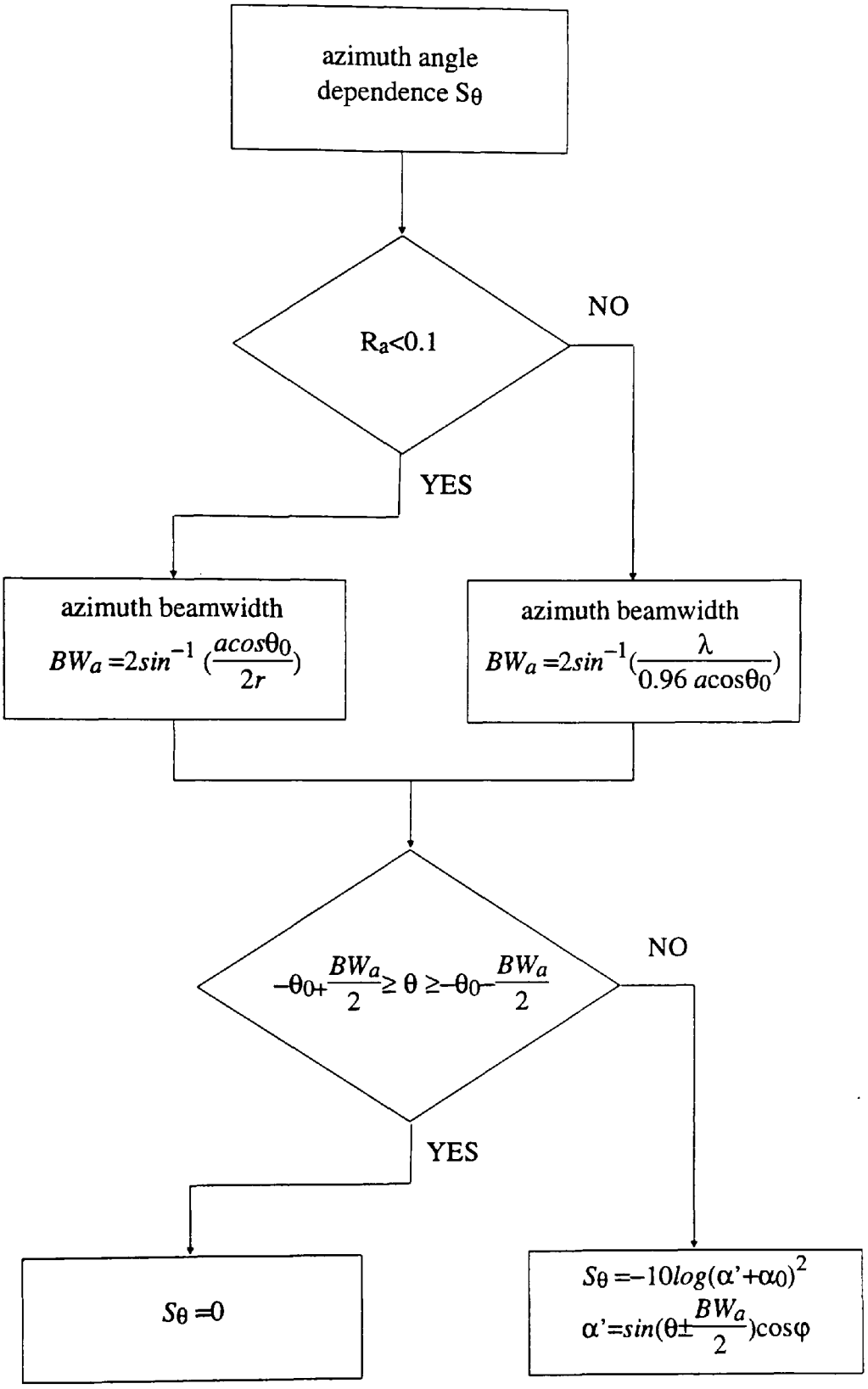

Figure 7.1 Flow chart of azimuth angle dependence Sθ.

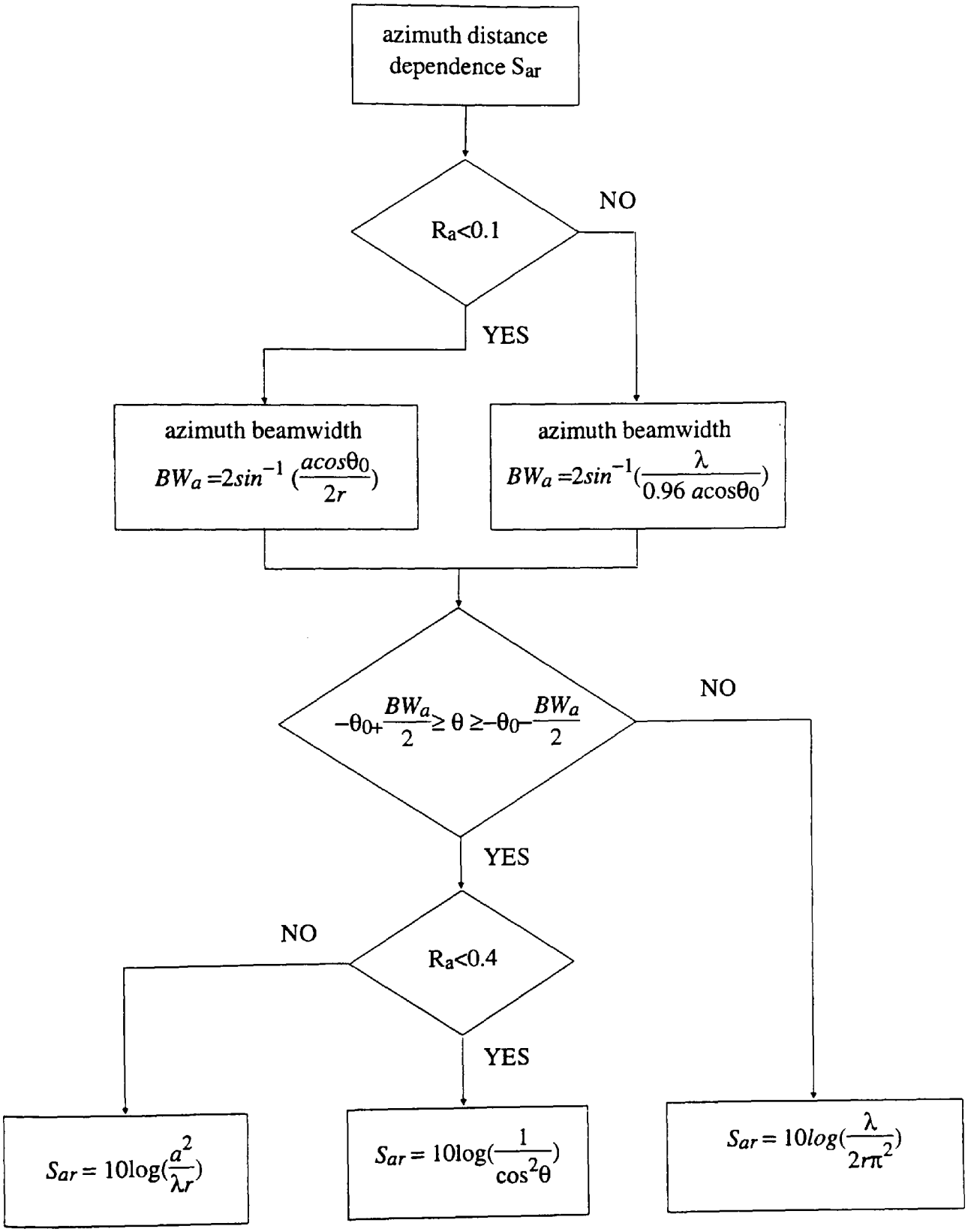

Figure 7.2 Flow chart of azimuth distance dependence S_{ar}.

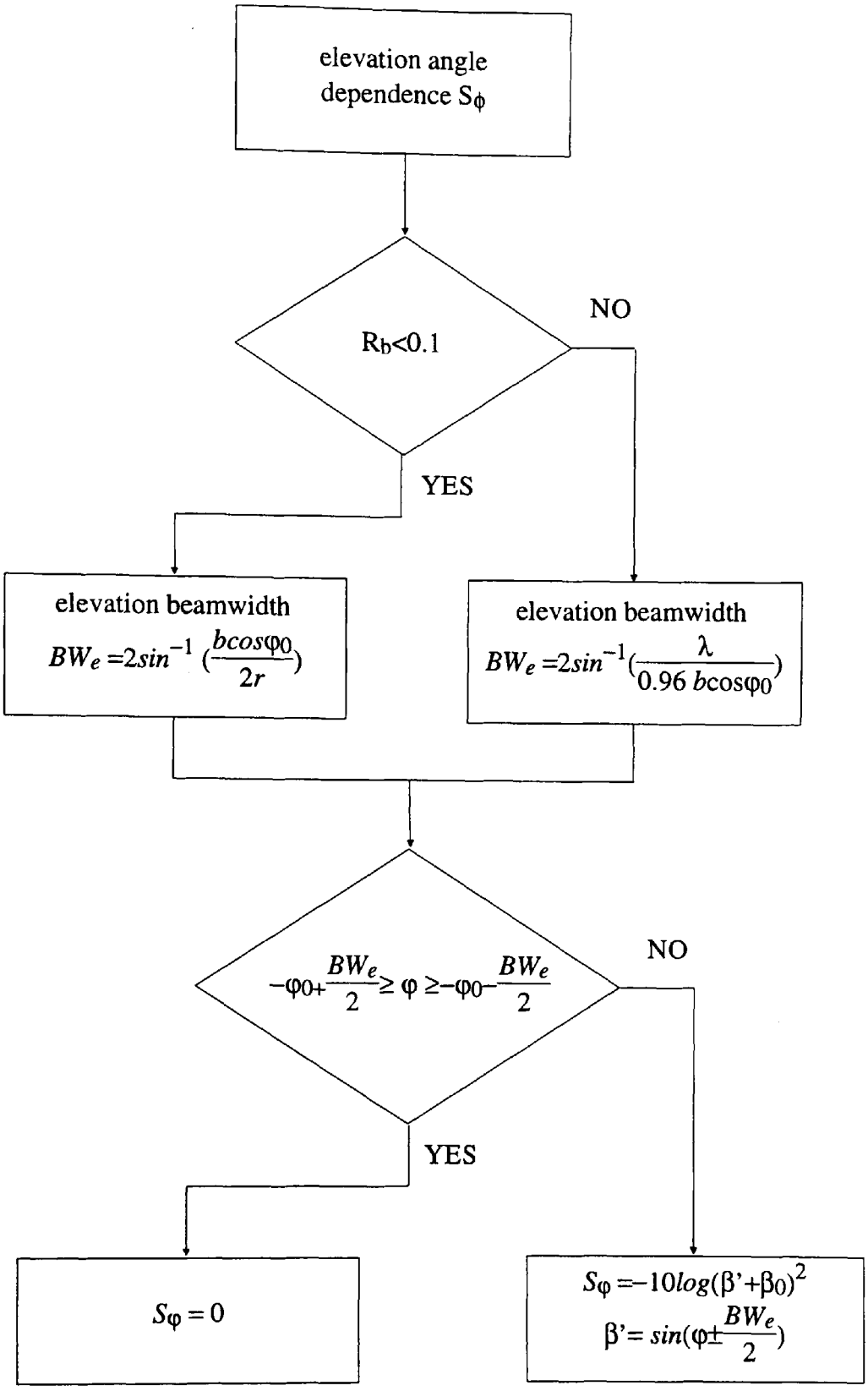

Figure 7.3 Flow chart of elevation angle dependence S_ϕ.

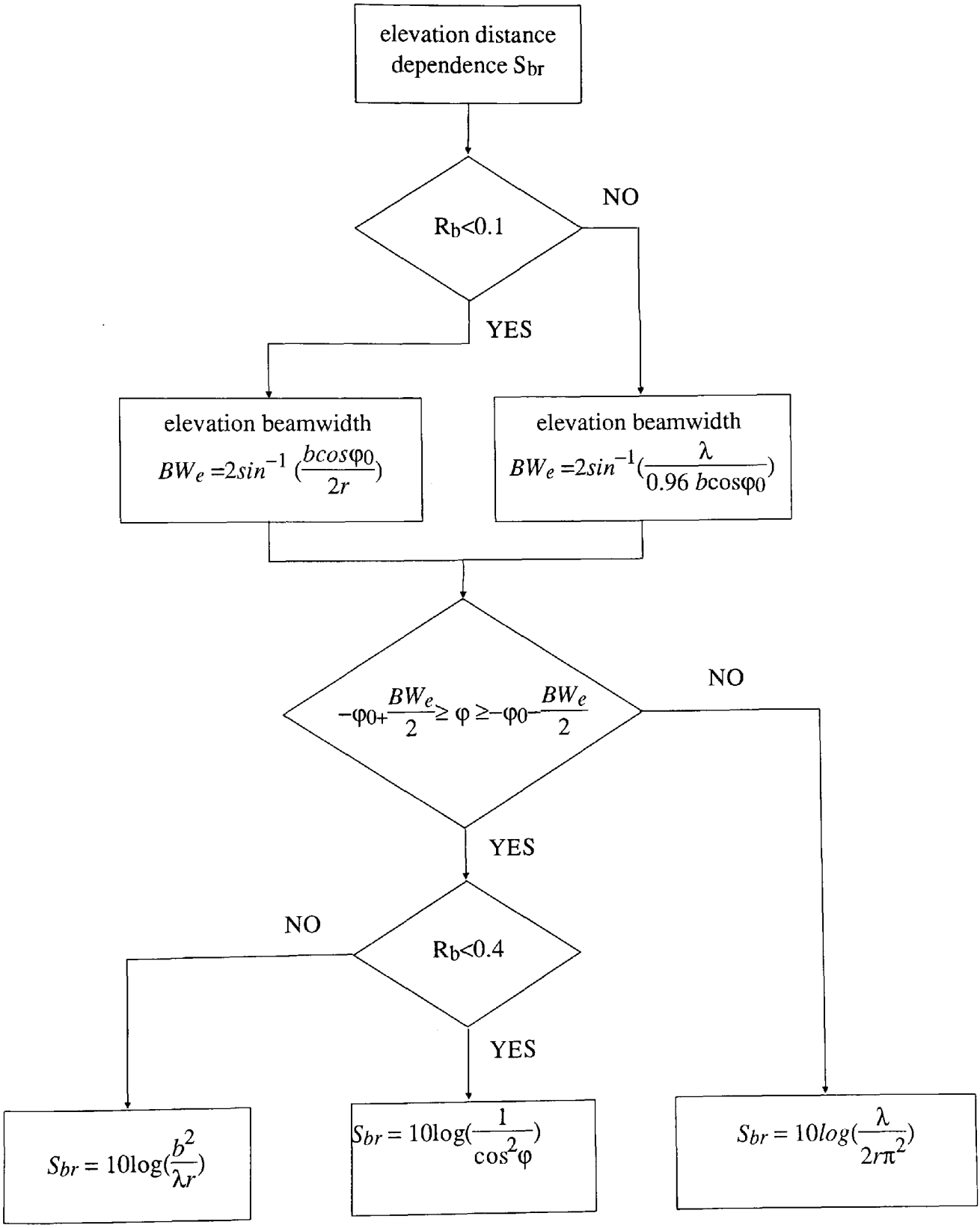

Figure 7.4 Flow chart of elevation distance dependence S_{br}.

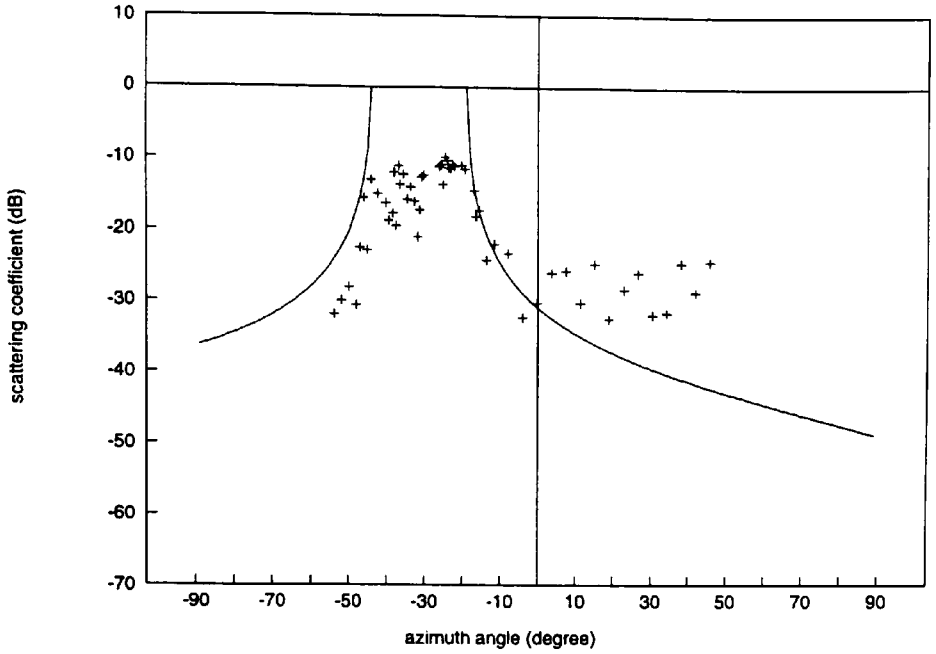

Figure 7.5 The predicted (using the engineering model) and measured results of the porter's house building, Sρ=-8 dB (brick surface).

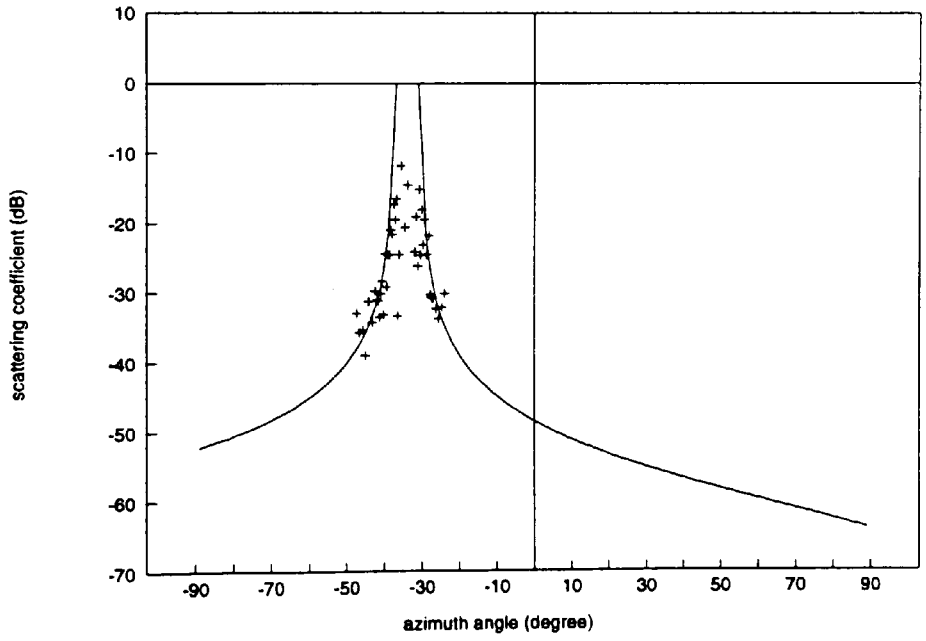

Figure 7.6 The predicted (using the engineering model) and measured results of the Butetown building, Sρ=-10 dB (for pebble-dash surface).

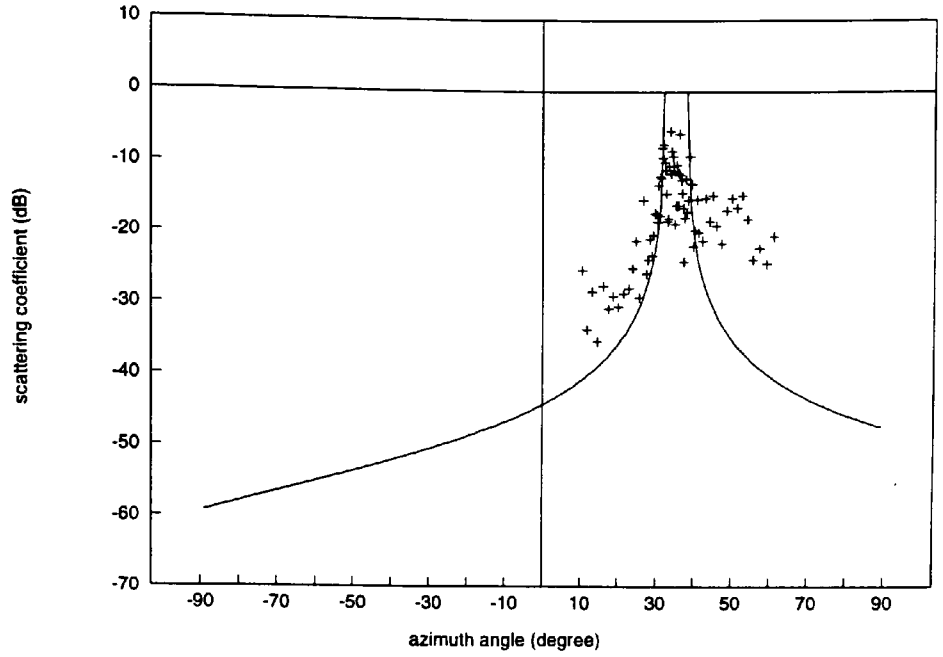

Figure 7.7 The predicted (using the engineering model) and measured results of Ringland 1, Sρ=-5 dB (for concrete surface).

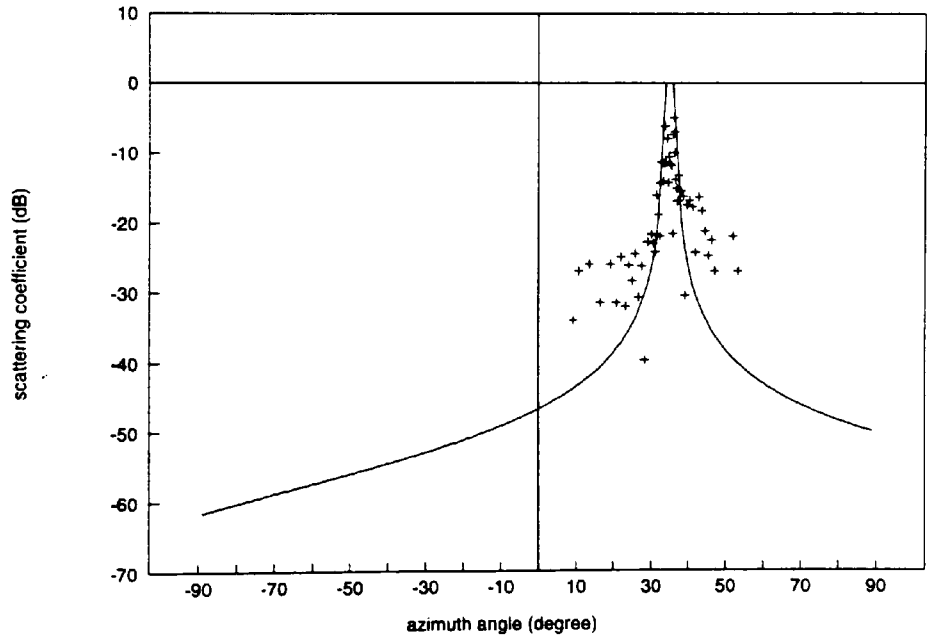

Figure 7.8 The predicted (using the engineering model) and measured results of Ringland 2, Sρ=-5 dB (for concrete surface).

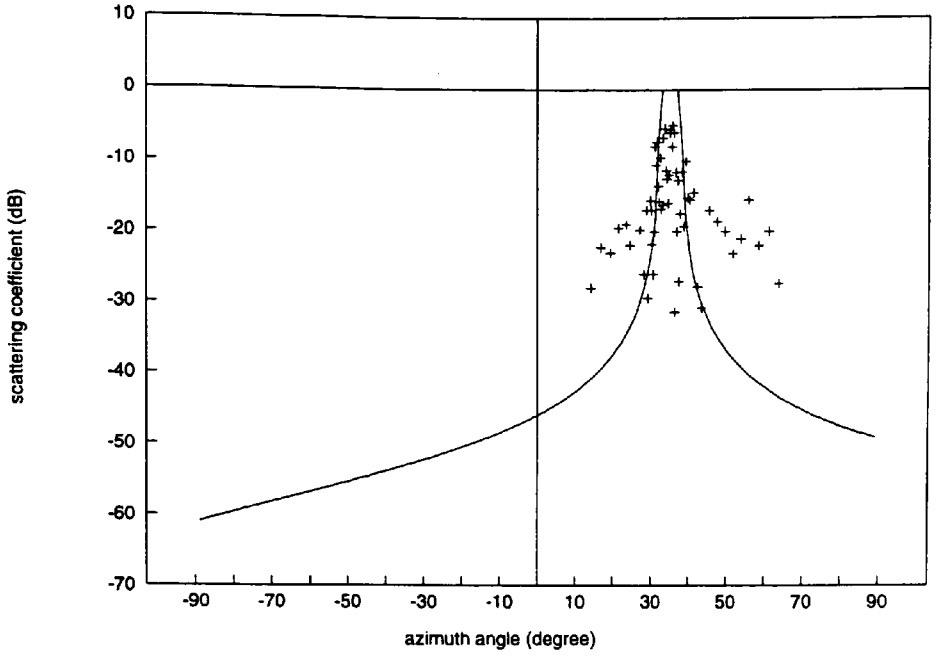

Figure 7.9 The predicted (using the engineering model) and measured results of Ringland 1, Sρ=-5 dB (concrete surface) on horizontal polarisation.

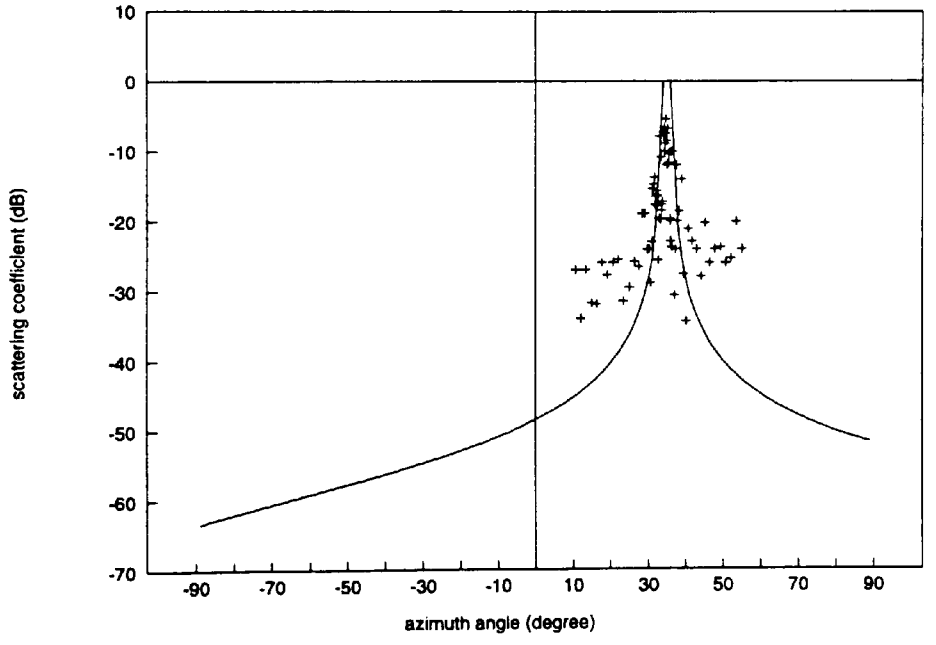

Figure 7.10 The predicted (using the engineering model) and measured results of Ringland 2, Sρ=-5 dB (concrete surface) on horizontal polarisation.

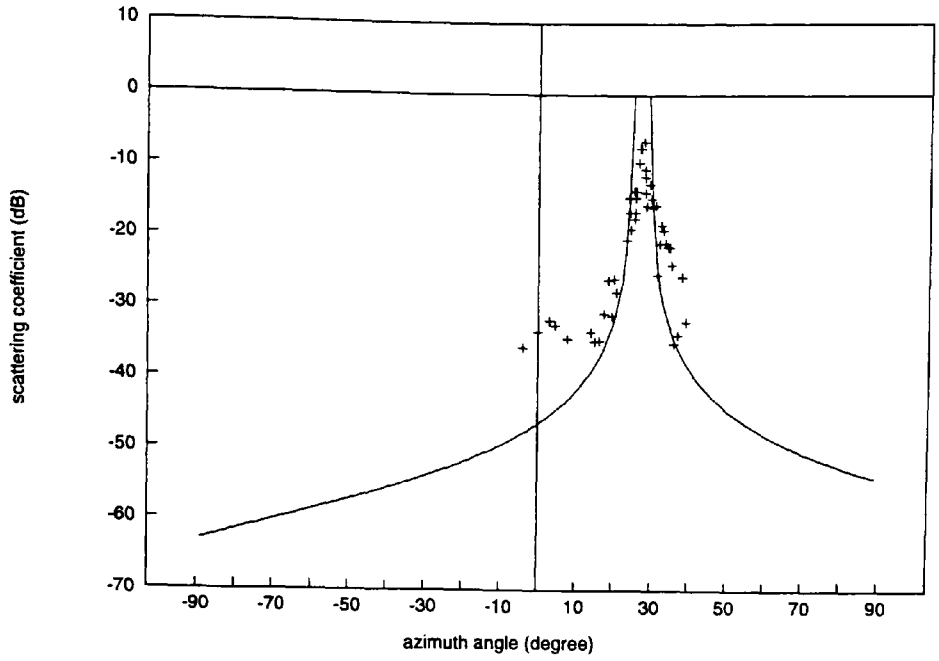

Figure 7.11 The predicted (using the engineering model) and measured results of St Julians 1, Sρ=-5 dB (concrete surface).

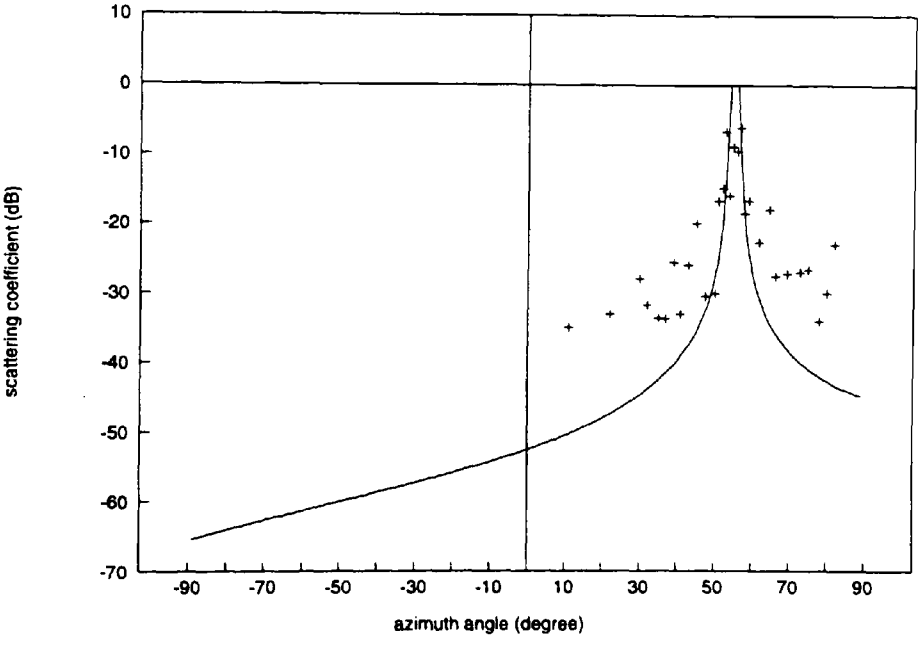

Figure 7.12 The predicted (using the engineering model) and measured results of St Julians 2 , Sρ=-4 dB (concrete surfacee).

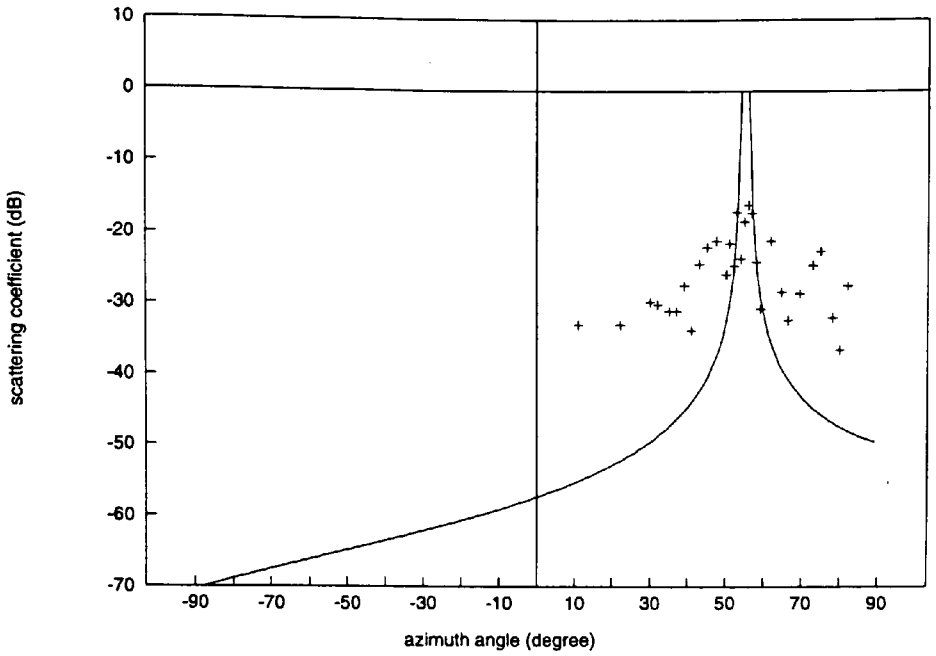

Figure 7.13 The predicted (using the engineering model) and measured results of St Julians 2, Sρ=-12 dB (concrete surface) on horizontal polarisation.

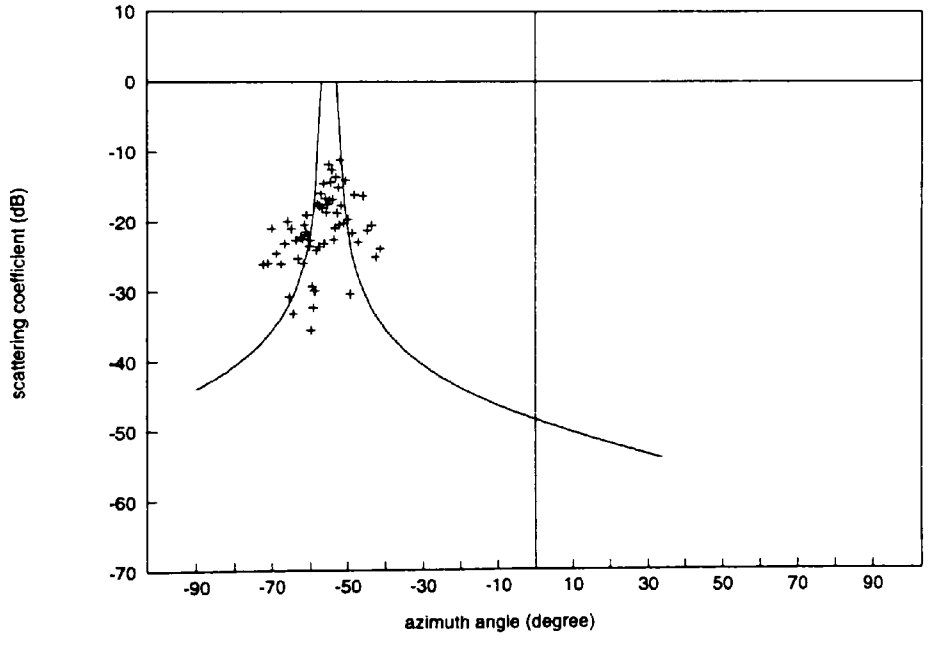

Figure 7.14 The predicted (using the engineering model) and measured results of the Merthyr Tydfil building, Sρ=-14 dB (pebble-dash surface, double reflections).

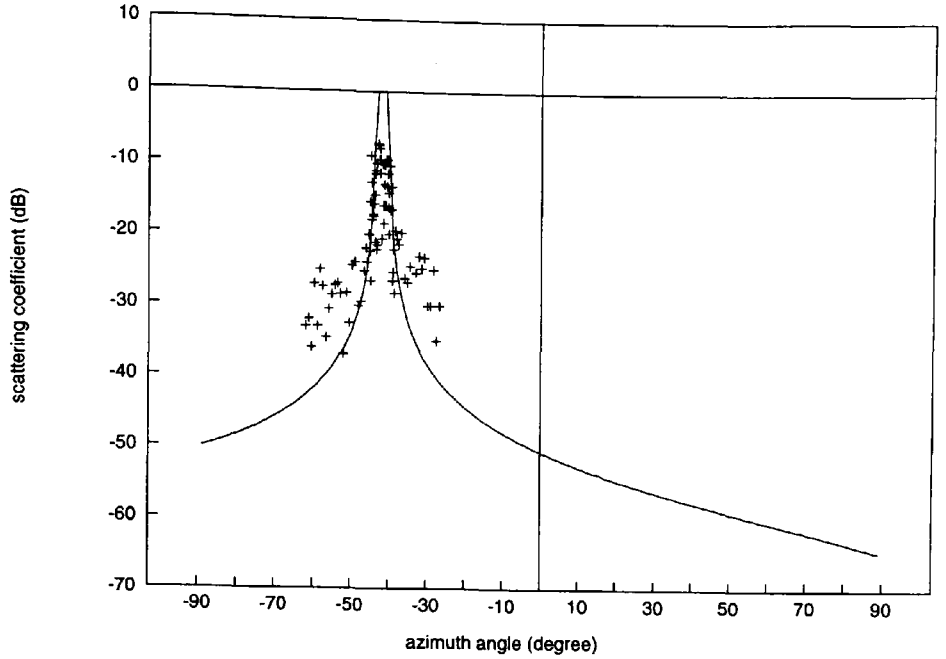

Figure 7.15 The predicted (using the engineering model) and measured results of Dudley 1, Sρ=-5 dB (concrete surface).

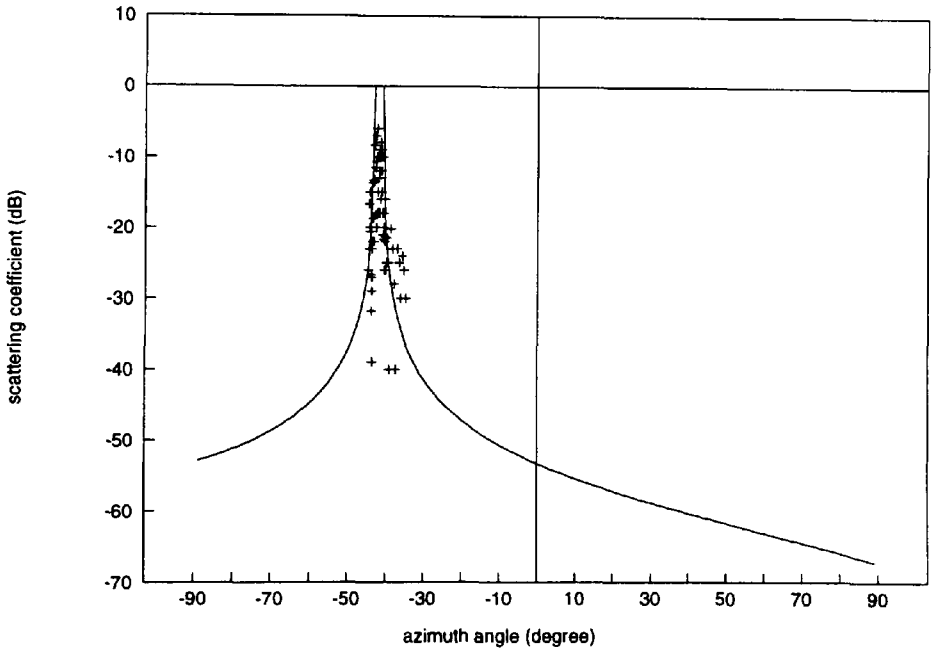

Figure 7.16 The predicted (using the engineering model) and measured results of Dudley 2, Sρ=-5 dB (concrete surface).

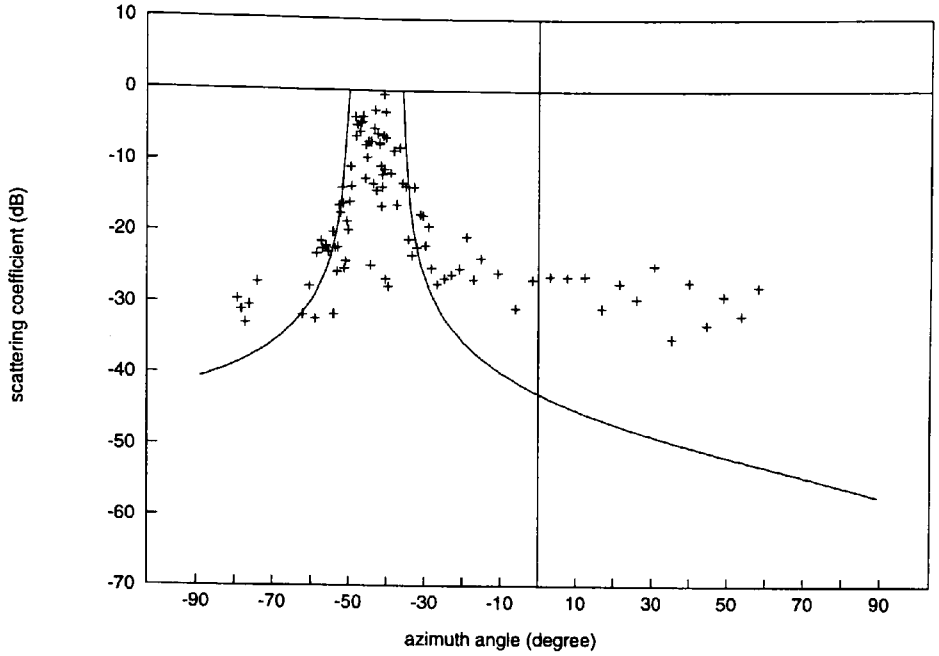

Figure 7.17 The predicted (using the engineering model) and measured results of Walsall 1, Sρ=-5 dB (concrete surface).

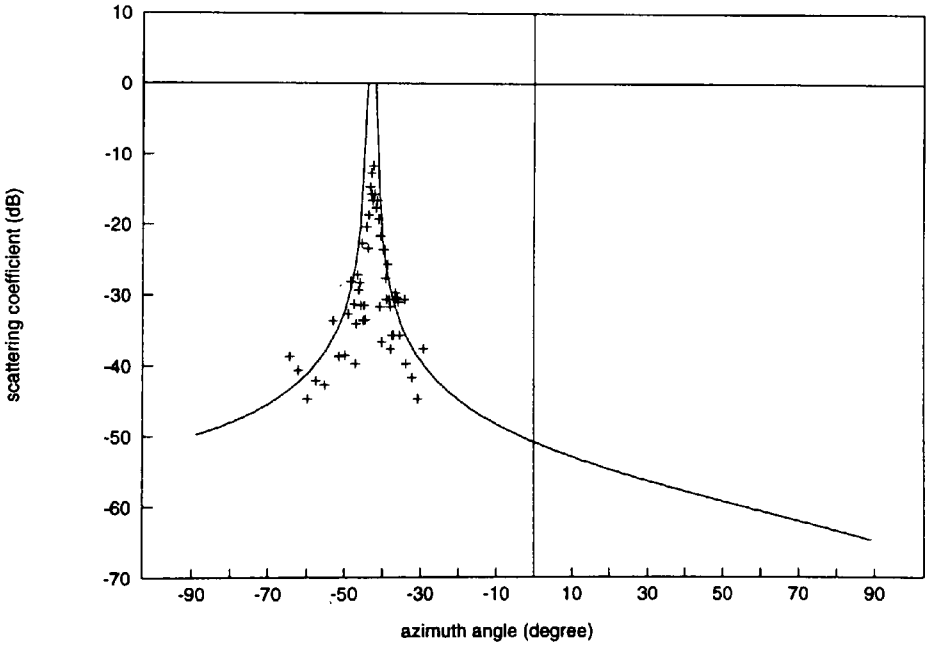

Figure 7.18 The predicted (using the engineering model) and measured results of Walsall 2, Sρ=-5 dB (concrete surface).

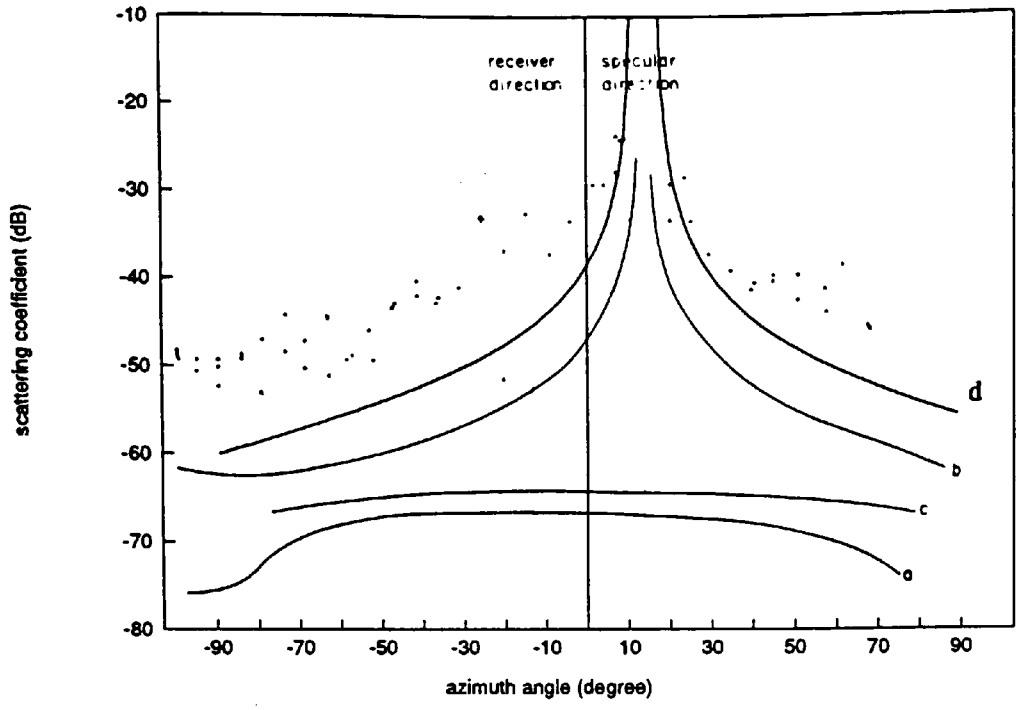

Figure 7.19 The predicted (curves a, b and c) and measured results of Dagenham in the CCIR reports [Bramley and Cherry (1973)], a=27 m, b=52 m, θ_0=-14 degrees and curve d (using the engineering model at r=250 m).

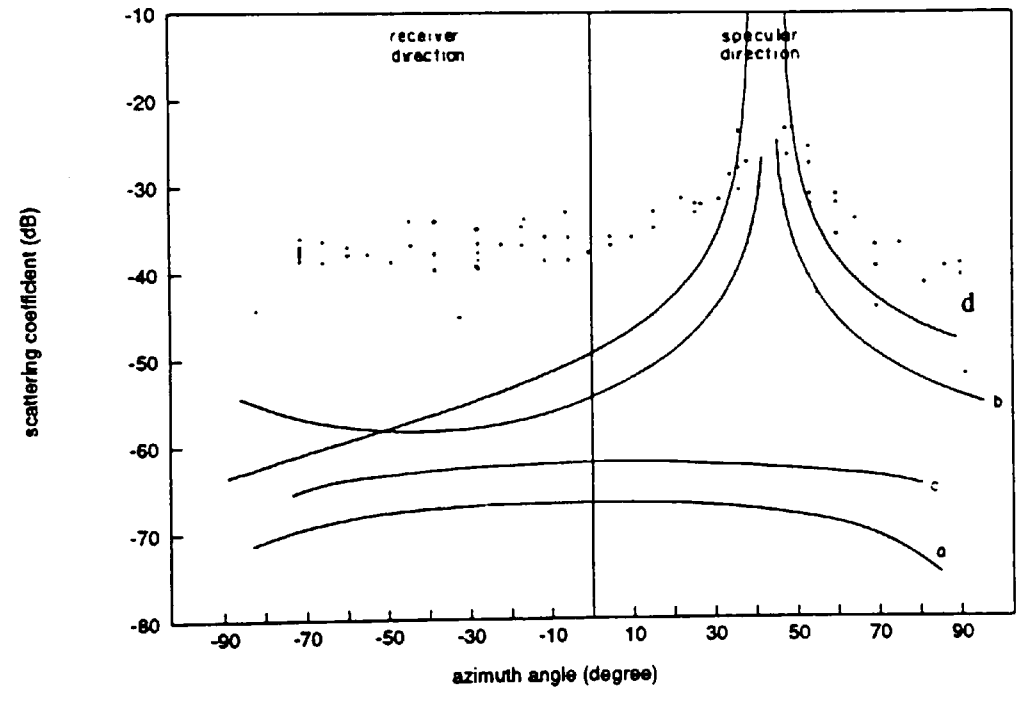

Figure 7.20 The predicted (curves a, b and c) and measured results of Bracknell in the CCIR reports [Bramley and Cherry (1973)], a=56.5 m, b=46 m, θ_0=-43 degrees and curve d (using the engineering model at r=300 m).

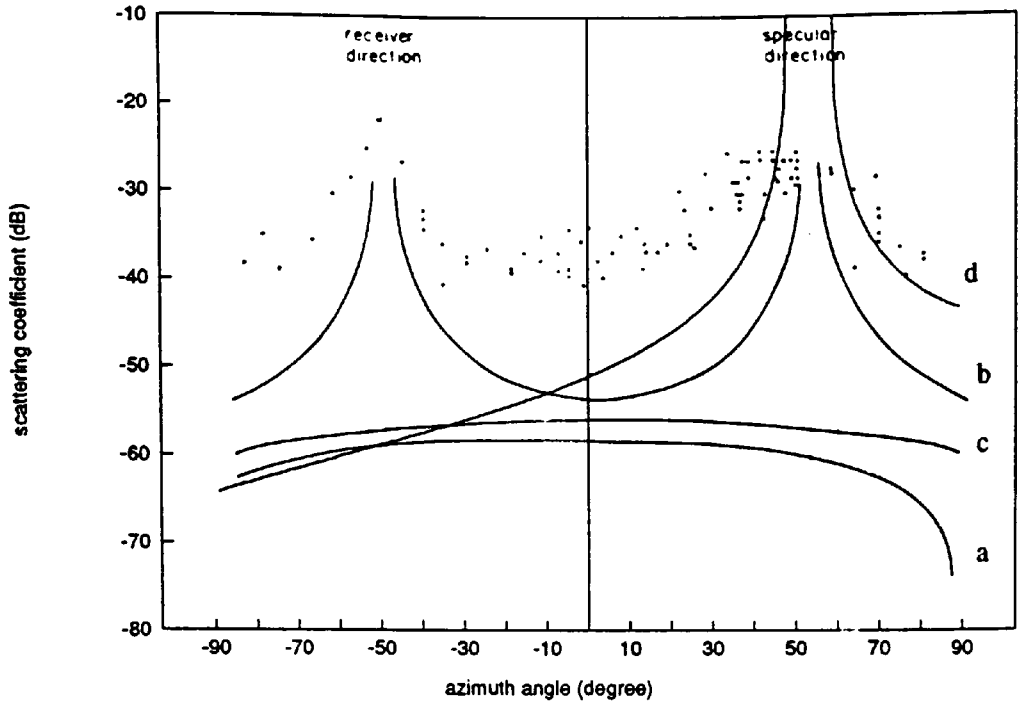

Figure 7.21 The predicted (curves a, b and c) and measured results of Norwich in the CCIR reports [Bramley and Cherry (1973)], a=76.5 m, b=44 m, θ_0=-53 degrees and curve d (using the engineering model at r=300 m).

CHAPTER 8 REVIEWS AND CONCLUSIONS

8.1 Review of the thesis

The recent growth in microwave frequency systems, particularly in urban areas has had the effect of making interference problems more likely and increasing the possibility of using site shielding to obstruct an interfering signal. In assessing the effect of site shielding in urban environments where multi-path interference is a distinct possibility, building scatter is regarded potentially as a most damaging source, along with vegetation scatter and terrain scatter. The work set out in this thesis is to provide the necessary tools so that system planners may assess the effect of building scatter interference on site shielding.

Such tools are required to provide practical guidance. This requirement however does not mean the diminution of analytical work since any worthwhile practical guidance must be based on appropriate theoretical foundation validated by suitable experiments. As well as "practical" any model, it is desired, must be easily applicable.

Significant progress was achieved with the preliminary experimental programme in which measurements were conducted to investigate the scattering characteristics of a perfectly conducting reflector. A great deal was learnt from this thorough investigation. It was realised that, although the assumptions of perfectly conducting and smooth planes were made, the most significant factors in determining the scattering characteristics were the dimensions of buildings, receiver-building distance and the microwave frequency used. The fact that scattering buildings are very large relative to the wavelength of the transmission used and that radio terminals are likely to be confined in urban areas, imply receiver-building distances of a few hundred or thousand metres, are only one hundredth or even one thousandth of their Rayleigh far field distances ($2a^2\cos^2\theta_0/\lambda$ or $2b^2\cos^2\phi_0/\lambda$). Therefore, scattering field solutions in the near and very near fields of the building surfaces became necessary.

The Fresnel-Kirchhoff diffraction theory was chosen to provide these solutions. The ability of mathematically expressing radiation fields in the method of approximated physical optics was exploited. Along the line, the well established field solutions of the far field aperture antenna model and the Fresnel integrals were tested to their limits in the near and very near fields. Significant errors occurred in the models in such difficult and unusual situations. In order to conduct theoretical and experimental investigations with sufficient confidence and integrity, a solid and reliable theoretical foundation was much needed. To this end, an "exact solution", where "exact" refers to expressions for the path differences, was implemented using the principle of the Fresnel-Kirchhoff method. It is accurate and extremely valuable as the scattering characteristics of the reflector could be accurately assessed in the very near field, but rather inappropriate for large surfaces (of typical building dimensions) simply because the computations would presently take too long to perform. This is overcome by an approximation to the exact solution, known as the "very near field model". The very near field model is demonstrated to be exact in two-dimensions and was used to produce an exact radiation pattern with limited errors in amplitude in three-dimensions. Significantly, the time needed for computations reduced to that amount required for numerical evaluations of the Fresnel integrals.

With "ease of applicability" in mind, theoretical models were analysed to mathematically summarise the scattering characteristics in terms of angular and distance dependence functions of the scattering coefficient. The Fresnel integral expansions proved suitable for this purpose and the representation of the scattering characteristics were again focused on the different field regions. In the near and very near fields, the beamwidths of scattering patterns were strongly distance dependent. This characteristic had to be reflected in any suitable mathematical formulation. The approximated expansion was considered to be more accurate than that recommended in relevant CCIR reports. Further approximations introduced the beamwidths into the expression. Although it was not mathematically rigorous and might seem to be a little arbitrary, the resulting formulations closely described the scattering characteristics not only in the near field but in the very near field region as well.

After prediction models were developed, the scope of the theoretical studies was extended to investigate the possible effects of building surface features. The effort made was intended to model some typical building features and gain knowledge about their effects on scattering behaviour in order to develop the models to include such effects.

For a subject as practical as building scatter, measurements from real buildings were seen as absolutely essential for the experimental investigation and the validation of the theoretical models. An intensive measurement campaign was carried out using seven buildings in typical urban environments. The measurement campaign was helped a great deal by the preliminary experimental programme and the theoretical analyses. Measurements of scattered signals from these buildings were made carefully in well chosen and controlled measurement environments (with variation of only one parameter at a time). This is in contrast to most of the available building scatter measurements reported in the literature which often involved the effects of several simultaneous parameter variations. The key scattering characteristics of these buildings used in the measurements are described by the angular and distance dependence functions of the scattering coefficient.

Each set of measurements were compared both with prediction and with other measurement sets. Although the scattering patterns varied from building to building, general scattering characteristics of plane surfaces in terms of the azimuth variations and range dependence of the scattering coefficient have been demonstrated. It is thus concluded that the main contribution of building scatter is made by plane surfaces. Using the normalised receiver-building distance (with respect to the Rayleigh far field distance), has allowed the distance dependence of the beamwidth and scattering coefficient to be uniformly characterised with identical characteristic values of the normalised receiver-building distance for buildings of any size. Meanwhile, to assist in interpreting the measured results and verifying the predicted cases, the reflection loss coefficients of several building surface materials were measured as well as their respective Fresnel reflection coefficients. The effects of building surface features were discussed and characterised using the predicted and measured results. At this stage,

sufficient confidence had been gained in the theoretical and experimental investigations undertaken. Finally, the project was directed to achieve its main objective of incorporating the results into prediction procedures aimed at extending those recommended by the CCIR. To assess building scatter interference in urban environments, prediction procedures are proposed for use by radio system planners. These procedures include the full theoretical prediction models and a simplified engineering model requiring readily obtainable data of path geometries of incidence and scattering and building surface data.

8.2 Conclusions

The main contributions from the work reported in this thesis to the subject are summarised in the following sections

8.2.1 Contribution to theoretical models

Reviewing available models led to the adoption of Fresnel-Kirchhoff methods in order to predict scattered field strength. These were chosen in preference to GTD methods because they provide a clear physical insight into the scattering process of buildings. Such ability is essential for radio terminals operating at microwave frequencies located in urban environments. Additionally, large building surface dimensions relative to the wavelength and the use of the Fresnel-Kirchhoff methods have not resulted in prohibitively complicated problems due to the relatively straightforward path geometries considered.

Initially the standard results of the Fresnel-Kirchhoff methods were changed to be presented in a coordinate system which consists of azimuth and elevation angles conventionally used in radio propagation. The methods in the far and near field were analysed. The author acknowledges that these models have been known for some time. The far and near field models were used in the large aperture antenna analyses by Clark [1980] and Jull [1983]. Bramley and Cherry [1973] developed the prediction model for building scatter which may

also be interpreted as the near field model but which was further improved to be suitable for oblique incidence and was recommended by the CCIR.

This thesis has extended these models by evaluating their relevance to scattering from real buildings in urban environments at microwave frequencies. At microwave frequencies, and with typical building dimensions, the receiver-building distances arising in urban environments are often only of the order of one hundredth or even one thousandth of the Rayleigh far field distances of buildings, namely in the very near field. As an approximated physical optics solution, the scattering field strength at a field point is considered in the Fresnel-Kirchhoff methods as phasor contributions from the scattering surface. The far and near field models are obtained by making suitable approximations of the differences between the ray paths from the surface to the point. The far field model has linear path differences assuming parallel ray paths. The near field models have additional quadratic terms. The Bramley and Cherry's near field model is more suitable compared to that of Jull for oblique incidence because of the cosine of the observer angle in the quadratic terms. The validity of these models was examined in the light of the preliminary experimental programme. Later analyses suggested that the far field model is valid in the field range described by the normalised distance $R_a > 0.5$ where the far field scattering characteristics have constant beamwidths and identical distance dependence of $1/r^2$ in the scattering patterns. The use of the near field model becomes necessary in the field range $R_a < 0.5$ where the scattering coefficients within the beamwidth vary rapidly in amplitude by a few decibels around a constant level (which would be the incident signal levels if the surfaces were perfectly conducting planes). The beamwidths of the patterns retain a constant behaviour until R_a reduces to 0.1. In the very near field range ($R_a < 0.1$), the beamwidths quickly become directly related to the width of the specular regions. The Bramley and Cherry's near field model can be considered valid for a small distance into this field range. As the receiver-building distance reduces further, the near field models become less valid due to the significant errors of "shifted" scattering patterns with respect to the specular regions which may be highly significant from an interference prediction viewpoint. In the very near field range, it was decided at an early stage in the investigation that, a more accurate

prediction model was needed. To improve the accuracy of the calculation of the scattering field strength, ray path differences have to be expressed more accurately in the analytical Fresnel-Kirchhoff methods. This led to the field solution with the exact path differences in the phase term and yielded the necessary accuracy for predictions in the very near field. However also because of this precision and the resulting complexity, calculations of the scattering field strength were found too long to perform that it could be considered practically useless when making predictions for real buildings. Considering both the accuracy and practical requirements, path differences were approximated as the sum of two exact path difference terms in two-dimensions. Analyses showed that this approximation is more accurate than all near field approximations. Most significantly since it is exact in two-dimensions, the predictions are shown to be virtually exact as far as the scattering patterns arising in practice are concerned. Using this model referred to as the very near field model, there is no shift in scattering patterns encountered with use of the near field models in the very near field regions. Errors are expected in amplitude but are constrained within a few decibels. The field solution with this approximation, namely the very near field model, makes accurate analyses and predictions of building scatter practically possible in typical urban environments.

An important further extension is the use of the very near field model to analyse the effects of building features. Typical building features are modelled using aperture analyses. The simulations reveal that the significant effects on the scattering patterns are manifest as double reflections, coherent effects sometime resulting in nulls within the specular region and broadened beamwidths.

Dependence of the scattering coefficient on angle and distance derived from the expansions of the Fresnel integrals were recommended in the CCIR reports. The angular dependence given is only suitable in the far field with regard to the constant beamwidths of the scattering patterns. To make the results also useful in the near and very near fields, the derivation is revised using more accurate approximations to introduce the beamwidths in the near and very near fields characteristics. These new results are used finally to develop an engineering model

which is valid in the far, near and very near fields.

8.2.2 Contribution to measured data

The experimental work undertaken, and reported in this thesis, used exactly the type of scattering obstacle for which the theoretical models were intended, namely buildings of typical dimensions. Measurements of scattered signal strengths from a perfectly conducting reflector and real buildings were carefully and strictly conducted in configurations of azimuth and distance scans in realistic environments. This led to reliable results being obtained in the near and very near fields. The results have been used to assess the validity of the theoretical models. The measurements of reflection loss coefficients of typical building surface materials formed the important data needed for practical predictions including the use of Fresnel reflection coefficients. Measurement data obtained in the course of this investigation has considerably added to the volume of measured results currently available, particularly at microwave frequencies.

8.2.3 Contribution to the published literature

During the period of the research, details of significant developments that were felt to make a new addition to published material were published. These are as follows:

i) A paper titled "Experimental and theoretical investigation of the effects of building scatter on site shielding" was presented at the fifth IEE international conference on antenna and propagation (ICAP '93) [Al-Nuaimi and Ding (1993)]

ii) A paper titled "Modelling and characterisation of building scatter of microwaves in site shielding", will be published in IEEE Transactions on Antenna and Propagation, August 1994 [Al-Nuaimi and Ding (1994)].

iii) A paper titled "Estimation models of radio path diffraction loss experienced by microwave signals in hilly terrain" was presented at the International Microwave Conference Brazil (SBMO 91) [Al-Nuaimi and Ding (1990)].

Additionally early work described in the thesis was presented at the National Radio Science Colloquium (URSI) held in Leicester 1991 (8th) and Bradford 1992 (9th). As well as these formal contributions regular technical reports have been presented to the management committees of COST programmes 210 and now COST 235. These committee papers are internal publications required to present research developments, aid discussions and form the basis of the final reports of the programmes. It is expected that the final report of COST 235 will contain significant material from work reported in this thesis. Further to this, results of work have been reported to UK Study Group 5 of the CCIR (now Study Group 3 of ITU-R). It is this Study Group that produces UK contributions to future recommendations and reports of the ITU-R for radio propagation in non-ionised media. It is expected that revisions will be made to CCIR report 569 [1990] in relation to building scatter in urban environments as a result of work performed at the University of Glamorgan. The custom of publishing on a four yearly basis is now changed and ITU-R will publish recommendations and reports as seen fit. This is to keep radio system users informed of the latest developments in recommended procedures.

8.3 Building scatter and site shielding

The methods and results reported in this thesis should provide the radio system planning engineers with the necessary tools to make reasonably accurate predictions of the level of building scatter likely to arise at a proposed radio terminal site in urban environments. The engineering model has been developed for the benefit of radio system planners and designers so that relatively straightforward predictions of the scatter levels can be made. In obtaining these predictions, the proposed procedure has succeeded in characterising building scatter from a specified building and in determining its effects on the site shielding factor (SSF)

offered by another obstacle. These effects could result in a quite dramatic reduction in the site shielding factor if the relative geometry of the building is such that radio terminal falls within the beamwidth of the scattering building. While building scatter is important in its own right as far as radiowave propagation in urban environment is concerned, the procedures and results contained in this thesis will form an important part of a generalised site shielding prediction procedure. This is one of the main tasks of COST Project 235.

8.4 Further studies

The scatter models described in the previous chapters have assumed radio path geometries which are in the main, well defined and clearly specified. Many discussions with radio system planners and users have indicated the need to consider geometries where it is not always possible to define accurately the building responsible for scatter or indeed parameters relevant to its scattering surfaces. For instance, data relating to the reflection loss coefficients of surface materials and structure variations may only be known in the form of global or average values which pertain to a particular category of the building content in a given area.

The background scatter which is well observed in practice is a good example of the type of interfering signal which arises due to contributions from various radio paths interacting at random. Some preliminary measurements have been conducted to characterise and verify the level of background scatter. The results are described in Al-Nuaimi and Ding [1994] using the concept of the radar cross section per unit area which may be employed to define the scatter signal level emanating from an urban environment situated in the beamwidth of a radio transmitter. The results show a background scatter level of around -30 dB which is highly consistent with the levels observed and measured in this investigation. This value is highly significant since it shows that an upper limit on the Site Shield Factor (SSF) exists and it is about 30 dB in an area containing several buildings.

Further modelling and measurements are planned to extend the models to more general path

geometries and to incorporate these models with building scatter and terrain database so that building scatter effects are appropriately accounted for in radio system planning and coordination.

In addition to building scatter, effects of other propagation mechanisms which arise in urban areas, e.g. diffraction over and around buildings, transmission through buildings and scatter from other objects, e.g. trees, should be included in a generalised site shielding procedure. As stated in the beginning these mechanisms have formed separate studies whose results are published regularly.

Appendix 1 Stationary phase method for double integral

Considering the double integral

$$I = \iint_D f(x,y)\exp[jKg(x,y)]dxdy \qquad a.1$$

in which the functions f(x,y) and g(x,y) are real and continuous over the domain D of the integration. Assume the g(x,y) is stationary for $K\to\infty$ at the point $x=x_0$, $y=y_0$ within D, so that

$$\left.\frac{\partial g}{\partial x}\right|_{\substack{x=x_0\\y=y_0}} = \left.\frac{\partial g}{\partial y}\right|_{\substack{x=x_0\\y=y_0}} = 0 \qquad a.2$$

Expanding g(x,y), in a Taylor's series in two variables at the stationary point gives

$$g(x,y) = g(x_0,y_0) + \frac{1}{2}\left[\xi^2 g_{xx} + 2\xi\eta g_{xy} + \eta^2 g_{yy}\right] + \ldots \qquad a.3$$

where $g_{xx} = \left.\frac{\partial^2 g}{\partial x^2}\right|_{\substack{x=x_0\\y=y_0}}$, $g_{xy} = \left.\frac{\partial^2 g}{\partial x\partial y}\right|_{\substack{x=x_0\\y=y_0}}$, $g_{yy} = \left.\frac{\partial^2 g}{\partial y^2}\right|_{\substack{x=x_0\\y=y_0}}$ and $\xi = x - x_0$, $\eta = y - y_0$.

Then according to the physical argument given above, for $K\to\infty$ the only significant contribution to the integral I comes from the neighbourhood of the stationary point. Hence it is given asymptotically

$$I \approx f(x_0,y_0)\exp[jKg(x_0,y_0)]\int_{-\infty}^{\infty}\int_{-\infty}^{\infty}\exp\left\{j\frac{K}{2}\left[\xi^2 g_{xx} + 2\xi\eta g_{xy} + \eta^2 g_{yy}\right]\right\}d\xi d\eta \qquad a.4$$

Using the standard integral

$$\int_{-\infty}^{\infty}\exp(-a^2 \pm jbx)dx = \sqrt{\frac{\pi}{2}}\exp\left(\frac{-b^2}{4a}\right) \qquad a.5$$

Let $a = j\frac{K}{2}g_{xx}$ and $b = K\eta g_{xy}$, then the double integral reduces to a single integral as

$$I \approx f(x_0,y_0)\exp\left[jKg(x_0,y_0)\right]\sqrt{\frac{j2\pi}{Kg_{xx}}}\int_{-\infty}^{\infty}\exp\left[j\frac{K}{2}\xi^2\left(g_{yy}-\frac{g_{xy}^2}{g_{xx}}\right)\right]d\eta \qquad \text{a.6}$$

Again, let $a=-j\frac{K}{2}\left(g_{yy}-\frac{g_{xy}^2}{g_{xx}}\right)$ and b=0, then

$$I \approx f(x_0,y_0)\exp\left[jKg(x_0,y_0)\right]\sqrt{\frac{j2\pi}{Kg_{xx}}}\sqrt{\frac{j2\pi}{K\left(g_{yy}-\frac{g_{xy}^2}{g_{xx}}\right)}}$$

$$\approx f(x_0,y_0)\exp\left[jKg(x_0,y_0)\right]\frac{\pm j2\pi}{K\sqrt{g_{xx}g_{yy}-g_{xy}^2}} \qquad \text{a.7}$$

Appendix 2 Fresnel integral derivation

The angular spectrum (in equation 3.23) with the near field path difference can be derived into the Fresnel integral. This is shown as below.

$$\int_{-\frac{a}{2}}^{\frac{a}{2}} \exp\left\{ jk\left[-\frac{x^2\cos^2\theta}{2r} + x(\alpha+\alpha_0)\right]\right\} dx$$

$$= \int_{-\frac{a}{2}}^{\frac{a}{2}} \exp\left\{ -j\frac{\pi}{2}\left[\left(\frac{2x\cos\theta}{\sqrt{2r\lambda}}\right)^2 - 2\left(\frac{2x\cos\theta}{\sqrt{2r\lambda}}\right)\left(\frac{\sqrt{2r\lambda}}{\lambda\cos\theta}\right)(\alpha+\alpha_0)\right.\right.$$

$$\left.\left. + \left[\left(\frac{\sqrt{2r\lambda}}{\lambda\cos\theta}\right)(\alpha+\alpha_0)\right]^2 - \left[\left(\frac{\sqrt{2r\lambda}}{\lambda\cos\theta}\right)(\alpha+\alpha_0)\right]^2\right]\right\} dx$$

$$= \exp\left[j\frac{\pi r}{\lambda\cos^2\theta}(\alpha+\alpha_0)\right]\frac{\sqrt{2r\lambda}}{2\cos\theta}\int_{-\frac{a}{2}}^{\frac{a}{2}} \exp\left\{ -j\frac{\pi}{2}\left[\frac{2x\cos\theta}{\sqrt{2r\lambda}} - \frac{\sqrt{2r\lambda}}{2\cos\theta}(\alpha+\alpha_0)\right]^2\right\}$$

$$d\left[\frac{2x\cos\theta}{\sqrt{2r\lambda}} - \frac{\sqrt{2r\lambda}}{2\cos\theta}(\alpha+\alpha_0)\right]$$

$$= \exp\left[\frac{j\pi r}{\lambda\cos^2\theta}(\alpha+\alpha_0)\right]\frac{\sqrt{2r\lambda}}{2\cos\theta}$$

$$\int_0^{\frac{a}{2}} \exp\left\{ -j\frac{\pi}{2}\left[\frac{2x\cos\theta}{\sqrt{2r\lambda}} - \frac{\sqrt{2r\lambda}}{2\cos\theta}(\alpha+\alpha_0)\right]^2\right\} d\left[\frac{2x\cos\theta}{\sqrt{2r\lambda}} - \frac{\sqrt{2r\lambda}}{2\cos\theta}(\alpha+\alpha_0)\right]$$

$$\int_0^{-\frac{a}{2}} \exp\left\{ -j\frac{\pi}{2}\left[\frac{2x\cos\theta}{\sqrt{2r\lambda}} - \frac{\sqrt{2r\lambda}}{2\cos\theta}(\alpha+\alpha_0)\right]^2\right\} d\left[\frac{2x\cos\theta}{\sqrt{2r\lambda}} - \frac{\sqrt{2r\lambda}}{2\cos\theta}(\alpha+\alpha_0)\right]$$

$$= \exp\left[\frac{j\pi r}{\lambda\cos^2\theta}(\alpha+\alpha_0)\right]\frac{\sqrt{2r\lambda}}{2\cos\theta}\left[\int_0^{u_2} \exp\left(-j\frac{\pi}{2}u^2\right)du + \int_0^{u_1} \exp\left(-j\frac{\pi}{2}u^2\right)du\right]$$

$$= \exp\left[\frac{j\pi r}{\lambda\cos^2\theta}(\alpha+\alpha_0)\right]\frac{\sqrt{2r\lambda}}{2\cos\theta}\left[F(u_2)+F(u_1)\right] \qquad \text{a.8}$$

where

$$F(u_2) = \int_0^{u_2} \exp\left(-j\frac{\pi}{2}u^2\right)du$$

$$F(u_1) = \int_0^{u_1} \exp\left(-j\frac{\pi}{2}u^2\right)du \qquad \text{a.9}$$

and

$$u_2 = \frac{a\cos\theta}{\sqrt{2r\lambda}} - \frac{\sqrt{2r\lambda}}{\lambda\cos\theta}(\alpha+\alpha_0)$$

$$u_1 = \frac{a\cos\theta}{\sqrt{2r\lambda}} + \frac{\sqrt{2r\lambda}}{\lambda\cos\theta}(\alpha+\alpha_0) \qquad \text{a.10}$$

Appendix 3 Scattering pattern beamwidth in the far field

When $\sin\left[\frac{\pi a}{\lambda}(\alpha+\alpha_0)\right]=0$, $\alpha+\alpha_0=\lambda/a$. If elevation angle ϕ is small, then it can be written as $\sin\theta+\sin\theta_0=\lambda/a$ at $\theta=-\theta_0\pm BW_a/2$ where BW_a is the beamwidth of the azimuth pattern between the first two nulls. Thus

$$\sin\left(-\theta\pm\frac{BW_a}{2}\right)+\sin\theta_0=\frac{\lambda}{a} \qquad \text{a.11}$$

Let $A=\frac{1}{2}\left(\theta_0-\theta_0+\frac{\pm BW_a}{2}\right)$ and $B=\frac{1}{2}\left(\theta_0+\theta_0-\frac{\pm BW_a}{2}\right)$. Thus, the left hand-side of equation a.11 is written as

$$\begin{aligned}\sin(A-B)+\sin(A+B)&=2\sin A\sin B\\&=2\sin\left(\frac{\pm BW_a}{4}\right)\cos\left(\theta_0-\frac{\pm BW_a}{4}\right)\\&=2\sin\left(\frac{\pm BW_a}{4}\right)\left[\cos\theta_0\cos\left(\frac{\pm BW_a}{4}\right)+\sin\theta_0\sin\left(\frac{\pm BW_a}{4}\right)\right]\end{aligned} \qquad \text{a.12}$$

Since building surfaces are very large apertures, BW_a is a very small angle. Then, $\cos\left(\frac{\pm BW_a}{4}\right)\approx 1$ and $\sin\left(\frac{\pm BW_a}{4}\right)\approx 0$ can be approximated, equation a.11 becomes

$$2\sin\left(\frac{\pm BW_a}{4}\right)\cos\theta_0\approx\frac{\lambda}{a} \qquad \text{a.13}$$

Thus

$$BW_a\approx 4\sin^{-1}\left(\frac{\lambda}{2a\cos\theta_0}\right)\approx\frac{2\lambda}{a\cos\theta_0} \qquad \text{a.14}$$

REFERENCES:

Abramowitz, M. and Stegun, I. A., "Handbook of mathematic functions with formulas, graphs, and mathematic tables", Dover, 1964

Al-Nuaimi, M. O. and Ding, M. S., "Estimation models of radio path diffraction loss experienced by microwave signals in hilly terrain", Proc. International Microwave Conference SBM091 Rio de Janeiro, Brazil, July 1991.

Al-Nuaimi, M. O. and Ding, M. S., "Experimental and theoretical investigation of the effects of building scatter on site shielding", 8th Inter. Conf. Antennas and Propagation, IEE Conf. Pub 370, pp.812-815, Edinburgh, UK, March 1993.

Al-Nuaimi, M. O. and Hammoudeh. A., "Theoretical and experimental and theoretical study of attenuation and scatter of microwave signals by trees", 8th Inter. Conf. Antennas and Propagation, IEE Conf. Pub 370, pp.808-811, Edinburgh, UK, March 1993.

Al-Nuaimi, M. O. and Hasllett, C. J., "Investigation of microwave diffraction and scatter by buildings at the Polytechnic of Wales", Internal Report, 1990.

Baker, B. B. and Copson, E. T., "The mathematical theory of Huyghen principle", Clarenton Press, Oxford, 1950.

Barclay, L. W., "the need for propagation studies", Jnl. IERE, Vol.58, 6 (supplement), pp.S135-S139, 1988.

Bahar, E., "Radio wave propagation over a rough variable impedance boundary: Part I - full wave analysis", IEEE Trans. Vol.AP-20, N0.3, May, 1972.

Bahar, E., "Scattering cross sections for random rough surfaces: Full wave analysis", Radio Science, Vol.16, No.3, pp.331-341, May, 1981.

Barnum, J. R., "High-frequency backscatter from terrain with cement-block walls", IEEE Trans. AP-19, No.3, pp.343-347, May, 1971.

Beckmann, P., "The depolarization of electromagnetic waves", the Golum Press, Boulder, 1968.

Beckmann, P. and Spizzichino, A. "The scattering of electromagnetic waves from rough surfaces", Pergamon, 1963.

Boithias, L., "Screening effect of the terrain for various propagation mechanisms", AGARD Conf. Proc. No.127, pp.S3/1-S3/9, Rome, Italy, May 1973.

Booker, "Slot aerials and their relationship to complementary wire aerials", IEE Proc. 93111A, pp.620-626, 1946.

Bramely, E.N. and Cherry S.M., "Investigation of Microwave scattering by tall buildings", Proceedings of the IEE, Vol.120, No.8, August 1973.

Causebrook, J. H. and Palmer, H. P., "Reflection and scatter of television signals by the blades of large wind turbines", IBC 86. International Broadcasting Convention, Brighton, UK, 1986.

Clarke, R.H. and Brown, J., "Diffraction theory and Antennas", Ellis Horwood, 1980.

Clemmow, P.C., "The plane wave spectrum representation of electromagnetic fields", Pergamon, 1966.

Collin, R. E. and Zucker, F. J., eds., "Antenna theory Part I", McGraw-Hill, 1969.

Fock, V. A., "Electromagnetic diffraction and propagation problems", Pergamon Press, 1965.

Freeman, R. L., "Radio system design for telecommunications (1-100 GHz)", Wiley-Interscience, 1987.

Giger, A.J. and Shapira, J., "Interference caused by ground scattering in terrestrial microwave radio systems", IEEE Inter. Conf. Commun., Boston, USA, June 1983.

Giger, A.J., Alley, G.D. and Sullivan, P., "Interference in radio relay systems caused by terrain scattering", IEEE Global. Tele. Conf., Houston, USA, December 1986a.

Giger, A.J., Alley, G.D. and Sullivan, P., "Time and frequency fluctuation of microwave interference due to terrain scatter", IEEE Global. Tele. Conf., Houston, USA, December 1986b.

Gould, R. G. and Schmitt, C., "Interference reduction techniques for satellite earth stations",

2nd symposium and technical exhibition on electromagnetic compatibility, pp.285-292, Montreux, Switzerland, June 1977.

James, G. L., "Geometrical theory of diffraction for electromagnetic waves", 3rd ed., Peregrinus, 1986.

Jordan, E. C., "Electromagnetic waves and radiating systems", Prentice/Hall, 1968.

Jull, E.V., "Aperture antennas and diffraction theory", Peter Peregrinus, 1981.

Keller, J. B., "Diffraction by an aperture", J. Appl. Phys., 28, 1957.

Keller, J. B., "Geometrical theory of diffraction", J.Opt.Soc. Am., 52, 1962.

Kerr, D. E., "Propagation of short radio waves", McGraw-Hill, 1951.

King, H. E., eds., "Tarrain backscatter measurements at 40 to 90 GHz", IEEE Trans. APS Vol.18, No.6, pp.780-784, November, 1970.

Kouyoumlian, R.G., "The geometrical theory of diffraction and its application", R. Mittra, 1975.

Lee, B. K., "Dynamic and static reflection of microwaves from buildings", The radio and electronic engineers, Vol.51, No.2, February 1981.

Lo, Y.T. and Lee, S.W., eds., "Antenna Handbook", Van Nostrand Reinhold Company, 1988.

Long, M. W., "Radar Reflectivity of land and sea", Lexington Books, 1975.

Lucia, E. F., "Additional measurements on pit shielding for communications satellite earth stations", IEEE Trans. on Aerospace and Electronic Systems, Vol. AES-8, 2, pp.251-253, 1972.

Lucia, E. F., "Artificial site shielding for communications satellite earth stations", IEEE Trans, Aerospace and Electronic Systems, Vol. AES-6, pp.612-619, September 1970.

Lucia, E. F., "Pit shielding reduction of interference between satellite earth stations and terrestrial radio-relay stations", NEREM'70, Rec., pp.230-231, November 1970.

McArthur, R. J. and Craig, K. H., "Propagation in the urban environment using building cover databases", URSI Commission F Symposium, Ravenscar, 1992.

Medgyesi-Mitschang, L. N. and Putnam, J. M., "Electromagnetic scattering from extended wires, and two- and three-dimensional surfaces", IEEE Trans. Antennas Propagat. Vol. AP-33, p.1090, 1985.

Millington, G., Hewitt, R. and Immirzi, F. S., "The Fresnel surface integral", Proc. IEE, 1962.

Newman, E. H. and Schrote, M. R., "An open surface integral formulation for electromagnetic scattering by material plates", IEEE Trans. Antennas Propagat., vol. AP-32, p. 672, 1984.

Noerpel, A. R., "Use of phasical optics to characterize building reflections", Conference Rec., IEEE Int. Conf. Commun., June 1986.

Noerpel, A. R. and Ranade, A., "Scattered microwave energy and building surface features", Globe COM'89 IEEE Global Telecom Conf&Exhibition, Vol.1, pp.72-77, 1989.

Ranade, A., "A computer simulation of local access radio interference due to building reflections", IEEE, ICC, pp.842-846, 1986.

Ranade, A. and Noerpel, A.R., "Microwave energy scattered off building surfaces shows strong dependence on orientation of city blocks," Electronics Letters, Vol.23, No.18, August 1987.

Rhodes, D. R., "Synthesis of planar antenna sources" Oxford, 1974.

Satoh, A. and Ogawa, E., "An evaluation method for the reflection coefficient of building walls", Elec. and Comm. in Jap., Part.1, Vol.73, No.3, pp.92-101, 1990.

Scheeren, P. M. J., "Interference reduction techniques for earth stations and the specific problem of near field site shielding against terrestrial interference", IEE colloquium digest No.1988/99, September 1984.

Shigekazu Shibuya, "A basic atlas of radio-wave propagation", Wiley-Interscience, 1987.

Silver, ed., "Microwave antenna theory and design", Peter Peregrinus, 1984.

Smith, W. E., Sullivan, P. L., eds., "Recent advances in microwave interference prediction", IEEE International Conference on Communications'87, Seattle, USA, June 1987.

Violette, E. J. and Espeland, R. H., eds., "Urban Millimetre Wave Propagation studies", U S Army Communications-Electronics Command Centre For Communication Systems, CECOM/DRSEL-83-3, April 1983.

Zamarayev, B. D. and Fuks, I. M., "Frequency and angle of incidence dependence of the average scattering coefficient of some surfaces", Eng. Trans. of Radiotekhnika, Vol.32, No.8, pp.160-162, August 1987.

Final report of Cost Project 210, "Influence of the atmosphere on interference between radio communications systems at frequencies above 1 GHz", CEC, EUR 13407, 1991.

CCIR Reports (Vol. V 1990):

Report 238, "Propagation data and prediction models required for terrestrial trans-horizon systems".

Report 382, "Determination of co-ordination area".

Report 569, "The evaluation of propagation factors in interference problems between stations on the surface of the earth at frequency above 0.5 GHz".

Report 715, "Propagation by diffraction".

Report 1054, "Interference in radio relay systems caused by terrain scattering".

Report1145, "Propagation over irregular terrain with and without vegetation".

Report 1146, "Terrain scatter as a factor in interference".